

Università degli Studi di Torino
Scuola di Dottorato

Fabrication and characterisation of luminescent point defects in solid-state platforms by keV ion implantation

Emilio Corte

Università degli Studi di Torino
Scuola di Dottorato

Dottorato in Fisica

Fabrication and characterisation of luminescent point defects in solid-state platforms by keV ion implantation

Emilio Corte

Tutor: Prof. Jacopo Forneris

Co-Tutor: Dott. Sviatoslav Ditalia Tchernij

1 Chapter 1 7
1.1.2 Single photon sources 7
1.1.3 Characterisation: Mathematical Models 9
1.1.4 Practical applications of quantum technologies 12
1.2 Diamond 16
1.2.2 Diamond properties 17
1.2.3 Production and classification 19
1.3 Point defects in diamond 22
1.3.1 Generation of colour centres 23
1.3.2 Classes of colour centres 25
2 Chapter 2 33
2.1 Ion matter interactions 33
2.1.1 Stopping Power 34
2.1.2 Straggling, ion distribution 39
2.1.3 Fabrication of colour centres by means of ion implantation and thermal annealing 41
2.1.4 Fabrication challenges 43
2.2 Electrostatic accelerators 45
2.2.1 Source area 45
2.2.2 Electric beam elements 47
2.2.3 Magnetic beam elements 48
2.3 Focused Ion Beams implanters 50
3 Chapter 3 52
3.1 Development of keV implanter 52
3.1.1 Source 53
3.1.2 Beam transport 55
3.1.3 Irradiation Chamber 59
3.2 ns-pulsed laser 63
3.3 Confocal Microscope setups 64
3.3.1 Spatial resolution and optical sectioning 64
3.3.2 Experimental implementation 67
3.4 Hanbury-Brown & Twiss interferometer 68
4 Chapter 4 72
4.1 Group IV colour centres 73
4.1.1 Diamond surface functionalisation for the tuning of the SnV spectral lines 73
4.1.2 Investigation of PbV colour centre upon diverse thermal annealing processes 83
4.2 Emerging classes of colour centres 98
4.2.1 Magnesium vacancy colour centre 99
4.2.2 Fluorine-based colour centre in diamond 111

5 Summary and discussion 117
6 Acknowledgements 120
7 Appendix I 121
7.1 Two level model 121
7.2 Three level model 123
8 Appendix II 126
8.1 Source and beamline software 126
8.2 Mass spectrometry software 128
8.3 Irradiation chamber software 129
9 Bibliography 131
10 Publications 146

Introduction

We are now in the middle of the Second quantum revolution. Respect to the first Quantum Revolution, where the aim was to understand the quantum laws and fundamental principles, now the goal is to employ the fundamental knowledge on quantum physics to realise devices exploiting such properties.

Among the most promising solutions based on quantum mechanics, photonic systems are the most studied since they allow to decode the information in the non-classical properties of light. Indeed, the second quantum revolution is based on sources of light emitting single photons defined as Single Photon Sources (SPSs in the following). The requirements for such sources are the hight emission rate, monochromacy, stability as stated by the Quantum Flagship.

The scientific research in the field of advanced technologies aims to develop devices more precise, more compact, more sensitive and faster in fields such as computing, cryptography and sensing among others. To reach such goal, different key requests must be met: the generation of reliable single photon sources, the implementation of reliable protocols to interact with quantum systems with high fidelity, high sensitivity at the nanoscale. The solid-state research and photonics have been conspicuously funded in recent years with the aim of realising compact quantum devices.

Fabrication of different systems based on solid-state platforms to generate SPSs, initialisation and readout of quantum systems with high efficiency and fidelity, such as the Optically Detected Magnetic Resonance (ODMR) for example, with solid-state based SPS, are possible solutions to reach the aims of the second Quantum Revolution. In this sense, this Dissertation is inserted in the research field related to the engineering of reliable SPS based solid-state platforms using low energy ion beam implantation to incorporate deterministically the defects in the host crystal.

Various platforms are being considered for the implementation of quantum technologies. These classes can be distinguished in probabilistic and deterministic. The firsts do not rely on trigger event to generate single photons and are based on probabilistic sources (i.e. attenuated lasers). The seconds are based on trigger events to generate single photons, among which point defects in diamond play an important role.

The choice of diamond as suitable platform is explained considering its peculiar properties. It is, in fact, a semiconductor with a large energy gap (5.5 eV), thus allowing to incorporate multiple energy levels in the gap acting as isolated molecule-like systems. Such value for the energy gap makes diamond transparent in the visible range, therefore the optically active defects in diamond are referred as *colour centres* (emitting photons in the visible range). Diamond is chemical inert and very stable, hence less prone to degradation. Due to the low density of phononic states at room temperature, the electronic transitions of the embedded impurities display a high quantum efficiency making those sources reliable for various applications.

Among the different optically active defects in diamond, the Nitrogen-Vacancy is the most studied to this date in literature due to its unique spin properties. In fact, it has been demonstrated to be an extremely responsive sensor at the nanoscale in fields as magnetometry, thermometry but it displays several drawbacks that makes it not the best option for quantum information protocols as SPS (broad emission, relatively low emission rate, presence of a metastable level). To overcome these limitations, other impurity-related defects have been studied such as the group IV-related (Si, Ge, Sn, Pb) in the recent years. Particularly the Sn-based defects display a great interest for their remarkable properties such as narrow emission line (referred as Zero Phonon Line), high emission rate, lower excited state lifetime with respect to the NV centre. The fabrication of reliable platforms based on these impurities is yet to be achieved. For example, due to the large masses with respect to the diamond lattice (particularly for Ge, Sn and Pb), different strategies are under exploration to comprehend the best and effective solution to properly fabricate single emitters with the desired optical properties such as the high-pressure high temperature thermal annealing (at temperature above 2000 °C and pressure of few GPa) or the chemical functionalisation of the diamond surface to stabilise the charge environment of the defects. Both techniques are discussed in the Result Chapter (4.1).

To further comprehend the large number of optical lines associated with diamond, other impurity-related defects have been recently explored (e. g. Magnesium and Fluorine-related) to keep researching for quantum emitters displaying optimal properties acting both as SPS or for sensing purposes that could meet the standard required for the implementation in quantum technologies.

The comprehension of deterministic protocols to fabricate reliable sources would then pave the way for the technological scalability of compact quantum devices. Different drawbacks need to be overcome for the deterministic fabrication: for example, the ion implantation is a versatile tool to deterministically place dopants in the host lattice, yet it produces also undesired defects that acts as decoherence sources for the SPS thus attenuating the sensitivity or the fidelity for quantum protocols. On this regard, ion implantation of heavy masses such as Sn and Pb impurities was performed to better comprehend the formation of both the interesting defects, SnV and PbV, as well as all the decoherence or undesired defects associated to the implantation that are not relevant for application in the Quantum Technologies field.
Another relevant issue related to the activation of such dopants in the host crystals is yet to be mastered, in fact the typical creation yield is in the order of few % for shallow emitters to few tens % for buried emitters (depth greater than few hundreds of nm). Different techniques can be explored to further push the knowledge on the processes involved in the fabrication of defects. Typically, the fabrication strategy relies on the ion implantation (discussed with higher degree of detail in Chapter 1.3) via both focussed beams or collimated beams at bot high energy regimes (MeV) and low energy regimes (keV).

As discussed, the ion implantation is a powerful technique to introduce dopants into semiconductors, in this regard part of the activity carried during the PhD was centred on the commissioning of the keV ion implanter at the Department of Physics in Torino. It was not possible to employ it for the implantations of the discussed samples since it was built and developed during the three years of activity (starting from the second) and hence it was mainly adopted to perform test and implantation for external users or it did not lead to data for this Dissertation.

This Dissertation is centred therefore on two main topics: the characterisation of solid-state based quantum emitters in diamond exploiting the ion implantation technique at keV energies primarily and under different post-processing functionalisation, standard furnace annealing, high-pressure high temperature annealing and chemical functionalisation of the surface. Along with the fabrication, the optical characterisation of these classes of emitters was performed under different experimental constraints with the aim of understanding the formation yield as well as their quanto-optical and spectral properties. Namely, various optical setups were adopted exploiting different excitation wavelengths, to probe the emission of the emitters and to gain a deeper understanding of their optical features, as well as different temperature regimes, namely cryogenic temperatures (from 8 K to 250 K) with the aim of reducing the phononic coupling of the emission lines as well as understand the possible occurrence of spectral features not observable at room temperature.

The Dissertation is thus divided as follows:

- Chapter 1: Introduction of the physical principles of a SPS and of the diamond properties along with the most relevant classes of known emitters.
- Chapter 2: Discussion of the ion-matter processes involved in the implantation and discussion of the ion implantation tool for the fabrication of SPS in diamond.
- Chapter 3: Description of the experimental apparatuses adopted.
- Chapter 4: Discussion of the main results obtained during the research work.

1 Chapter 1

In this chapter the main features and needs of photonic quantum technologies are introduced as well as potential applications. The definition of single photons sources is presented together with the mathematical formalism describing their properties. Finally, applications of single photon sources in quantum technologies are discussed.

Different single photon sources platforms are discussed with an emphasis on diamond as material and as a host platform for quantum light sources.

1.1.1.1 Quantum technologies

The second quantum revolution is based on the adoption of quantum systems for practical technological applications. Among different approaches based on quantum systems, key-enabling elements for the realisation of such technologies are photons, particularly single photons [1]. Generation and manipulation of systems emitting single photons is regarded as a cornerstone application such as quantum communication [2], computing [3], quantum sensing [4] and metrology [5].

Single photon sources are essential building blocks for photonic quantum technologies. In this section such systems are defined, different platforms are described, potential application are discussed. Finally, the experimental apparatus allowing for their characterisation is presented.

1.1.2 Single photon sources

Systems that emit single photons are of great interest for quantum optics protocols and are generally referred to as Single Photon Sources (SPS in the following). The ideal characteristics that a SPS should meet are the following [6]:

- Deterministic: emission of single photon upon proper excitation
- Monochromatic
- Photostable: no blinking behaviour or photobleaching
- High emission rate
- High quantum efficiency: low probability of non-radiative channels decay

Different platforms that allow to generate single photons are under investigation and are typically divided in two different classes: probabilistic and deterministic. Attenuated lasers, Parametric Down conversion belong to the first class; in the second class fall quantum dots, cold atoms and solid-state defects. The core of this Dissertation is the characterization of sources in wide gap materials and therefore it will be discussed with more emphasis this class of SPS. The main definitions are taken from refs [6], [7], [8].

Probabilistic Sources

Probabilistic sources are those that emit single photons without an external trigger, but they rely on probabilistic methods. The typical SPS generation has a probability lower than unity [9].

To this class belong attenuated lasers and parametric down conversion among the others.

Attenuated lasers rely on a strong attenuation pulsed laser so that statistically a single photon per pulse is generated. To reach ~pW from a mW optical power, it is performed an attenuation of a factor 10^{10} with a neutral filter, thus corresponding to an emission rate of 10^6 Hz. The simplified operational scheme is reported in Figure 1.2.1a.

Such method can be comfortably performed and it provides monochromatic (since it is employed a laser as source) single photons that follows a Poissonian distribution:

$$P(n) = \frac{e^{-m}}{n!} m^n \qquad \text{Eq. 1.2-1}$$

Where P(n) is the Poissonian distribution, m = $\frac{2\pi E}{hv}$, E the pulse energy, h the Plank constant, v the photon frequency. Being based on a probabilistic generation, the probability of generating no photons per pulse or multiple photons is rather large. For example for a red laser with energy of 2 eV, a number of emitted photons per time m=0.1, the probability of emitting zero photons P(0) = 90%, one photon P(1) = 9%.

The parametric down conversion is a system whose working principles consist of the generation of a pair of correlated photons. Its schematic representation is displayed in Figure 1.2.1b, a laser beam impinges on a non-linear crystal and the generation of the pair is performed. Such phenomenon is parametric, since there is no energy transfer and the conservation of energy and momentum determines the vector relations between the pumping laser and the generated pair of photons. This condition is referred as Phase-Matching [10]. The emitted photons, referred as idler and signal, displays non-classical properties and they are typically adopted in the quantum cryptography field [11]. The main drawback of this technique is the low emission efficiency which is in the order of 10^{-10}.

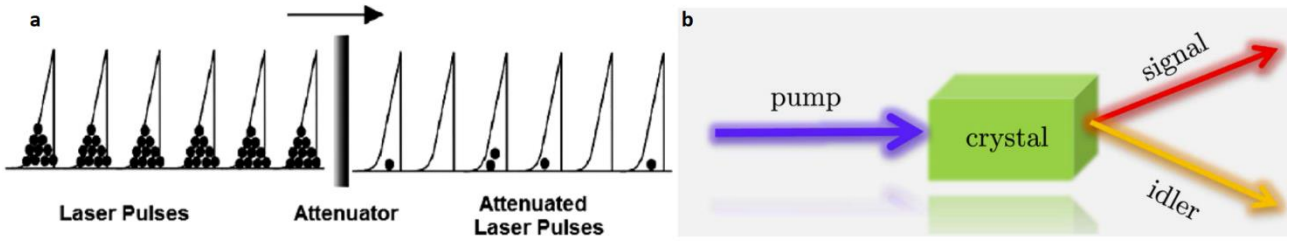


Figure 1.2.1 Probabilistic sources simplified scheme. a) Attenuated laser source. b) Parametric down conversion implementation scheme. Sources from [10], [12].

Deterministic Sources

Deterministic sources are those that emit single photons when triggered by an external input such as laser or electrical pulse.

To this class belong cold atoms, quantum dots and solid-state defects. A more detailed description of solid-state platforms (diamond-based) is given in Chapter 1.3.

Atomic transitions of cold atoms trapped in cavities can be used to generate single photons, such systems offer the on-demand generation of single photons with high indistinguishability but they their implementation is complex because of the need of high vacuum apparatuses and cryogenic temperatures. These systems consist in optical resonators (referred as Quantum Electrodynamics QED) with trapped atoms inside [8], [13]. The SPS generation is achieved exploiting the atomic transitions of the trapped ions upon electromagnetic excitation [13].

Quantum dots are nanostructures embedded in semiconductors obtained via epitaxial growth [14], [15], a defined gap semiconductor is grown on a larger gap semiconductor that produces confined electronic levels. The carriers can be confined in the structure and optical transitions can occur. Its functioning requires cryogenic temperature typically causing a technological disadvantage. Yet, quantum dots are SPSs with a highly monochromatic emission, hence very suitable platforms for the generation of single photons [16].

Solid-state defects

Optically active point defects in solid-state platforms display SPS properties, typically semiconductors. These sources are obtained exploiting the electronic transitions between the discrete energy levels that are found in the energy gap. The transitions can be triggered deterministically with a laser pulse and several SPS are found to be attractive for the quantum technologies due to their peculiar properties. Among the advantages regarding these classes of SPS, the most relevant is the possible operation capabilities at room temperature, making them easy to control and cost-effective the apparatuses to interface to these SPSs.

The technological advantage is also related to the mature process of the synthesis of the host matrix [7]. The request for ultrapure substrates is crucial to fabricate reliable SPSs in semiconductors, hence minimising the presence of undesired traps that would act as decoherence sources.

The point defects in semiconductors are referred as colour centres since the electronic transitions give rise to luminescence in the visible range (from the UV to the NIR). An overview of diamond-based colour centres is discussed in Chapter 1.3.

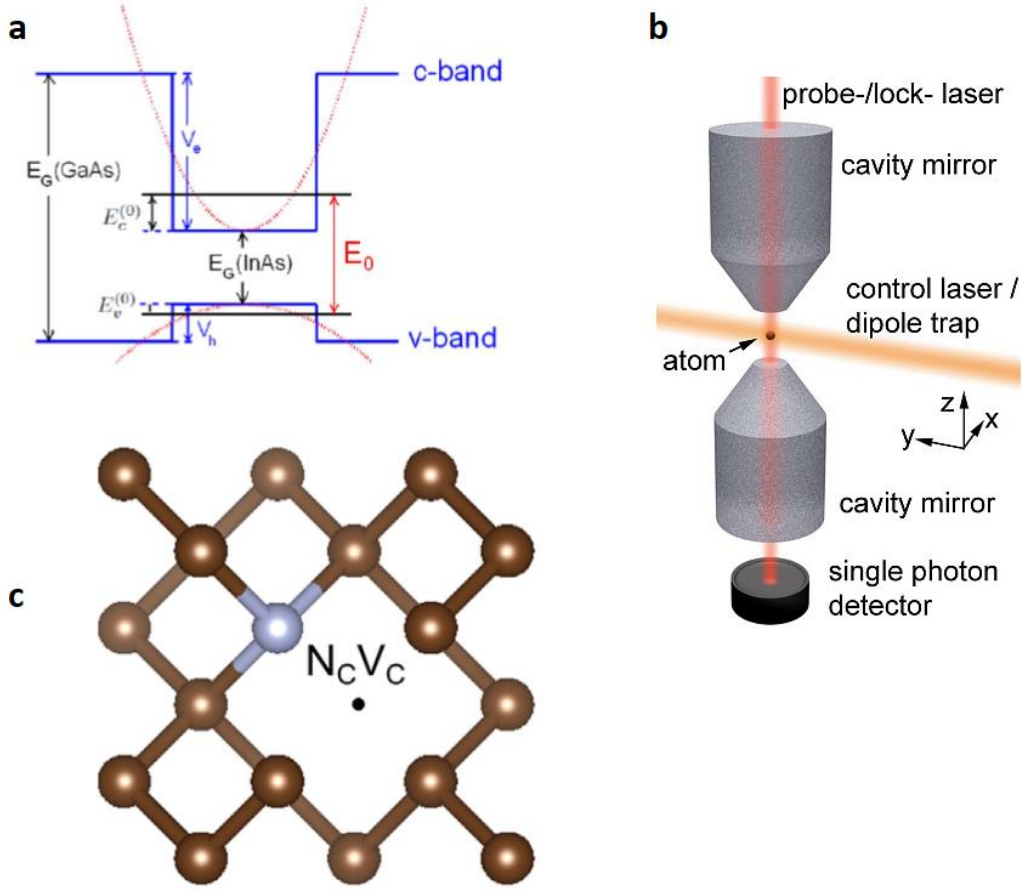


Figure 1.2.2 Scheme of the deterministic SPSs. a) Representation of the energy levels of the InAs quantum dot in a GaAs substrate. B) scheme of the QED cavity. C) Nitrogen Vacancy colour centre in diamond Lattice, the grey atom represents the N while the missing brown point represents the diamond vacancy. Figures from [17], [18], [19].

1.1.3 Characterisation: Mathematical Models

It is here discussed the mathematical model that describe the emission statistic of an electromagnetic radiation source. The main experimental technique to characterise a light source is the second order autocorrelation function along with the Hanbury-Brown and Twiss interferometry.

Three main statistics describe the light sources: sub poissonian, poissonian, super poissonian. These statistics allow to describe the nature of the emitted photons by the source. In the following cases, n represents the number of emitted photons.

1. Super Poissonian

Thermal light: An example of light following a super-poissonian type of statistic is the thermal light. The wire of a light bulb when the current flows through it, emits packets of light due to fluctuations of intensity of the source itself. The statistics that follow the photons emitted from a source of this type is that of Bose-Einstein, where λ is the mean value and Δn the standard deviation. This implies a maximum probability for simultaneous emission of photons that are hence grouped in packets.

$$P(n)=\frac{1}{1-\lambda}\left(\frac{\lambda}{1+\lambda}\right)^n \qquad \Delta n > \sqrt{n}$$ Eq. 1.2-2

2. Poissonian

monochromatic light: A laser source reflects the most representative case of a Poissonian-type temporal statistics of photons, with expression and related error in the following expression, where λ is the mean value and Δn the standard deviation. This means that it exists an equal probability of emitting photons in every time lapse.

$$P(n)=\frac{\lambda^n}{n!}e^{-\lambda} \qquad \Delta n=\sqrt{n}$$ Eq. 1.2-3

3. Sub Poissonian

A quantum source, such as an emitter of a single photon, has a sub-Poissonian distribution, with a standard deviation lower than the Poissonian case, which cannot be explained from the classical point of view. This means that it exists a maximum probability of emitting photons individually.

$$\Delta n < \sqrt{n}$$ Eq. 1.2-4

The concept of coherent states is introduced along with the criterion adopted to characterise the electromagnetic source under analysis formalised by the second order autocorrelation function [20]. The equation is reported in the following:

$$g^{(2)}(t) \equiv \frac{\langle \overrightarrow{E^*}(\vec{r}_1,t_1)\cdot\overrightarrow{E^*}(\vec{r}_2,t_2)\cdot\vec{E}(\vec{r}_1,t_1)\cdot\vec{E}(\vec{r}_2,t_2)\rangle}{<|E(\vec{r}_1,t_1|^2>\cdot<|E(\vec{r}_2,t_2)|^2>}$$ Eq. 1.2-5

Where E is the electric field at the position and time $\vec{r}_{1/2}, t_{1/2}$, <> represents the mean value. For a plane stationary wave approximation, the function becomes:

$$g^{(2)}(t) \equiv \frac{\langle I(t_0+t)\cdot I(t_0)\rangle}{\langle I(t_0)\rangle^2}$$ Eq. 1.2-6

Where I = $|E(t)^2|$; t_0 t_2-t_1 and t = t_1.

In quantum formalism the electric field can be rewritten in terms of annihilation and creation operators [20]. The rules for a generic Fock state |n> are reported as follows:

$$\hat{a}\,|n> = \sqrt[2]{n}\,|n>$$
$$\widehat{a^\dagger}\,|n> = \sqrt[2]{n+1}\,|n+1>$$
$$\left[\hat{a}(t_0);\widehat{a^\dagger}(t_1)\right]= \partial_{t_0,t_1}$$
$$\widehat{a^\dagger}\,\hat{a}=\hat{n}$$
$$\hat{n}\,|n> =n|n>$$ Eq. 1.2-7

The second order autocorrelation function becomes as follows:

$$g^{(2)}(t) = \frac{\left\langle \widehat{a^\dagger}(t_0+t)\cdot\widehat{a^\dagger}(t_0)\cdot\hat{a}(t_0+t)\cdot\hat{a}(t_0)\right\rangle}{\left\langle \widehat{a^\dagger}(t)\cdot\hat{a}(t)\right\rangle^2} \qquad \text{Eq. 1.2-8}$$

Where $E^* \propto \widehat{a^\dagger}$; $\vec{E} \propto \hat{a}$.

Finally, considering the simultaneous emission:

$$\lim_{t\to 0} g^{(2)}(t) = \frac{<\widehat{a^\dagger}\widehat{a^\dagger}\hat{a}\hat{a}>}{<\widehat{a^\dagger}\hat{a}>^2} = \frac{<\hat{n}^2>-<\hat{n}>}{<\hat{n}>^2} \qquad \text{Eq. 1.2-9}$$

The variance of the distribution is defined as follows:

$$\Delta n^2 = <n^2> - <n>^2 = <\widehat{a^\dagger}\hat{a}\widehat{a^\dagger}\hat{a}> - <\widehat{a^\dagger}\hat{a}>^2 \qquad \text{Eq. 1.2-10}$$

Inserting $\Delta n2 = <n^2> - <n>^2 = <\widehat{a^\dagger}\hat{a}\widehat{a^\dagger}\hat{a}> - <\widehat{a^\dagger}\hat{a}>^2$ Eq. *1.2-10* in $limt\to 0 g2t = \frac{<\widehat{a^\dagger}\widehat{a^\dagger}\hat{a}\hat{a}>}{<\widehat{a^\dagger}\hat{a}>^2}$ = $\frac{<\hat{n}^2>-<\hat{n}>}{<\hat{n}>^2}$ Eq. *1.2-9*, it is obtained the second order autocorrelation function in terms of the variance:

$$g^{(2)}(0) = \frac{<\hat{n}^2>-<\hat{n}>}{<\hat{n}>^2} = \frac{\Delta n^2 - <\hat{n}>}{<\hat{n}>^2} + 1 \qquad \text{Eq. 1.2-11}$$

Depending on the nature of an electromagnetic source, three different emission statistics can be then outlined:

1. Sub-Poissonian: Quantum light such as a single photon source.
   $\Delta n^2 < <n>$ and therefore the $g^{(2)}(0) = 0$
2. Poissonian: Monochromatic light such as a laser.
   $\Delta n^2 = <n>$ and therefore the $g^{(2)}(0) = 1$
3. Super-Poissonian: Thermal light such as the filament of a bulb
   $\Delta n^2 > <n>$ and therefore the $g^{(2)}(0) > 1$

In Figure 1.2.3 it is reported the second order autocorrelation function for the three treated cases. The green curve represents the thermal light, the photons are bunched and emitted as packets. The random source is represented with the yellow curve, since the photons are emitted with a random rate, the function has a fixed value of one in the whole time-interval. The quantum light is represented with the red curve. Since only one photon can be emitted from such source, the function presents a minimum (referred as anti-bunching behaviour) for τ = 0.

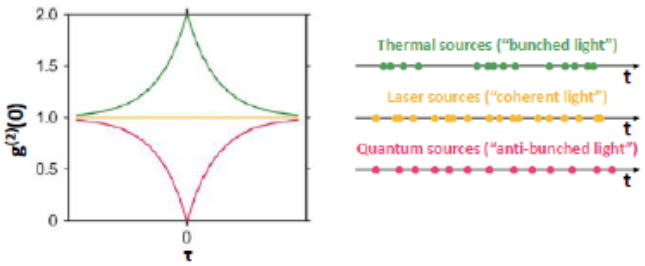


Figure 1.2.3 Second-order autocorrelation function for the three cases: green curve is the thermal source; yellow curve is the coherent case and red curve is the quantum source. Figure from [21].

1.1.4 Practical applications of quantum technologies

Among the main application fields of quantum technologies there are quantum sensing, computation, cryptography and metrology. A brief description of sensing, cryptography and metrology is presented in the following.

Quantum sensing

A quantum sensor is a device that possesses quantum properties that can be adopted to detect with greater precision with respect to classical sensors. Such properties are quantum in nature such entanglement of states, quantum interference, squeezing, coherence. The quantum devices must meet different criteria to be employed as sensors [4]: a system with discrete and resolvable levels with the possibility to be initialised to perform a readout of the quantum state, coherence should be a key parameter allowing to manipulate the sensor and finally the device must interact with external fields with tangible response to be read out. The realisation of these devices can be performed with different platforms, depending on the physical properties to be detected; for example, spin-based systems are more susceptible to magnetic fields while charged systems to electric fields [4]. A key parameter is referred as sensitivity, the response to external fields from the sensor. Sensitivity scales typically as [4]:

$$\frac{1}{\gamma\sqrt{T_x}}$$

Where γ is the transduction parameter and T_x the decoherence time scale of the system. The ideal sensor should interact with low noise with external fields, decoherence is a quantity that mirrors the non-susceptibility to noise.

Specific classes of SPS can be used in the field of high-precision sensing. Particularly, certain classes of solid-state SPSs are employed for magnetic field sensing [22], [23] and temperature sensing [24]. Among the most used solid-state SPSs for sensing applications, the Nitrogen-Vacancy centre (NV) in diamond [25] is one of the most studied and employed. The negatively charged configuration of this colour centre is widely used as magnetic field sensor, reaching a sensitivity down to 7 $\mathrm{nT}/\sqrt{Hz}$ [26].

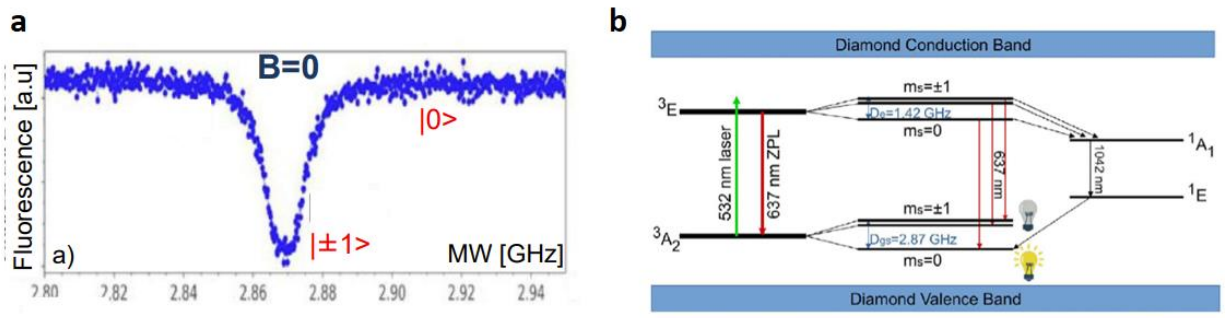


Figure 1.2.4 a) ODMR spectrum of the NV⁻ colour centre under no external magnetic field applied. b) Energy diagram of the NV⁻ centre in diamond. Figures from [25].

The technique adopted to probe the NV centre as sensor is referred as Optically Detected Magnetic Resonance (ODMR in the following). This technique allows to initialise and readout the spin state of the defect as follows: a 532 nm laser (green pulse arrow in Figure 1.2.4b) promotes an electron to the excited state that decay radiatively with a ZPL of 637 nm (red arrow in the Figure). The system is hence initialised meaning that the electron is in the m_s=0 state. If a Radio Frequency is applied, it can be matched the energy difference between the m_s =0 and m_s =±1 states (referred as Zero Field Splitting) thus promoting the electron to the m m_s ±1. This phenomenon causes a decrease in the PL signal (as depicted in Figure 1.2.4a) because the probability of non-radiative paths during excitation and relaxation cycles.
Alternatively, to NV^-, other colour centres such as the Silicon Vacancy (V_{si}^-) in silicon carbide have been proved to be promising systems for magnetic field [27] and temperature sensing [28].

Along with the NV^- centre, other colour centres can be adopted for temperature sensing. Particularly, the group IV emitter (discussed more in detail in Chapter 1.3.2.2) displays interesting properties making them potential temperature sensors with high sensitivity [29] (i.e. for the SnV colour centre, the temperature sensitivity is estimated to be 0.501 mK/Hz). The Group IV- related colour centres display interesting spectral features (high Debye Waller Factor) having most emitted photons in the ZPL.

Quantum cryptography

The cornerstone on which these techniques are based consists of the encoding a private message through a private key, only known by the sender and the receiver, which is indecipherable by an external hand. Modern cryptography is based on symmetric and asymmetric encoding keys. The first is based on the sharing of the same key for the reading and protection of the message. The second approach consists of using two separate private keys related to the encryption and the decodification of the message. The safety of both approaches, however, is based on the complexity of the correlation between the keys and with a quantum computer, if equipped with superior computational capabilities, could decipher such keys.

Quantum cryptography is a method that permits to encode information in polarised states of light. The protocol on which quantum cryptography is based is referred as Quantum Key Distribution (QKD) and the main difference with respect to classical approaches are the followings [30]:

- It is based on universal physical laws and mathematical proof of inviolability (Shannon's Theorem).
- It allows to reveal a potential eavesdropper.
- The no-cloning theorem ensures the impossibility of measuring a quantum state without perturbing it and therefore with the eventual loss of the information.

Among the different quantum cryptography schemes, the main protocol is called BB84 and was demonstrated in 1992 using attenuated coherent sources [31], [32].
In Figure 1.2.5 it is reported the scheme of the quantum cryptography between the sender Alice and the receiver Bob along with the eavesdropper Eve.

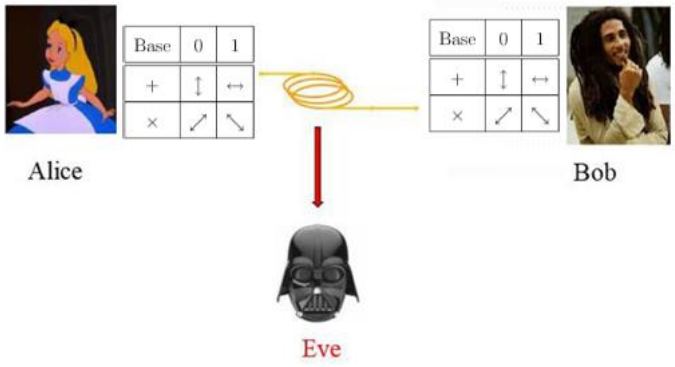


Figure 1.2.5 Quantum cryptography scheme. The base is written with binary representation.

Two channels for the communication are available: the classical and quantum channels. Alice sends a random sequence of single photons with defined basis to Bob via the quantum channel. Two bases are available and both have a defined polarisation state (0 or 1).
Bob selects randomly one of the two available bases for the decoding of the message sent by Alice. As the Heisenberg uncertainty principle states, If Bob chooses the correct base (i.e. the codification base), Bob will be able to measure the polarisation of the photons. Otherwise, the result is random, this means that Bob has a 50% probability of measuring 0 or 1.

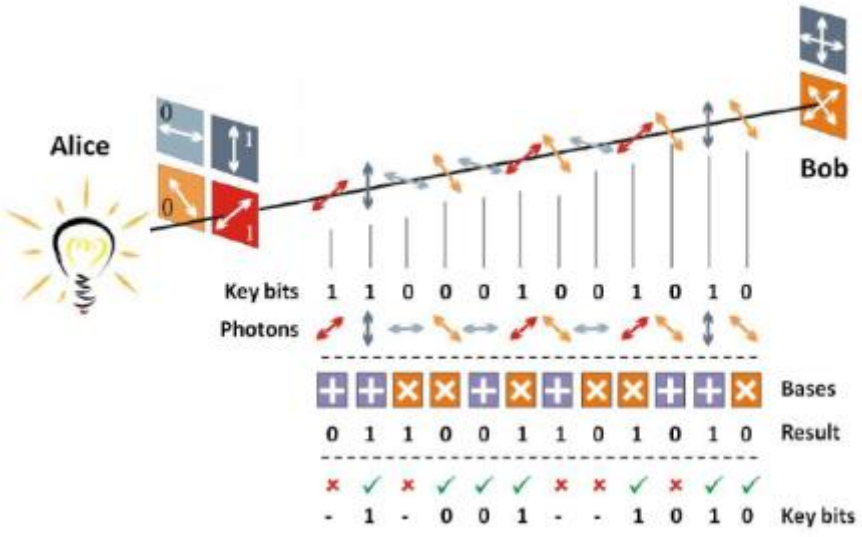


Figure 1.2.6 Schematic of the principles of the BB84 protocol. Figure from [33].

Bob sends to Alice via the classical channel the base sequence he selected for the polarisation measurement, hence fixing the photon subset with correct polarisation detection. Due to the nature of the public channel, the communication is carried out diverting the revelation of the outcome of the photons' polarisation bases.

Hence, the photon' subset displaying the correct base is then used as encoding key for the communication through the public channel.

The intrinsic key security is assured by sacrificing a portion of the key to verify the correspondence between the sender and the received bits: alterations in the bit sequence generated by Alice are used as an indicator of eavesdropping; the most important alterations are *bit flips*, i.e. non-correspondence between bits sent by Alice and the same bit received by Bob with the same base. If the occurrence of bit flops exceeds 12.5% the communication is interrupted, and the current key is destroyed to avoid exposing the encoded message.

Quantum metrology

In the field of metrology SPS represents an ideal candidate for the redefinition of the fundamental unit of measurement for intensity of light, the Candela [cd]. Historically the candela is defined as follows [34]: a source emits an intensity brighter than 1 cd in a given direction if its radiation is monochromatic with a frequency equal to 540 x 10^{12} Hz and its radiant intensity equal to 1/683 W per steradiant. In perspective, it is possible to provide an equivalent expression of the Candela in terms of the emitted photons, laying the foundation for its quantum realisation via an optical power measurement in agreement with Planck's law:

$$P = Nhv$$

Where N is the number of photons, h the Planck constant, v the frequency. With the above-mentioned definition, N is equal to 40.919429 10^{15} s^{-1}. The definition of the cd evolved from an artefact based on the emission by a black body to a more general definition allowing different realization techniques, based on the existence of known relation between lumen/Watt ratio at different frequency [35]. However, photometric quantities are integrated over a range of wavelengths and to derive photometric quantities from radiometric measurements it is necessary to weight those through an appropriate standard efficiency function.

The Consultative Committee for Photometry and Radiometry [35] introduced a fundamental constant of radiometry, the constant K_{CD}, where CD indicates the unit of luminous intensity and has been defined as 555 nm. The intensity is then defined as follows:

$$I(\lambda) = K_{CD} P_0(\lambda) V(\lambda)$$

where the terms represent in order the sensitivity curve at V(λ), P_0 the optical power.

The current standard for determining this quantity is that of the cryogenic radiometer shown in Figure 1.2.7. The optical power absorbed by a black body cavity is compared to that of electrical power supplied by a calibrated heat source. The lower limit of the sensitivity of this technique corresponds to values in the order of > 1 μW of optical power absorbed. Using an SPS the parameter P_0 becomes a function of a single wavelength and it can therefore be rewritten as follows:

$$P_0 = N_o \frac{hc}{\lambda_0} f$$

where N is the previously mentioned number of photons emitted, $\frac{hc}{\lambda_0}$ is the energy of SPS, f the repetition rate of the source.

The measurement of optical power corresponding to the emission of single photons of energy of 2 eV at a rate of 1000 kHz would correspond vice versa to 3.2 x 10^{13} W, i.e. a value 6 orders of magnitude lower, allowing to extend the candle's traceability range to the discrete packet regime of photons.

Therefore this new realization of the Candela, based on an a quantum emitter of photons is potentially capable of further reducing the certainty beyond the current relative value of (2 x 10^{14}), and thus the radio conventional cryogenic meter, used for absolute radiometric measurements on macroscopic scales (for incident optical powers of the order of mW) allowing to extend the traceability in the measurement regime of discrete packets of photons (P < 1 pW) [35].

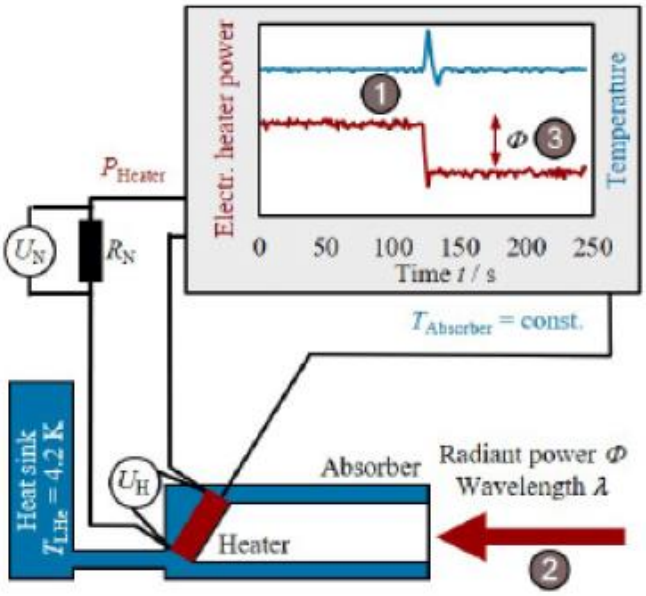


Figure 1.2.7 Schematic representation of a cryogenic radiometer. Figure from [36].

1.2 Diamond

Diamond is a promising material for technological applications due to its unique extreme properties. In this chapter the main properties of diamond are introduced, with an emphasis on the technological maturity of the material at the state of art for the engineering of optically active point defects.

Diamond has a crystallographic form based on carbon atoms. Carbon has an electronic configuration [He]2s2p and it has different allotropic forms, diamond and graphite but also carbon nanotubes, fullerene and particularly interesting graphene, a single layer of carbon atoms with remarkable properties.

The phase diagram of carbon, as depicted in Figure 1.2.1, shows that at room temperature and pressure conditions graphite is the stable form, offering a maximum binding energy. Diamond is thus a metastable form of carbon, however the potential barrier that needs to be observe a spontaneous conversion to graphite is high enough (about 2 eV) [37] to prevent this from happening.

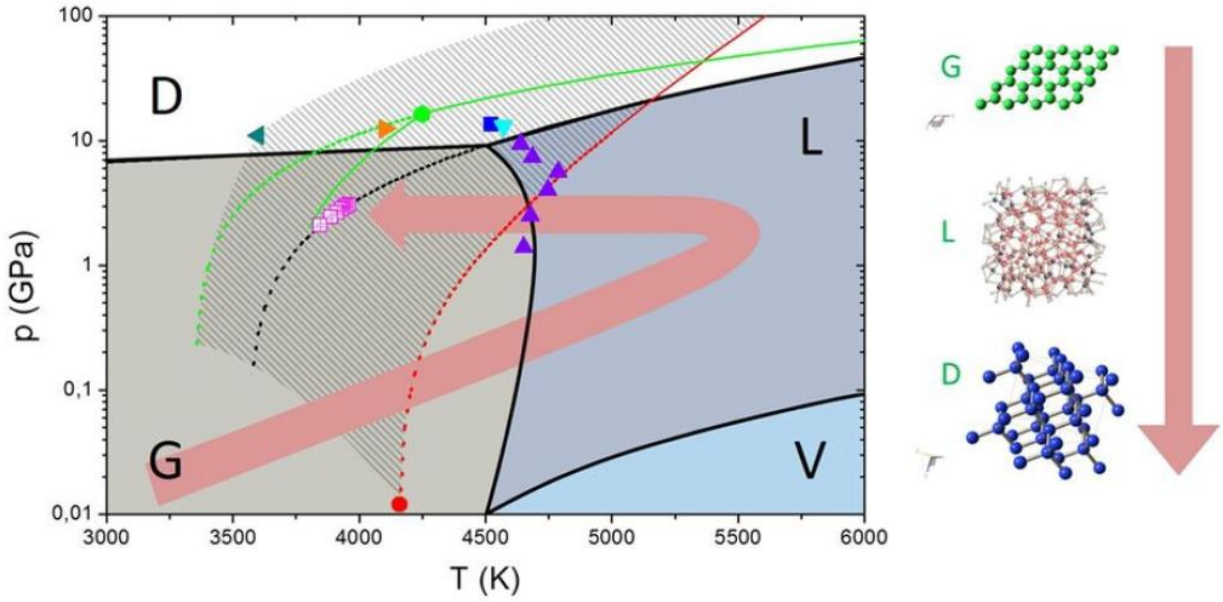


Figure 1.2.1 Phase diagram of carbon. Figure from [38].

1.2.1.1 Crystallographic structure

Diamond is formed by carbon atoms ordered in tetrahedral configuration. This is caused by the electronic configuration with which the atoms bond in the lattice at a distance of 1.54 Å: the orbitals 2s $2p_{xyz}$ tie together forming 4 covalent bonds hybridized sp^3 with the 4 neighbours at a distance of 109°. The lattice configuration is described by a faced-centred cubic geometry with 2 carbon atoms at the position (0; 0; 0) and $(\frac{1}{4};\frac{1}{4};\frac{1}{4})$ with lattice parameter a = 3.57 Å. Atomic density and mass density of diamond are respectively $1{,}77\times10^{23}$ atoms·cm^{-3} and 3.54 g·cm^{-3} [39] .

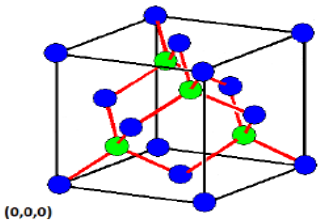


Figure 1.2.2 Diamond primitive lattice cell.

1.2.2 Diamond properties

The extreme properties cited at the beginning of this section are here described: particularly mechanical, electronic and electrical, chemical and optical.

1.2.2.1 Mechanical Properties

Diamond has a binding energy of 7.73 eV, it is a high value respect to silicon (4,63 eV), the most similar crystal from a structural point of view. Such value is responsible for certain properties such as Young Modulus (1220 GPa) and the sound velocity (18 kms^{-1}), the hardness ranks highest in the Mohs scale [40].

The density of phononic states (DOS) shows a large number of available states at high frequencies (1.6 THz) as shown in Figure 1.2.3, this justifies the Deby Temperature particularly high (2200 K) [41]. At room temperature the number of occupied states is very low respect to other crystals, this reflects little probability of phononic collisions granting diamond a high thermal conductivity.

1.2.2.2 Electronic and electrical Properties

Carbon has an electronic configuration $1s^1\ 2s^2\ 2p^3$. Since in diamond each carbon atom is bound to 4 first neighbours, in tight binding approximation, the band structure calculation should consider only the 2s and 2p electrons. Such configuration can be seen as four electrons described by the hybridized sp^3 orbitals. The band structure (reported in Figure 1.2.3) is similar to other semiconductors such as Silicon and Ge[41]. The four orbitals generate eight sub-bands. Four are filled and correspond to bonding states, the valence band is constituted of these four sub-bands. The remaining four correspond to anti-bonding states (referred as conduction sub-bands). Between Γ and X direction (in the first Brillouin zone) the conduction band has a minimum, its sub-bands are crossing each other in several points resulting in an articulated shape. Valence band has a minimum in the Γ point; two sub-bands are degenerate at this point and they are referred as *heavy-hole* and *light-hole* sub-bands. The third sub-band has a minimum again in the Γ point but, due to spin-orbit interaction, its energy is split downward, it is referred as *split-off* band (not shown in Figure 1.2.3). The last sub-band is the one corresponding to the most bonded configuration and its curvature is inverted respect to the other three.

Diamond has an energy gap on 5.47 eV determining it insulating behaviour but it can be more properly described as a semiconductor with a large gap, denoted by optical transparency in a wide range of wavelengths. In fact, doping can be exploited to tailor its electrical properties. Dopants can be introduced in the lattice during the synthesis [42] as well as by ion implantation and subsequent annealing [43]. Boron and phosphorus are the most common and they induce p-type and n-type conductivity respectively. Their incorporation in diamond is challenging due to their high activation energy, respectively 0.37 eV for B above the valence band and 0.57 eV for phosphorus below the conduction band [44], [45].

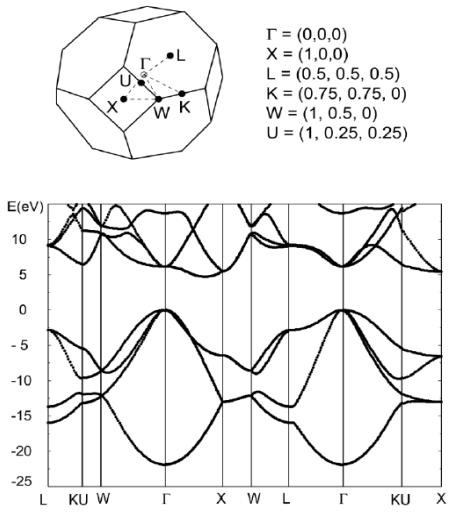


Figure 1.2.3 Diamond crystallographic and band diagram [46].

Chemical functionalization can also be exploited to tune the surface conductivity of diamond: p-type conductivity can be obtained upon hydrogen termination [47]. Hydrogen saturates the dangling bonds of the surface inducing a low ionisation energy favouring electron transfer from valence band to physisorbed

adsorbate, like water [48]. Oxygen is also used to modify surface conductivity but, on the opposite, it induces insulating behaviour.

1.2.2.3 Optical Properties

Diamond is transparent in the visible range due to its large bandgap energy. Its absorbance due to indirect inter-band transitions starts from 225 nm [49] towards the infrared. IR absorption is very weak. This lies in the fact the diamond is a covalent crystal and therefore do not possess a permanent dipole moment. Nevertheless, despite being not much probable, transitions in the two/three-phonon region occur [49] Such absorption is two-three orders of magnitude weaker with respect to ionic crystals. For this reason, diamond is adopted also in IR spectroscopy and in particular for TIRF (Total Internal ReFlection) technique where also a high refractive index is required. Ideally diamond has only two absorption bands but defects affect its transmittance. Dispersed nitrogen can give rise to a more intense in the blue and less in the red resulting in a yellowish colour, as for HPHT diamonds [50].

Diamond has one of the highest refractive index among crystals transparent in the visible range, this is due to the high density of the lattice and polarisability. The mean value is n = 2.42 [49]. Reflectance reaches a value of 17% which means that a high portion of the incident light is backscattered. For application in quantum optics the polishing of the surface is particularly important reducing the dispersed light, however being one of the hardest material such technique is not trivial.

It is worth mentioning the Raman scattering of diamond, particularly the first and second order respectively at 1332 cm^{-1} and 2467 cm^{-1} [49]. The first order Raman scattering peak is intense and sharp with FWHM typically in the order of 5 cm^{-1}. The second order is weaker in terms of luminescence and consists in a more articulated band ranging for ~ 300 cm^{-1}.

1.2.2.4 Chemical Properties

The crystalline structure and high binding energy make diamond chemical inert. This allows to chemically functionalize the surface. Oxygen or hydrogen are typically adopted to saturate the dangling bonds of the surface changing the conduction properties or to control the charge state of the shallow defects [51], [52]. This particular property was explored during the research work carried out during the three years' work.

Surface termination can be achieved upon different approaches: thermally induced[53]; exploiting wet chemistry approaches [54]; microwave plasma induced [55].
The termination of the surface dangling bonds induces not only diverse electrical conductivities, but it allows to study the effect of water absorption on the surface, particularly the H-terminated surface hydrophobic and the O-terminated surface has a hydrophilic behaviour enabling the use of such diamond particles (typically having nanometric or micrometric size) in biomedical fields [56].
Diamond displays another interesting property being biocompatible [57], being entirely carbon-based completely and chemical inert: this feature motivated the Research Community to use this material for biosensing [58] and in-situ dosimetry applications [59]. Diamond is a suitable material to develop solid-state detectors [60] due to the above-mentioned properties; its tissue-equivalence is also a key feature motivating the adoption of diamond-based detectors for a direct measurement of the absorbed radiation [61] in dosimetry applications.

1.2.3 Production and classification

As already mentioned, diamond is not the stable form of carbon at ambient conditions. It is formed in the lithosphere where the thermodynamic conditions for its aggregation are met. It can be extracted from mineral deposits. Natural diamond has poor reproducible characteristics, for this purpose different techniques have been developed to allow its usage for technological applications.

The two main techniques are here explained to produce synthetic diamond: High Pressure and High Temperature (HPHT) and Chemical Vapour Deposition (CVD) synthesis.

1.2.3.1 HPHT Synthesis

Such techniques are based on the reproduction of the thermodynamic conditions where diamond is formed in Nature. A diamond (called seed) is inserted in a mixture with catalyst as Fe, Co and Ti and graphite [62]. The catalyst permits to dissolve graphite and facilitates diamond precipitation at the proper conditions.

The seed is then set into a press under 100kbar pressure and 1500 °C. Such conditions allow the seed to crystallize into diamond at different rates depending on the crystal orientation. Typically, during the growth several orientations are involved. The result is a monocrystalline diamond, but it has several zones (called growth sectors) belonging to different crystal orientations. Impurities can experiment segregation during the growth, such sectors can grow at faster pace and they incorporate larger amount of foreign atoms, typically nitrogen [63]. To reduce the incorporation of such impurities and produce higher quality diamonds, other catalysts can be adopted during the growth such as Ti, Al, Zr. These catalysts bond with the impurities reducing the incorporation into the final product [62][64].

This technique is relatively cost-effective and fast and it is largely used to produce large crystals (more than 10 mm) [62] and gems [65]. The disadvantage of this technique is the relatively high incorporation of impurities. HPHT diamonds typically appear as yellow, due to the high concentration of nitrogen, and they are used for cutting purposes or as seeds for subsequent CVD growth because of the higher crystalline quality of the latter.

1.2.3.2 CVD Synthesis

This technique is of recent introduction [66] and it is more costly. With respect to the HPHT synthesis, where the thermodynamic equilibrium conditions are met, such technique is a non-equilibrium process.

Being a slower process, CVD synthesis allow a more efficient control over the incorporation of impurities resulting in a production of more pure diamond. This technique consists in progressively condensing from individual vapour phases atomic layers on a substrate, which contains the deposition to follow the structure and crystal orientation.

The substrate is kept at temperature of 1000 K in a vacuum chamber where gases, called precursors, such as hydrogen and hydrocarbons, are inlet [67]. Microwaves pulses produce a chemical reactive plasma, composed of carbon and hydrogen. Carbon deposit onto the substrate forming sp^2 and sp^3 bonds, forming therefore diamond and graphite. Conversely, the hydrogen plasma allows to break the graphite chemical bonds and leaving mainly the sp^3 bonds producing diamond. During the process other gases can be inlet depending on the purpose. Silicon and Nitrogen can be inlet into the vacuum chamber allowing to incorporate optically active defects [68], [69] or in can be introduced boron and phosphorus to dope the material [70], [71] for electrical applications.

Homoepitaxy, up to now, is the more advanced technique to produce high quality diamonds, for this reason the final product is consists of slabs that will be later cut at the end of the process. Such diamonds are larger in terms of surface but thinner: typical sizes are between 2x2x0.5 mm^3 and 5x5x0.5 mm^3.

The difference between these two synthesis processes consists in the quality of the final product, the size, the purity and finally the cost. The quality and purity of these substrates depends on the concentrations of impurities embedded in the lattice.

1.2.3.3 Classification

The classification of diamonds is now introduced. It is divided into 4 classes and is based on the purity [49]. The most common are boron and nitrogen and therefore this classification is based on the concentration of such chemical species.

- Type I: Diamonds with N and B concentrations that can be measured with IR spectroscopy. To such class mainly natural and HPHT diamonds belong. There are two subtypes:
    - Ia: nitrogen concentration is between 100 and 1000 ppm and this causes aggregation into the lattice. These diamonds have poor optical properties. Their main technological usage is their hardness and therefore they are typically referred as “mechanical grade”.
    - Ib: very rare in nature, nitrogen concentration is about 500 ppm. They have an absorption band in the green range giving a typical yellow colour.
- Type II: N and B concentration are lower respect to type I diamonds. Typically, these diamonds are produced by CVD synthesis. There are two subtypes:
    - IIa: N concentration is lower than 10 ppm making the diamond transparent in the VIS range. They are typically called “optical grade”. During the growth by CVD, it is possible to further reduce the concentration of N and B, if it is below 50 ppb it is possible to isolate single optically active defects. Such diamonds are called “detector grade”. Due to the low presence of traps level in the gap such diamonds are also used for high-performance electronic devices.
    - IIb: extremely rare in nature. N concentration is lower respect to type IIa. B is now the impurity more present in the lattice and they behave like p-type semiconductors. If B concentration is around hundreds of ppm, it can give this diamond a bluish colour.

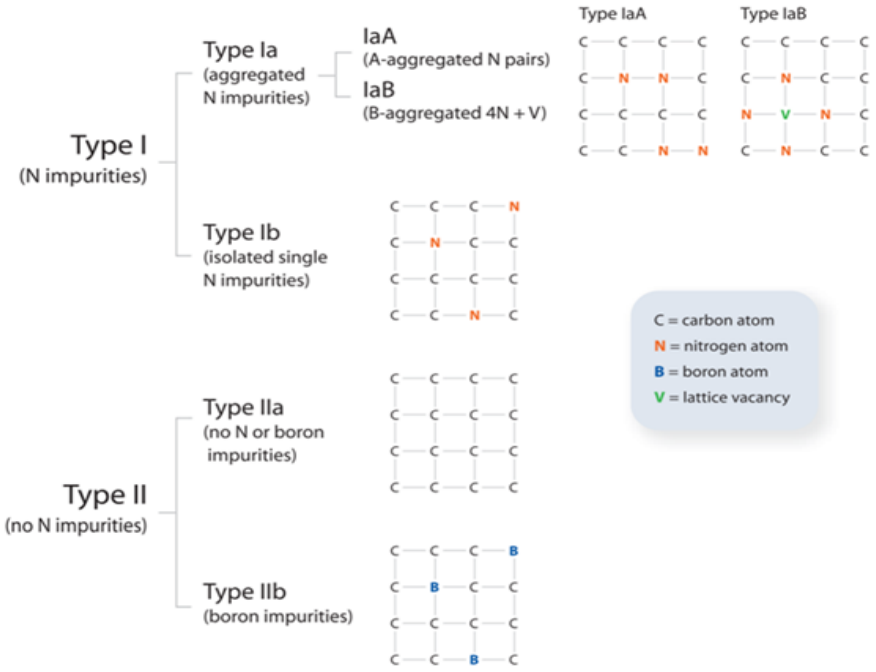


Figure 1.2.4 Diamond classification based on impurities concentration. Figure from [72].

1.3 Point defects in diamond

Diamond crystal can host several types of defects: vacancies, interstitials, substitutional and their combinations. Defects in semiconductors can introduce additional energy levels in the gap and different classes of defects can modify the electrical and optical properties of the host substrate.

Such defects can be divided into two classes: intrinsic and extrinsic. The intrinsic defects, also referred as stoichiometric defects [73], are the one related to the rearrangement of the atoms in crystal lattice without any change of the stoichiometry of the lattice. The rearrangement can occur both naturally and by irradiation (ion, electron, or gamma irradiation [73]). Intrinsic defects are typically vacancies, interstitials (often referred to as Frenkel defects [74]), and a combination of those.

Extrinsic defects are related to the presence of impurities in the lattice. The most typical defect is nitrogen but other defects related to nickel, boron, hydrogen have been observed [49].

The interaction between the intrinsic and extrinsic defects lead to the formation of new complexes. Often such complexes form optically active defects [49], but for many of the spectral lines observed in both natural and synthetic diamond are still of unknown nature. Different complexes can be reconducted to specific chemical species [75], [76], [77].

Optically active defects in diamond are referred as *colour centres* because they typically emit photons, mostly in the visible range. In this section an overview of the most interesting for their optimal quanto-optical properties for application in quantum optics and quantum technologies are reported.

Such defects can be regarded in first approximations as atom-like systems embedded in the gap with a 2-energy level system. In Figure 1.3.1 a simplified energetic scheme is reported along with the PL spectrum of the Nitrogen Vacancy centre. The emission between the excited state towards the ground state is called Zero Phonon Line (ZPL) while the relaxation coupled to the phonons are called quasi-local phononic replicas [78].

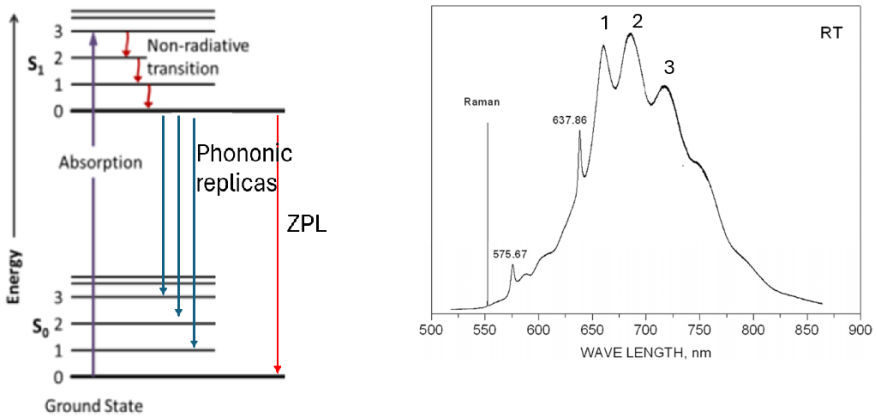


Figure 1.3.1 Nitrogen vacancy simplified energy levels and emission spectrum [79].

Each class of emitters possesses different properties depending on the localization of their levels in the gap, the energetic configuration of the ground and excited states and the excitation and relaxation processes. To characterize the luminescence of such emitters different techniques can be adopted.

The most used and reliable excitation source for the photoluminescence characterisation is monochromatic light [80] or LED light [81]. Different approaches have emerged to stimulate electroluminescence (EL) [82]

offering a straightforward path towards the integration of colour centres in high-density optoelectronic devices [83].

Not all the defects with deep energy levels in the gap produce optically active emitters due to a higher probability of relaxation via non-radiative channels. Typically, the defects emission can be more properly described by introducing a third level, called shelving state or dark state, describing such interactions. The optical transitions happen between electronic states with defined spin numbers, typically triplet states or singles states. It is possible that the spin-flip phenomenon can occur. Such transitions being forbidden in the dipole approximation can signify that the system goes in a dark state, their lifetime is in the order of 100-1000 time higher than the radiative ones, and the phenomenon is called *blinking.*

One of the advantages of diamond as platform to generate SPSs is the possibility of operating at room temperature, thus reducing the cost of the experimental setups, as well as the high probability of emitting a single photon per excitation cycle. The possibility of operating such systems at room temperature is relative to the low density of phononic states at room temperatures and the wide gap of diamond, therefore the thermal energy is not sufficient to excite electrons from the valence to the conduction band.

An overview of the state of the art of colour centres will be discussed in the following. Particularly, the well-known Nitrogen Vacancy (NV) centre [75], the defects related to group IV [84], the so-called NIR (Near Infrared) defects and finally other recently discovered defects will be introduced.

1.3.1 Generation of colour centres

Colour centres can be fabricated upon different techniques: during the creation/growth of the substrate [68], [85], via laser writing, via electron irradiation, via ion implantation both upon focussed and collimated beams onto the substrate [86]. The main differences between the techniques consists in the capability of positioning of the defects into the substrate according to predefined patterns, the technique-dependent formation yield, the quanto-optical/spin quality of the colour centres generated. Ion implantation is the most versatile method currently available that allows to introduce extrinsic impurities into the substrate post synthesis.

Here the defect engineering techniques are discussed with particular emphasis on the ion implantation technique being the focus of this Dissertation. Firstly, it will be introduced the theoretical related to the formation of colour centres, finally the techniques will be briefly discussed.

1.3.1.1 Colour centres formation

To create a colour centre in a solid-state platform different requirements need to be fulfilled [86]: the presence of one or more vacancies and/or the presence of a nearby ion(s) in a specific lattice location (interstitial, substitutional or other combinations) and/or (depending on the technique adopted to create vacancies and introduce dopants into the substrate) a thermal annealing process. To form an extrinsic optically active defect in diamond it is required to create a bond between vacancy/vacancies and the impurity atom(s), for example in the case of the Nitrogen Vacancy defect (see Chapter 1.3.2.1) a carbon vacancy is linked to a substitutional nitrogen atom, for any of the group IV related colour centres (Si, Ge, Sn, Pb) two vacancies are bonded to an interstitial impurity. The thermal process has two main goals: the first to restore the damaged lattice after the bombardment of any given type of beam (electron, proton, ions) and the second is to let vacancies diffuse into the substrate to be then captured by an impurity to form a stable chemical bond. The thermal annealing can be divided in two main strategies for diamond: low pressure low temperature and high-pressure high temperature. The first consists in a thermal treatment under low pressure conditions such as 10^{-6} mbar at temperatures ranging between 800 °C to 1400 °C. The second method replicates the thermodynamical conditions where diamond is the stable allotropic form of carbon. At pressures in the order of few GPa at temperatures around 2000 °C. The choice of LPLT or HPHT is mainly given by the type of colour centres to be formed, in fact for heavier ion masses such as Ge, Sn, Pb it has been

demonstrated that stronger annealing conditions have as outcome a better optical quality of the defects [87], [88],[89].

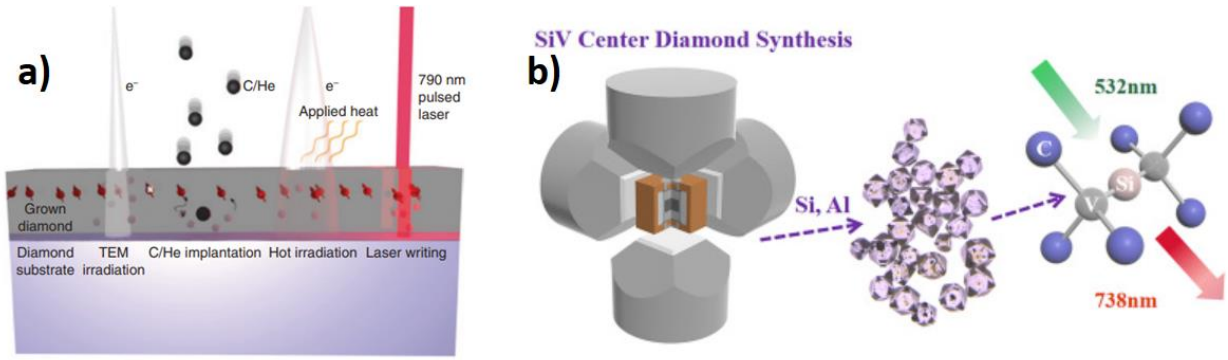


Figure 1.3.2 Schematic representation of the different techniques to fabricate colour centres. a) overview of techniques to create defects in diamond, figure from [86]*. b) Schematic representation of HPHT synthesis to promote the creation of SiV centres, figure from* [90].

1.3.1.2 Creation during synthesis of the substrate

The creation/growth of the substrate, as reported in Chapter 1.2.3, consists in HPHT synthesis or CVD growth and during the process it is possible to embed defect into the substrate. In the case of incorporation during HPHT synthesis it is required to mix during the preparation of the catalyst the desired impurity. The achieved defects are related to N, Si, Ge, Sn impurities typically [85], [91],[92], [90], [93]. As specified in Chapter 1.2.3.1, the nitrogen presence in the final product can be minimized adding Nitrogen getter. The distribution of the defects in the substrate is random and each plane can contain colour centres while the quality of the defect is generally better due to a better incorporation during the synthesis.

In is also possible to incorporate during CVD synthesis extrinsic defects adding in the precursor nitrogen gas. Tuning the precursor flow with the desired impurity allow for a better incorporation and better-quality final product. The CVD method permits to perform the so-called *delta doping.* During the deposition the mixture of gas inlet in the reactor is changed inletting a higher amount of the desired doping gas, forming the delta layer of variable thickness depending on the flow rate. To cover the doped layer with intrinsic diamond it is inlet a dopant getter to minimize the incorporation of the doping gas [94].

Such technique has been explored for N, Si, B, P impurities [93], [95]. Regarding the N delta doping it has been also demonstrated the possibility of tune the orientation of the defects in a defined crystal orientation adopting a (111) crystal as substrate for the growth [96].

The distribution of the defects in the substrate is random and each plane can contain colour centres while the quality of the defect is generally better due to a better incorporation during the synthesis.

1.3.1.3 Femtosecond laser writing

The laser writing techniques has been used for decades to fabricate structure inside transparent substrates [97], [98]. Its usage to fabricate colour centres is of recent discovery [99], the ability to create organised pattern of colour centres is of great interest for quantum technologies applications such as quantum nodes and quantum repeaters. This technique consists in creating localised vacancies within a certain volume of the substrate in with an ultrashort laser pulse.

The ultrafast laser pulse and the nonlinear process result in a confined creation of vacancies in a small volume stemming a low degree damage of the lattice. This feature allows therefore for a generation of better-quality

colour centres due to the lower strain/damage created during the process. It is indeed possible to change the number of generated vacancies tuning the pulses parameters also the optics play a crucial role enabling to inspect different volumes of the substrate [98]. A thermal annealing process is then performed to promote the vacancy diffusion and fabricate the colour centres [86].

1.3.1.4 Electron/ion irradiation

This technique consists in irradiating the substrate with an electron beam to promote the formation of lattice vacancies. The beam can be generated by different apparatuses such as MeV accelerator, Transmission Electron Microscopy (TEM)[100], [101], the main constraint is that the electron beam has sufficient energy to displace the lattice atoms from their sites, for example for diamond the minimum energy to displace a C atom is 30 eV which translate in minimum kinetic energy of 145 keV [101].
Electron irradiation is usually employed with diamonds with high concentration of Nitrogen to create dense ensembles for sensing application [102].

Electron or ion implantation (implanting C [103], [104], He [104]) can be used to induce the creation of intrinsic defects, normally vacancies, at different depths depending on the energy of the beam. After the irradiation it is required to perform a thermal annealing to promote the diffusion of vacancies and to form firstly the colour centre but also to minimise the presence of other defects that could act as decoherence sources [86].

1.3.1.5 Ion implantation

Ion implantation is the only method that permits to incorporate impurities into substrates after the material synthesis. This technique consists in accelerating an ion beam to a specific substrate. The ions impinging in the lattice first introduces the accelerated chemical species into the crystal while at the same time creating damage.

This technique has been employed largely in the semiconductor industry for Silicon doping for the last 50 years [105]. In the recent years[106], it raised the use of ion implanters to fabricate optically active defects at the solid-state via collimating masks [107], via Focussed beams [108]. With respect to the during growth/incorporation of defects in diamond, the ion implantation is a more versatile tool. In fact, such technique allows to introduce in a controlled matter specific ion species with a higher degree of control over the number and depth. The final location of the impurities is then bound to a specific position and it is not randomly and homogeneously distributed on the sample, feature not possible with the above-mentioned techniques.

Two main conditions must be fulfilled to make colour centres usable for quantum technology:

1. Deterministic implantation of single countable impurities with a fine control over their depth and position.
2. Ensuring that each impurity atom is converted to the desired colour centre and assumes a stable and defined state of charge with all other necessary quantum properties.

The ion implantation technique will be more extensively discussed in Chapter 2.

1.3.2 Classes of colour centres

The aim of this work is the study and discovery of different classes of emitters that hopefully meet the characteristics of ideal single photon sources (discussed in more detail in 1.1.2) for quantum technological applications.

Different classes of colour centres have been explored since the early 2000 [109]. Recently, the field is polarised towards both the discovery of new classes of defects optically active in diamond as well as the

development of suitable fabrication technique to improve the quanto-optical properties of the known defects as well as the creation yield. The most relevant classes are represented by Group IV-related and the Nitrogen-Vacancy (NV) colour centres.

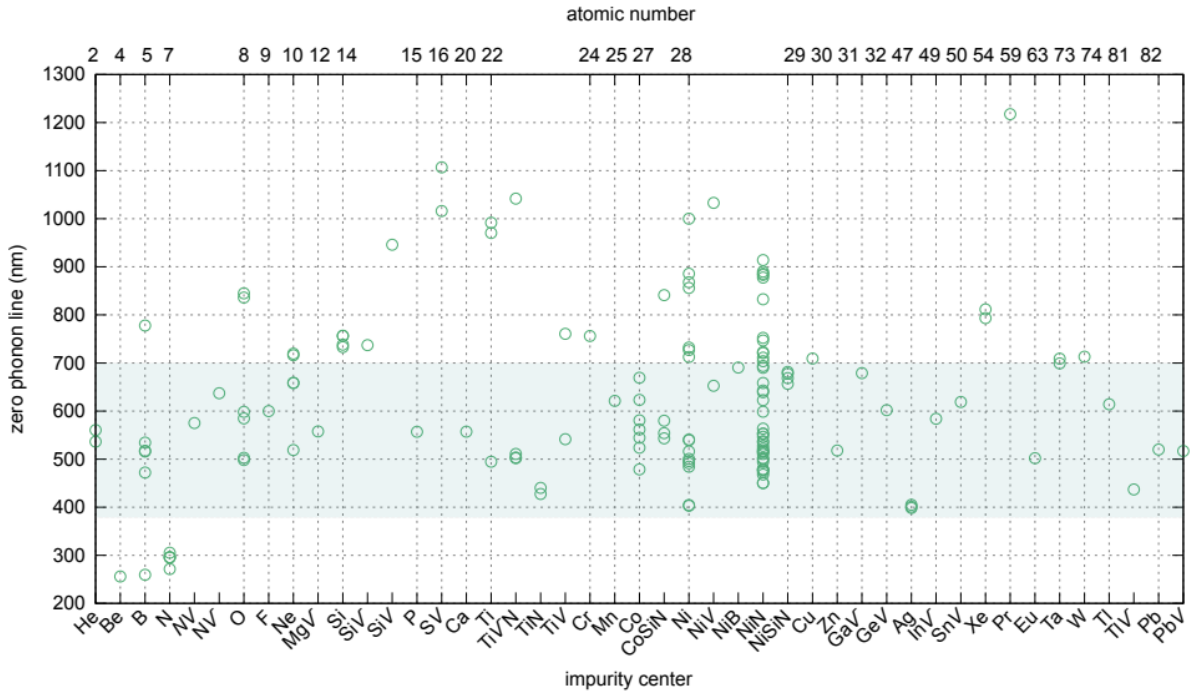


Figure 1.3.3 Plot of zero phonon lines as function of both atomic number and impurity configuration, the green band represents the visible spectrum. Figure from [110].

In Figure 1.3.3 it is reported a graph containing zero phonon lines of known colour centres as function of atomic mass. Many defect configurations are known in literature, but only a subset has been demonstrated so far at the single photon emitter level. In the following section an overview of the most explored defects is presented, their principal properties are discussed as well as their drawbacks for quantum technology applications.

1.3.2.1 Nitrogen Vacancy centre

The Nitrogen Vacancy centre is the first defect isolated at single emitter level in the early 2000s [109]. The centre displays a pyramidal symmetry [111] with the symmetry axis passing between the reticular vacancy and the nitrogen atom. Four orientations of this defect occur in diamond along 4 crystallographic orientations. The NV centre exhibits two optically active charge states NV^0 and NV^- corresponding to a different number of electrons surrounding the defects in the lattice (5 or 6, respectively) [112]. The PL spectra, as shown in Figure 1.3.4, are characterised by a broad emission band composed of a weak ZPL (575 nm and 637 nm [112] respectively for neutral charge state and negative charge state) and an intense phononic (150 nm) band. The low Debye-Waller factor, corresponding to the emission of a large fraction of photons in the phonon sideband with respect to the ZPL, is the most severe disadvantage, along with the relatively high excited state lifetime (13 ns) [112], for the utilization of the NV centre to approximate an ideal single-photon source [113].

The strong interest in such emitter consists of the singlet spin state of the negative charge state that can suitably be optically initialized and read-out enabling room temperature [68] sensing of temperature variations [114], magnetic and electric fields [115]. These limitations have pushed the research activity to isolate new classes of emitters with properties that meet better the ideality criterion for real SPS applications. [44]

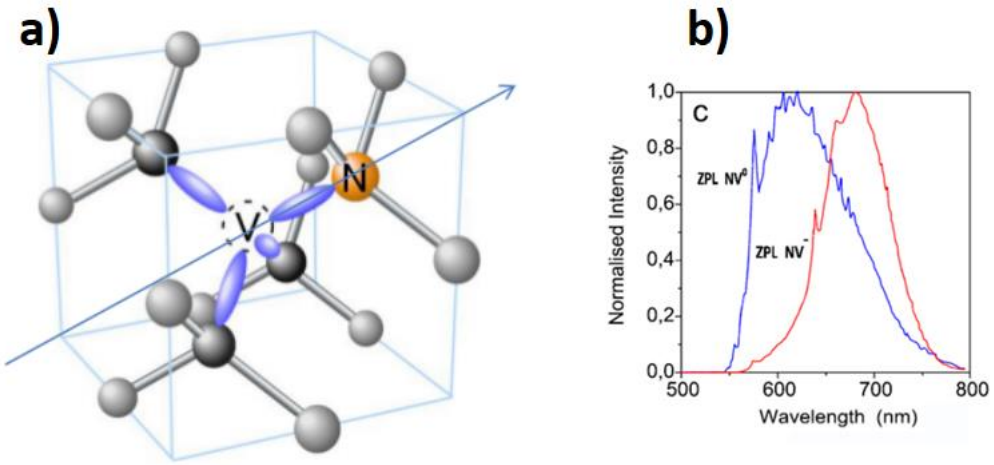


Figure 1.3.4 a) Crystallographic structure of NV centre, figure from [116]*. b) PL spectra of the charge states. Figures from*[117] .

1.3.2.2 Group IV impurity related colour centres

Silicon, germanium, tin and lead all form optically active colour centres in diamond [5], [6]. They show remarkably interesting properties such as low excited state lifetime, high Debye-Waller Factor, splitting of the ZPL (which can be optically addressed) and they are very bright with respect to the NV centre.

In Figure 1.3.5a schematic representation of the atomic structure of the group-IV (GIV) emitters is reported, the associated room temperature spectra are reported. As shown in Figure 1.3.5b, the PL spectra show an intense and sharp ZPL with low phonon coupling (see Table 1)

Both theoretical predictions and experimental observations suggest that the defect configuration is split vacancy, where the M ion is in interstitial configuration embedded between two lattice vacancies [5] [6]. The defects show a centrosymmetric configuration where the symmetry axis passes through the vacancies and M ion. All group IV emitters are in a negative charge state [118]. The neutral charge state of the defects has been observed in PL and EL for the SiV centre (946 nm) [119], [120], while it has not been reported yet for the other group-IV-related emitters. The emission rate of SiV and GeV is in the order of 150/200 kcps for a single emitter [120], SnV and PbV show both emissions up to 1 Mcps at room temperature [87], [121]. Such interesting property make this class of defects very appealing as SPS and the research community is widely active in the development of quantum protocols with this class of defects [76], [118]. The excited state lifetime is lower with respect to the NV, it is in the range of 1/3 ns for the SiV [122], 3/5 ns for the GeV [89],6/7 ns for the SnV [87], [121] and 3/4 ns for the PbV [88], [123].

The ZPL of GIV is indeed composed of a doublet denoted typically as C and D lines, such transitions are optically tunable.

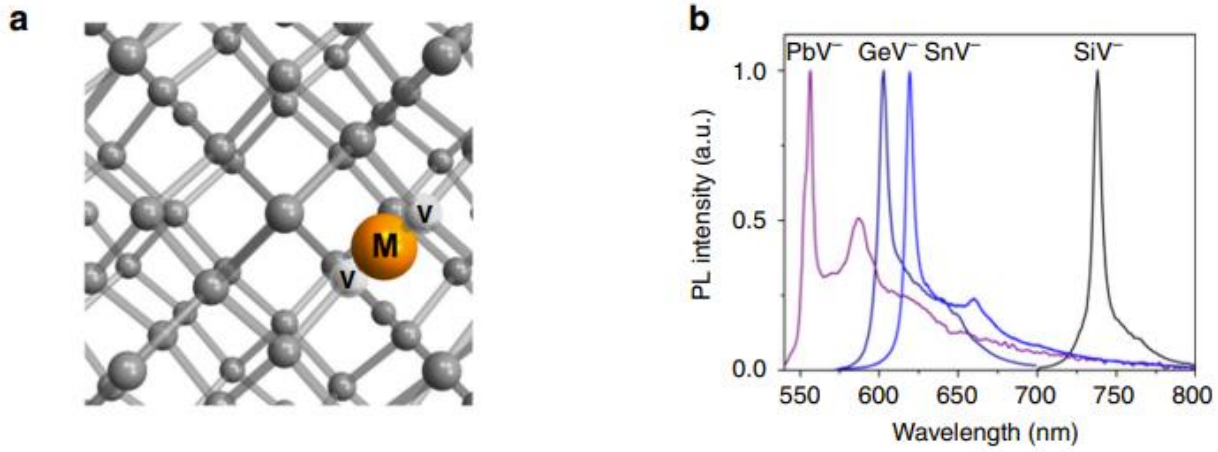


Figure 1.3.5 a) Atomic structure of group IV defects. B) PL emission spectra of group IV emitters at room temperature. Figures from [76].

As depicted in Figure 1.3.6a), the energy diagram of GIV emitters is composed of 4 different lines. Transitions C and D are the most intense while A and B lines are typically less bright and observable at higher temperatures respect to C and D transitions because it is required additional thermal energy to excite electrons to the higher excited state level. It is worth mentioning that for PbV transition A and B have not been observed yet experimentally, therefore the splitting of the excited state is still unknown.

As a function of the mass of GIV emitters, the spin-orbit coupling increases and the first effect of such phenomenon is the increasing of the ground state splitting [124].

To generate high-quality entangled photons, it is required a source with transform limited photon emission. In Figure 1.3.6b) it is reported the transform limited ZPL of GeV, SnV and PbV as a function of temperature, SiV it is left outside the temperature range since it has a transform limited ZPL only below 1 K. A clear trend observable is that for heavier masses the ZPL remains transform limited for higher temperature, as for SnV the limit is crossed at 3 K while for PbV the limit is demonstrated to be at 12 K.

GIV emitters have near-ideal properties to be exploited as SPSs, particularly they show weak interaction with external electromagnetic fields [76], [125] making them better candidates to be used as qubit [126] or quantum repeaters for quantum information purposes [126]. Different approaches have been pursued to use the SnV defect in quantum information protocols applications [113]. Coherent control of the GIV defects is crucial for proper initialisation of the spin state of the SPS [127], [128] for QIP applications. Drawbacks of group IV indeed are the loss of coherence during resonant excitation, crucial for all optical initialisation and readout of the spin state. It has been demonstrated by different works [113], [127], [128] that Group IV emitters under resonant excitation tend to turn to non-radiative states and such behaviour is attributed to charge conversion. Another drawback related to GIV emitters is the spectral inhomogeneity associated with standard LPLT annealing. Different approaches are studied to enable a better and more satisfactory method to reduce such broadening of spectral lines such as HPHT annealing or chemical functionalisation of the surface. Both techniques are4.1 discussed in Chapter 4.1.

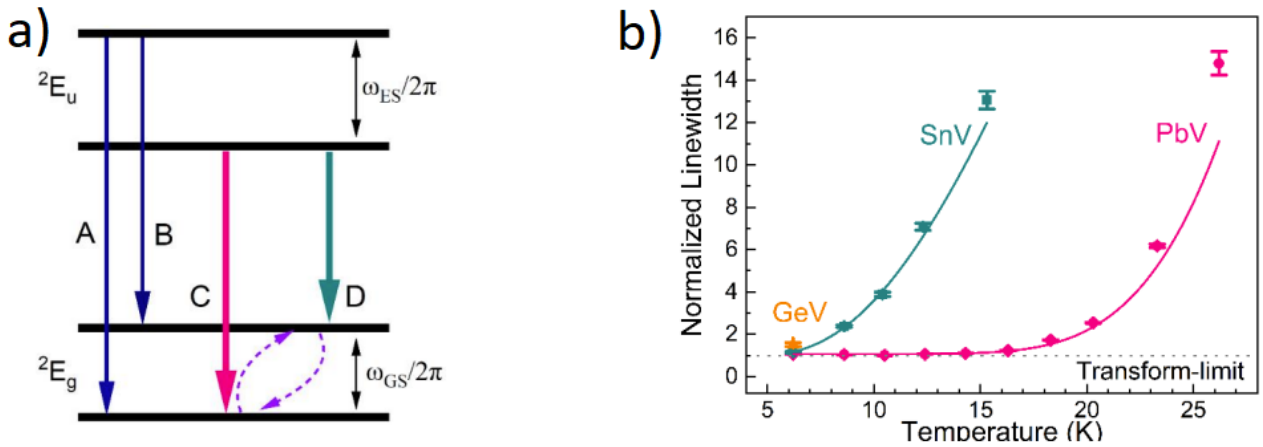


Figure 1.3.6 a) Energy diagram of GIV emitters. b) Normalized linewidth of GeV, SnV and PbV as function of temperature. The SiV is missing since it is out of scale, it remains transform limited below 1K. Figures from [128].

In the following table the most relevant properties of NV and Group IV defects are reported, particularly displaying the ZPL, the quantum efficiency, the excited state lifetime, the splitting of the ground state and finally the working temperature for application in quantum information protocols.

defect	ZPL (nm)	Radiative lifetime (ns)	Ground state splitting (Ghz)	Excited state splitting (GHz)	Operating temperature (K)
SiV^-	737	1-7	47 GHz (0.2 meV)	258 GHz (1.07 meV)	0.1
GeV^-	602	1.4-6	170 GHz (0.7 meV)	1088 GHz (4.5 meV)	0.4
SnV^-	620	4.5-7	830 GHz (3.5 meV)	3000 GHz (12.5 meV)	1.8
PbV^-	520/552-557	3-4	3700 GHz (13 meV)	Not applicable	7-10
NV^-	637	11-13	Not applicable	Not applicable	Not applicable

Table 1 Summary table of the main parameters of the GIV emitters and the NV for comparison. The values are taken from the references in the main text.

1.3.2.3 Noble gas related colour centres

The Xenon-related centre is a defect observed after Xe ion implantation and annealing with emission signals at 811.5 nm and 793.5 nm that could arise from a splitted excited level [129], as shown Figure 1.3.7. Numerical methods were proposed to describe the defect structure [130]. The proportionality between implantation fluence and photoluminescence emission intensity suggests that just one Xe atom is incorporated into the centre [131]. The capability of Xe-centre to work as SPS has not yet been demonstrated.

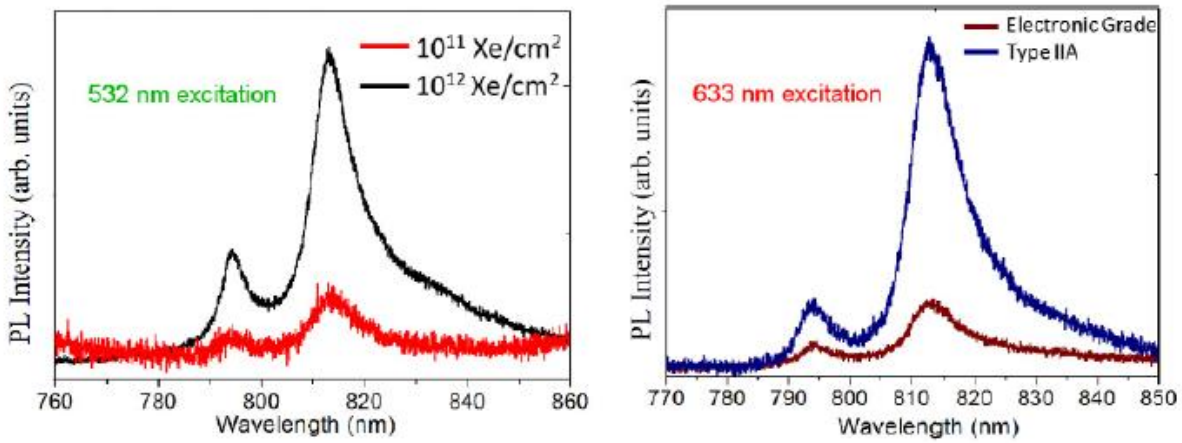


Figure 1.3.7 Photoluminescence spectra of Xe-related colour centres under green and red excitation. Figures from [129]

The He-related colour centre is another noble-gas based point defect that is optically active in diamond. Such defect was already reported in electroluminescence and cathodoluminescence [132]. The PL spectrum show two sharp lines at 536.5 nm and 560.5 nm [133], as shown in Figure 1.3.8. As for the Xe-related defect, it is not yet reported the emission at single emitter level, this may lie in the fact the defect shows a rather long excited state lifetime.

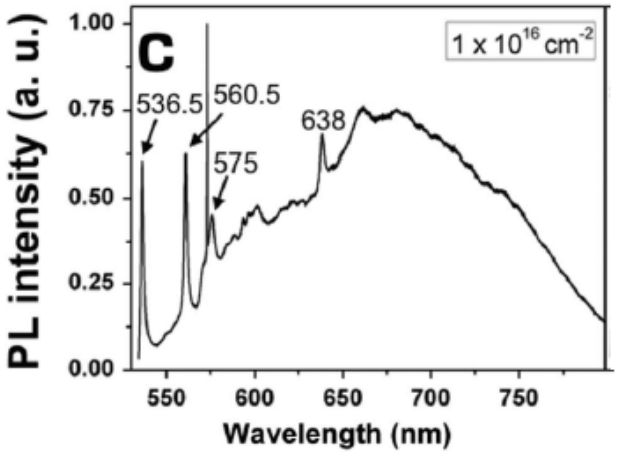


Figure 1.3.8 PL spectrum of He-related colour centre. The peaks at 575 nm and 638 nm are related to NV fluorescence. Figure from [133].

1.3.2.4 NIR colour centres

Many emitters in the NIR region were observed in diamond in the past years, and most of them have the necessary quantum efficiency and absorption cross section to be visible at single-centre level. For these defects an unequivocal attribution has not been yet formulated, as often the attempts to create them in a controlled way are limited in their reproducibility. Nevertheless, they seem to be related to complexes involving transition metals like chromium or nickel, plus common impurities of diamond such as silicon or nitrogen. They have different properties, although some common features can be found for many of them:

- Narrow spectral emission (from 10 nm up to less than 1 nm at room temperature)
- Emission in the spectral range 730 – 800 nm
- Shorter lifetime (few ns) with respect to the NV centre (12 ns), allowing a high photon emission rate

A brief summary of the most relevant results in literature is presented in the following.

1.3.2.4.1 Nickel-related centres

In these papers, the presence of nickel is believed to be probable, but properties seem to be different from the NE8 complex:

[134]: ZPL at 768 nm, no phonon sidebands, 2 ns radiative lifetime. It was found in CVD nanodiamonds implanted with 30 keV Ni ions. A complex involving Si-Ni was proposed, however in another paper [135] the same samples are studied and this hypothesis is not confirmed, here several centres are reported with ZPL in the region (770 ± 15) nm.

[136]: ZPL in the 767 – 775 nm spectral region, 1.1 ns radiative lifetime and presence of shelving state. No phonon sidebands. This centre is found in optical-grade IIa CVD single-crystal diamond (Element Six) irradiated with high-energy Si and Ni ions. Fully polarized light was observed for one of the two emitters under exam.

1.3.2.4.2 Chromium-related centres

Such colour centres look equivalent to the nickel-silicon related ones (at least with respect to the observed parameters) and were observed both in nanodiamonds and in single-crystal samples, like the nickel-silicon ones. In case of nanodiamonds, the role of Cr in the centre structure is hypothesized because the growth substrate is sapphire – a crystal that easily hosts Cr ions –, while for the case of bulk, co-implantation of Cr and O ions was performed.

[137]: the ZPL is in the range 740 – 770 nm, the radiative lifetimes range from 1.4 ns to 14 ns. It is observed a variable presence of shelving states. It was observed in CVD nanocrystals grown on sapphire substrate.

[138], [139]: the ZPL is in the 748 – 765 nm spectral range. It was observed in CVD optical-grade IIa diamond (Element Six) after co-implantation of Cr and O at keV and MeV energies and subsequent 2 hours annealing at 1000 °C in forming gas (95% Ar and 5% H_2). Not observed in HPHT Ia, nor in electronic grade IIa CVD single crystals. Radiative lifetimes in the order of few ns, shelving state present. Fully polarized light observed.

1.3.2.5 Recently explored classes of colour centres in diamond

Screening of novel classes of defect in diamond is an active quest. The work from Luhmann et al [140] is dedicated to that purpose: particularly the chemical impurities studied are oxygen, calcium, magnesium, fluorine and phosphorus. These classes of defects were obtained by ion implantation and thermal annealing to promote their stable formation as possible colour centres. The results presented in the work are preliminary but show the possibility of fabricating interesting defects in diamond with different properties with respect to the above-mentioned classes.

The PL spectra are reported in Figure 1.3.9 [140], the main observation from F, O and Ca-related defects is the presence of a broad band with similar broadening (150 to 200 nm) centred respectively at 680 nm, 640nm and 650 nm; O and Ca-related present a visible ZPL (584.5 nm and 557.2 nm respectively) while F-related spectrum does not show any visible ZPL. The magnesium-vacancy emission spectrum shows interesting features such as a visible, sharp ZPL at 557.4 nm and a series of sidebands attributed to the phononic replicas.

Such screening is still preliminary in terms of results and further characterisations are needed to estimate the quantum-optical properties, the structural configuration of the defect and their creation yield. A more detailed analysis on magnesium and fluorine defects was carried out during the PhD work and it is presented in the Chapter 4.

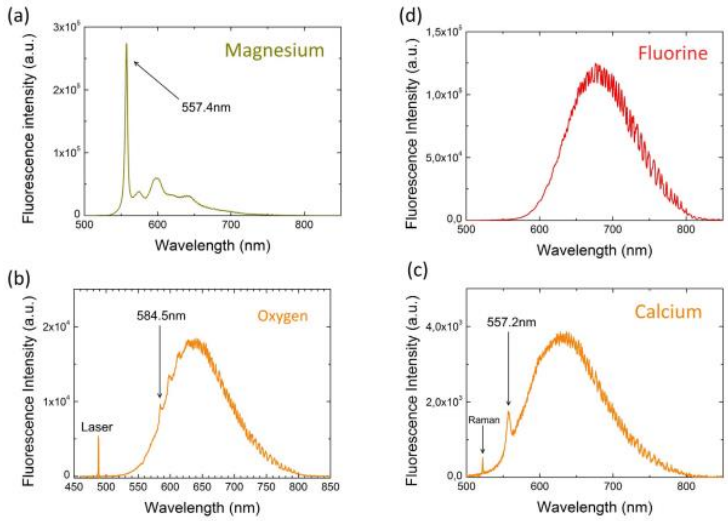


Figure 1.3.9 PL spectra acquired from IIa diamond implanted with (a) Magnesium, (b) Oxygen, (c) Calcium, (d) Fluorine implanted areas. Spectra are acquired following LPLT thermal annealing. Figure from [140].

2 Chapter 2

Ion implantation is widely used in semiconductors industry. This technique is the most versatile method of introducing extrinsic defects and produce as well intrinsic one such as vacancies, which are crucially important to achieve a colour centre formation.

Most of the work carried out in this Dissertation is related to the use of an ion implanter to induce the formation optically active defects. In this Chapter it is introduced the ion-matter interaction, the ion implantation technique to fabricate colour centres and finally different type of implanter are discussed.

An overview of the theoretical framework is presented. It will be defined the stopping power of the target material (related to nuclear and electronic scattering), the ion distribution while penetrating the material. Finally, a description of the ion implantation and thermal annealing of the defects is discussed along with its limitations and eventual path to overcome such drawbacks.

2.1 Ion matter interactions

An energetic ion impinging into a substrate releases its energy as consequence of two concurrent physical phenomena. The ion interacts with both the nuclei and the electrons of the target and while penetrating the lattice is then stopped by these interactions. While travelling through the solid, the ion undergoes collisions with the stationary target atoms, deflecting their trajectory. The loss of energy can be attributed to different phenomena [141]: it could be manifested as temperature rise (heat) as well as chemical and physical state change (ionisation, creation of radicals, elastic scattering with target nuclei, nuclear reactions).

The deposition of energy is not the only process involved; the ions also pick up electrons from the target. Finally, a slow ion stops into the substrate in a certain lattice position, at this stage the ion is said to be thermalized because its kinetic energy is compatible with the target atoms.

The stopping power has a maximum towards the end of the range (referred as *Bragg Peak*), surpassed the maximum the energy drops abruptly to zero for MeV ions while for keV ions it decreases to zero in a less pronounced way. The curve describing such phenomenon is referred as *Bragg curve*. This maximum is related to the loss of energy from electronic interactions. In Figure 2.1.1it is reported the Bragg curve for 50 keV and 1 MeV for He ions in diamond.

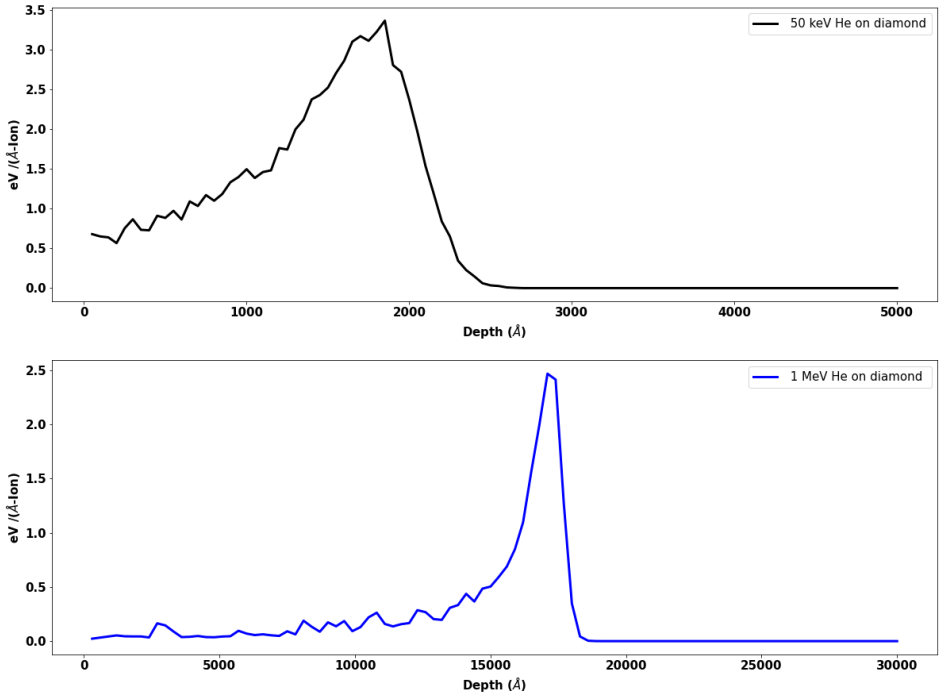


Figure 2.1.1 Bragg curves for low energy (50 keV) and high energy (1 MeV) He in diamond.

2.1.1 Stopping Power

The ions penetrating a solid keep losing energy via elastic and inelastic collisions with atoms and electrons. The energy loss along the path x of the ion in the material has three components as follows [141]:

$$-\frac{1}{N}\left(\frac{dE}{dx}\right) = S = -\frac{1}{N}\left(\frac{dE}{dx}\right)_{nuclear} - \frac{1}{N}\left(\frac{dE}{dx}\right)_{electronic} - \frac{1}{N}\left(\frac{dE}{dx}\right)_{radiation} \quad \text{Eq. 2.1-1}$$

N is the target density of the material.

The energy loss for radiation processes, such as Bremsstrahlung and Cherenkov radiation, is negligible with respect to nuclear and electronic scattering and it is neglected in this discussion [141].

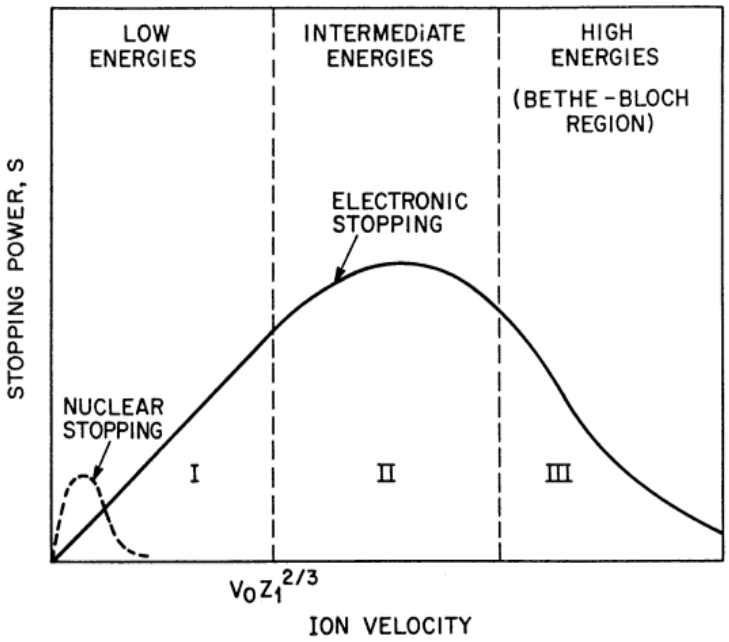


Figure 2.1.2 Stopping power as function of projectile velocity. The term v_0 is the Bohr velocity, Z is the ion atomic number. Figure taken from [142]

The ions (referred as projectiles), penetrating the target material, experience a Coulomb interaction with both the atom's electrons or/and the atom's nuclei. When the ion passes at a distance larger than the atomic radius, the interaction involves the atom's electrons. Vice versa, a Coulomb interaction between the electromagnetic field of the atom electrons and nuclei occurs. The stopping power mechanism can be divided as function of energy regime of the ions. For low energy it dominates the nuclear stopping power while for high energy the electron stopping power dominates. In Figure 2.1.2 it is pictured the Stopping Power as function of projectile velocity. Three regions are observable, the description presented is focussed on the low energy and high energy regimes. Two basic energy transfer mechanism are involved [141], [143]:

- Elastic collisions with nuclei of target atoms, the energy is transmitted to the atom as whole. This mechanism dominates for energy typically in the range of 10 keV/amu and the main and it is typically referred as nuclear stopping power.
- Inelastic collisions with electrons of the target atoms, the impinging atom causes ionisation or excitation to the target atoms. Such mechanism dominates for energies higher than 100 keV/amu and it is typically referred as electronic stopping power.

To describe the nuclear and electronic stopping power, the introduction of the cross section and mean free path are needed [141], [143]. The cross section σ defines the probability of scattering between particles. The average transferred energy per collision can be written as follows:

$$\hat{T} = \frac{\int T d\sigma}{\int d\sigma}$$

Where T is the transferred energy and σ is the cross section. The mean free path λ is described as average distance over which a particle travels before deviating its original trajectory.

$$\lambda = \frac{\sigma}{N}$$

Where σ is the cross section and N the density of the material.

The stopping power is the energy loss per path length of a particle through a medium. It can be described as the ratio of the average energy transfer over the average distance travelled by a particle before changing its trajectory, its mathematical expression therefore is the following [143]:

$$\frac{dE}{dx} = \frac{\hat{T}}{\lambda} = N \int T d\sigma \qquad \text{Eq. 2.1-2}$$

2.1.1.1 Nuclear stopping power

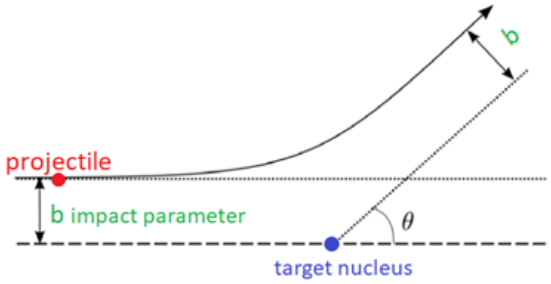


Figure 2.1.3 Scattering representation of an energetic projectile and a target ion at rest in the laboratory frame.

Nuclear interactions produce a lattice disorder by the displacement of the target atoms from their lattice positions. Such interaction can be described by classical kinematics. The nuclear stopping power is related to ion-atom scattering leading to a deviation of the ion while penetrating the target. In Figure 2.1.3 it is represented a simplified scattering scheme for the ion (projectile) and the atom (target nucleus) along with the main parameters: the impact parameter, (defined as the perpendicular distance between the velocity of a projectile and the centre of the electrostatic field *V(r)*), and the scattering angle θ.

If elastic scattering happens between the projectile and the target atom initially at rest (in the centre of mass frame), the conservation of momentum yields a transferred energy as follows [143]:

$$T = \frac{4M_1 \cdot M_2 \cdot E}{(M_1+M_2)^2} sin^2 \frac{\theta}{2} \qquad \text{Eq. 2.1-3}$$

Where E is the energy of the projectile, M_1 and M_2 are the masses of the atoms involved in the collision, θ is the scattering angle. Tha maximum transferred energy is in a head-on collision ($\theta = 180°$). The scattering angle is related to interatomic potential and the impact parameter b through the following equation:

$$\theta = \pi - 2b \int_{R_{min}}^{\infty} \frac{\frac{dr}{r^2}}{\sqrt{1-\frac{V(r)}{E}-\frac{p^2}{r^2}}} \qquad \textit{Eq. 2.1-4}$$

Where E is the energy of the projectile, V(r) is the electrostatic field created by an object that the projectile is approaching. When determining the stopping power, it is crucial and typically very complex to evaluate the repulsive interaction potential (V(r)).

Such potential in all calculations is a screened coulombic potential due to the screening of the bare nuclei of the projectile and the electronic cloud of the target atom. Its expression is linear dependent on the screening potential as follows:

$$V(r) = \frac{Z_1 Z_2 e^2}{4\pi\epsilon_0 r} \Phi(x) \qquad \text{Eq. 2.1-5}$$

Z_1, Z_2 are the atomic numbers of the atoms involved in the scattering event, r is the distance between the nuclei, $\Phi(x)$ is the screening potential. Different approaches in determining the screening potential were

proposed, the most appropriate analytical expression for the screening potential was proposed by Ziegler, Littmark and Biersack in [143]. The formula is referred as the *universal screening potential and its expression is the following:*

$$\Phi(x) = 0.1818e^{-3.2x} + 0.5099e^{-0.9432x} + 0.2802e^{-0.428x} + 0.02817e^{-0.2016x} \quad \text{Eq. 2.1-6}$$

The differential cross section over the solid Ω angle for ion-atom interaction in a classical picture is linked to the impact parameter as follows:

$$\frac{d\sigma}{d\Omega} = \frac{d\sigma}{2\pi sin\vartheta d\vartheta} = \frac{2\pi b db}{2\pi sin\vartheta d\vartheta} \quad \text{Eq. 2.1-7}$$

It is possible to derive the average nuclear stopping power $S_n(E)$ which defines the average energy that is transferred by each nuclear collision. $S_n(E)$ can be calculated by integrating the energy transfer of a nuclear collision event over all possible impact parameters *b*:

$$S_n(E) = \int_0^\infty T d\sigma = 2\pi \frac{4M_1M_2E}{(M_1+M_2)^2} E \int_0^\infty sin^2\frac{\theta}{2} b db \quad \text{Eq. 2.1-8}$$

The scattering occurring between the projectile and nuclei can therefore modify and cause damage to the crystal lattice. Such interactions can be simulated adopting SRIM [144].

Particularly, the event can be divided in different cases differentiated by the energy transfer of the collision and the displacement energy (minimum energy required to knock out an atom from its crystal site). The following description is based on refs [144], [145], [146]. The collision can be divided as function of comparison (greater or lower) between the displacement energy (minimum amount of energy to displace an atom from its lattice position) and threshold energy (energy above which the atom leaves its lattice site).

If the transferred energy is greater than the displacement energy threshold, the atom can escape its crystal position leaving a vacancy thus igniting a cascade event. The displaced atom is referred as primary knock-on atom, if it still possesses enough energy, it can cause the displacement of other atoms referred as secondary, tertiary knock-on ions etcetera.

If the transferred energy is lower than the displacement energy, the atom does not leave its site and the excess energy is transferred to the medium via phonons. In Figure 2.1.4 it is reproduced a schematic picture of the scattering event. The projectile in purple ignites the primary knock-on atom that can cause the cascade event as well as the sputtering event if the knocked-on atom is close enough to the surface. Sputtering is the phenomenon in which particle ejection in a solid material occur at the surface. In a scattering event this can happen if the secondary ion has enough energy to overcome the surface binding energy barrier and leave the medium, the phenomenon is described with grey trajectory.

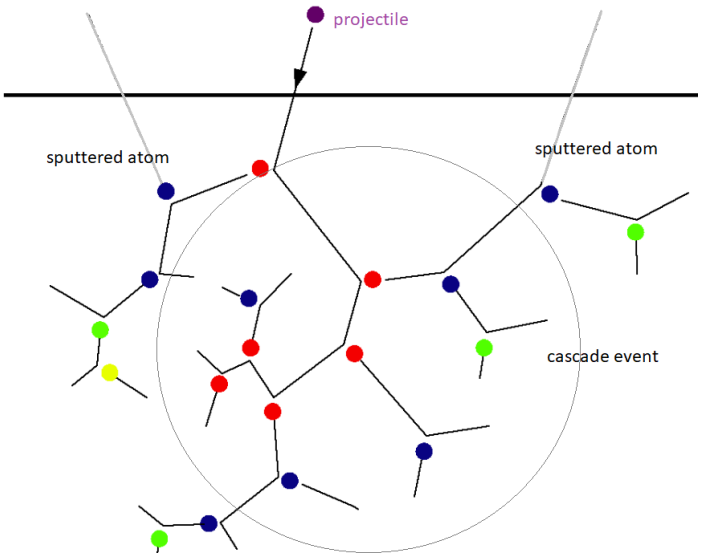


Figure 2.1.4 Schematic representation of different scattering related events of projectile-nuclei interaction, the purple ion represents the projectile, the red, blue, green, yellow represent the cascade event. Figure from [147].

2.1.1.2 Electronic stopping power

Electronic interactions are more frequent, they typically involve small energy loss and small deviations from the original trajectory. This can lead to significant deflections of the projectile respect to its original trajectory. The interaction of the projectile and target electrons can be explained in different approximations and therefore different models are required to describe the processes involved [141], [143], [148]. For instance, the electrons can be excited to higher discrete energy levels, can be ejected (ionization)[149] or can be excited in collective motion (plasmons) [150].

Ion velocity respect to the target electron velocity is the main physical parameter that discriminate the type of interaction and therefore the adopted physical model to describe it. In the following two approximation will be discussed, the low velocity regime and the high velocity regime.

In the low velocity regime, the electronic stopping power is linearly dependent on the ion velocity. The model can be described considering the scattering between electrons not bounded to any specific atom but embedded in a gas with positive charge. The Lindhard-Scharff-Schiott (LSS) [141], [143], [148] formula was derived to explain such interaction:

$$\frac{dE}{dx} = k\,E^{\frac{1}{2}} \qquad \text{Eq. 2.1-9}$$

Where K consists of the following terms: $Z_{1/2}$ is the atomic number of the projectile and target, $M_{1/2}$ is the mass of the projectile and target.

Eq. 2.1-10 is valid up to 1 MeV energies, when the ion velocity is proportional to the outer electrons for the target's nuclei. The interaction is maximised, and the energy transfer occurs between the projectile and target electrons.

At high projectile energy, the ion has its electrons stripped and with good approximation the interaction can be seen as Coulomb scattering between the ion and target electrons. In such approximation, the target nuclei are considered at rest due to heavier mass respect to the projectile one; the electrons are approximated to be in a fixed position around the mean distance from the atom's nucleus. The stripping of a nucleus' electron from the projectile minimum energy is now given by the Bethe formula [151] and its expression is the following:

$$\frac{dE}{dx} = \frac{8\pi \cdot Z_1^2 \cdot e^4}{I_0 \cdot \epsilon_b} \ln\left(1+\epsilon_b + \frac{5}{\epsilon_b}\right) \qquad \text{Eq. 2.1-11}$$

$$\epsilon_b = \frac{4E \cdot \frac{m_e}{M_1 \cdot m_0}}{I_0 \cdot Z_2}$$

where Z_1 and Z_2 are the core charges of the ion and of the target, e is the elementary charge, m_e is the electron mass, m_0 the atomic mass unit, M_0 the relative atom mass of the ion, and I_0 the so-called Bloch constant determined in units of eV.

Nuclear stopping is the most important process at low energies, reaching a maximum around ε = 0.35 and then falling off with increasing ε. Electronic stopping, however, increases linearly with ion velocity and becomes the dominant process for energies greater than ε ≅ 3.

2.1.2 Straggling, ion distribution

The ion while penetrating the target material deviates, mainly due to nuclear interactions, its trajectory as a result the implantation volume is broadened [79], [86]. For this reason, each individual ion nominally impinging the target at the same place is thermalized at different positions. The deviation from the initial trajectory is defined as straggling, the implantation volume it is then function of energy, chemical species, target material and crystallographic orientation [152]. Such phenomenon is one of the intrinsic physical limits that cannot be technologically overcome, although it can be minimised with very shallow implantation (i.e., energies below 5/30 keV [153]) or through channelled implantation [154], although at the price of an increased variability in the penetration depth.

The mean value of the penetration depth is referred as *projection range.* The deviation of this distribution is called *longitudinal straggling*. *Lateral straggling* is defined in the transverse direction of ion's stopping positions distribution assuming cylindrical symmetry.

The projection range for an ion with initial energy E_0 can be derived from the total stopping power S(E):

$$R_p = \int_0^{E_0} \frac{dE}{S(E)} \qquad \text{Eq. 2.1-12}$$

Where S(E) is the total stopping power.

Another important parameter to be discussed is the ion distribution. Its mathematical expression is written as follows:

$$N(x) = \frac{\varphi}{\Delta R_{\mathrm{p}} (2\pi)^{1/2}} e^{-\frac{1}{2}\left(\frac{x - R_{\mathrm{p}}}{\Delta R_{\mathrm{p}}}\right)^2} \qquad \text{Eq. 2.1-13}$$

Where φ is the fluence (defined as number of ions per surface expressed in cm^{-2}, ΔR_{p} the straggling associated to the projected range R_{p}.

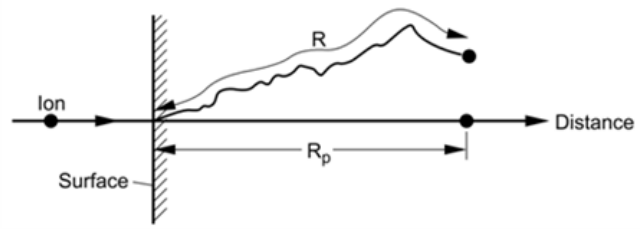


Figure 2.1.5 An ion incident on a semiconductor penetrates with a total path length R, which gives a projected range Rp, along the direction parallel to that of the incident ion. Figure from [142].

The gaussian expression is a simplification but it is a useful picture to describe the ion profile.

Different tools can be adopted to simulate such collisions and they all rely on Monte-Carlo simulation. The most used and popular is called SRIM (Simulation of Range of Ions in Matter) developed by James F. Ziegler and Joachen P. Biersack in 1983 [144]. It simulates the trajectory and the damage events, the depth of the implanted ions. This software has been used extensively for the simulations during the Thesis. The main aspect of ion matter interaction is discussed in this Chapter with special focus on creation of colour centres and beam lithography underlying the limits of such techniques and possible solutions to overcome these limitations.

The output from the SRIM simulation is characterised by *moments*: the first moment is the projected range, the second the standard deviation (i.e., the straggling), the third is referred as skewness, the fourth one is referred as kurtosis. Skewness and kurtosis are related respectively to the asymmetry of the distribution and to the flatness of the distribution [144].

With SRIM software it is possible to simulate the distribution of an implanted ion into a specific substrate the simulation performed are related only to the gaussian profile. The software does not consider the crystal structure of the target material, the interatomic distance is randomly selected with a probability distribution depending only on the atomic density. The simulation is performed considering the material as amorphous, this approach works acceptably if the ion trajectory is not parallel to a certain high-symmetry crystal orientation.

Electronic interaction is a process that happens continuously and because electronic collisions are so frequent it would be impossible to take them into account individually. In the Monte-Carlo simulation their effect is already substituted by a mean value energy loss and a standard deviation. On the other hand, interactions with nuclei can be considered individually, because of their lower frequency and their greater capability of deviating ion's trajectory, as well as creating defects and initiate cascade events. The energy loss due to collisions with the target atoms is always sensibly lower with respect to the electronic counterpart for light MeV ions (Figure 2.1.6).
To quantify the differences between implantation energy and ion mass in terms of stopping power, two set of data are simulated: hydrogen ions in diamond and silicon ions in diamond for 3 sets of energy, namely 25 keV, 200 keV and 1 MeV. Optimal SRIM settings for implantations in diamond are the following:

- density of the material equal to 3.52 gr/cm^3;
- *displacement energy threshold:* 50 eV (according to [155], [156]).

The *surface* and *lattice displacement energy* are not considered in detail since sputtering in diamond is not a relevant phenomenon with these employed ions and is not important for our applications.

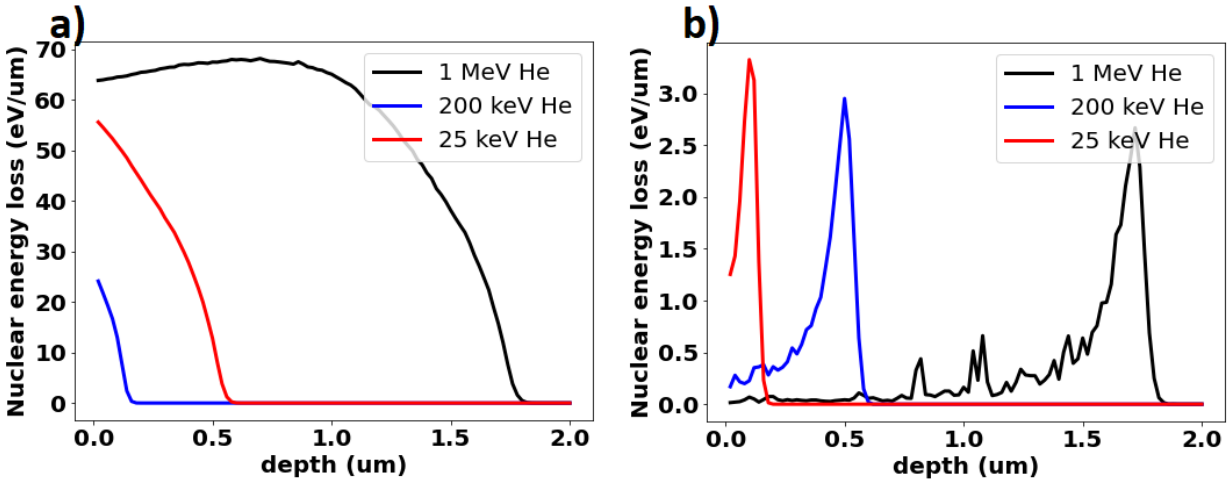


Figure 2.1.6 Electronic Energy loss (a) and nuclear energy loss (b) for 1 MeV, 200 keV and 25 keV He ion implantation in diamond.

To determine the straggling and ion distribution of energetic ions in diamond it is performed a simulation with SRIM for three cases: 25 keV, 200 keV and 1 MeV. In Figure 2.1.7 the result of such simulations is presented. It is observable a different penetration profile and enlargement of the implantation volume with highest straggling for the 1 MeV ions and lowest for the 25 keV. The same scale is portrayed to give a visual picture of the implantation volume size.

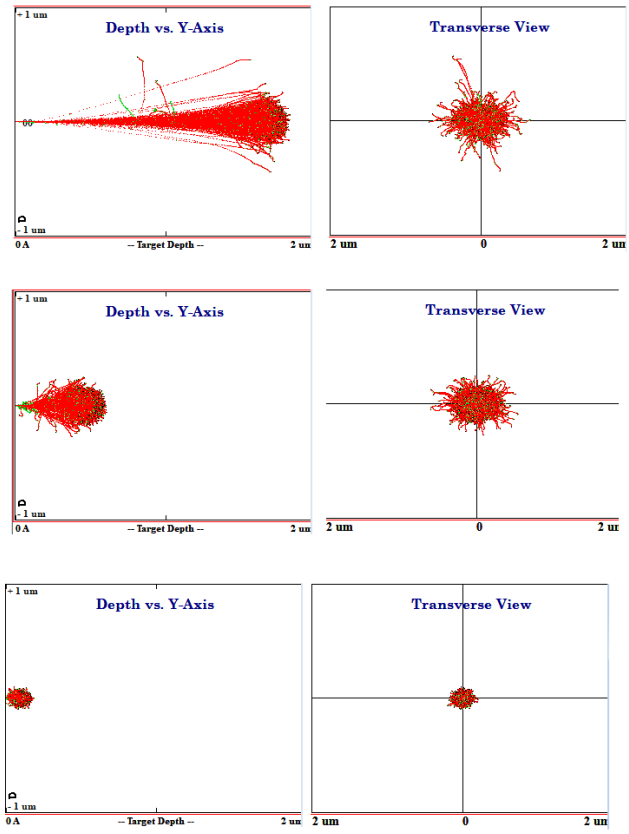


Figure 2.1.7 Longitudinal (left) and lateral (right) view of 1 MeV(top), 200 keV (central), 25 keV (bottom) He+ on diamond. The red paths represent the ion's trajectories and the green the recoils.

2.1.3 Fabrication of colour centres by means of ion implantation and thermal annealing

The fabrication of colour centres in diamond or any semiconductor can be achieved by ion implantation as stated in Chapter 2. In this section a more detailed description of this technique is presented, finally the limits and eventual solutions are given.

Defect engineering by ion implantation consists in two main subsequent steps, as simplified in Figure 2.1.8: the bombardment of a pristine substrate (1) with specific ions and specific energy (2) and a thermal annealing aiming at both recover the crystal lattice and promote the vacancy diffusion [79] to ease the incorporation of the implanted ions int structurally sable lattice defects (3). Different techniques for annealing are existing up to this date: furnace annealing; rapid thermal annealing and laser annealing.

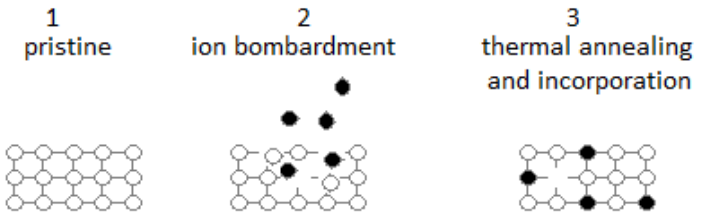


Figure 2.1.8 Simplified scheme of ion implantation. 1) pristine diamond. 2) ion bombardment, introduction of vacancies and ions in the substrate. 3) thermal annealing and incorporation of defects.

A key parameter to normalise the number of implanted ions is referred as Fluence, the integral over the implantation time of the beam current normalised on the beam area.

$$\phi = \frac{\int I\, dt}{QA} \text{ [cm}^{-2}\text{]} \qquad \text{Eq. 2.1-14}$$

Q is the charge of the implanted ion, A the area, I the beam current, t the implantation time.

Typical fluence values for functionalisation of semiconductors are $10^{9}/10^{18}$ cm^{-2} [87], [157], [158]. To create single defects the fluence upper limit is typically 10^{13} cm^{-2} [80], to modify the structure of the substrate the typical values are above 10^{17} cm^{-2}[159]. To modify the electrical properties of the substrate the typical fluencies are $10^{15/16}$ cm^{-2} [158].

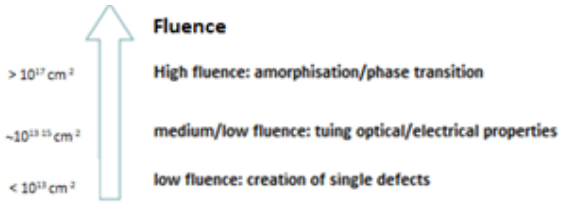


Figure 2.1.9 Schematic representation of implantation fluence and effects.

In diamond, depending on the ion mass, it is important to maintain the vacancies profile below the so-called *graphitisation threshold* [160] e.g. the upper limit where the lattice is distorted in such a way that even after the thermal annealing the crystalline form and sp^3 bonds are no longer recovered and the presence of a defect region composed of sp^2 bonds is formed.

To activate the dopants, it is required an annealing process [161], [162], [163]. The furnace annealing consists in heating the sample up to 1400 °C [164] in high vacuum regime for several hours or to heat the sample above 2000 °C temperatures under high pressure regime [87], [165]. The temperature is held constant on the substrate and the timing and temperature is chosen to perform a recrystallisation of the lattice and to promote the diffusion of impurities [166], [167], typical durations of these process is in the range of several hours [79].

Rapid thermal annealing is a process consisting of heating the sample up very quickly (seconds to minutes) at temperatures up to 1000 °C [168]. This technique has the advantage of being of shorter duration and different wafers can be processed in minutes respect to hours. It has been demonstrated that RTA is better to activate dopants minimising the dopants diffusion for silicon [168].

Laser annealing is a technique that involves the adoption a pulsed laser to anneal the lattice with duration typically in the nanosecond [169] or femtosecond [170] regimes. This technique consists of focussing a laser to the surface of a sample, the high energy density at the point of impact is absorbed by the material, thus heating locally the layer. The absorption of photons from the lattice permits to locally activate the defect [163], [171] and allows to better reduce the diffusion of dopants in silicon and therefore having better performances for dopants activation [163].

2.1.4 Fabrication challenges

Various challenges need to be addressed to engineer arrays of emitters useful to achieve the *second quantum revolution* (the use of technologies relying on quantum mechanics properties). Particularly, the necessity of fabricating with accuracy arrays of emitter is key-enabling factor [172], [173], [174] but significant drawbacks at the state of the art are still to be overcome:

- Formation yield: the low efficiency (typically < 10% [175]) in the conversion of individual impurities into structurally stable optically active defects play a crucial role for a scalable fabrication of arrays. The necessity to implant more than one ion (in the range of hundreds [108]) to form a single emitter means that the process follows a Poissonian-type uncertainty [176].
- Ion straggling: when impinging the substrate, an ion loses its energy due to the interaction with the crystal lattice causing a deviation from its original straight path. This unavoidable effect is strictly related to ion-matter interaction.
- Single ion implantation: low fluence implantations are achievable using the state-of-art ion implanters, possibly reaching in principle very low currents (pA-fA) [79], however single ion delivery is challenging due to the difficulty of measuring accurately low currents.
- Single ion counting: the capability of implanting single ions requires a proper counting which is greatly challenging. Different techniques can be adopted: pre or post impact on the sample. due to the low charge generated in the material (diamond especially).

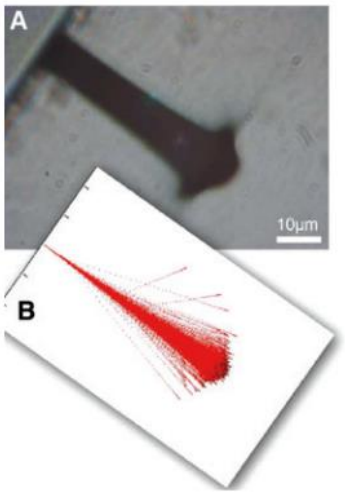


Figure 2.1.10 Schematic representation of straggling in diamond of 3 MeV proton irradiation. a) Optical image of implantation volume. B) simulated lateral and longitudinal straggling with SRIM. Figure from [86].

To overcome such challenges different approaches may be explored:

a. Hot implantation [177]: heating up the substrate during the implantation would favour the mobility of the vacances and therefore the conversion efficiency. Such method in principle allows to fabricate more optically stable defects, minimising the presence of defects in the crystal that could act as decoherence source [98] for the application of the colour centre.
b. Emission channelling analysis: such technique is a versatile tool allowing to both predict and evaluate the lattice location of the implanted ions [178], [179]. A radioactive probe beam is implanted in the substrate and the electron produced by nuclear reaction (β^-) are detected by a position-sensitive detector. The electrons flow through the low index crystallographic orientation and the detector allows to reconstruct the emission pattern.
c. Focused ion beam and micro masking [180], [181], [182]: masking the substrate with proper pattern have been demonstrated to be an efficient statistic approach to fabricate arrays of emitters. Focusing the beam below 100 nm is also permits to implant very localised and low struggled ions. Adopting low energy and well-defined beam spots is an efficient method to reduce the current achievable and obtain countable single ions.
d. Charge imaged detectors, electron-hole pairs detection, secondary electrons detections: many techniques in recent years have been developed to count single ions [106]. In Figure 2.1.11 these techniques are reported. The first rely on the production of secondary electrons generated by the impinging ion on the substrate [183]. The second rely on the ionisation and electron-hole pair generated by the implanted ion based on the IBIC (Ion Beam Induced Charge) [184].The third one relies on the charge detection of the accelerated ion before impinging on the substrate while passing through a conductive set of rings [185]. It is worth mentioning that for the low energy regime (i.e. < keV) these techniques are complex to be achieved [98].
e. Low energy implantations: it could be limited adopting low energy implantations (< 10^3 eV) and by selecting impurities significantly larger than that of the lattice atoms [153].

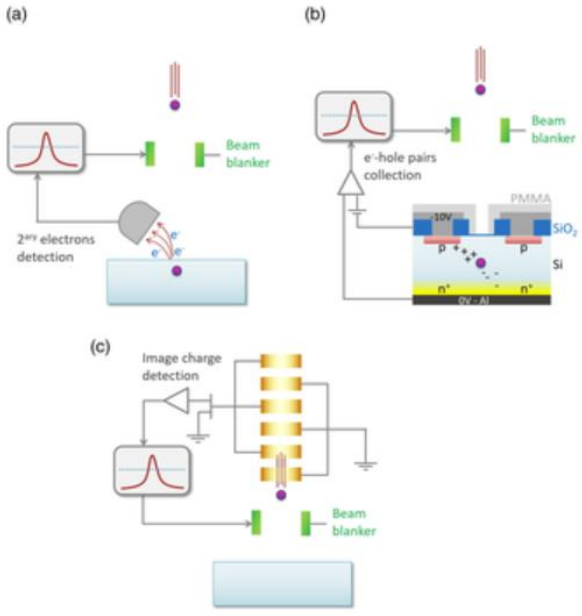


Figure 2.1.11 Schematic representation of different ion counting techniques. a) secondary electron technique. b) electron-hole pair collection. c) charge image detecting technique. Figure from[106]

2.2 Electrostatic accelerators

An electrostatic accelerator is a system that accelerates at certain voltages particles produced by different means. The system runs in high vacuum regime, to reduce the gas present in the beamline is crucial to maximise the mean free path (average distance that a gas molecule travels before colliding with another molecule) of the particles to reduce the scattering occurring between the accelerated particles and the gas present in the accelerator. Typical pressure values are 10^{-6} mbar [186].

In this section the components of electrostatic accelerators are described. In particular, the sections are divided as source area (where the ions are produced), electrostatic and magnetic components.

The medium energy regime accelerators are typically in the range of hundreds of keV to tenth of MeV [187]. Low energy electrostatic accelerator can be classified by their physical design (single-ended or tandem), by the source type (production of ion beam) as well as by their voltage generation method. Depending on the type of source adopted, the ions can be or positive or negative. There are two main classes of ion sources depending on how the ions are generated: a) solid-based type of sources based on sputtering phenomenon; b) gas-based sources are based on production of ions by Radio Frequency (RF) discharge, Duoplasmatron sources among the others. The beam is guided in the beamline through other electromagnetic components [186]:

- Electric beam elements
    - Focussing elements: Einzel lens, Quadrupoles
    - Steering elements: electrostatic dipoles
- Magnetic beam elements
    - Bending elements: Dipoles
    - Focussing elements: Quadrupoles

2.2.1 Source area

The ion can be generated with solid based and gas-based sources [186]. The first rely on the sputtering of ions from a solid cathode and its description is given with high degree of detail in Chapter 3. Gas-based sources are briefly discussed to give an insight of their working principles. A neutral gas is ionised by impact of energetic electrons (typically Radio Frequency fields or hot filaments). The ionised gas (plasma) is composed of positive, negative ions as well as neutral gas particles. Using suitable electrodes, the beam is extracted and accelerated towards the accelerating tube.

Filament sources are designed to work with thermoionic effect, the filament is coated with low working function metals that properly heated can emit electrons. The electrons are now injected in the gas chamber and the ionisation process occurs. Radiofrequency (RF) sources are filament free design chambers where RF fields are used to create the ion plasma. The ionisation occurs or via induction coupling, a discharge tube is placed into a solenoid of a resonant circuit, or via capacitively coupling, the RF field is connected to two rings placed around a discharge tube. Typical ion production is H^+ or He^+ [186].

RF sources' working principle is the adoption of radio frequency to produce positive protons and Helium (typically). These systems are filament-less and the primary source of electrons are the one already present in the gas, RF fields excited imprinting enough kinetic energy to create the plasma.

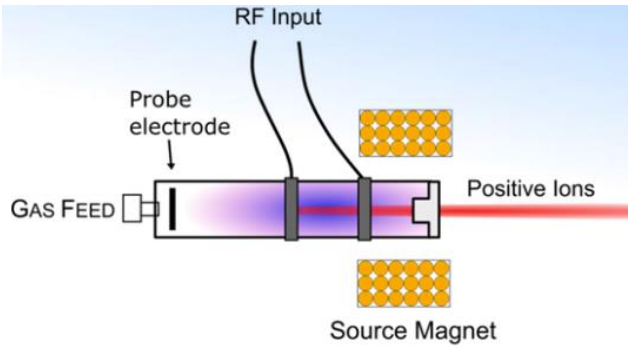


Figure 2.2.1 Working principle of the RF source. Figure from [188].

The Duoplasmatron source is depicted in Figure 2.2.2. Its working principles consist in two discharge stages. The first discharge is assisted by electrons produced by thermoionic effect (see the filament in the Figure). An intermediate electrode is built with an aperture, and it is polarised to attract the plasma through its centre by an axial magnetic field towards the second discharge area. In this area the ions are produced, the voltage difference between the anode (acting as a cathode) and the extractor guides the ions through a second aperture towards the beamline [189].

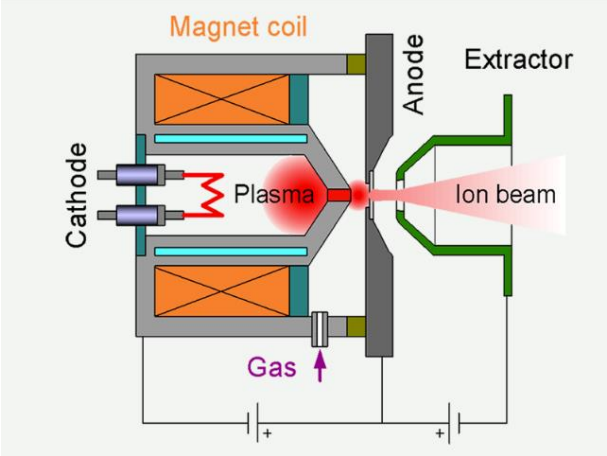


Figure 2.2.2 Working principle of the Duoplasmtaron source. Figure from [190]

In single ended accelerators, typically the ions are generated by positive ion source connected to a positive high voltage terminal. The terminal is the linked to an accelerating tube that accelerates the ions towards the ground potential. The energy gain is proportional to the voltage applied and the charge state of the ions. Tandem accelerators consist of two stages accelerations. The first stage is typically composed of a negative ion source that injects ions in the first accelerating tube towards the positive terminal. In the positive terminal, via stripping of electrons, the negative ions become positive, and they are accelerated towards the ground. Tandem accelerators enable much higher beam energies respect to single-ended [186].

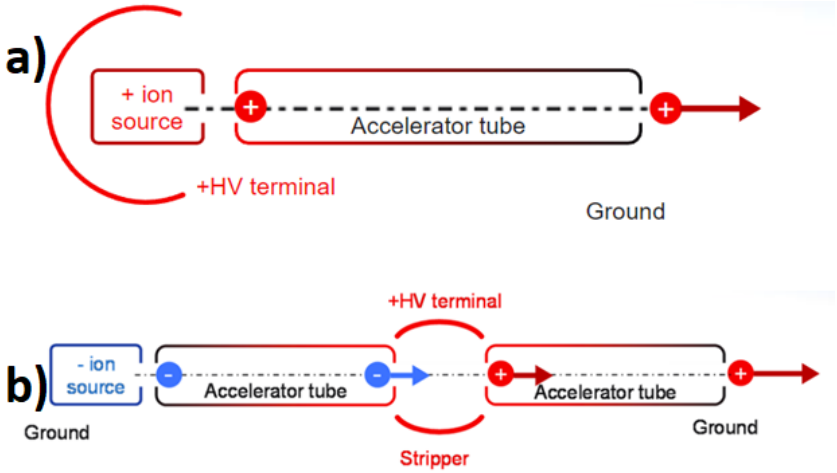


Figure 2.2.3 Typical design for electrostatic accelerator: a) single ended; b) tandem [186]. *Figure from* [188].

Electron stripping can be performed when the beam passes through a low-pressure gas tube or with a carbon foil.

Typically, mechanical systems consisting of a belt generator (Figure 2.2.4a) or chain generators (Figure 2.2.4b) are adopted as high voltage supplies [186]. These generators are similar in the charging of the terminal. The belt generator is composed of a belt made of volcanic rubber coated multi-layer carcass linked to a high voltage source; the induced charge is transferred onto the belt via a high voltage biased screen which contacts the belt to the grounded end of a column. The belt transports the charge to the terminal where it is removed by a screen that contacts the belt to the terminal. The chain generator is composed of a steel pellet coupled to insulating nylon links chain. A grounded drive pulley moves the chain, as the pellets passes the negatively biased inductor, electrons are pushed off the pellet onto the drive pulley leaving positive charge transported to the terminal by the chain. At the terminal the pellet passes a negatively biased suppressor electrode preventing sparks. On the contact with the pulley, the positive charge is transferred to the terminal. Chain generators are more durable that belt ones, charge transfer is more reliable and efficient also it eliminates the dust related problems of the belt systems.

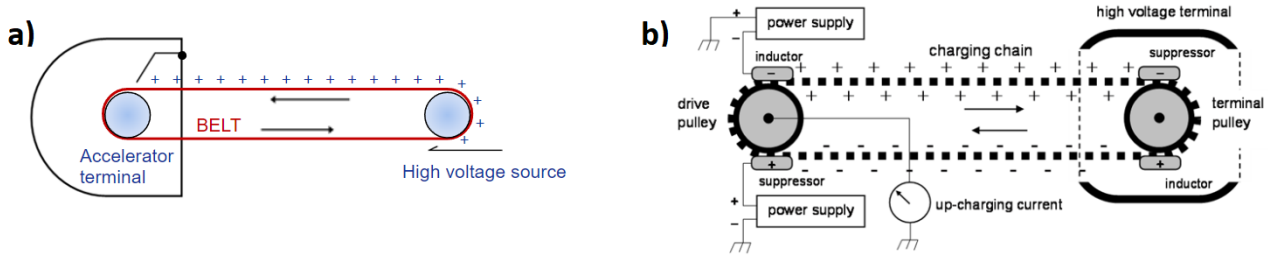


Figure 2.2.4 Types of mechanical generators for high energy accelerators in MeV ranges. a) Belt generator. b) chain generator, figure from [186]. *Figure from* [188].

2.2.2 Electric beam elements

Electric beam elements can be both focussing and steering elements. Among the focussing ones, the Einzel lens represents a widely used system to focus the beam. The Einzel lens is typically used with low to medium accelerators, typically up to tens of keV [186], since high energy ones would require large polarising tensions and therefore causing breakdown to the lens. This component is made of three coaxial cylinders with the central one electrically isolated from the outer 2 and it is inserted in the source area before the main

accelerating stage [191], [192]. In Figure 2.2.5 it is reported the simplified scheme of an Einzel lens, the two outer cylinder are kept at the reference potential while the central one is polarised with voltages up to few tens of kV [191] to produce focussing effects on the beam.

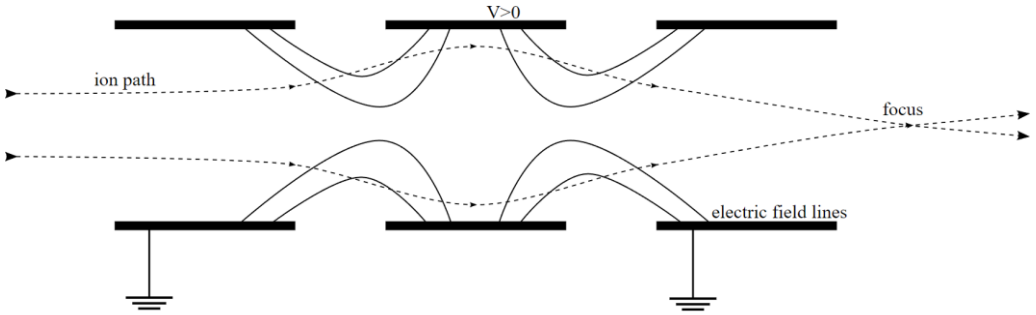


Figure 2.2.5 Working principle of the Einzel lens. Figure from [193].

The electrostatic dipole functioning is similar to a parallel plate capacitor. An electric field is applied to the plates with the purpose of or blanking the beam or to align the beam to be parallel to the beamline. The electric field is varied with the purpose of better aligning the beam through the main axis. Charged particles in an electric field experience a force parallel to the field lines and therefore a deflection α (see Figure 2.2.6) proportional to the charge-mass ratio.

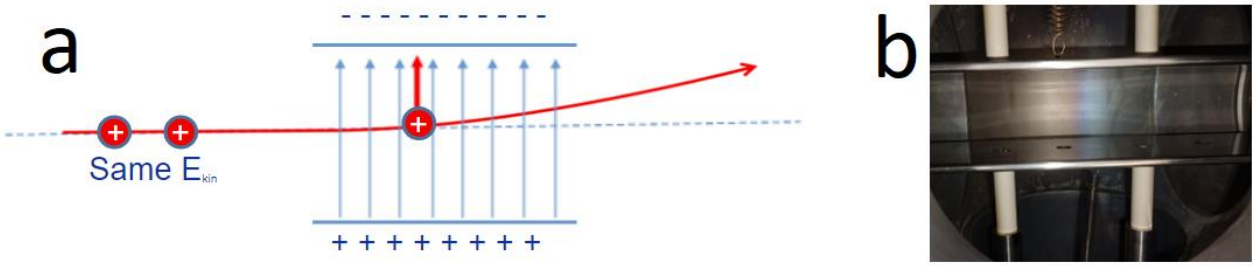


Figure 2.2.6 a) Working principle of the electric steering system. b) Picture of a typical electric steerer (acquired from the installed accelerator).

2.2.3 Magnetic beam elements

The most used system based on magnetic field manipulation are the bending magnets, the magnetic quadrupoles [186].

The bending magnet is the core of the mass spectrometry system. It consists of two magnetic coils set in a parallel geometry. The ions enter the magnetic field with a certain velocity (proportional to their accelerating voltage) and the Lorentz force is the main force acting on the ions passing through the system. Only the particles with the proper charge-mass ratio exit the magnet. The derivation of the equation governing the motion of the particles through the magnet is performed with more details in Chapter 3. In Figure 2.2.7 it is reported the working principle of a particle entering a magnetic field (Figure a) and the resulting effects depending on the charge-mass ratio for a fixed bending radius (Figure b).

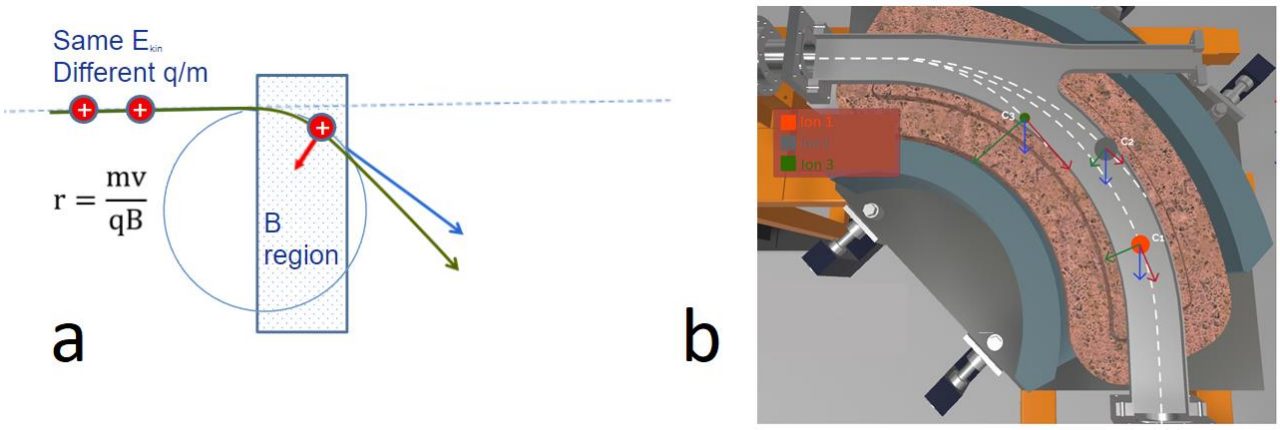


Figure 2.2.7 a) simplified working principle of particle passing through a magnetic field. b)Bending magnet (90° angle) working principles. The relation between the masses of the three ions depicted is Ion 3 < Ion 1 < Ion 2. The Green arrow represent the red arrow represents the velocity of the ion, the green one the resulting force and the blue one the magnetic field.

The magnetic quadrupole consists of a system with 4 poles, each being opposite in polarity with the adjacent one generating hyperbolic fields profile, as depicted in Figure 2.2.8. This system is typically used in pairs since only one quadrupole focus only in one direction.

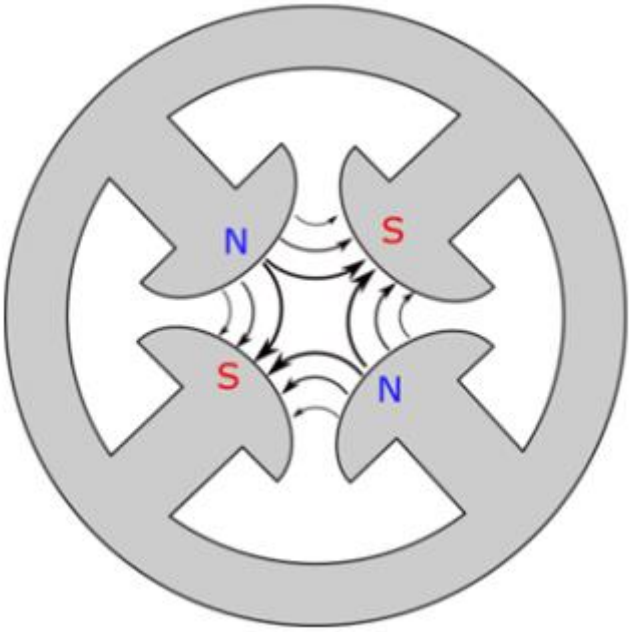


Figure 2.2.8 Single quadrupole scheme. The 4 adjacent poles are opposite in polarity.

The working principle of this system is based on magnetic field variation resulting in a force that focus one axis (horizontal) and defocus on the second axis (vertical). In Figure 2.2.9 it is reported the simplified scheme of the mentioned focussing effects, the magnetic field is represented with a black arrow and the resulting effect force is represented in green.

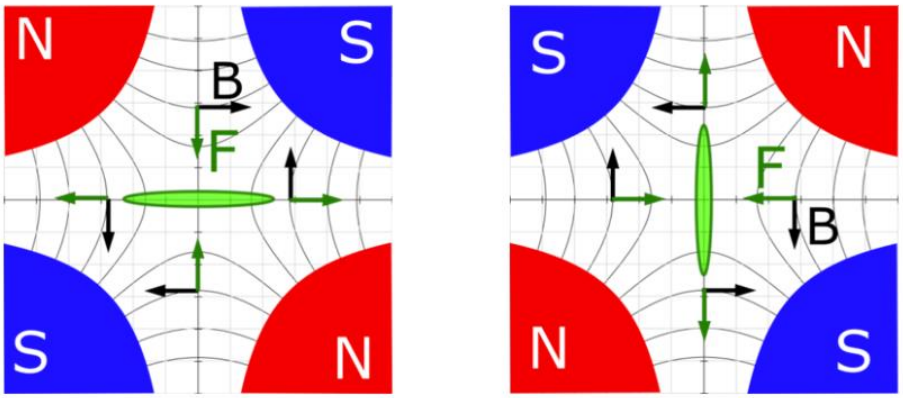


Figure 2.2.9 Illustration of a focusing fields by a pair quadrupole lenses (both horizontally and vertically). The magnetic field B is represented with a black arrow while the resulting forces are represented with a green arrow.

2.3 Focused Ion Beams implanters

The Focused Ion Beam (FIB in the following) implanters are low energy accelerating systems, typical values are around 25 to 50 kV.

The FIB is a system that focus and scan low energetic ions to a substrate, it is typically adopted for two objectives: to fabricate nanostructures in different materials via sputtering; to image systems with high precision acquiring the secondary electrons generated by the ions-matter interaction. Recently, it is used to perform ion implantation with fixed number of ions per spot to fabricate optically active defects in semiconductors [108].

Historically such accelerators were provided with Gallium source for micromachining of structures in materials.

The FIB apparatus, pictured in Figure 2.3.2, consists of different sections. The source area is typically a liquid metal ion source (LMIS) [194]. The source area is composed of a tungsten needle, while operating the source, the metal is heated so that it melts towards the tip of the needle. The wet metal reaches the apex forming the so-called Taylor cone; then the beam is extracted with suitable electrodes towards the optical components. The FIB column is provided with a Wien filter to perform mass spectrometry to allow the user to select specific chemical species and specific charge state [195].

Once produced the ion beam, it is necessary to separate the chemical species of which it is composed of. Two different systems are typically employed to perform mass spectrometry: the 90° bending magnet system and the Wien filter system.

The Wien filter [196], as depicted in Figure 2.3.1, consists in system where an electric and magnetic field (orthogonal to each other with respect to the beam axis). The system is designed so that the Lorentz force (F_L = $q\vec{v}$ x $\vec{B}$) and the Coulomb force (F_C = $q\vec{E}$) are antiparallel in directions. The two forces compensate exactly (F_L = F_C) each other and the following condition is fulfilled:

$$v = \frac{E}{B} \qquad \text{Eq. 2.3-1}$$

All particles entering the filter have the same kinetic energy, therefore the same velocity provided they are with same q, as described by the following equation:

$$Qe\ \Delta V = \frac{1}{2}mv^2 \qquad \text{Eq. 2.3-2}$$

where

Therefore, the velocity is function of the mass and charge

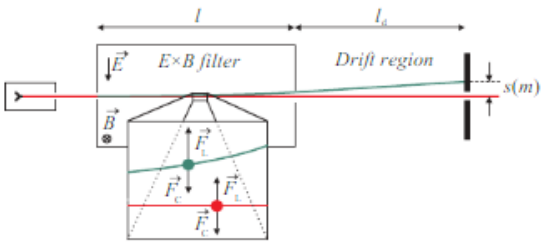


Figure 2.3.1 Working principles of Wien filter. Figure from [196]*. If the Lorentz and Coulomb forces are matched (red line), the particles exit the filter, otherwise (green line) the particles are deflected. To gain a higher mass resolution, the beam drifts in a zero field region increasing by geometrical consideration the deflection parameter s(m).*

The extracted beam passes through different electrostatic lenses that has the purpose of defining the beam size and focussing it on the target. The beam can be steered to perform scan of the target and blanked to stop the ion beam. To read the beam current it is mounted a Faraday cup on the sample holder or during the beamline. The final beam spot size can be in the order of < 100 nm.

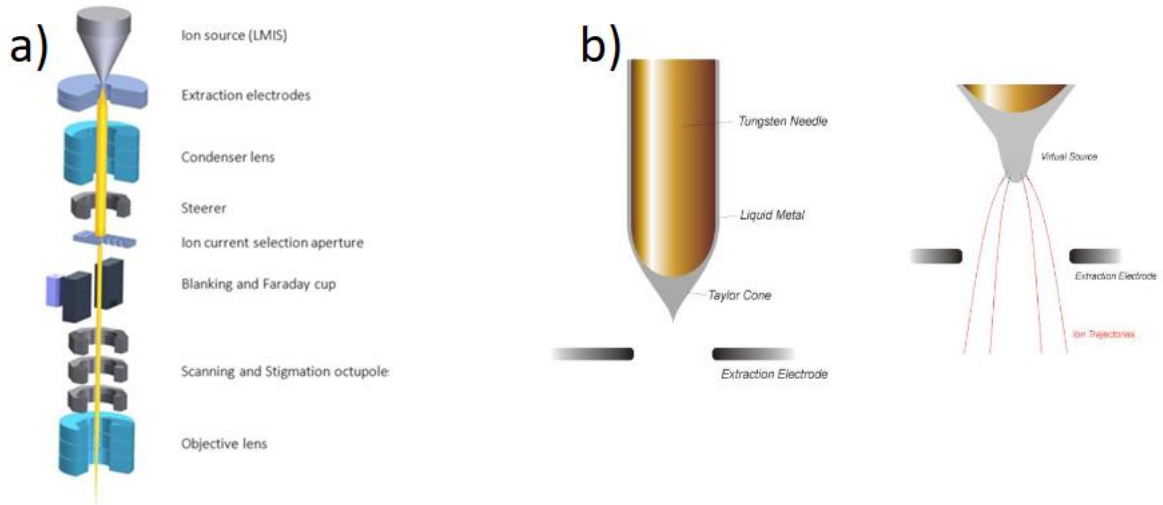


Figure 2.3.2 Schematic representation of a FIB apparatus. A) FIB column with its beam manipulator elements. B) Liquid metal ion source zoom. Figure from [194].

3 Chapter 3

In this chapter, the adopted experimental setups will be described.

A significant part of the work carried out in the context of this thesis, was related to the commissioning of the 100 keV Ion Implanter installed at the Department of Physics of Torino. The activities are related to the installation (alignment of the beamline, vacuum testing, equipment testing) and development of the software interface of the Implanter, described in detail in Appendix II. In this Chapter the main components of the implanter will be discussed, namely the ion-source, the beamline components, consisting of the mass spectrometry apparatus, the electrostatic optical elements, the control software and finally the irradiation chamber.

Further the ns-pulsed laser which was adopted for the optical lithography and the fabrication of the collimation masks will be described.

Finally, the characterisation setup is discussed, namely the confocal microscope and the Hanbury-Brown & Twiss interferometer setup and the optical cryostat used for measurements in the range 8 K to 300 K.

3.1 Development of keV implanter

The Ion Implanter installed at the Department of Physics of Torino is portrayed in Figure 3.1.1. The description will be divided in three sections: Source area (black circled area), Beamline (red circled area), irradiation Chamber (green circled area).

The electrostatic accelerator consists of a multi-elemental source of negative ions produced by Cs sputtering. The beam is bent by a 90° magnet and focused or steered by electromagnetic optics such as quadrupoles and magnetic and electrostatic steerers. Finally, the beam is propagated across the beamline to the irradiation chamber where the sample is mounted and the implantation is performed. The maximum achievable energy is 100 keV. A second beamline is under development to perform ion implantations at different experimental conditions respect to the first line (i.e. hot substrate implantation, broad beam etc.). Indeed, a switching magnet at 21° was installed during the first installation in order to allow the development of a second beam line.

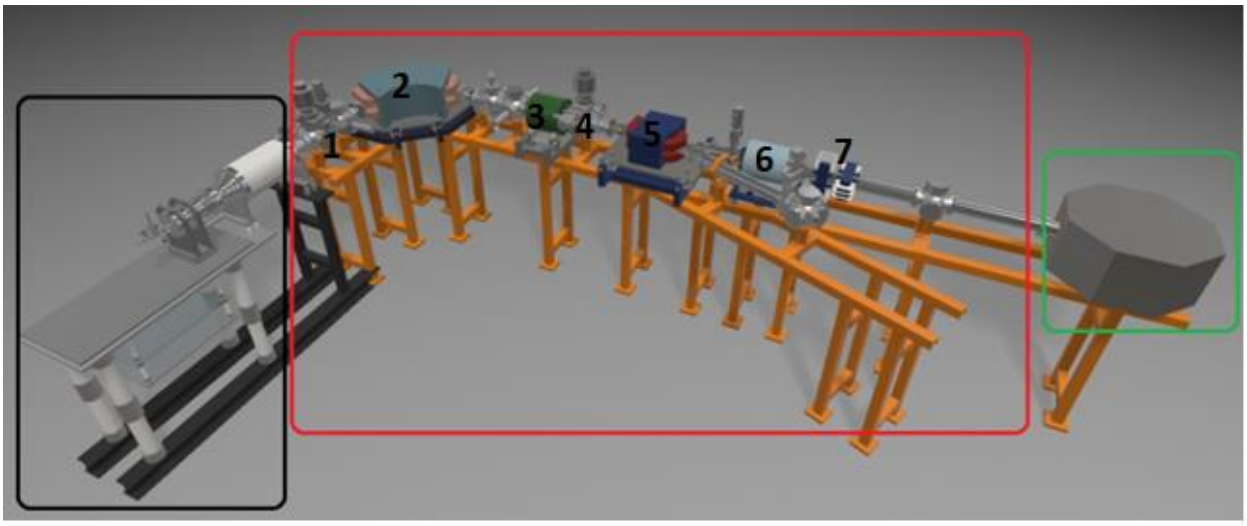


Figure 3.1.1 Scheme of the Ion Implanter installed in the Department of Physics of Torino. The black circled embed the source area, the red one the beamline and the green one the irradiation chamber.

3.1.1 Source

The ion source is where the ions are produced. The source installed, produces an ion beam by sputtering of ionised Cs to a solid target. Such source is defined with the acronym SNICS (Source of Negative Ions produced by Cesium Sputtering). In Figure 3.1.2a) a schematic representation of the SNICS is reported: it is composed by a reservoir that contains the Cs, an ionizer (shaped as a concave truncated cone) and a cathode containing the compressed target material. The operation of the SNICS can be summarized by the following steps. The Cs is heated up and when it evaporated it flows into the chamber; the ionizer is heated by Joule effect injecting current. Most of the Cs is ionised while a portion of it condenses on the surface of the cathode, about few monolayers. The Cs^+ ions are attracted to and focused onto the target in a cooled cathode (typically with petrol), the Cs^+ impact onto the target and sputters atoms out. A charge exchange transfer may occur between the Cs^+ and the neutral sputtered atom creating a negative ion. With a suitable bias voltage, the ions are then extracted on the extractor electrode towards the accelerating tube (in the case of the accelerator built at the Department of Physics 100 kV maximum potential).

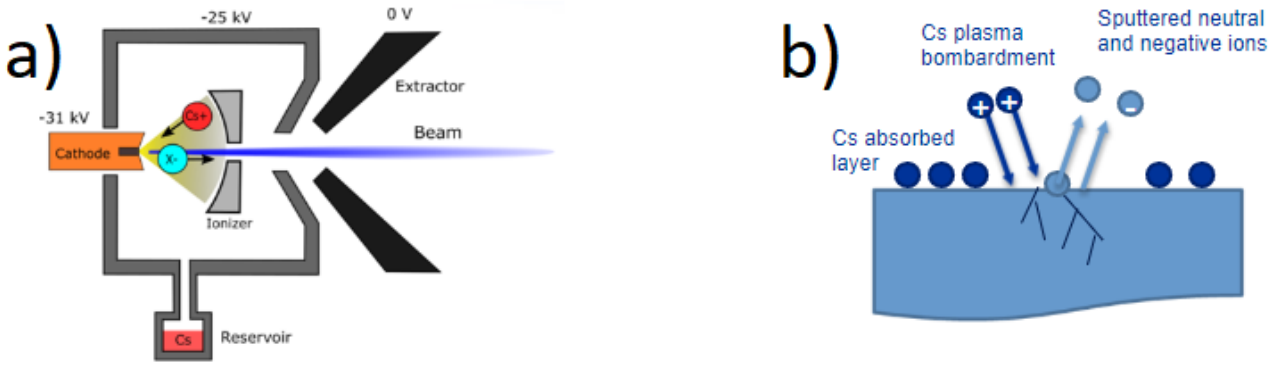


Figure 3.1.2 a) Schematic of the SNICS source. b) Operation principle of the SNICS source.

The production of ions is realised by sputtering, in Figure 3.1.2b the scheme of the working principle is reported. The ionised Cs^+ is accelerated towards the cathode (kept at a potential of 5-6 kV typically) and the sputtering event occurs. Each element has a characteristic parameter that distinguishes its negative ion state, such parameter is the binding energy of the additional attached electron or the so-called *electron affinity* (E_A). E_A must be positive to form a metastable negative ion state. The probability of creating negative ions from solid targets depends also on the surface *work functions* (ϕ), (i.e. the minimum energy required to

remove an electron from a solid to the vacuum level), hence the probability to obtain a negative ion from a surface by sputtering in proportional to the difference between the electron affinity and the work function. The Cs condensed on the surface has the important effect of reducing the work function [197] thus increasing the probability of creating negative ions. In the following Figure the values for the periodic table are reported acquired from ref [191]. The red marked elements do not form stable negative ions, but molecular beams can be created containing such chemical species: typically, oxides, hydride and carbide[191]. Depending on the cathode voltage, Cs flowing inside the ionizer, electron affinity of the cathode' chemical species, the beam current at this stage is varying in the range from µA to few mA.

IA	IIA	IIIA	IVA	VA	VIA	VIIA	VIIIA
1H 13.59 0.754			Ionization Potential Electron Affinity				2He 24.48 0.078*
3Li 5.39 0.618	4Be 9.32 0.195*	5B 8.30 0.277	6C 11.26 1.263	7N 14.53 -0.07	8O 13.61 1.461	9F 17.42 3.399	10Ne 21.56 < 0
11Na 5.14 0.548	12Mg 7.64 < 0	13Al 5.98 0.441	14Si 8.15 1.385	15P 10.48 0.747	16S 10.36 2.077	17Cl 13.01 3.617	18Ar 15.76 < 0
19K 4.34 0.501	20Ca 6.11 0.043	31Ga 6.00 0.30	32Ge 7.90 1.2	33As 9.81 0.81	34Se 9.75 2.021	35Br 11.81 3.365	36Kr 14.00 < 0
37Rb 4.18 0.486	39Sr 5.70 < 0	49In 5.79 0.3	50Sn 7.34 1.2	51Sb 8.64 1.07	52Te 9.01 1.971	53I 10.45 3.059	54Xe 12.13 < 0
55Cs 3.89 0.472	56Ba 5.21 < 0	81Tl 6.11 0.2	82Pb 7.42 0.364	83Bi 7.29 0.946	84Po 8.42 1.9	85At 9.5 2.8	86Rn 10.75 < 0

Figure 3.1.3 Table of ionisation energy and electron affinity[191]*. The elements marked in red do not form a stable negative ion.*

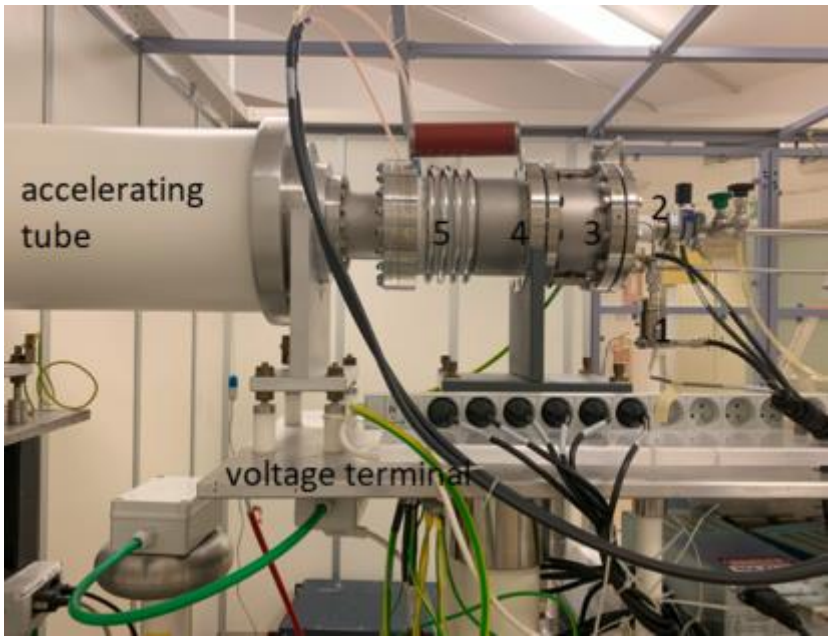


Figure 3.1.4 Picture of the source area installed in the Solid-State Laboratory. 1 represents the reservoir filled with the Cs; 2 the cathode feedthrough;3 the Ioniser; 4 the extractor; 5 the einzel lens. The voltage terminal is the reference voltage for the instruments of the source area and the accelerating tube is the main accelerating component.

3.1.2 Beam transport

Once the ion beam is extracted from the source and accelerated to reach the desired energy, it is necessary to measure its current, select the desired chemical species, focus and steer the beam towards a target. The beamline is composed of different elements. It is equipped with two faraday cups (labelled as 1 and 4 in Figure 3.1.1), one before the selecting magnet (to read the beam current produced) and one after to perform mass spectrometry, two quadrupoles (labelled as 3 and 6), a set of electrostatic and magnetic steerers (labelled as 7) right before the entrance to the irradiation chamber. The first element outside the ion source is a circular aperture, mounted with the purpose of selecting its size. Afterwards the beam current can be measured by means of the first Faraday cup. This is done to measure the overall beam current, consisting of the sum of the currents of each chemical species. Both the aperture and the Faraday cup are water cooled; this is done to reduce the overheating due to the current since it is not uncommon that at this stage the beam current reaches several μA. Then the beam enters the bending magnet (labelled as 2) where the mass spectrometry scan is performed (more details are given in following paragraph). To handle the beam, i.e. correct possible aberration related to small misalignment of the beamline components, different electrostatic and electromagnetic components are mounted. A set of electric steerer aims to correct the vertical direction of the beam (considering as z direction the one where the beam propagates), an applied voltage to the planes of the steerer allow to move over the y direction the beam. Typical voltages applied are below 500 V, the effect can be monitored on the Faraday Cup 2 or 3 observing an increasing or decreasing of the beam current measured. Then, the beam passes inside a double quadrupole system where a magnetic field acts as focussing system on the x and defocuses it on y (or vice versa as discussed in Chapter 3). The quadrupoles are current regulated and typical current values depends on the energy of the beam and the mass selected (from 1 A to 6 A typically). The beam passes through a switching magnet (labelled as 5) where it can be directed towards a second beamline (not yet mounted at the time of the writing of this Dissertation) and encounters a second double quadrupole (acting in the same manner as the first) that focuses the beam into the irradiation chamber. Finally, to act on the coordinates orthogonal to the beam propagation direction (x and y), a set of magnetic steerers is mounted at the entrance of the irradiation chamber with the aim of bending the beam towards the target and correct eventual misalignment, the steerers are current regulated and the typical working values are in the range 1-4 A. To reach the desired beam current on the faraday cup in the irradiation

chamber (i.e. to reach the desired fluence ass discussed in Chapter 2), to obtain a homogeneous beam spot, typically the user works in parallel with the quadrupoles and the magnetic steerers, aiming to align the beam and reach the maximum homogeneity of the spot or the proper current, depending on the application, beam spot size among the others. For example, considering that the fluence to be implanted is in the range < $1x10^{11}$ cm^{-2} within an area of 1.5 mm, if the beam current is ~10 pA the time for the implantation is 28 seconds, for ~5 nA the time is 0.05 seconds. Contrary, for a fluence of $1x10^{13}$ cm^{-2} within the same area, if the beam current is ~10 pA the implantation time is 2831 seconds (~47 minutes), while for ~5 nA the time is ~5 seconds. The implantation are typically performed extracting the Faraday Cup 2 for the implantation time and inserting automatically at the end. It is worth mentioning that, for implantation shorter than 1 second, the error is rather large since the Faraday Cup is inserted/extracted with a pneumatic system which has a rather large delay between the input to the pneumatic system and the insertion/extraction of the Faraday cup itself.

The beam spot is then imaged in the chamber observing the spot imprinted on a PMMA coated silicon sample or by observing the Ionoluminescence produced by a CsI film. At this point, the beam is *prepared* and the user can perform the irradiation of the desired target.

3.1.2.1 Mass spectrometry

The core of the mass spectrometry of an accelerator is a bending magnet, which is a system with planar geometry with a scanning magnetic field perpendicular to the beam plane that allows to select specific isotopes and chemical species. The working principle of operation is based on the Lorentz force. From $\frac{mv^2}{r} = QevB$ Eq. *3.1-1* it is possible to obtain the relation linking the velocity of the ions to the applied magnetic field as reported in the following equation:

$$\frac{mv^2}{r} = QevB \qquad \text{Eq. 3.1-1}$$

Where *m* is the mass of the accelerated ion, v its velocity, *r* the radius of the analysing magnet, *Q* the charge state of the accelerated ion, *e* the elementary charge, *B* the magnetic field inside the magnet. This formula stands considering the magnetic field always orthogonal to the beam propagation direction, this approximation is possible given the magnet geometry.

The ions energy is written as:

$$E = Qe\,\Delta V = \frac{1}{2}mv^2 \qquad \text{Eq. 3.1-2}$$

Where Q is the charge state of the accelerated ion, e the elementary charge, ΔV the accelerating potential, m the mass of the ion and v its velocity.

Placing *Eq. 3.1-3 in Eq. 3.1-4* it is possible to obtain the relation between the magnetic field and the applied voltage at the accelerating stage as function of atomic mass (m = AM, where A represents the atomic mass and M the nucleon mass):

$$B = \sqrt{\frac{2AM\Delta V}{r^2 Qe}} \qquad \text{Eq. 3.1-5}$$

From the datasheet of the magnet, it is reported the curve linking the current passing through the coils and the magnetic field, its expression is the following:

$$B[T] = (4.903 \pm 0.007) \cdot 10 - 3[T/A] \cdot I\,[A] + (1.8 \pm 0.7) \cdot 10 - 3[T] \qquad \text{Eq. 3.1-6}$$

From $B = \sqrt{\frac{2AM\Delta V}{r^2 Qe}}$ Eq. *3.1-5* and $B[T] = (4.903 \pm 0.007) \cdot 10 - 3[T/A] \cdot I\,[A] + (1.8 \pm 0.7) \cdot 10 - 3[T]$ Eq. *3.1-6* it is possible to obtain the calibration curve linking the current flowing in the coils and the atomic mass of the ions for a certain accelerating voltage, considering that the magnet has a radius of 500 mm, M the nucleon mass is 1.67·10−27 kg:

$$I\,[A] = 0.059 \cdot \sqrt{A\Delta V} - 0.36 \qquad \text{Eq. 3.1-7}$$

To fully calibrate the mass of the accelerated ions different spectra were acquired at different acerating voltages with a cathode containing PbZnS. The choice of such cathode is based on the presence of different isotopes for Zn and S allowing for a more precise calibration of the system. In Figure 3.1.5 it is shown the mass spectrum acquired for 40 keV accelerating voltage for the cathode containing PbZnS. The Pb peaks cannot be seen due to the constraints of the analysing magnet maximum current, it would be located after the maximum magnet current, hence it is not visible in the spectrum. *Figure 3.1.5* is divided in different coloured areas to highlight the different chemical species of which the mass spectrum is composed of. The red area represents the oxygen peak. The green areas highlight the sulphur chemical species, notably S does present different isotopes, hence numerous peaks. The green areas represent the Zinc related peaks. Zinc does not produce a stable negative ion but forms molecular beam bonding with H or O.

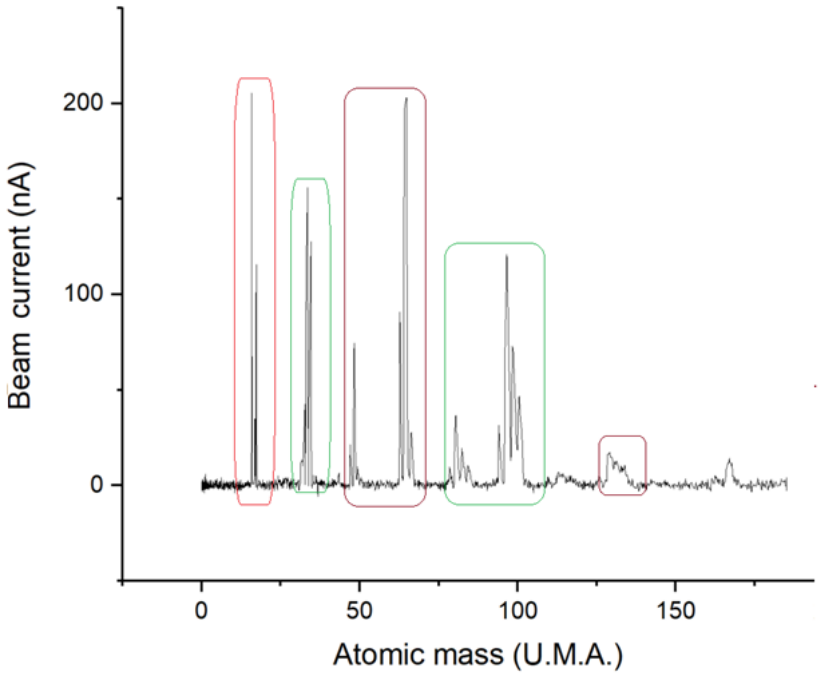


Figure 3.1.5 Calibrated mass spectrum of the cathode containing PbZnS. The peaks are coloured to highlight the different chemical species. The multitude of peaks for the same-coloured region represents the isotopes of the same chemical species.

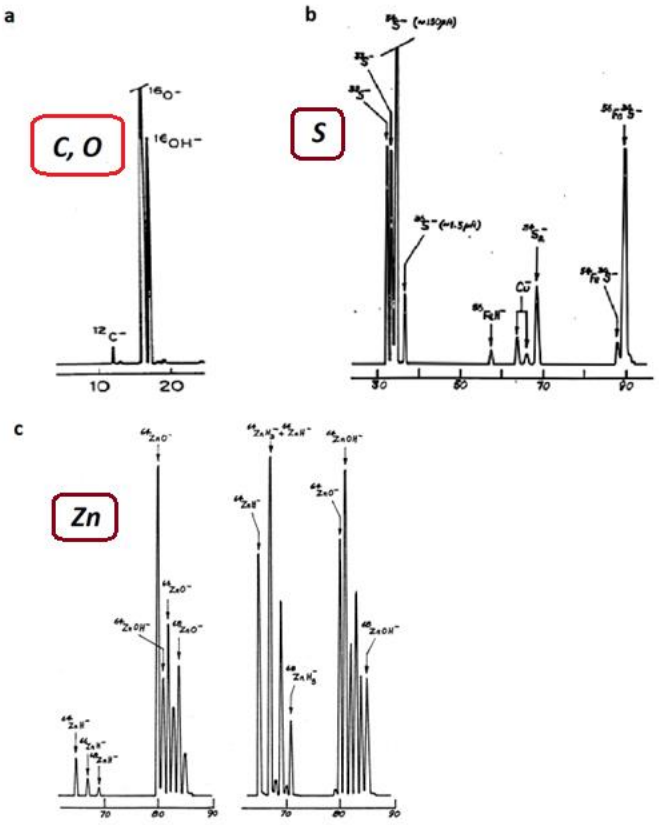


Figure 3.1.6 Different mass spectra used as reference for the calibration of the bending magnet. A) Carbon and Oxygen peaks. B) Sulphur peaks. C) Zinc peaks. The figures are taken from ref [191].

The mounted model magnet is a Bruker 5981000, it has a maximum magnetic field applicable of 0.81 T and a maximum current that can flow into the coils of 170 A. The water cooling maintains it fully operational minimising the heating due to Joule effect. The reading of the beam current is performed via a picoammeter, particularly a model Keithley DAQ6510.

The faraday cup that measures the beam current is custom made and composed as depicted in Figure 3.1.7. An external shield contains a three-layered system, labelled as I, II and III. The I and II layers, respectively the measuring plate and the defining aperture for the current readout, are attached via a cylindric component (C in the Figure) that guide the beam towards the measuring plate (layer I). The length of the cylinder is chosen to enhance the readout of the current, minimising the secondary electron leaving the system. To further maximise the readout, it is mounted a secondary electron suppressor (labelled as III). The electron suppressor is polarised at -200 V and its purpose is to push the secondary electrons generated by the impinging ions on the layer I. The different parts of the Cup are electrically insulated by ceramic cylinders (labelled as B). Particularly, the layers I and III are insulated from the external shielding as well as the electron suppressor and the layer III and I.

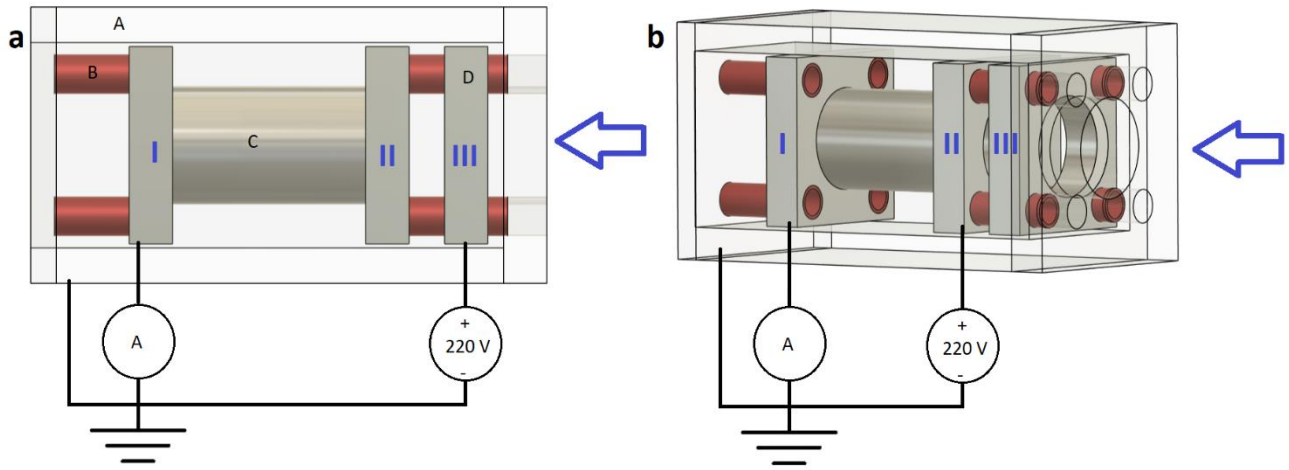


Figure 3.1.7 Schematic representation of the custom Faraday Cup a) side view and b) tilted view. The electric schema is reported in the bottom of the Figure. A in figure a) represents the external shielding of the Faraday Cup; B represents the ceramic insulator to electrically separate the different components; C represent a tube that improves the readout of the beam current; D represents the electron suppressor plate which is polarises to 220 V. The purple arrow represents the beam direction with respect to the Faraday cup entrance.

3.1.3 Irradiation Chamber

Special effort was carried out on the development of an irradiation chamber that suited the desired objectives, i.e. collimation of the beam over µ-sized apertures onto the target, read-out of the beam current at the plane of the sample, imaging system with hundreds of µ-sized field of view to mm-sized.

The irradiation chamber, as reported in Figure 3.1.8, is divided in main body and cover. The main body consists of a cylindrical geometry with a diameter of 60 cm. It has 12 feedthroughs on the side walls allowing to interface the inside equipment with the outside controller and software, for example BNC connectors, optical feedthroughs and cable connectors. The cover plate is divided in two different covers, the main one has a diameter of 60 cm and it is unmounted only when it is necessary to interface the chamber main body in its full size, if not, the second smaller upper plate allows to mount the samples inside the chamber.

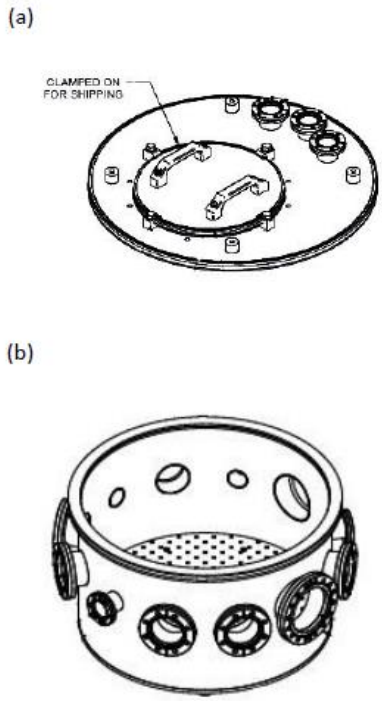


Figure 3.1.8 Representation of the irradiation chamber, both the cover plate (a) and the main body (b).

A picture of the irradiation chamber is shown in Figure 3.1.9. The different sections are now discussed, namely the scanning system and the imaging system. The green circled area in Figure 3.1.9 represents the aperture mounted where the beam the chamber, the red circled area represents the scanning system and the blue area the imaging system. The aperture consists of a metallic plate with a through hole with different sizes (1 mm to 3 mm) with the aim of selecting different maximum beam diameter. It can be easily changed or unmounted completely.

The irradiation chamber is equipped with a custom-made optical breadboard with an aperture of 150 mm at the centre as depicted in Figure 3.1.9. The aperture at the centre is designed to improve the vacuuming efficiency of the system. The adoption of an optical breadboard is helpful for the fixing of the equipment mounted inside in an arbitrary geometry, for example: the imaging system, the installation of the positioners and other possible improvements.

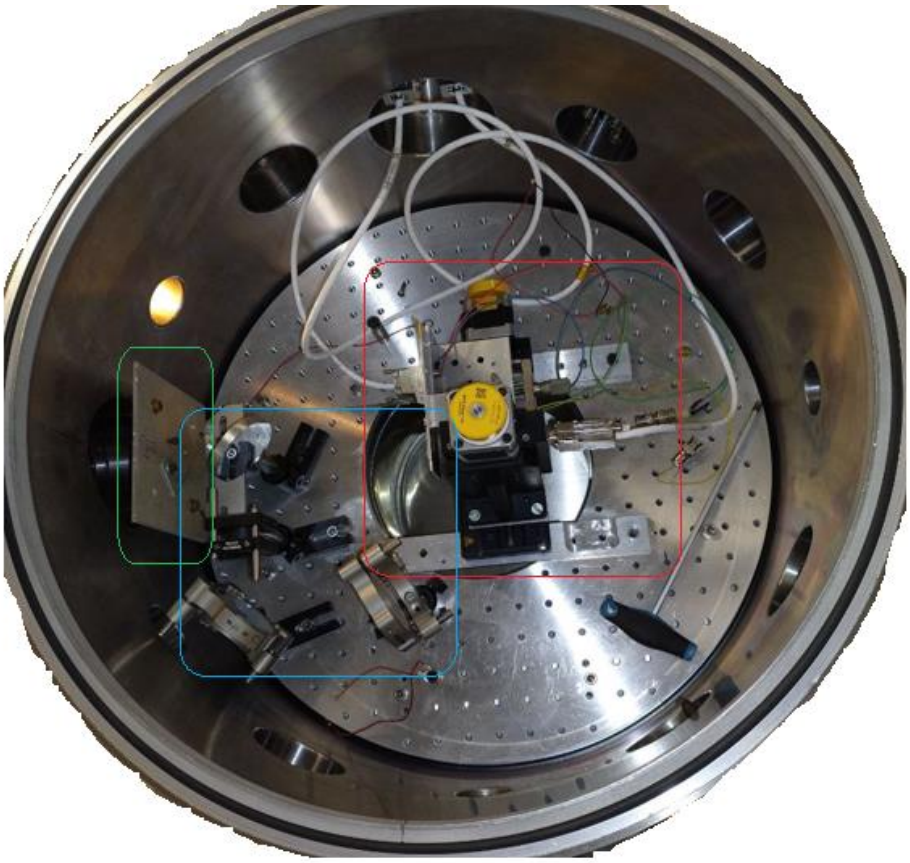


Figure 3.1.9 Picture of the inside of the irradiation chamber. The red circled area represents the scanning system, the green one the selectable aperture size at the entrance of the chamber (from 500 µm to 3 mm), the blue area represents the imaging system.

Scanning system

To reach the desired configuration, firstly it was developed the scanning system composed of two positioners from Physik Instrumente (Model 6230V6400 and 6230V1000) guided by Mercury cards (Model C-663). The range for the two positioners is respectively 100 mm and 25 mm allowing to move the samples attached to the sample holder. A custom-made Faraday Cup is mounted on the sample holder.This is done to monitor the ion beam on the same plane of the sample and optimize the size and the current by focusing at the same spot. The geometry is identical to what reported in the previous paragraph, consisting of a three-layer system. The main difference is the size of the cup, the entrance aperture is 1.5 mm instead of 5 mm.

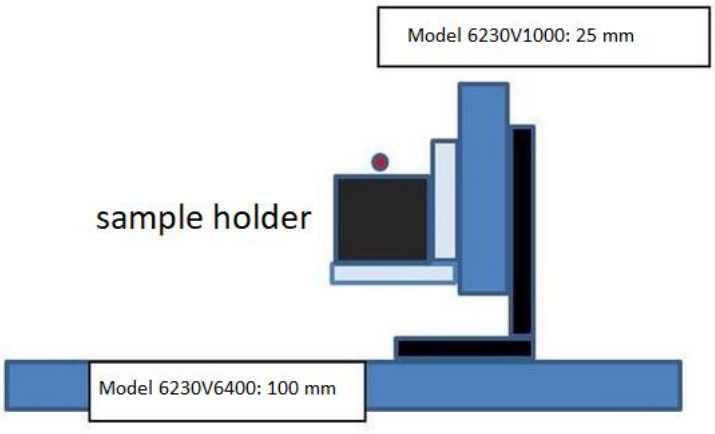


Figure 3.1.10 Scheme of the sample holder positioning inside the irradiation chamber. The labels in the picture represent the adopted motors with the range and model from Physik Instrumente.

The positioners are moved by a custom-made software in Labview code allowing to both move the sample holder to specific positions and moreover, to perform scans with a double purpose. Firstly, scan over the aperture of the Faraday cup allows to reconstruct the beam size and the beam position on the field of view, and to check the homogeneity while focusing the beam onto the sample holder. Secondly, to perform scanned implantations, instead of scanning the beam onto the sample. In this specific configuration the faraday cup is then linked via a BNC feedthrough to a picoammeter (Model Keithley 6485) to perform the readout of the beam current.

Figure 3.1.1 displays the intensity plot obtained scanning the sample holder over 7.5 mm on x and y direction around the centre where the Faraday Cup is mounted. The aperture of the Faraday Cup is 1.5 mm as obtained while scanning the beam and the beam size is ~1mm. The maximum current is reached when the beam impinges perpendicular to the cup and reaches smaller values when just a portion of the beam is scanned.

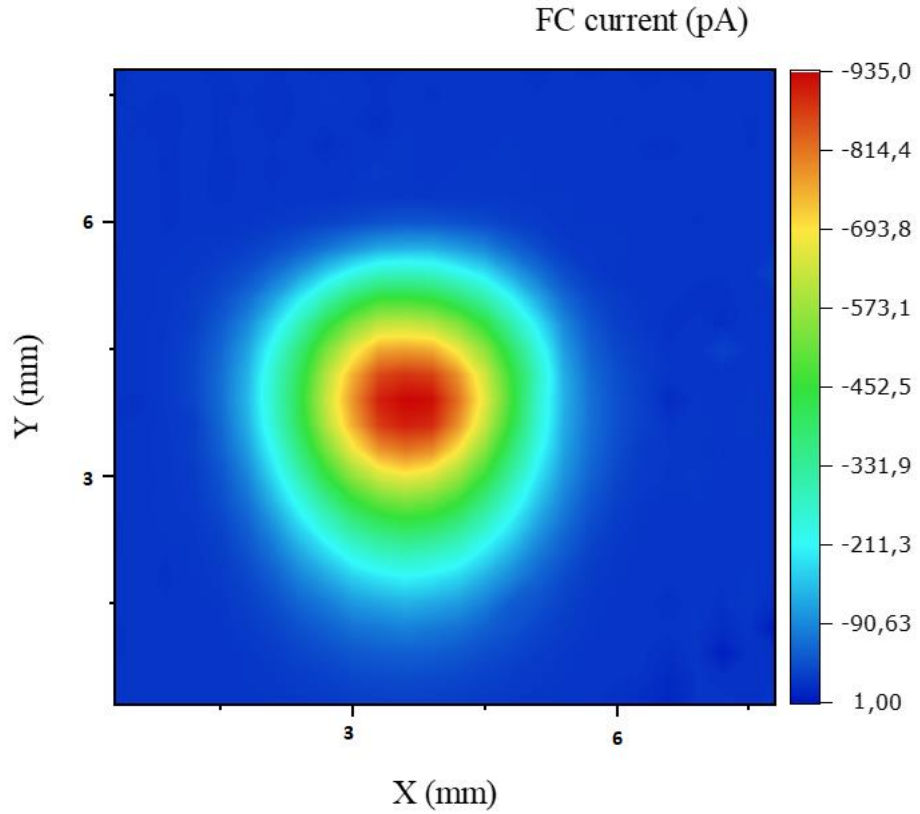


Figure 3.1.11 Intensity plot of the scanned Faraday Cup mounted onto the sample holder.

Imaging system

The imaging system is home built to match the need of the implantation schemes to be adopted. Due to the dimensions of the irradiation chamber and the desired field of view size (~ 1 - 5 mm), the system consists of a series of lenses and mirrors set at specific focal distances from the used camera (usb camera with magnification ranging from 40x to 100x and a focal distance of ~1 cm). The simplified scheme is represented in Figure 3.1.12, the camera is mounted outside the chamber, and it is set on a vacuum window feedthrough. A set of two lenses allow to focus the object (mounted in the sample holder on the scanning system) onto the camera. The camera is focussed onto the first lens, the rays are reflected by to flat mirrors set at 45° each towards a second lens. The second lens collimate the beam towards the sample holder via the reflection on the through holed mirror. The hole in the mirror allows the beam to pass through and impinge on the sample holder. The light source is mounted close to the through holed mirror inside the chamber. The choice of using a holed

mirror permits to reduce the parallax while imaging the samples and therefore performing more accurate implantations.

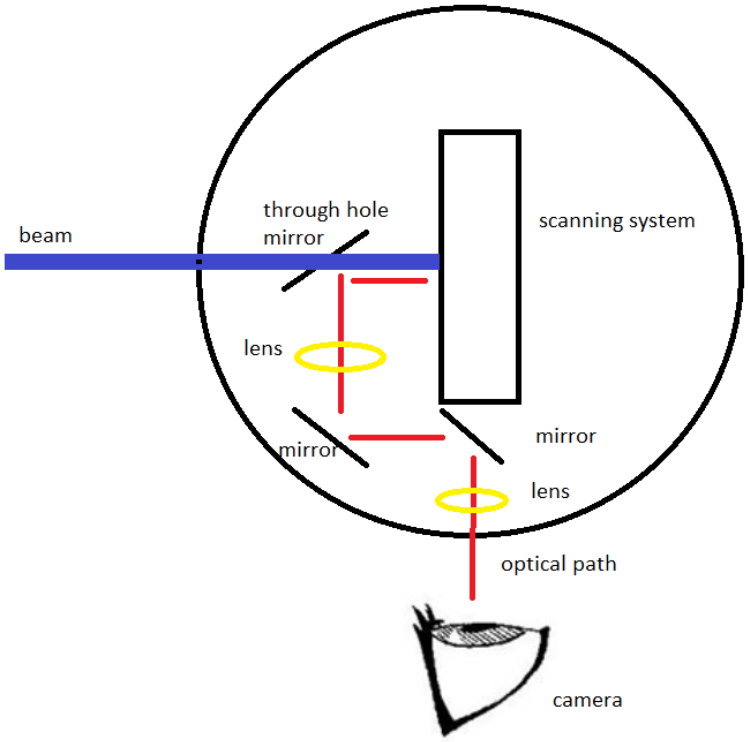


Figure 3.1.12 Schematic representation of the custom-made imaging system mounted in the irradiation chamber. The focal distance of the first lens (closer to the camera) is 250 mm, the focal distance of the second lens is 125 mm.

3.2 ns-pulsed laser

In order to produce collimating or in general masks to place on the top of the pristine diamonds, it was adopted a high-power laser. The masks were produced from an aluminum thin foil where different apertures of different geometries (typically squared) in the range of hundreds of µm were cut with the laser.

The model is *EzLaze 3,* from New Wave Research. This device is a Nd:YAG (neodymium-doped yttrium aluminum garnet; Nd:Y3Al5O12) pulsed laser operating in "Q-switching" mode: the emission is enabled after the maximum population inversion is achieved. The maximum obtained output energy is 0.6 mJ with a pulse duration of 4 ns. The dimension of the aperture is 2.5 x 2.5 mm2, leading to a maximum power density of 2.4 MW cm^{-2}.

The available wavelengths are the first three harmonics of the Nd:YAG: 1064 nm in the infrared (IR), 532 nm, in the green, and 355 nm, in the UV. The last two are obtained through a second and third armonic generator placed after the laser head. The laser is coupled with an optical microscope system, equipped with different objectives (20X, 50X Near-UV and 100X) and filters (IR 1X, VIS 2X, UV 1X) to focus the output beam.

Furthermore, the device can work in multiple-pulse mode: *continuous mode*, with 1 Hz repetition rate; and *burst mode,* with 5 Hz repetition rate. The maximum number of pulses in burst mode is 50, followed by a 20s cooling period.

The device is equipped with a manual control module to select the following parameters:

- Laser wavelength (1064 nm – 532 nm – 355 nm)
- Dimension of the irradiated region

- Attenuation (from 0.3 to 100 % of the total power density)
- Working mode (single pulse – *burst* – *continuous*)

3.3 Confocal Microscope setups

The confocal microscope is the preferred system for the PL characterisation of the SPSs for two main reasons: the spatial resolution achievable and the optical sectioning capabilities.

Such system is based on a laser source that acts as trigger for the emission from the defects embedded in the crystal lattice. In Figure 3.3.1 displays a generic confocal microscope layout; its working principle is the following: the light source (represented with green lines) propagates trough a dichroic mirror, which is a mirror acting as a filter with a specific cutoff wavelength, onto the sample. The sample absorb the excitation light and emits as fluorescence (red lines) light which passes through the dichroic mirror towards the collecting path for the light. Although the excited volume is small enough since the numerical aperture of the adopted objective is high, the fluorescence can originate from not in focus optical planes in the system. To overcome such inconvenient, the pinhole is inserted in the collection path of the PL signal and along with the point-like excitation, the PL not in the focal plane is removed (such phenomenon is referred as optical sectioning).

The term confocal is ascribed to the 3 conjugated points of the system in Figure 3.3.1, meaning that the focal point of the whole apparatus in identical for the laser excitation (f_1), focal plane on the sample (f_2) and the collecting point of the fluorescence (f_3).

The confocal microscope is in the following sections explained in terms of spatial resolution, optical sectioning and experimental implementation.

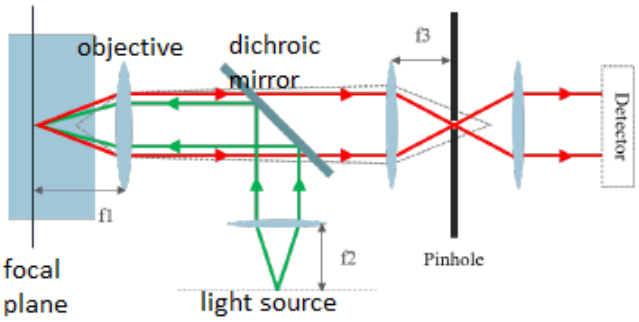


Figure 3.3.1 Schematic representation of the confocal microscope. The green lines represent the excitation light source, the red lines stand for the fluorescence light from the SPSs in the sample.

3.3.1 Spatial resolution and optical sectioning

The confocal microscope outperforms the widefield microscope with similar magnification lenses, it has a higher spatial resolution.

The optical resolution of a microscope is typically limited by aberrations and diffraction [198]. The first are related to the chromatic and non-paraxial conditions in the alignment of the setup and they result in distortion of the image. Aberrations can be, thus, minimised adopting well-pondered optical components and through aa careful alignment of the setup.

Diffraction is the physical limit of the microscope, light in fact, due to its wave-like nature, produces diffraction phenomena while interacting with the lenses present in the system.

The limiting effect of diffraction can be discussed considering that the object is point-like and it is on the focal plane of an objective, as depicted in Figure 3.3.2.Figure 3.3.2 Diffraction pattern produced by a circular aperture. Under this hypothesis, the light is collected by the objective and focussed to the image plane as a bidimensional circular pattern formed by a central disk (referenced as Airy Disk) surrounded by concentric rings.

The axial and transversal dimensions of a point-like object can be esteemed calculating the amplitude of the electric field on the optical axis, such function is referred as Point Spread Function (PSF in the following) [199]. In every microscope, the image is given by the convolution of the image function and the PSF [200].

PSF represents the intensity distribution in the image plan and describes the response of the optical system to an object point in real space, hence, tighter the PSF better the spatial resolution of the system.

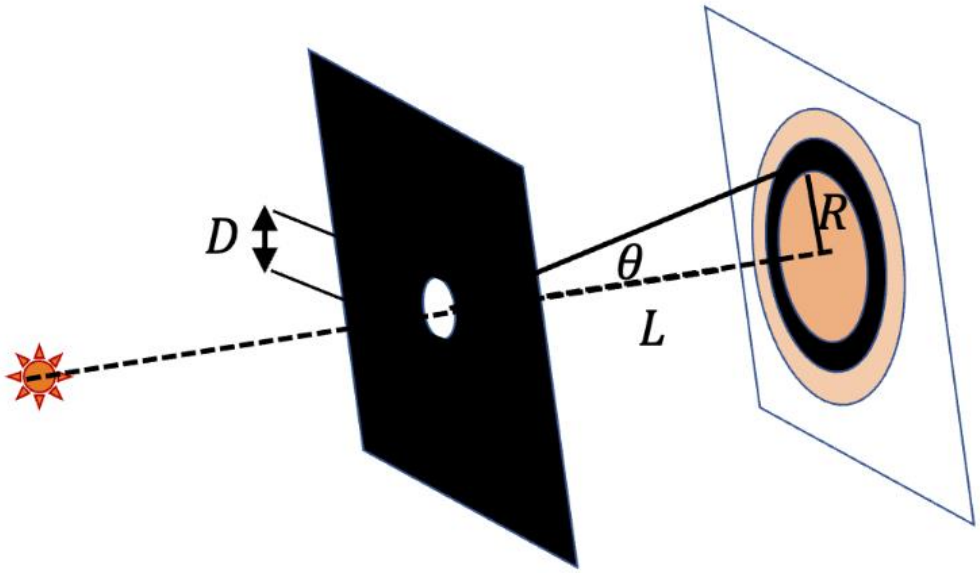


Figure 3.3.2 Diffraction pattern produced by a circular aperture. Figure from [201].

To measure the intensity in a point on the image plan, the Huygens-Fresnel principle for the wave propagation is adopted. Therefore, in the case of a circular aperture, the intensity is divided in spherical secondary sources originated from the first spherical wave on the aperture. The total intensity can be obtained as function of the angle θ, angle comprised between the optical plane and the line joining the centre of the aperture and a point on the optical plane. The Huygens-Fresnel principle therefore allow to determine the angle θ at which the first minimum on the intensity (i.e. the angle subtended by the radius of the Airy Disk on the image plane):

$$\sin\theta = 1.22\frac{\lambda}{D} \qquad \text{Eq. 3.3-1}$$

Where θ is the angle above discussed, λ the wavelength of the adopted light source, D the diameter of the aperture. For the visible radiation, λ is comprised between 400 nm and 700 nm, D has a dimension of 1 mm [202]. Thus, it can be adopted the approximation sinθ ≈ θ since λ << D. According to the Rayleigh criterion [203], the optical resolution of two points is defined as the angular separation (α_R) of two points where the intensity maximum of the first point is superimposed on the intensity minimum of the second one [203].

Under this assumption $\sin\theta = 1.22\lambda D$

Eq. *3.3-1* becomes:

$$\alpha_R = 1.22\frac{\lambda}{D} \qquad \text{Eq. 3.3-2}$$

The last equation can be written in the case of an optical microscope, in term of minimum distance s between two distinguishable points on the image plan. If the 2 points lies on the focal plane of the objective, to them it is subtended the angle α = s/f, where f is the focal length of the objective.

Consequently, the Reyleigh criterion becomes:

$$s = f\,\alpha_R = 1.22\frac{\lambda}{D}f = 0.61\frac{f}{R}\lambda \qquad \text{Eq. 3.3-3}$$

The ratio f/R is the sinus of the acceptance angle φ of the objective, i.e. the semi-aperture of the light exiting cone:

$$s = 0.61\frac{\lambda}{sin\phi} = 0.61\frac{\lambda_0}{nsin\phi} = 0.61\frac{\lambda_0}{NA} \qquad \text{Eq. 3.3-4}$$

Where λ_0 is the wavelength in vacuum and the refraction index *n* of the material where the radiation is propagating, $nsin\phi$ is the adimensional value referred as Numerical Aperture (NA) which is typically used to classify the optical components.

The PSF permits to determine the axial resolution, calculating the intensity profile of the point-like source on projected on the optical axis:

$$S_z = 2\frac{\lambda_0}{NA^2} \qquad \text{Eq. 3.3-5}$$

The above discussed mathematical expressions evidence how diffraction is the intrinsic limit of the optical microscope. The minimum angular separation that can be measured with an optical system is thus proportional to the wavelength of the electromagnetic radiation and to the reciprocal of the numerical aperture of the optical components adopted.

Above the spatial resolution of the confocal microscope, the peculiar characteristic that makes more suitable such instrument for the characterisation of the SPSs is the *optical sectioning*. Adopting a pinhole, the fluorescence light originated from optical planes not on focus can be excluded from the collection path. In such a way, the reconstructed image has a better resolution.

In Figure 3.3.3 it is displayed the axial intensity profile for the case of a widefield and confocal microscope. For the case of a widefield microscope, the total intensity is given by the superposition of the intensities at any given focal plane. It is possible to observe in Figure 3.3.3a that the spatial distributions are different. It can be thus demonstrated that all the contributes are constant in terms of intensity [199]. In the case of the confocal microscope, Figure 3.3.3b, the advantage of the optical sectioning is explained considering that the PSF has a depth profile with a maximum in the focal plane. Therefore, the intensity profile has mainly the contribution from the selected focal plane, thus improving the quality of the image.

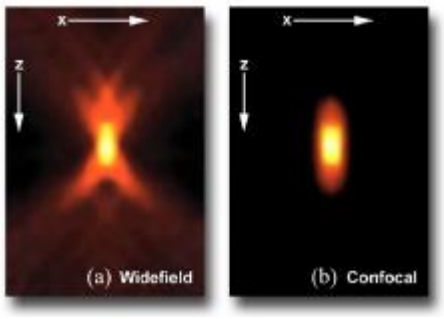


Figure 3.3.3 Comparison of the axial intensity profiles between the widefield and confocal microscope [204].

3.3.2 Experimental implementation

Different confocal microscopes were used during the research activity of presented in the Dissertation. In Figure 3.3.4 it is reported one of the adopted configurations for the confocal microscope adopted during the research activities (with 490 nm excitation laser) as well as the schematic representation.

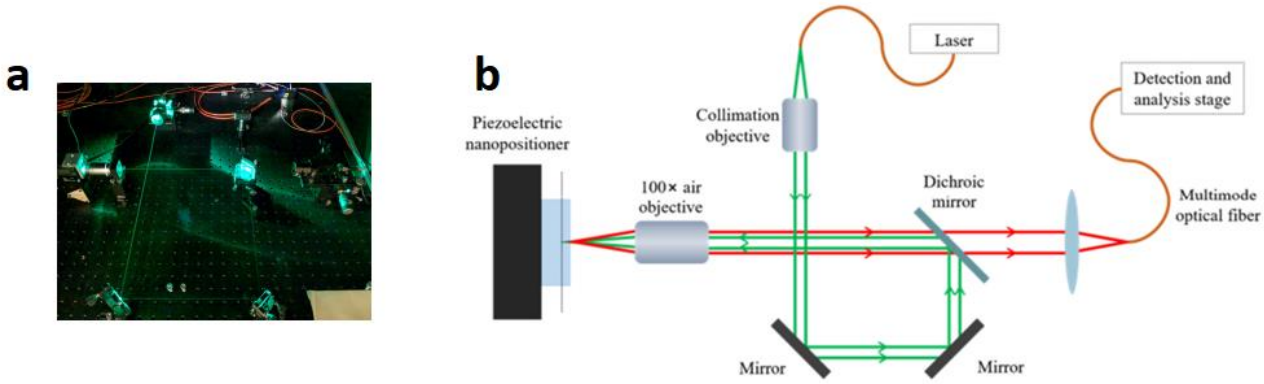


Figure 3.3.4 a) Home-made confocal microscope adopted for the measurements with 490 nm laser excitation. b) Schematic representation of the home-made built confocal microscopy systems adopted during the PhD word. Figure from [80].

The scheme of the confocal adopted remained identical over the different campaigns of measurements, yet the optical components varied as function of the excitation wavelengths and PL spectral range. Various lasers were employed, namely: CW 405 nm, 450 nm, 490 nm, 509 nm, 520 nm and a supercontinuum white laser ranging from 405 nm to 750 nm. Depending on the laser different dichroic mirrors were used and different spectral filters were chosen, to suitably select or cut undesired fluorescence.

The lasers are fiber coupled to a collimating system consisting in a 4x objective, a set of two alignment plane mirrors bend the beam towards the dichroic mirror that direct the laser to the optical path of the microscope.

The employed dichroic mirror works as long-pass filter, it transmits the light with $\lambda > \lambda_{cut-off}$. The choice of $\lambda_{laser} < \lambda_{cut}$ permits to select only the PL radiation and filter out the laser light.

The laser beam reaches the objective (100x) set in front of the sample that focusses the beam onto the sample. The PL signal then is transmitted through the dichroic mirror roughly collimated by the objective, and it is focussed by a achromatic doublet onto the pinhole (in the described case the core of a multimodal fiber with radius of 50 µm and NA of 0.22). The three conjugated points of the microscope are then the core of the monomodal fiber, the focal plane of the analysed sample and the core of the multimodal fiber of the PL collecting path.

Two main apparatuses were used during the activities, a room temperature system and a cryogenic system. The main difference on the building of the microscope is the adopted objective: 100x for both systems but the NA for the room temperature case is 0.9 and the NA for the cryogenic case is slightly lower with 0.85.

Since the confocal microscope has only one point on focus, to reconstruct the image it is necessary to use a positioner to move the sample and reconstruct the intensity PL profile. Typically, it is adopted a piezoelectric system in closed-loop configuration. Other system can be adopted, such as galvanometric mirrors that scan the beam across the focal plane of the sample over the objective pupil.

Optical cryostat

At the laboratories of the Quantum Optics group of INRiM, where part of the research activity was performed, is installed a confocal microscopy apparatus operating at cryogenic temperatures, consisting of a cryostat,

with optical windows and vacuum-compatible objective, inside of which it is possible to place a sample. The supplied model is the S100 from Montana Instrument, which provides a system cooled by liquid helium closed-loop.

The cryostat can maintain the sample at a minimum temperature 3.8 K. The cooling cycle takes about 5 hours to reach values close to 5 K, typically used for the work presented in the Dissertation, starting from room temperature. An integrated heater allows the temperature to be controlled by supplying heat to the sample only, thus keeping the cryostat temperature unchanged. This expedient makes it possible to achieve thermal stability at low temperatures quickly. The cryostat operates under high vacuum, with pressure less than 10-4 mbar. This condition makes it possible to minimize any phenomena of condensation inside the chamber.

The coupling of a closed-loop cryostat with a confocal microscope in photoluminescence involves additional precautions taken during the design phase of the instrument. In fact, the system is equipped with a technology of vibration damping that allows isolation of both the sample and the elements attached to the optical bench from the cryostat, so that the pumping of liquid helium inside it does not alter the functionality of the confocal microscope. In addition, the process chamber is equipped with side optical windows; on one of these is faced a 100x, vacuum-compatible objective with a numerical aperture of 0.85. Figure 3.3.5 Internal structure of the chamber used for cooling and control the sample. Figure 3.3.5 shows the internal structure of the optical chamber of the cryostat, it is possible to observe the objective housing (on the right), the sample holder (in the centre) and the piezoelectric positioners (on the left).

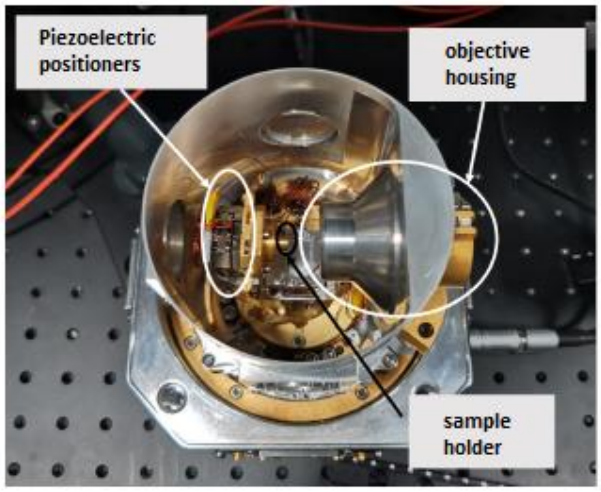


Figure 3.3.5 Internal structure of the chamber used for cooling and control the sample.

3.4 Hanbury-Brown & Twiss interferometer

To carry out a study of the source emission statistics and evaluate the non-classical behaviour, it is used the Hanbury- Brown & Twiss interferometric system. From an experimental point of view, this system consists of a beam splitter integrated in fiber optics with a transmittance of 50% that separates the beam luminous in two distinct optical paths, each conveyed towards a detector independent single photon-sensitive detector. In Figure 3.4.1 it is displayed the scheme of the interferometer used.

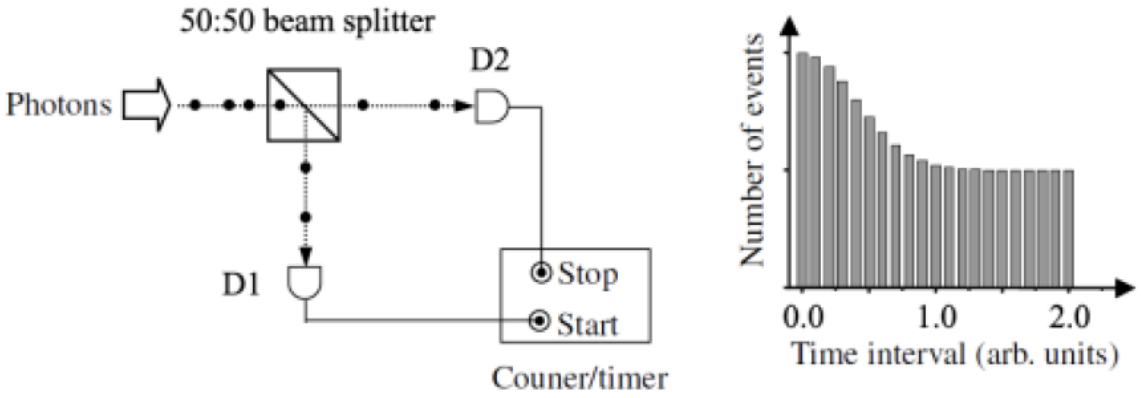


Figure 3.4.1 Scheme of the HBT interferometer.

The purpose is to correlate the intensity variations, therefore the counts between the two detectors through a start and stop process and generate a histogram of the distribution of delay times. A photon of the first branch hits the first detector which begins its acquisition period (start), the measurement remains open until one photon in the second branch of the beam splitter is not revealed (stop). This technique allows you to measure coincidences and the anticoincidences of the light of fluorescence and excitation under analysis.

Figure 1.3.3 shows the scheme of this technique and the related histogram generated. A photon that travels along the first branch is absorbed by the first detector, which emits an electrical impulse at the moment of its detection. This pulse (start signal) opens an acquisition window that comes closed when a photon, traveling along the second branch of the beam splitter, is detected by the second detector (stop sign). The time between two signals (coincidence time t_C) can thus be acquired for a high number of pairs of photons in order to construct a histogram that allows for obtain an experimental measurement of the g2(t_C) function.

From a hardware point of view, the correlation consists of a high-performance FPGA board that carries out functions in digital mode of a Time to Amplitude Converter (TAC) connected to the Multichannel Analyzer (MCA). When a pair of photons hits the detectors, their signal is received empty from the two input channels of the TAC, which generates (in its analog version) a TTL pulse proportional to the interval time between the signal of start and stop. The recuperator therefore extracts the delay between the photons that hit find the detectors and correlate them. Once the start and stop cycle is completed, the TAC generates a rectangular signal with amplitude proportional to the time difference between the two correlated photons. The TTL pulses output from the TAC are analysed from the MCA, which generates a histogram as a function of their amplitude. Such histogram corresponds to the distribution of delay times between pairs of events recorded between the start and stop signals.

Figure 3.4.2 shows an example of a histogram generated by the correlation apparatus. In addition to the characteristic dip of emission from a source quantum, it is possible to observe two peaks corresponding to the times of delay of 80 and 310 ns, called backflash peaks. To be able to carry out a precise measurement of the phenomenon, they are introduced two delays in the system, one optical and one electronic. The optical delay (a multimode fiber that increases the length of one of the two optical paths in output from the beam splitter) has the task of spacing the backflash peaks. For allow greater control of the acquisition window by inserting the electronic delay chain. This allows to measure the single photon a time greater than zero as shown in Figure 3.4.2 where the dip is located at a time interval of 80 ns. The electronic delay allows a best convergence of the analysis t to obtain the parameters mentioned in the Appendix I.

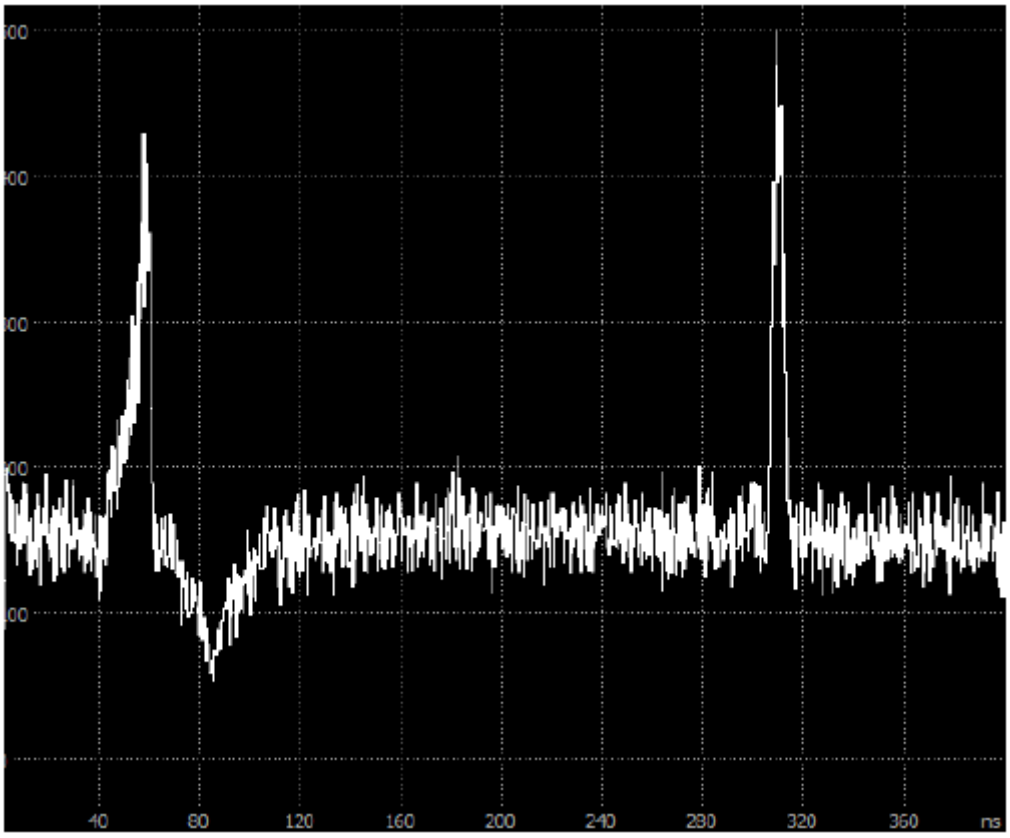


Figure 3.4.2 Typical histogram obtained for an emitter using the HBT interferometer.

These peaks are due to the fact that a photon hitting a detector can induce a luminescent emission from the same detector as a photon in the infrared. The latter is counter propagates into the revealed optical fiber from the second detector, at a characteristic time determined by the length of the fiber itself. The time difference between the position of the corresponding dip at zero delay time and the backflash peak provides incidentally an estimate of the length of the optical fiber used. If the source under analysis is of a quantum nature, we will see an advantage lament in the histogram and thus derive characteristics on the quantum system under analysis, such as the decay time and the principal parameters derived from models for a two- or three-level system.

Experimentally, the histogram generated by the instrumental apparatus c(t) it must be traced back to the autocorrelation function, then normalized to 1, via the following expression:

$$g(t)^2 = \frac{c(t)}{R_1 R_2 w T} \qquad \text{Eq. 3.4-1}$$

Where c(t) is the non-normalised histogram of time delays, $R_{1/2}$ are the rates detected for the two channels, w the amplitude of the binning, T the acquisition time for the measurement.

Experimentally, the contribution to the radiation revealed by a detector consists of the quantum light source (signal) in addition to further components (background), interpretable as noise terms and described by a single source of Poissonian light. At the origin of these are: background luminescence of the sample, emission from additional sources in the vicinity of the emitter in analysis, a fraction of the pump laser radiation is not completely filtered ta from the optical components of the confocal microscope, and the dark counts of the detectors. The net result of this noise source will be to, on the one hand, provide higher emission rate from the point being measured, compared to real number of photons emitted by the quantum source, and on the other to translate towards unity the value $g^2(t = 0)$ measured experimentally due to its non-classical nature.

In order to correctly qualify the properties of the non-classical source object of investigation, after having normalized the counts to 1 it is necessary to correct ger the value of the $g_{experimental}^{2}(t)$ function taking into account the actual ratio signal-to-noise.

The procedure followed to correct the counts is to measure the emission intensity of the single defect under analysis. The measurement will produce the value of the I counts, which are due to the sum of the intensity of the photons emitted from the defect (S) and related to the noise sources (BG): I = S+BG.

At this point, assuming that the noise's contribution does not depend on the point of chosen measurement, it is possible to directly measure its contribution in a position in which luminescent defects are absent, preferably in a region adjacent to the defect under examination. By exploiting $g^{(2)}(t) \equiv \frac{\langle \overrightarrow{E^*}(\vec{r}_1,t_1)\cdot\overrightarrow{E^*}(\vec{r}_2,t_2)\cdot\vec{E}(\vec{r}_1,t_1)\cdot\vec{E}(\vec{r}_2,t_2)\rangle}{<|E(\vec{r}_1,t_1|^2>\cdot<|E(\vec{r}_2,t_2)|^2>}$ Eq. 1.2-5 it is therefore possible to carry out the correction:

$$g(t)^2 = \frac{<(S(t+t_0)+BG(t+t_0))(S(t)+BG(t))>}{<S+BG>^2} \qquad \textit{Eq. 3.4-2}$$

The equation is then used to perform the fitting procedure to gain the typical parameters described in Appendix I.

4 Chapter 4

In this Chapter, the main results achieved during the three years of my PhD research are presented and discussed. The results are divided in two main sections: the first related to group IV colour centres in diamond, particularly on SnV and PbV defects; the second is focussed on the fabrication and characterisation of emerging classes of colour centres, namely Fluorine-based and Magnesium-based.

The PL characterisation presented in the chapter was performed on sample implanted both before the start of the PhD or during the three years in external facilities. Different samples were implanted for external collaborations and are outside of the discussion as main results obtained during the presented activities.

The following Table summarise the sample adopted for the research along with the implantation energies, fluences, thermal treatment, implantation facility, discussion chapter, type of sample.

Sample id	Chemical species	Energy [keV]	Fluences [cm^{-2}]	Annealing Temperature [°C]	Facility	Chapter discussion	Sample type
1	Sn^-	60	$5x10^{10}$	1200 (2 hours)	Univ. Leipzig	4.1.1	IIa, quantum grade
2	PbO_2^-	35	10^{11}-10^{12}-10^{13}	1200 (2 hours)- 2200 (15 min)	Univ. Lepizig	4.1.2	IIa, quantum grade
3	Pb^-	20	10^{13}	1200 (2 hours)- 2200 (15 min)	Univ. Lepizig	4.1.2	IIa, optical grade
4	O^{4+}	9000	10^{13}	1200 (2 hours)	Ruder Boskovic Institute	4.1.2	IIa, quantum grade
5	Mg^+	100	10^9-10^{12}	1200 (2 hours)	KU Leuven	4.2.1	IIa, quantum grade
6	F^-	50	10^{10}-10^{15}	1200 (2 hours)	Univ. Lepizig	4.2.2	IIa, quantum grade
6	F^{2+}	1470	10^{12}	1200 (2 hours)	Ruder Boskovic Institute	4.2.2	IIa, quantum grade
6	C^-	35	10^{15}	1200 (2 hours)	Univ. Lepizig	4.2.2	IIa, quantum grade
7	N^+	10	10^{14}	950 (2 hours)	ANSTO *Centre for Accelerator Science*	4.2.2	IIa, quantum grade

Table 2 Summary of the adopted samples. The implanted most relevant parameters such as Chemical species, fluence and facility are reported along with the main thermal treatment that the sample underwent.

4.1 Group IV colour centres

Colour centres in diamond are widely studied for their appealing single-photon emission properties, with enticing perspectives in emerging fields such as sensing [205], quantum information processing [127].

As mentioned in Chapter 1.3.2, group IV emitters are being extensively studied for their remarkable properties [76], particularly for their possible applications in quantum information protocols [125], [127], [206]. In this paragraph, dedicated studied on optical properties related to SnV and PbV defects is presented. Particularly, regarding SnV colour centres, a dedicated analysis on their emission properties as a function of surface chemical functionalisation of bulk diamond, namely by means of oxygen, and thermal processing is presented. This study has the purpose of understanding a possible strategy to tune the spectral emission lines [51].

Secondly, an analysis on the effects of different thermal annealing approaches (low-pressure low-temperature and high-pressure high temperature) is performed to assess the optical and spectral features of PbV defect in diamond at the ensemble and single defect level [207]. The aim is to understand the formation process of the PbV defect upon ion implantation and to explain certain emission lines associated to the Pb implantation. In fact, the attribution of its ZPL is not trivial and unequivocal in literature. Hence a systematic characterisation under different post implantation treatments would enable a more detailed understanding of such problem.

4.1.1 Diamond surface functionalisation for the tuning of the SnV spectral lines

As mentioned in Chapter 1, the second quantum revolution is based on devices with “quantum” properties. The fabrication by ion implantation of shallow emitters in diamond is among the various path that can be followed to achieve photonic devices usable for practical applications. A key parameter in the tuning of the emission properties of shallow implanted defects based on the NV centre has been demonstrated to be the chemical functionalisation of the surface by means of both hydrogen and oxygen [208], [209], [210]. Moreover, ab-initio simulations have predicted the possibility of observing a different charge state of the SnV [118], [211] as for the neutral charge state of the SiV defect [120]. The SnV complex at ensemble level displays a series of different spectral lines:

- 595 nm line. It was observed mainly for annealing temperatures below 1000 °C [87] whose attribution is still unclear. It is considered to be related to the Sn ion implantation but not as possible SnV other charge state [118].
- 620 nm line. Unanimously attributed as ZPL of the SnV^- defect [76], [118], [121].
- 631 nm line. Such spectral feature was tentatively attributed as quasi-local mode of the SnV [153], [212] under symmetry breakdown condition for the defect within the crystal (e.g. Strain) [213], [214]. Another interpretation is that this line is associated to the Sn implantation but not to the SnV^- defect. In fact, the large Sn ion produces massive damage to the crystal hence needing extreme conditions to restore the lattice (i.e. HPHT annealing) [87]. It has been demonstrated the possibility to minimise the presence of this spectral line performing shallow implantation and subsequent overgrowth followed by a LPLT annealing [153]. This implies that such feature can be indeed attributed to strain induced residual damage to the lattice, hence as quasi-local phononic sideband.
- 647 nm line. The occurrence of this spectral line was demonstrated to vary with respect to the thermal annealing temperature: above 1200 °C it starts to decrease until annealing out for HPHT

annealing [87]. The work from Luhmann et al. [215] is related to the electrical-tuning of such complex within a p-doped, intrinsic, p-doped junction. Due to the inability to switch between the 647 and 620 nm lines as for the NV between the 575 and 637 nm lines, this line was suggested to be related to different complex rather than as another charge state of the SnV^-.

- 663 nm feature. This line is attributed as radiation damage of the crystal due to the Sn ion implantation.

Thus, the work here presented aims at systematically investigate the effects of chemical functionalisation with O treatments and annealing on the spectral lines of the SnV defect in diamond. The adopted scheme consists in PL characterisation after LPLT annealing and O functionalisation of the diamond surface. This study would thus allow to verify the eventual activation of specific spectral features under different processing methods.

4.1.1.1 Experimental and chemical functionalisation

The sample adopted in this study is a synthetic single crystal diamond from ElementSix type IIa with <100> crystal orientation (in the following denoted as sample 1). The tin implantation was performed at the University of Leipzig with 60 keV Sn^- ions over a 200x200 μm^2 region resulting in ~ 20 nm deep emitters, as simulated by SRIM [144]. The fluence implanted was $5x10^{10}$ cm^{-2}, the use of a collimating mask placed at a distance of ~ 5 mm allowed the implantation of low fluence of isolated emitters by means scattering over the edges of the mask. The implantation depth results sufficient to allow chemical surface functionalisation to tune possible charge states of the defects [208].

Sample 1 underwent 2 hours furnace thermal annealing at 1200 °C in high vacuum regime (pressure below 10^{-6} mbar) to activate the SnV defects and consequent oxygen plasma treatment to remove eventual organic contamination as well as conductivity from the surface due to graphite mixed phases. Chemical functionalisation of (100) diamond orientation has been proven to have major effects on the localised surface charge density. This effect has been extensively studied for the NV centre[216]. As-grown CVD diamond (e.g. as-implanted unless other post growth treatments are performed) has the surface characterised by hydrogen termination resulting in a negative electron affinity of 1.7 eV [217]. Annealing as high as 1000 °C results in desorption of H from the surface [218] and in the recombination of C atoms implying formation sp^2 bonds [219]. Contrarily, diamond surface terminated with O displays a positive electron affinity of 2.4 eV [220]. The desorption of O from the diamond surface has been demonstrated to happen up to 600 °C [221].

The whole work consisted of a systematic study at the single emitter level only. The measurement scheme was the following:

- PL mapping over the region of interest to assess single-photon emission from isolated emission spots by means of HBT interferometry.
- spectral characterization of the PL emission from individual colour centres.

This scheme was iterated upon annealing and oxygen functionalisation. The experimental constraints are the followings: green excitation (namely 522 nm laser), spectroscopic characterisation with a fiber coupled single photon avalanche photodiode (SPAD) to a monochromator with ~4 nm resolution (based on the FWHM on the first order Raman peak). The peaks position was analysed by means of a routine based on the first derivative analysis, it was then set a threshold as discrimination filter to only pick the those with 10% higher signal over the baseline acquired in the proximity of the defect.

4.1.1.2 Single emitters analysis

As above-mentioned, the systematic analysis was carried on the as-annealed and the O-terminated sample.

Mainly three spectral features are observed, 620, 631, and 647 nm, and they are attributed to SnV defect considering the relative occurrence of the same features within the same emitters. It is demonstrated the possibility of tuning the spectral lines by means of surface oxidation and thermal annealing. In Figure 4.1.1 it is shown a typical confocal map acquired using the Qudi software [222]. To permit a systematic optical characterisation, the sample was marked on a specific region at the edges of the implanted region to select the region of interest.

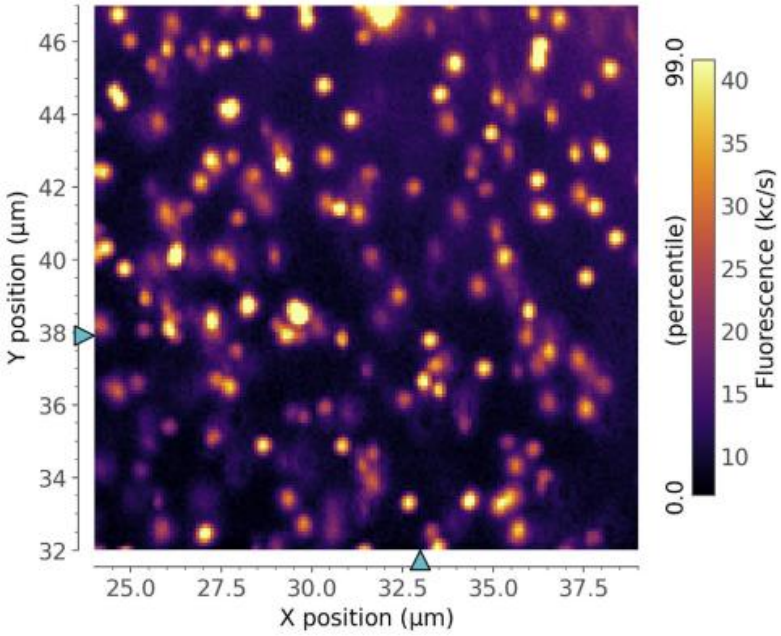


Figure 4.1.1 PL confocal scan of the Sn edge of the implanted region acquired under 522 nm excitation laser and 0.06 mW optical power.

Various isolated spots are observable with a relative density of 1 per μm^{-2}. The HBT interferometer allowed to characterise only the single emitters ($g^2(0) < 0.5$) and investigate their spectral properties. Particularly, around 30 single emitters were examined for the as -annealed investigation and around 40 for the O-terminated case. The main physical parameters inspected are the excited state lifetime, the shelving state lifetime, the saturation parameters (both intensity and power) and finally the PL spectrum. In the following the main 4 categories of single emitters are investigated: particularly, those displaying individual spectral lines, namely the 620 nm (labelled as S1 in the following), 631 nm for (S2) and 647 nm (S3) peaks, and those concurrently emitting at two of the aforementioned lines.

The analysis was carried out considering as fitting model a three-level system [121], [223], the second order autocorrelation function equation was thus the following:

$$g^2(t) = 1 - a_1 e^{\frac{t}{\lambda_1}} + a_2 e^{\frac{t}{\lambda_2}} \qquad \text{Eq. 4.1-1}$$

Where a_1 and a_2 represent respectively the non-classical bunching behaviour and the bunching behaviour of the emitter, λ_1 and λ_2 represent the coefficient associated to the excited state lifetime (as discussed in Appendix I). To evaluate the saturation parameters, the following expression was adopted[121], [223]:

$$I(P) = I_{sat}\frac{P}{P+P_{sat}} \qquad \text{Eq. 4.1-2}$$

Where I_{sat} and P_{sat} are the saturation intensity and power respectively.

S1 emission line

The results for the emitters displaying the sole 620 nm line are reported in Figure 4.1.2and they are associated with the spectrum shown in Figure 4.1.2

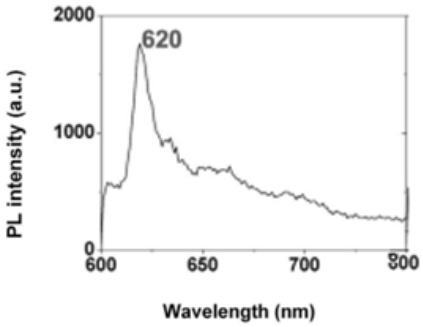


Figure 4.1.2 PL spectrum of the 620 nm (S1 spectral feature).

The second-order autocorrelation function for different optical power displays single emitter behaviour since the $g^2(0) < 0.4$ with background correction. The $\lambda_1(0)$ parameter corresponds to a value of (6.0 ± 0.8) ns which is in agreement with the reported values in literature [87], [118], [121]. The λ_2 parameter corresponding to the shelving state de-excitation leads to a value of (68 ± 9) ns. The saturation curve (in Figure 4.1.3b) with background subtracted is fitted with the curve in Figure 4.1.3d leading to a saturation power (P_{sat}) of (0.32 ± 0.07) mW and a saturation intensity (I_{sat}) of (186 ± 15) kcps. The P_{sat} could be compared to a previous value of (1.11 ± 0.01) mW, since the optical power in Ref [121] was measured on the objective pupil and was delivered to the sample with a 60x oil objective. In fact, it was observed a 60% reduction of the transmitted power through the objective adopted in the confocal microscope. The I_{sat} was a factor 10 lower with respect of what previously reported [121], the difference could lie in the adopted experimental constraints. Indeed, an air-coupled system was adopted with respect to the fiber-coupled adopted for this work.

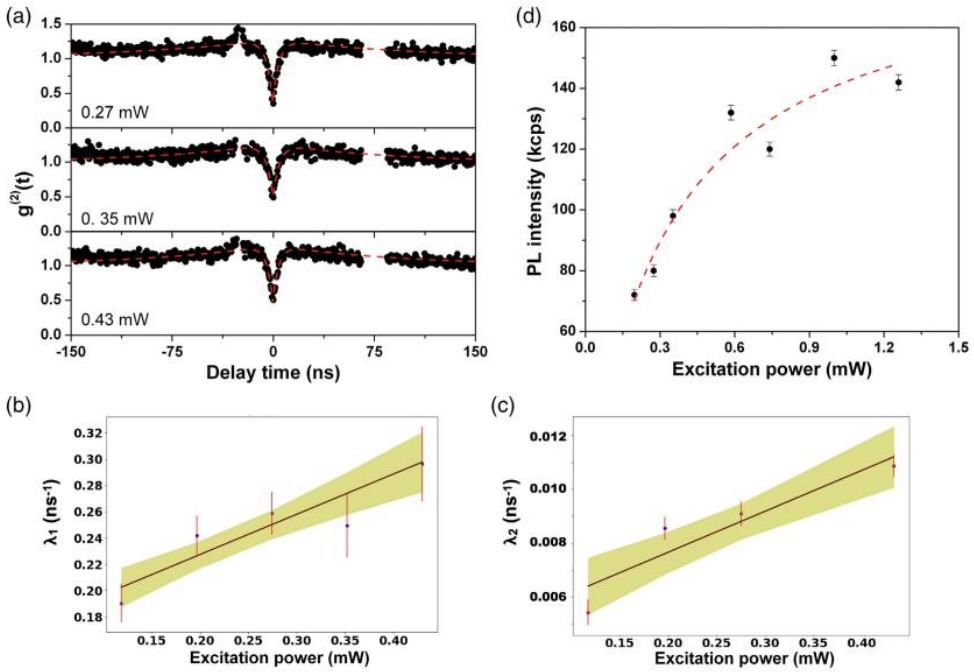


Figure 4.1.3 S1 optical characterisation by means of HBT interferometer and fitted curves. a) (g(2)(t) curves) for three different excitation powers: 0.27 mW, 0.35 mW, 0.43 mW. The missing points in the time interval 70-85 ns are related to the backflash peaks, removed for the best fitting procedure (as discussed in Chapter 3). b) Linear fit of the λ_1 parameter and c) b)Linear fit of the λ_2 parameter from the experimental $g^2(t)$ curve as a function of the excitation power. d) Saturation curve, red line is the fitted curve over.

S2 emission line

It was possible to isolate various single defects emitting at 630 nm (spectrum in Figure 4.1.4), the characterisation for one of those is reported in Figure 4.1.4.

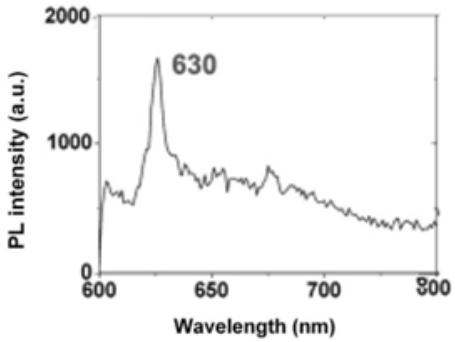


Figure 4.1.4 PL spectrum of the 631 nm (S2 spectral feature).

The second order autocorrelation function allowed to estimate the excited state lifetime and shelving state behaviour (as seen in Figure 4.1.5b and c), agreeing again with the adopted model. The obtained value for $\lambda_1(0)$ is (4.8 ± 1.7) ns. Regardless of the compatibility with the same value for the S1 line, the saturation parameters are instead higher. The I_{sat} is equal to (300 ± 40) kcps while maintaining a similar P_{sat}, (0.42 ± 0.08) mW.

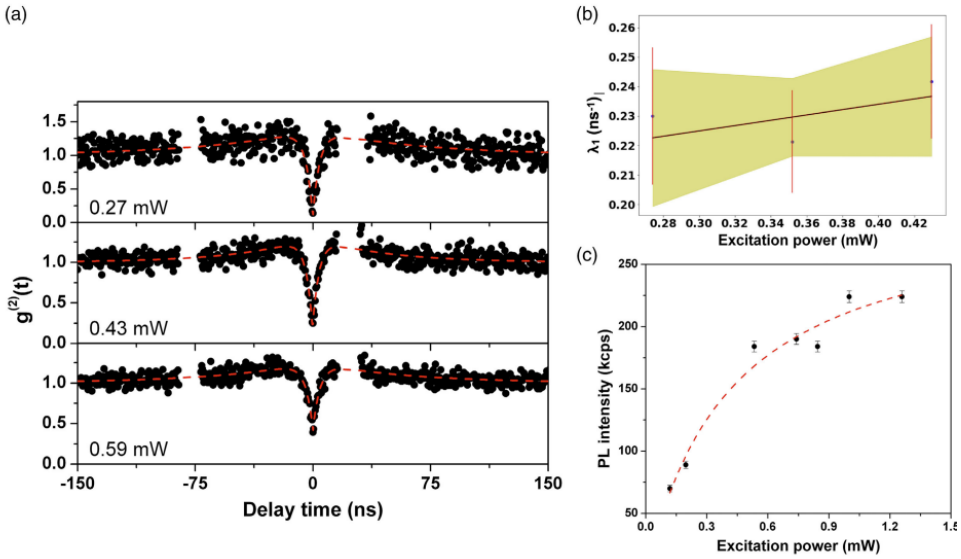


Figure 4.1.5 S1 optical characterisation by means of HBT interferometer and fitted curves.. a) (g(2)(t) curves) for three different excitation powers: 0.27 mW, 0.35 mW, 0.43 mW.. b)Linear fit of the λ_1 parameter from the experimental $g^2(t)$ curve as a function of the excitation power. d) Saturation curve, red line is the fitted curve over.

The observed emission S2 line was observed also in the case study after the HPHT annealing of the PbO_2 implanted sample discussed in the following paragraphs. The obtained values are slightly different, but the emission line can be reasonably attributed to the same emitting defect as it lies within the spectral setup constraints (4 nm resolution). To further support this interpretation, in ref [224] a study (published after the finalisation of the present work) on HPHT microdiamond reported on defects emitting at 630 nm. Those microdiamonds are produced by HPHT technique under two different doping: Ge-doped crystals and undoped crystals were produced. Elemental analysis on higher concentration of emitters with 630 nm lines did not point to other extrinsic impurities than Carbon, Silicon, Oxygen and Nitrogen. Hence, the attribution of this spectral line can be considered to be related to the Sn ion implantation rather than to Sn-containing defects. Yet, the occurrence of the concurrent observation of the S2 and S3 lines withing the same emitter (as discussed in the following) as well as the different lifetime, count rate, might signify that this line could be also attributed to complex Sn-containing defect configurations.

S3 emission line

The measurements regarding the 647 nm emission line are now discussed. The PL spectrum is reported in Figure 4.1.6 and it display a sharp peak at 647 nm with a small phononic sideband.

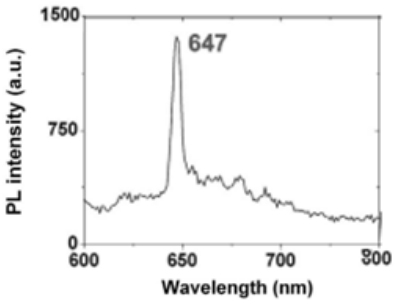


Figure 4.1.6 PL spectrum of the 647 nm (S3 spectral feature).

As shown in Figure 4.1.17a, the second-order autocorrelation function allowed to characterise the main parameters associated with the $g^2(t)$ analysis. Indeed, the excited state lifetime of the analysed emitter was evaluated as (7.4 ± 1.0) ns. The λ_2 parameter in this case was not following what expected from the adopted three level system model. Particularly, it showed a decreasing behaviour stemming a λ_2 (0) = (68 ± 9) ns possibly meaning that the emitter could experience a depletion of the shelving state in favour of an additional level [223]. An unambiguous attribution of such phenomenon was out of the scope for this work and future works would be required to evaluate the actual occurrence of fourth additional level, to be identified in a surrounding defect in the gap or to the energy bands of the semiconductor.

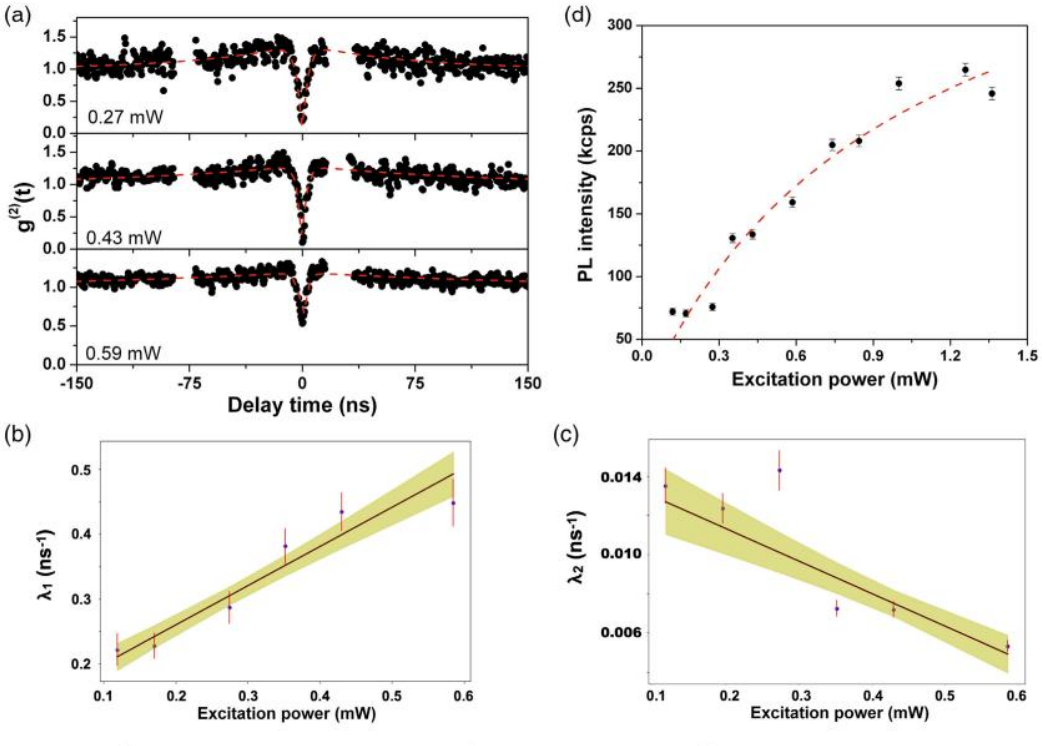


Figure 4.1.7 S1 optical characterisation by means of HBT interferometer and fitted curves. a) (g(2)(t) curves) for three different excitation powers: 0.27 mW, 0.35 mW, 0.43 mW.. b)Linear fit of the λ_1 parameter and c) Linear fit of the λ_2 parameter from the experimental $g^2(t)$ curve as a function of the excitation power. d) Saturation curve, red line is the fitted curve over.

The analysis also allowed to evaluate the single photon behaviour from different emitter displaying a double emission line. In Figure 4.1.8 a set of three spectra are shown in Figure 4.1.8 display double spectral line: S1-S2, S2-S3, S1-S3.

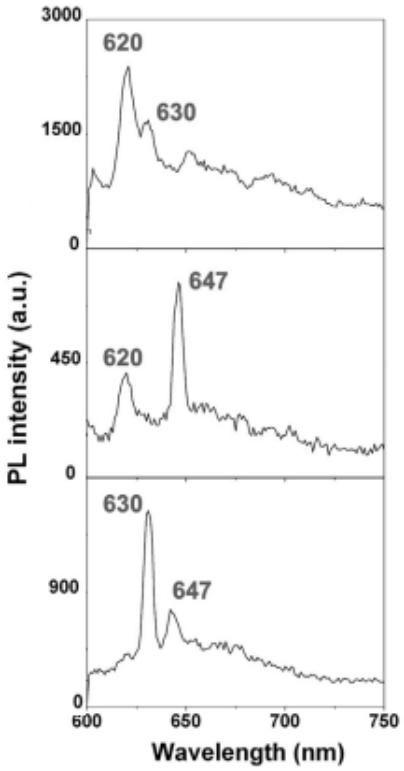


Figure 4.1.8 PL spectra of diffraction limited single emitters displaying double emission lines.

The second order autocorrelation function validated the observation as single emitters since the $g^2(0)$ was respectively below 0.2 and 0.1 after background subtraction as displayed in Figure 4.1.9. The observation of the sole emission lines and concurrently two emission lines within the same emitter could be attributed to different charge state of the same defect. The S1 line is, in fact, unambiguously accredited as the SnV^- configuration [76], [118]. Conversely, the work presented in ref [215] suggested that the S3 line could not be attributed as SnV^0 due to the inability of tuning the emission from the S1 to S3 upon electrical tuning of the Fermi level. Thus, another possible interpretation is that of two different emitting defects located within the same diffraction limited volume, whose alternate single-photon emission stems from a competition for the optically-active charge state via non-resonant energy transfer. Finally, it is worth mentioning in this regard that various diffraction limited isolated spots showed multiple spectral lines while being stable for only tens of seconds, therefore a complete characterisation was not possible.

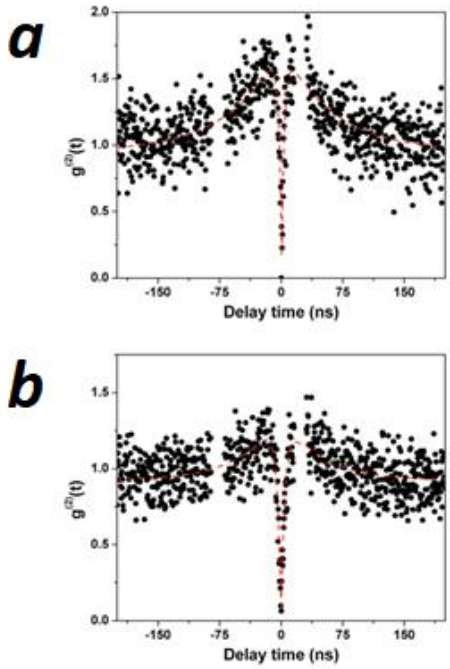


Figure 4.1.9 Antibunching behaviour measured by means of the second order autocorrelation function of two isolated emitters. a) a) Second-order autocorrelation function of the S1-S3 emitter. B) Second order autocorrelation function of the S2-S3 emitter.

4.1.1.3 Effects of the post-implantation treatment

The study highlighted the occurrence of three main categories of spectral features: 620-631-647 nm (S1-S2-S3 respectively). The emission lines detected are composed of only one emission line (Figure 4.1.2, Figure 4.1.4, Figure 4.1.6) as well as a double spectral lines consisting of a permutation of S1-S3 (Figure 4.1.8). A statistical analysis on the relative occurrence of the emission lines was performed on a set of individual emitters (75 in total) as displayed in Figure 4.1.10. The relative occurrence of the as-annealed case (grey dots) and the O-functionalised case (purple triangle) shows two different median values for the two populations.

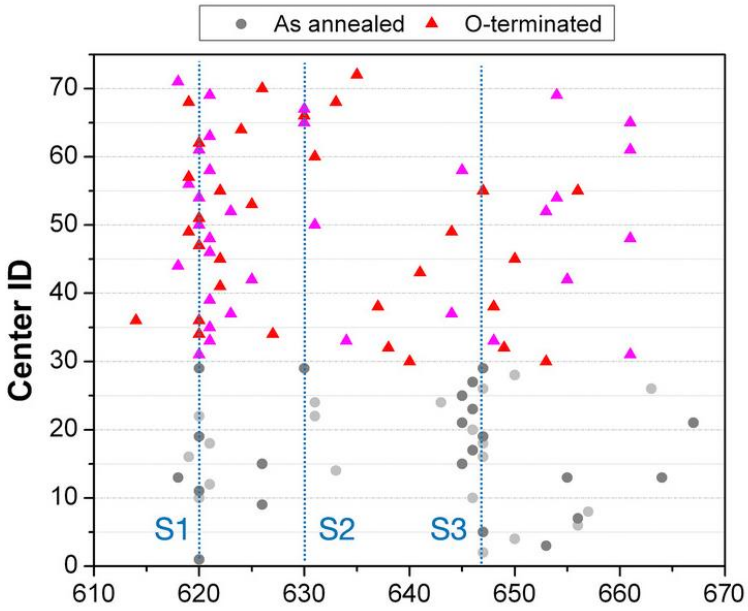


Figure 4.1.10 Statistical analysis showing the number of emitters as function of the associated spectral lines. The grey dots represent the as annealed case, the purple triangles represent the O-terminated case.

To further gain an insight in the distribution of the observed spectral lines, Figure 4.1.11a shows the different histogram for the two discussed cases (an-annealed and O-terminated). The as-annealed case study shows a prevalence of the S3 emission line (~40% of the studied emitters) while the S1 line occurred in a minor fraction (~25%). The opposite behaviour is observed in the case of oxygen surface functionalisation. It was recorded a set of two different spectral lines as function of the O treatment. In the annealed sample, the most abundant spectral lines observed are comprised around the S3 feature (40%) with respect to S1 (25%). The analysis following the plasma treatment yielded a diverse outcome. S1 is the most abundant spectral feature observed (40%) while the S3 line is reduced to a low number of emitters (6%).

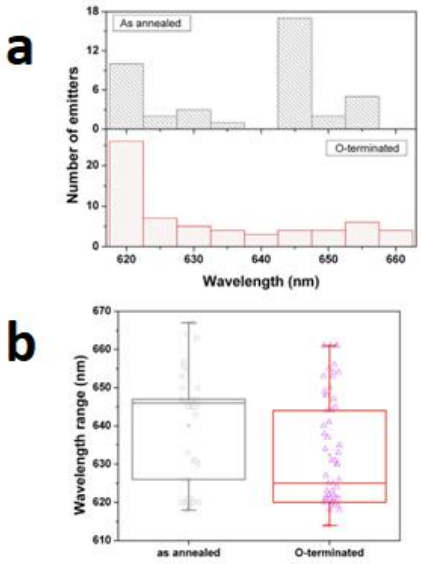


Figure 4.1.11 Histogram of the spectral positions for the different diffraction limited emitters in the two discussed cases. a) As-annealed, b) O-terminated case.

The box chart in Figure 4.1.11b reveals more clearly the above-mentioned different median values for the two studied cases: the median of the as-annealed (grey boxchart) matches with the S3 signature while for the O-terminated case (red boxchart) the median matches with the S1 signature. The histogram in Figure 4.1.11b does not show any significant contribution from other classes of spectral features for the two case studies, as the occurrence from the S2 line is limited.

It is worth mentioning the inhomogeneity of the spectral lines (around 25% of the total emission lines observed), confirming the results in refs [87], [89] stating that for large ion masses impurities it is needed a HPHT type annealing to reduce such effect.

In conclusion, the relative occurrence of the S1 (i.e. negatively charged SnV defect) upon O-termination is in agreement with what reported for the NV defect as stated in [52], where the functionalisation with positive electron affinity evidenced a stabilisation of the negatively charged NV centre. Still, due to the high purity of the adopted sample (therefore low concentration of N content, N<1ppb) and the chosen region of interest filled with SnV defects, it could not be performed a direct comparison.

4.1.2 Investigation of PbV colour centre upon diverse thermal annealing processes

The lead vacancy defect in diamond (PbV^-) is a promising candidate for implementation in quantum information protocols [123], [128], [225] due to its large spin-orbit coupling leading to a large ground state splitting (> 4 THz [88]), low excited state lifetime (3 ns [123]).

While SiV, GeV and SnV properties have been extensively explored [76], [87], [89], [121], [126], [127], [205], [226], [227], [228], [229], [230], [231], [232], the current understanding of the opto-physical properties of the (PbV^-) currently relies only on a limited amount of experimental results. Several ambiguities in the attribution of the PL features of Pb-implanted diamond still exist. The cause may lie in the non-trivial effects of the incorporation of a large impurity such as Pb in the dense diamond lattice, which results in a set of observed optical transitions lacking an unequivocal attribution [88], [118], [123], [207], [233]. Therefore, an adequate understanding of the optical signatures related to lead-related impurities and the identification of optimal processes for the consistent fabrication of the PbV^- centre while minimizing undesired photoluminescent features is crucial to enable its adoption for practical applications.

In this sense a systematic spectral characterisation, both at ensemble and single emitter level, was performed for different annealing temperature (1200 °C and 2200 °C) as function of different excitation wavelengths and measurement temperature.

4.1.2.1 Experimental

Three type of commercial synthetic single-crystal diamond substrates were adopted for this study: sample 2 and 4 are “detector grade” plates.

Three circular regions with diameter of 100 µm were implanted in sample 2 by means of a collimating mask using 35 keV PbO_2^- ions at 2 x 10 ^{13} cm^{-2}, 5 x 10^{12} cm^{-2} and 5 x 10^{11} cm^{-2} fluences. Sample 3 was implanted

with 20 keV Pb^- at a fluence of 2 x 10^{13} cm^{-2}. A reference marker was fabricated at the centre of each implanted regions to allow the investigation of the same PL features by means of different confocal microscopy setups. The control sample (sample 4) was implanted with 9 MeV O^{4+} ions with a fluence of 4 x 10^{13} cm^{-2}. The implantations of the PbO_2^- were performed at the University of Leipzig, the implantation of the O^{4+} were performed at the Ruger Boskovic Institute in Croatia.

All samples underwent firstly to a post-implantation LPLT (temperature: 1200 °C, pressure < 5 x 10^{-6} mbar, duration: 2 hours). Sample 2 and 3 underwent after a PL characterisation a HPHT thermal annealing process (2000 °C, 15 minutes), respectively. The HPHT process was performed at a stabilising pressure of 6 GPa to prevent the conversion of diamond to a graphitic phase [165]. The HPHT annealing was performed at the Institute of Geology and Mineralogy Siberian Branch of the Russian Academy of Sciences in Novosibirsk.

To summarise the discussion, the following Table shows the most relevant parameters:

Sample id	Implanted chemical species	LPLT annealing	HPHT annealing
2	PbO_2^-	X	X
3	Pb^-	X	X
4	O^{4+}	X	/

Table 3 Summary of the sample id, implanted chemical species and annealing treatments.

The single-photon sensitive PL was performed by adopting different excitation wavelengths, CW laser sources at 405 nm, 450 nm, 490.5 nm, 509.5 nm, and 522 nm, and a 80 MHz pulsed supercontinuum tunable laser (wavelength resolution: 10 nm). Room-temperature spectral measurements were performed using a Princeton PIXIS sensor fed by an HRS spectrograph fiber-coupled to the confocal microscope. Spectral measurements at cryogenic temperatures were performed coupling a confocal microscope integrated in a closed-cycle optical cryostat with a Horiba iHR320 monochromator fiber-coupled to a SPAD detector (3 nm spectral resolution). The adoption of a shortpass for the 405 nm laser is due to a signal originating from the optical components above 750 nm. Hence it was removed by means of optical filtering.

In the next table all the adopted configurations for the excitation wavelength, dichroic mirrors and Raman peak are reported. If the adopted configuration is different from the Table, it is reported in the text.

Excitation source (nm)	Dichroic mirror λcut−off (nm)	Spectral filtering (nm)	Raman Line (nm)
405	420	500-750	428.1
450	505	500	478.7
490.5	505/520	500	524.8
509.5	520/550	520/550	546.6
522	550/567	500	561.1
Supercontinuum white laser (λ<535)	Beam splitter (90/10) 550	550	x

Table 4 Summary table of the adopted optical components, spectral filtering and Raman lines for the excitation sources.

4.1.2.2 Ensemble characterisation: LPLT vs HPHT annealing

In the following section, different set of spectra for the same ensemble region of sample 2 are shown. The discussion is divided in LPLT annealing and HPHT annealing. The experimental parameters (such as excitation wavelength, Raman peak, spectral filtering) are those reported in Table 4. If any change from what stated in the table is adopted, it is discussed explicitly in the text. The adoption of different excitation wavelengths had

a twofold motivation: to probe energetically the optical transitions and to both disambiguate the attribution of the ZPL of PbV^- [118], [123], [211], [225] as well as the Raman signatures from the PL signals.

Low Pressure Low Temperature characterisation

In Figure 4.1.12 it is reported the set of spectra acquired after 1200 °C annealing temperature. Figure 4.1.12 PL spectra from Sample 2 acquired for (a) 405 nm, (b) 490.5 nm, (b) 522 nm excitation wavelengths at different temperatures: 4 K, 77 K and 300 K.

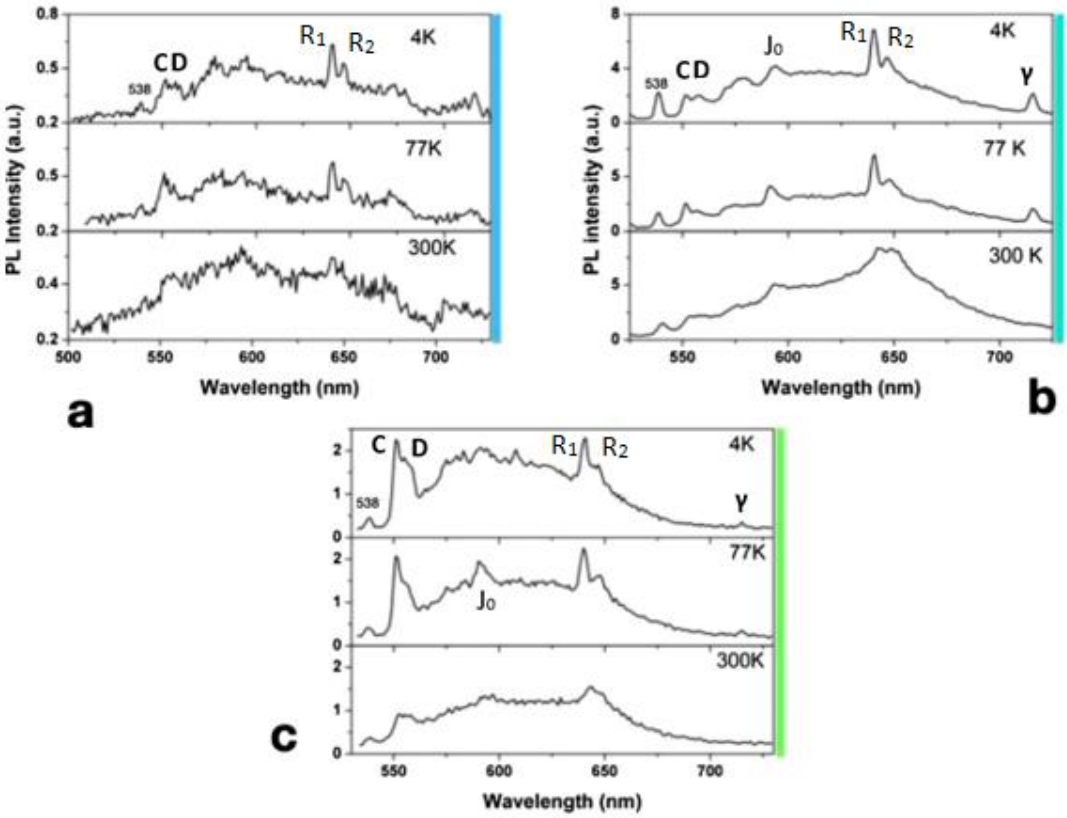


Figure 4.1.12 PL spectra from Sample 2 acquired for (a) 405 nm, (b) 490.5 nm, (b) 522 nm excitation wavelengths at different temperatures: 4 K, 77 K and 300 K.

The main observations are here reported for each excitation wavelength and the dataset is taken from ref [207].

405 nm excitation:

The main spectral features are reported in Figure 4.1.12a are mostly observable at cryogenic temperature, the optical power adopted to perform such characterisation is 10 mW on sample surface. They consist of a small peak centred at 538 nm and a band at ~ 550 nm labelled C and D. An intense doublet at 643 and 648 nm (labelled a R_1 and R_2) is clearly 85visible up to 77 K, at higher temperatures such doublet is convoluted in a larger band centred at 645 nm. The above-mentioned PL signals are consistent with what reported in ref [123].

490.5 nm excitation:

The main PL signals as reported in Figure 4.1.12b is observable at cryogenic temperatures, the optical power on sample surface was 3.5 mW. The spectra show different signatures, namely a peak at 538 nm, a doublet

at 552 and 557 nm (attributed as ZPL [88], [123], [128]). A set of small bands centred at 575 nm and 590 nm (observed in ref [233] with 532 nm excitation pump). The doublet at 643 nm and 648 nm is observable also with 490 nm excitation pump and it convolutes to a band for higher temperature. A small peak only observable at cryogenic temperatures centred at 715 nm is finally observed.

522 nm excitation:

The spectra shown in Figure 4.1.12c are acquired with an optical power on the sample surface of 3 mW. The signals are again mainly distinguishable at cryogenic temperatures as for the previous discussed cases. The most relevant PL signals are the peaks at 538 nm, C and D lines. Such features are brighter adopting the 522 nm excitation with respect to the blue ones. At increasing temperatures, it is observed a decrease of the D line, therefore the presence of the above-mentioned PL peaks is considered to be convoluted to the first order Raman but their attribution is confirmed to be Pb-related since it is observable at the same spectral positions also when different excitation wavelengths are used. The doublet R_1 and R_2has a similar behaviour to what described for shorter excitation wavelengths, the main difference is the intensity (lower with 5220 nm excitation than with 490.5 nm excitation). A band located at 590 nm (labelled as J_0) is visible in the spectra both at cryogenic and room temperatures. The peak at 715 nm (referred as γ) is also visible but barely and only at 4 K.

In order to disambiguate the presence of O-related PL signals from the Pb-related, an additional set of measurements was performed on Sample 4. In Figure 4.1.13 it is shown the set of spectra acquired under the same experimental conditions for the oxygen ensemble. The measurement was performed with 490.5 nm laser excitation at an optical power of 3.5 mW on the sample surface. The main signal consists in a peak at 590 nm, mainly observable at cryogenic temperatures only. A second weaker peak is observable at 650 nm and it convolves to a larger band for higher temperatures. Based on these measurements, it cannot be ruled out the attribution of the 590 nm signal to be O-related despite being also observable in ref [233] in a sample implanted only with Pb.

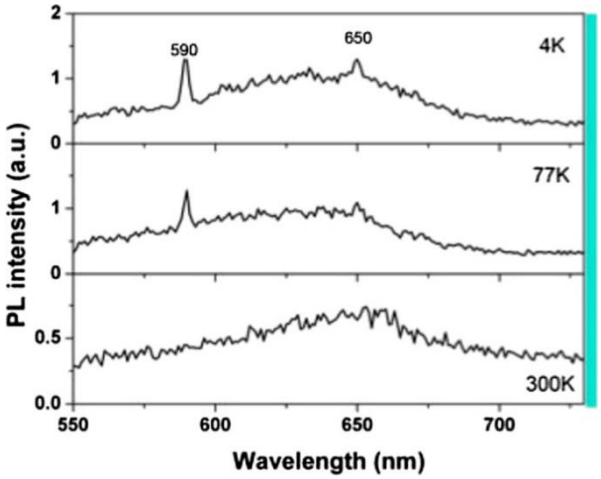


Figure 4.1.13 PL spectra acquired for oxygen implanted area (Sample 4) adopting a 490 nm laser. The spectra are acquired at 4-77-300 K. The sample underwent only LPLT annealing.

High Pressure High Temperature characterisation

In Figure 4.1.14 it is reported the set of spectra acquired after the HPHT annealing from Sample 2. Figure 4.1.12 PL spectra from Sample 2 acquired for (a) 405 nm, (b) 490.5 nm, (b) 522 nm excitation wavelengths at different temperatures: 4 K, 77 K and 300 K.

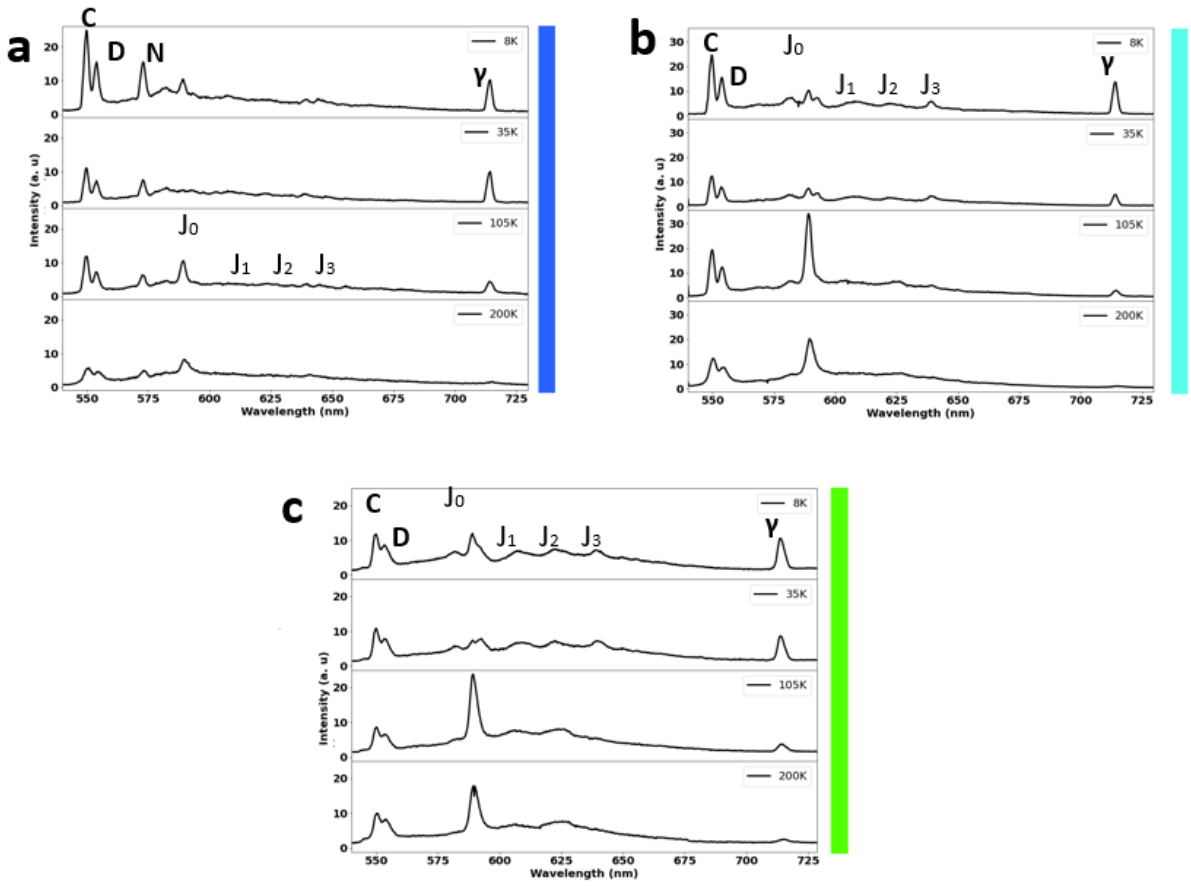


Figure 4.1.14 Ensemble PL spectra acquired from sample 2 following the HPHT treatment for (a) 450 nm, (b) 490.5 nm, (c) 509.5 nm excitation lasers at different cryogenic temperatures ranging from 8 to 200 K.

The main observations are here reported for each excitation wavelength. The same optical setup was employed as for the 1200 °C annealing. The only difference is the choice of the excitation wavelengths: 450 nm and 509.5 nm are the chosen different wavelengths to perform the measurement while the 490.5 nm excitation is identical to the above-mentioned characterisation. Such choice is dictated by the need of deconvolute the first order Raman for the case of the green excitation while for the blue excitation to explore the same conditions of ref [233] to observe the theoretically and experimentally predicted ZPL of PbV [118], [233] at 517 nm. The sets of spectra are acquired adopting an optical cryostat. The experimental constraints are those discussed in the experimental section.

<u>450 nm excitation:</u>

In Figure 4.1.14ait is reported the set of spectra acquired for 450 nm excitation, the optical power on the sample surface is 3 mW. The most relevant features are the doublet at 552 and 557 nm, labelled as typically with group IV [76], C and D. Such doublet is considered to be the ZPL of the PbV^- complex by certain works [88], [123]. A sharp peak (labelled as N in the graph) at 574 nm is visible only for this excitation energy and its intensity decreases with respect to temperature. Its attribution cannot be considered to be related to the presence of NV^0 since the NV complex anneal about at temperatures above 1400 °C [49] and the sample underwent HPHT annealing above 2000 °C.

A peak at 590 nm (labelled J_0) is again visible for all the measurement temperatures and its intensity increases with respect to temperature. The 590 nm peak is indeed reported to be a doublet as described in ref [88], but due to the constraint of the optical setup it was not always resolvable by the spectroscopic system under use. A set of smaller bands ($J_1 J_2 J_3$ respectively) are observable at 609 nm, 623 nm and 639 nm are visible.

The γ signal at 715 nm is mainly visible at cryogenic temperatures while decreasing in intensity and in FWHM reaching room temperature, such behaviour is in agreement with ref [88].

To investigate the presence of the 517 nm peak it was performed an analysis of both the implanted and unimplanted area. Figure 4.1.15reports a spectrum acquired at 6 K, it is clearly visible the presence of the 517 nm peak for both the ensemble region (black line in the Figure) and red line (unimplanted area in the Figure). Such observation agrees partially with what observed in ref [118], [233] but it is in contrast with the attribution given therein [118], [211]: being present in both implanted and non-implanted areas it is tentatively attributed to defects in the crystal lattice previously to the implantations. A possible explanation could be the occurrence of Zn-related impurities [49], possibly resulting from contaminations in the HPHT process. A more dedicated study is presented in the following sections.

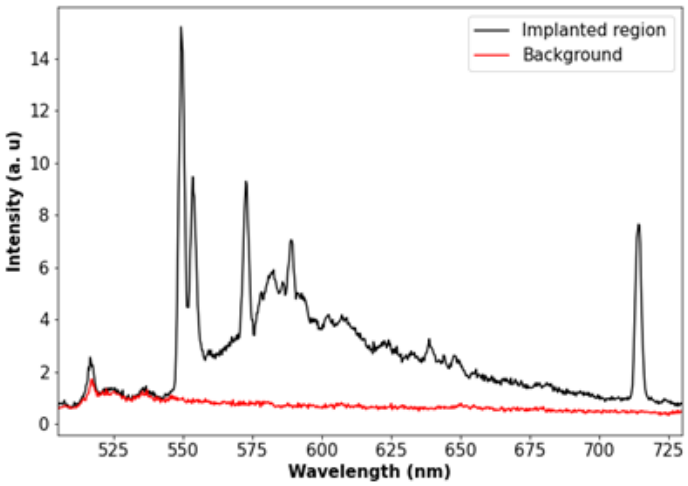


Figure 4.1.15 PL spectrum acquired from sample 2 following HPHT treatment under 450 nm excitation with an optical power of 3 mW at a temperature of 6 K. The black line represents the ensemble signal while the red line is the background signal acquired in an unimplanted sute in the same sample.

<u>490.5 nm excitation:</u>

The spectra are acquired with an optical power of 2.6 mW on the sample surface. The main peaks are the C and D transitions, therefore the doublet at 552 and 557 nm. It is present the peak J_0 (consisting in a doublet at 589 and 591 nm) and the small bands J_1, J_2, J_3. The peak at 574 nm is no longer visible in the spectra while the peak at 715 nm is observed and its behaviour is identical as for the 450 nm excitation case.

To evaluate the presence of the peak at 517 nm and disambiguate it from the first order Raman (at 526 nm), it is reported in Figure 4.1.16 the spectrum acquired in the spectral window from 508 nm to 590 nm acquired in a non-implanted area. The peak at 517 nm is clearly visible in the spectrum acquired under 450 nm excitation (black line), while the 490.5 nm laser (red line) such peak is not present, and it is only visible the

Raman signal at 526 nm, for the 450 nm excitation the Raman is at 478.5 nm, hence it is not related to observed spectral features.

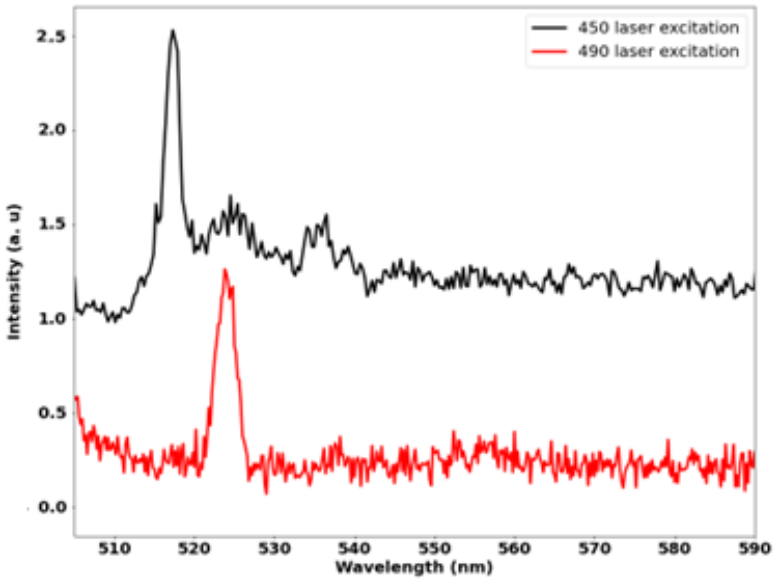


Figure 4.1.16 Overlay of spectra acquired in an unimplanted area of sample 2. at 8 K. The red line represents the observed signal acquired with 540 nm excitation laser; the red line represents the spectrum acquired in the same region with 490 nm excitation laser.

The C and D and γ signal decrease in intensity while the J transitions are increasing in intensity while reaching room temperature. It is clearly observed a non-monotonic increase of the latter as function of temperature, such observation could be justified under two separate assumptions. Firstly, technical constraints related to small vibrations of the optical cryostat adopted, might have moved slightly the focal point ergo changing the collection efficiency of the signal. Secondly, the local spatial charge within the diffraction limited spot was modifying the relative intensity of the peaks. Secondly, the local spatial charge within the diffraction limited spot was modifying the relative intensity of the peaks. To further prove this assumption, it was performed at room temperature a measurement consisting of irradiating the ensemble region with a high energy 532 nm pulsed laser and different spectra were acquired at various distances from the irradiated spot. In Figure 4.1.17 the spectra are reported, the peak at 545 nm is related to the first order Raman signal. Figure 4.1.17a displays the signal acquired far from the irradiated spot, it consists of the C-D, J and γ lines within the same measurement site in the ensemble. Figure 4.1.17b shows only the C-D lines while Figure 4.1.17c only shows

the J lines. The observed features are only visible in this sole case, to further substantiate the assumptions here discussed, a dedicated experiment would be required.

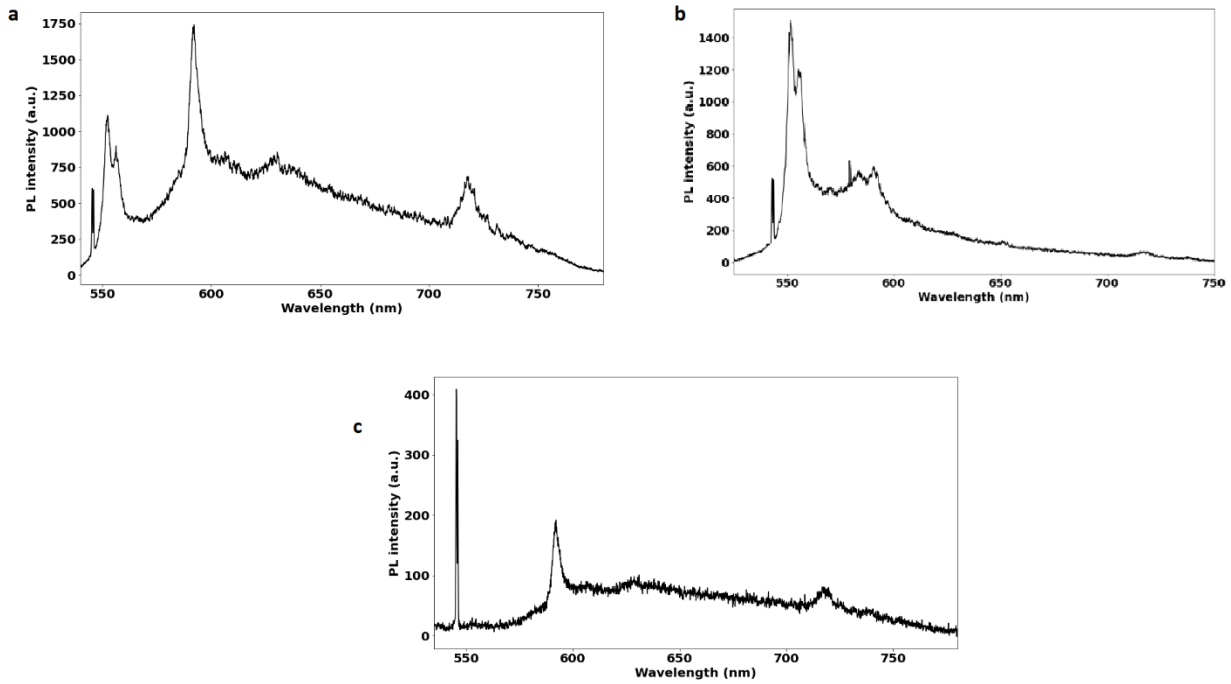


Figure 4.1.17 PL spectra at room temperature of the High fluence ensemble PbO_2 region from sample 2. The spectra are acquired on the same ensemble but in different positions within it. The spectra are acquired using a 509.5 nm laser and an optical power of 1.6 mW.

<u>509.5 nm excitation:</u>

The set is acquired with an optical power of 3.1 mW on the sample surface. The main observations are identical to the case of 490 nm excitation. Both the C and D lines, together with the group of J transitions as well as γ are present in the set of spectra. There are no remarkable differences with respect to the case of the 490 nm excitations. In Figure 4.1.8 it is reported a zoom of the spectral region 585-675 nm. The features $J_{0/1/2/3}$ are clearly visible and their position is respectively 609.21 nm, 622.86 nm, 639.15 nm.

They could be tentatively attributed to phononic replicas of the J_0 doublet In fact their relative shift with respect to the J_0 is ~ 60 meV for $J_{0/1}$ and ~40 meV for $J_{1/2}$ $J_{2/3}$. These observations agree with ref [88]. Moreover, no doublet is observed at 643 and 648 nm, differently from what observed in [207], [225] further supporting the hypothesis that the doublet at 643 and 648 nm could be related to or Pb-related defects or other intrinsic defects that anneals-out at higher temperatures. The disappearing of such peaks even at room temperature is in agreement with what reported in literature for HPHT annealing [88].

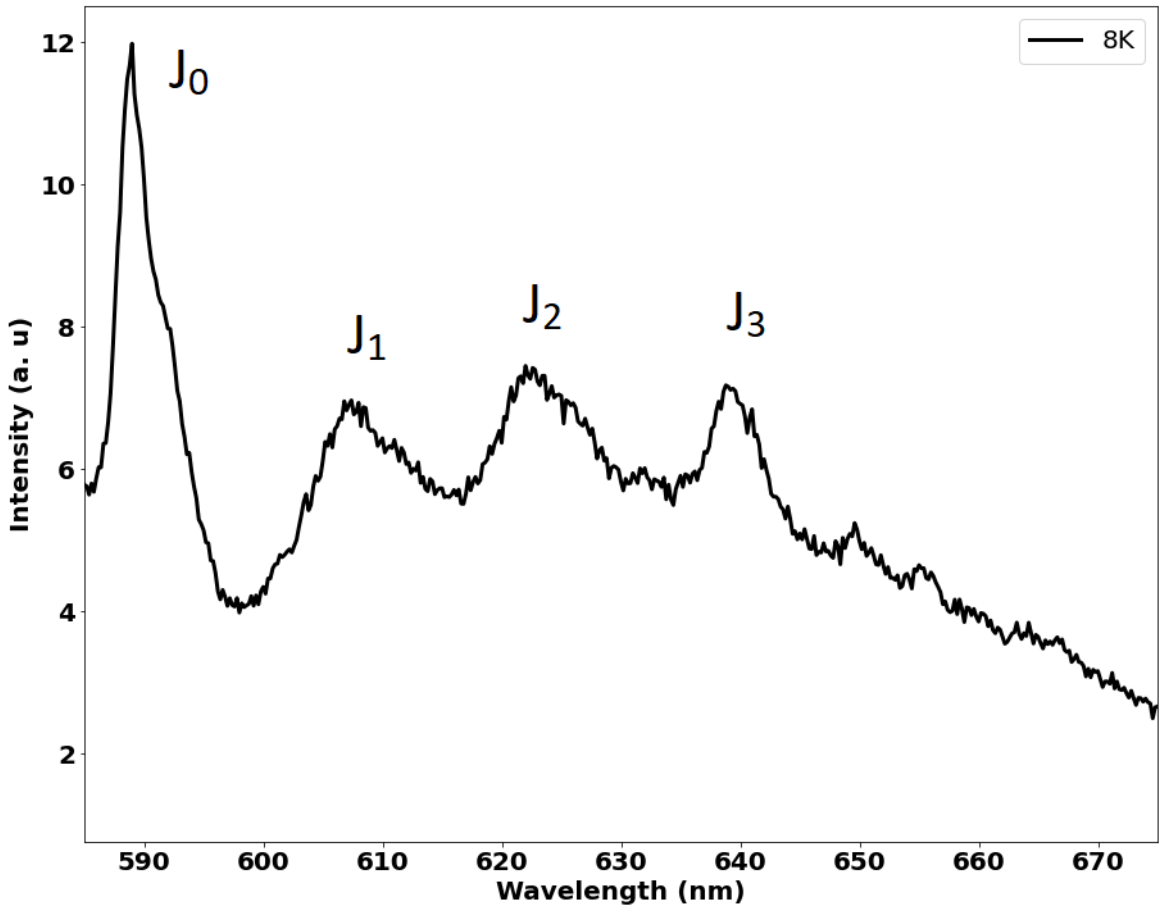


Figure 4.1.18 Zoom of the spectral region from 480 nm to 675 nm. The spectrum is acquired using a 509.5 nm laser and an optical power of 3.1 mW.

4.1.2.3 Spectral effect of the HPHT treatment on the sample

To identify whether any of the aforementioned optical signatures are unrelated to the lead implantation, an optical characterization was performed at room and cryogenic temperature on an unimplanted region of sample 2.

InFigure 4.1.19 two spectra are reported from sample 2 after the HPHT annealing: a) represents the observed 517 nm feature presented previously acquired with the CW 450 nm laser at 8 K; b) represents the optical signal acquired at room temperature with the tunable PW laser at 500 nm. The main features observable are the followings: a broad (80 nm) and weak band centred at 650 nm is observable, while increasing the excitation energy a peak centred at 630.7 nm elevates from this band.

Such optical feature was attributed in previous works to CVD as-grown diamond containing nitrogen and considered a stable defect above 2000 °C and with an optimal excitation wavelength of ~460 nm [49].

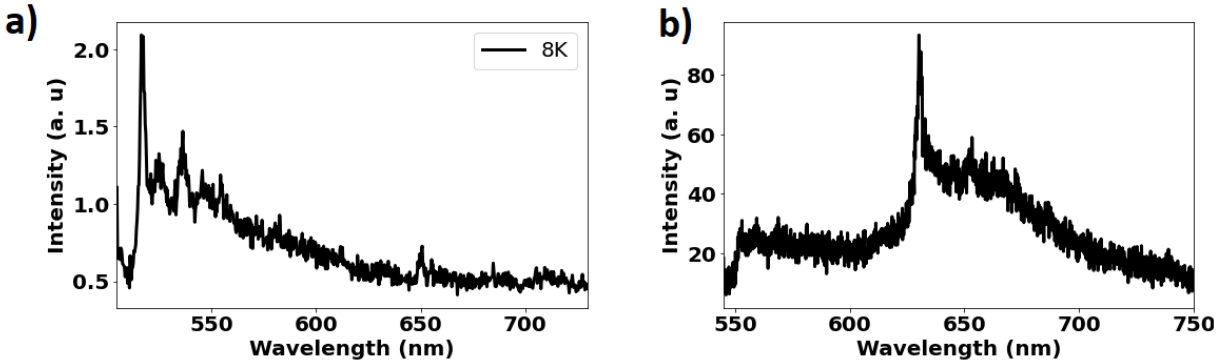


Figure 4.1.19 Spectral features observed in the unimplanted areas of sample A. a) the 517 nm feature observed only with 450 nm excitation at 8 K with an optical power of 2.3 mW. B) A peak at 630 nm with a band from 640 nm to 680 nm observed at room temperature. The spectrum is acquired with PW 460 nm excitation and an optical power of 0.82 mW.

To understand the nature of the 517 nm peak, an investigation as function of temperature was conducted. In Figure 4.1.20a it is reported a set of 4 spectra ranging from 8 K to 200 K of the unimplanted area of sample A. At cryogenic temperatures it is observable a small peak at 517 nm with two replicas 522.3 nm and 535.1 nm (the latter attributed to be phononic replicas of the 517 nm feature [49]). A series of weak peaks are visible at 653 and 658 nm. Overall, the intensity of the above-mentioned signals is decreasing reaching room temperature. This feature was observed under the same experimental conditions as in ref [233], the main difference here is resides in the attribution and concurrent observation of the C and D transitions at the same time than the 517 nm peak. This could offer a potential disambiguation in its attribution, to be considered not the ZPL of PbV [88] but possibly a Zinc-related as observed in only Cathodoluminescence in ref [49]. Otherwise, its attribution might be related to impurities present in the host crystal. During the ion implantation a large amount of vacancies are created hence permitted to form this optically-active defect that is here observed only after HPHT annealing but it is also observed after LPLT annealing as discussed in ref [225].

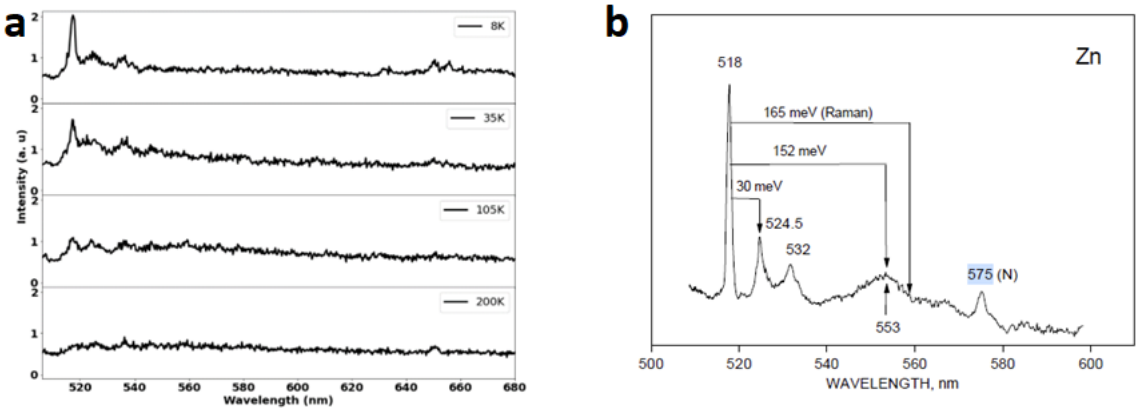


Figure 4.1.20 a) Set of spectra acquired with 450 nm excitation at 8 K with an optical power of 2.3 mW on the unimplanted area of sample 2. b) Cathodoluminescence spectrum from ref [49] *displaying similar features.*

4.1.2.4 Non-resonant photoluminescence excitation spectroscopy

I performed Photoluminescence Excitation Spectroscopy (in the following PLE) spectroscopy at room temperature in both the ensemble and unimplanted areas of sample 2. The analysis was carried after the HPHT

annealing only. Particularly, the PLE analysis is conducted on the C and D transitions, the N transition and the 630 nm feature. The measurements are performed adopting the same experimental conditions: the confocal microscope is equipped with a dichroic mirror with cutoff wavelength at 550 nm (partially suppressing the C transitions) and the supercontinuum white PW laser is kept at a bandwidth of 10 nm and an optical power of 0.82 mW on sample surface. The measurement is performed with steps of 5 nm for the N, C and D transitions up to 525 nm excitation wavelength. For the unimplanted area the shorter wavelengths are scanned every 10 nm (up to 450 nm) since it was not possible to observe any signal arising from the background. For each point in the graph, it was acquired a PL spectrum, the background was subtracted for the N, C and D transitions. The spectra acquired are then fitted (with a Lorentzian curve for the N transition and the 630 nm feature, a double gaussian for the C and D transition) in the specific spectral region to permit the construction of the plots in Figure 4.1.21.

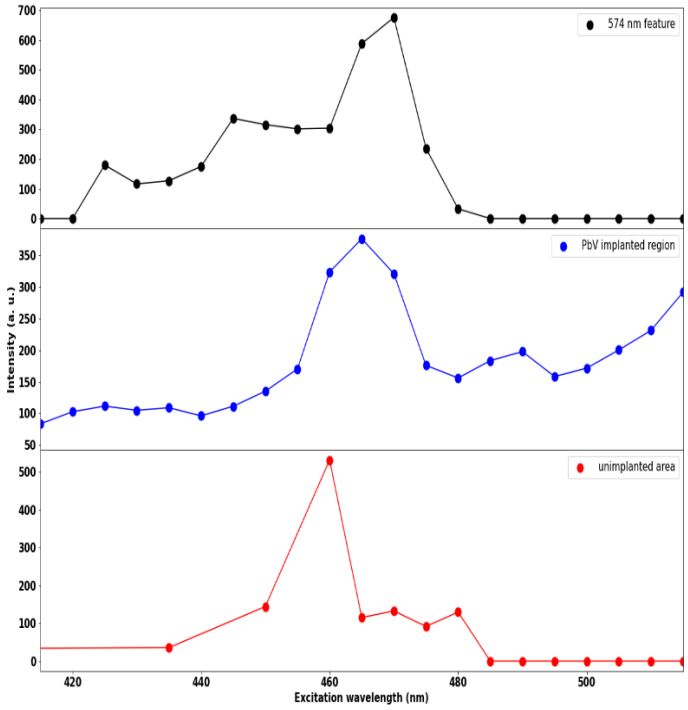


Figure 4.1.21 PLE spectrum of the N (black curve), C and D (blue curve) transitions and 630 nm feature (red curve) acquired at room temperature on sample A adopting the supercontinuum PW white laser. The optical power on the sample surface is 0.82 mW.

N transition

The N transition (situated at 574 nm) PLE spectrum showed an excitability up to the threshold value of 490 nm excitation wavelength. Above such threshold no N signature was observed. The attribution is of unclear nature. In fact, the attribution as neutral charge state of the NV defect is not possible since it anneals out for annealing temperature above 1400 °C [49]. Furthermore, the excitability of the NV^0 charge state is assessed by a large amount of scientific literature up to over 532 nm wavelengths [234], [235]]. The same optical feature was observed in PL in ref [233] under the same excitation wavelengths. Here it is presented for the first time at the ensemble level with concurrent observation of the ZPL (C and D lines) of the PbV defect, suggesting the attribution of such line to a defect related to the PbO_2 implantation, or to a possible state of the PbV complex. The observation of the N line is observed also in ref [49] and it is tentatively attributed to Zinc impurities.

PbO_2 ensemble

The PbV implanted region PLE analysis displayed in Figure 4.1.21 is characterized by three main bands: at (466.3 ± 1.2) nm, (488 ± 3) nm and (412 ± 3) nm. The most prominent observed resonance was tentatively attributed to be related to a higher lying excited state with A_{2u} symmetry as for other group IV elements. The width of such resonance being narrower than all group IV complexes [213], [236] is in optimal agreement with what predicted [118]considering that the a_{2u} orbital is closer to the valence band edge.

Unimplanted area: 630 nm feature

The unimplanted area, consisting of primarily the emission feature at 630.7 nm at room temperature, is characterised by a sole excitation resonance peaked at ~460 nm excitation wavelength. The attribution of such optical line is of unknown nature: it has been observed in samples implanted with high mass Sn ions (both at ensemble level and single emitter level as discussed in Chapter 1.3.2) and with Pb implantation. It is here observed for the first time both at the ensemble and at the single emitter level. A similar defect structure (PL signal and excited state lifetime) is observed in ref [224]. The interpretation of the resonance in the spectrum in Figure 4.1.21Figure 4.1.21 PLE spectrum of the N (black curve), C and D (blue curve) transitions and 630 nm feature (red curve) acquired at room temperature on sample A adopting the supercontinuum PW white laser. The optical power on the sample surface is 0.82 mW. it is explained as stated in ref [49], that suggests that such optical line is observed in as-grown CVD diamond films containing Nitrogen and has the optimal excitability of the defect is in the range 450 nm and its stability is pronounced after HPHT treatment. Such emission line was in fact not observed in the LPLT analysis.

4.1.2.5 Single emitters analysis

The following analysis is allowing to understand, at single emitter level, the spectral lines associated with the ensemble spectra. The occurrence of three different emitters is presented. Particularly an emitter associated to the doublet at 643 nm and 648 nm; various emitters associated with the spectral line at 630 nm and, finally, the PbV^- colour centre with a doublet at 552 and 557 nm.

LPLT annealing analysis

The single emitter analysis was developed starting from the acquisition of various spectra at the edges of the high fluence ensemble as reported in Figure 4.1.22. The acquisition was taken with 532 nm excitation laser. Different emission lines are observable associated to isolated spots (for whom no HBT measurement was taken). The ensemble spectrum was then compared to the signals from the isolated spots and no clear unambiguous attribution was achievable. It is evident that the emission lines can be grouped in different classes:

- 557 nm and 643 nm feature (observable Figure 4.1.22e). Such lines are visible as well in the ensemble in Figure 4.1.2.
- 554 nm signal. With respect to the spectral resolution adopted for this work, this emission line is concordant with the 552-557 nm line (attributed as ZPL of the PbV complex). Accrediting such line as ZPL is not straightforward, in fact the signal could originate from lattice strain shift or from a 555 nm line associated with proton and neutron irradiation in diamond [49].
- Recurring PL signals not associated to the ensemble (namely the lines in at 564, 567, 581, 605, 651, 665, 658 nm). The lines might be associated to different complexes not fully incorporated in the dense diamond lattice or to radiation induced defects or, finally, to Pb related defects (as the lines 563 nm [49] and 656 nm [49] are observed in irradiated diamond).
- The lines 564-567-651-658 nm were observed in ref [225] under 450 nm excitation and at 4 K temperature.

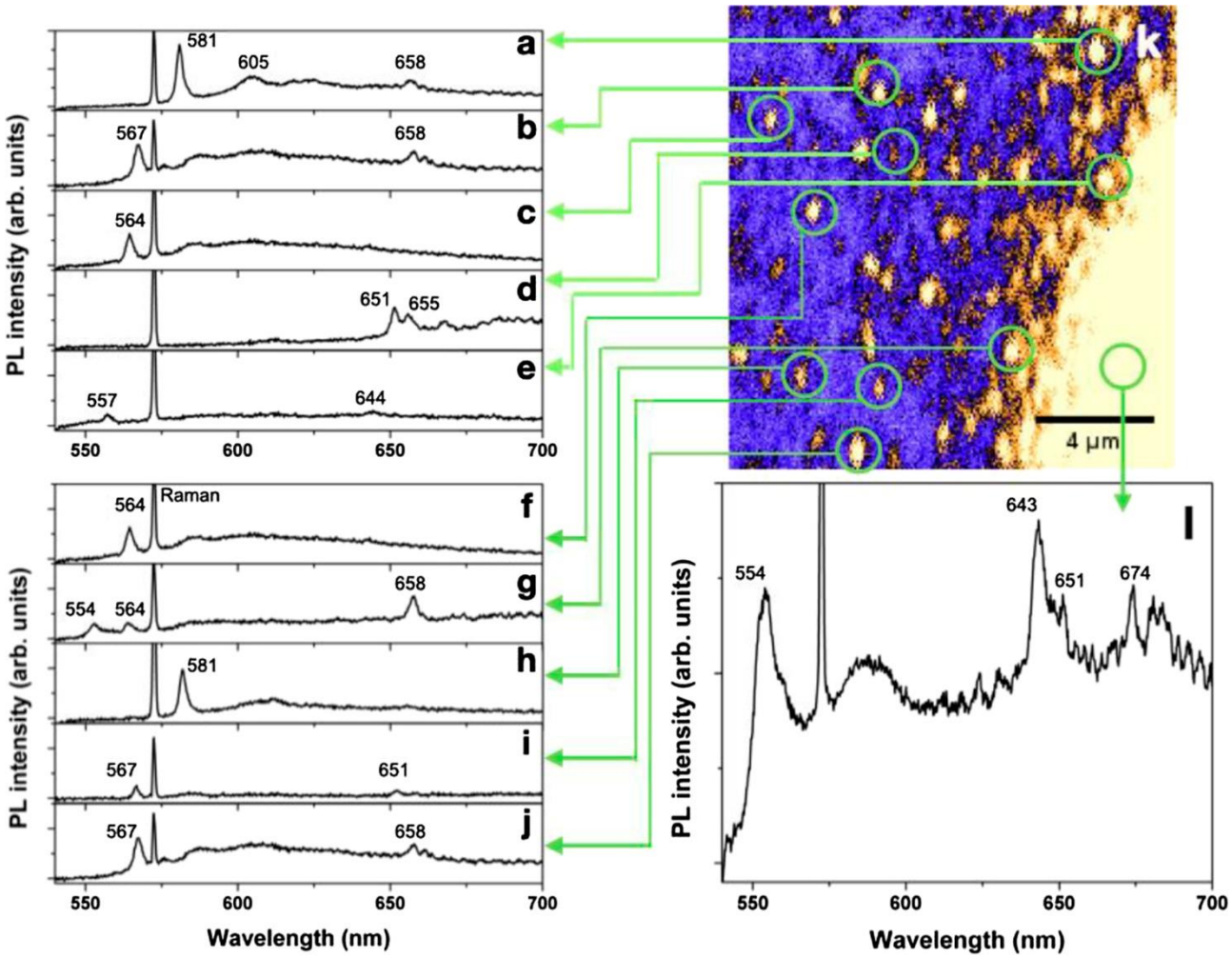


Figure 4.1.22 Different isolated spots (not associated with any HBT interferometry analysis) displaying a inhomogeneous discrete set of emission lines.

In Figure 4.1.23 it is reported a typical PL map obtained under 490.5 nm excitation wavelength on sample A with an optical power of 1.3 mW, the map is acquired at the edges of the $5x10^{11}$ cm^{-2} ensemble. The spot circled in Figure 4.1.23a consists in the emission line at 643 nm, reported in Figure b. The main parameters were explored as the excited state lifetime by means of HBT interferometry. Such spectral line is considered to be associated to the PbO_2 implantation since its occurrence in the ensemble is the most prominent under all the excitation regimes as well as it is reported in ref [233].

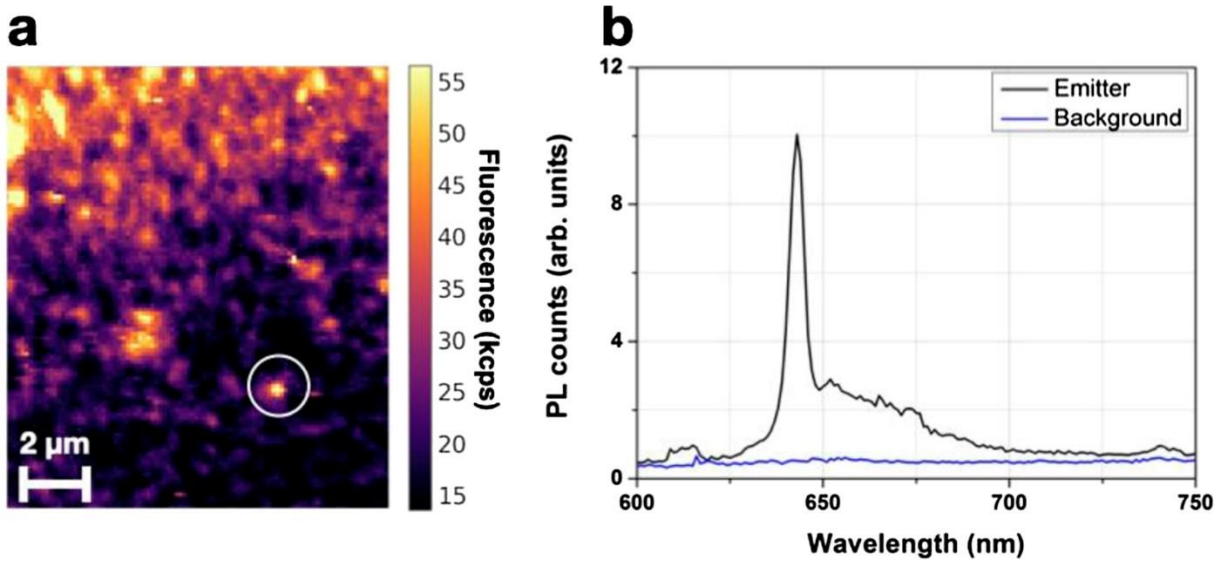


Figure 4.1.23 Room temperature analysis of single emitter with 490 nm excitation. a) PL confocal map acquired at the edge of an implanted region. b) Spectra of the single emitter circled in a) with background overlaid. Figure from [207].

It is worth mentioning that at the ensemble level no clear 643 nm peak was observable at room temperature, but a broader spectrum was detected, possibly suggesting that different emission lines are associated to the band centred at 650 nm. To gain a more detailed understanding of the spectral inhomogeneity a dedicated investigation addressing at single emitter level the PL signal is shown in Figure 4.1.23b.

The second order autocorrelation function displayed in Figure 4.1.24a for different optical power in the range 0,40-0,93 mW, the background corrected analysis showed a minimum reaching 0 which means that the under-analysis defect is indeed single. The model applied for the characterisation consisted of a 2-level model, the linear fit of the λ parameter stemmed to a lifetime value of (4.5 ± 0.3) ns. The measured lifetime is in good agreement with what reported for the Pb defect, both the predicted DFT calculations[118] as well as the ZPL of the lead complex (552-557 nm) [88], [123].

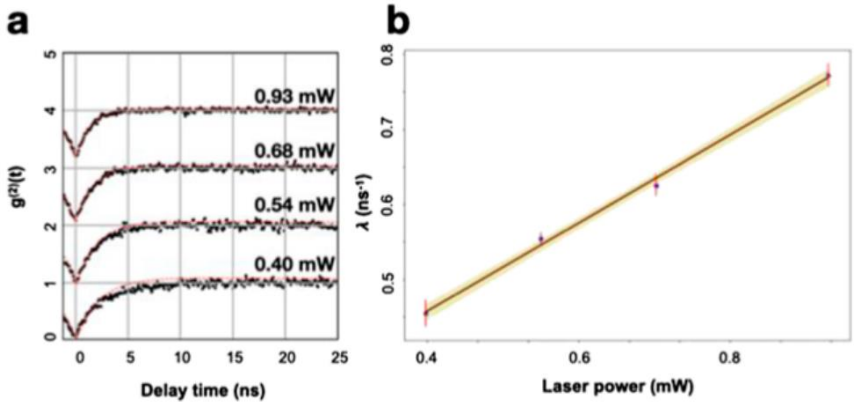


Figure 4.1.24 a) Second order autocorrelation function as function of optical power. b) Linear fit of the λ parameter, the intercept represents the inverse of the excited state lifetime of the analysed defect.

HPHT annealing analysis

The sample underwent to a HPHT annealing after the above-mentioned analysis and was again characterised to locate single emitters.

The majority of the analysis at ensemble level was performed on Sample 2 due to the intense background present in sample 3 related to H3 component under excitation wavelength < 522 nm. The specification of the samples are reported in Table 3.

Under 522 nm excitation wavelength the edges of the implanted areas were mapped to locate isolated spots allowing to perform the single emitter analysis. It was not possible to investigate the sample under blue excitation (i.e. < 509 nm) since the presence of the H3 [49] defect was too intense with respect to the single emitter intensity.

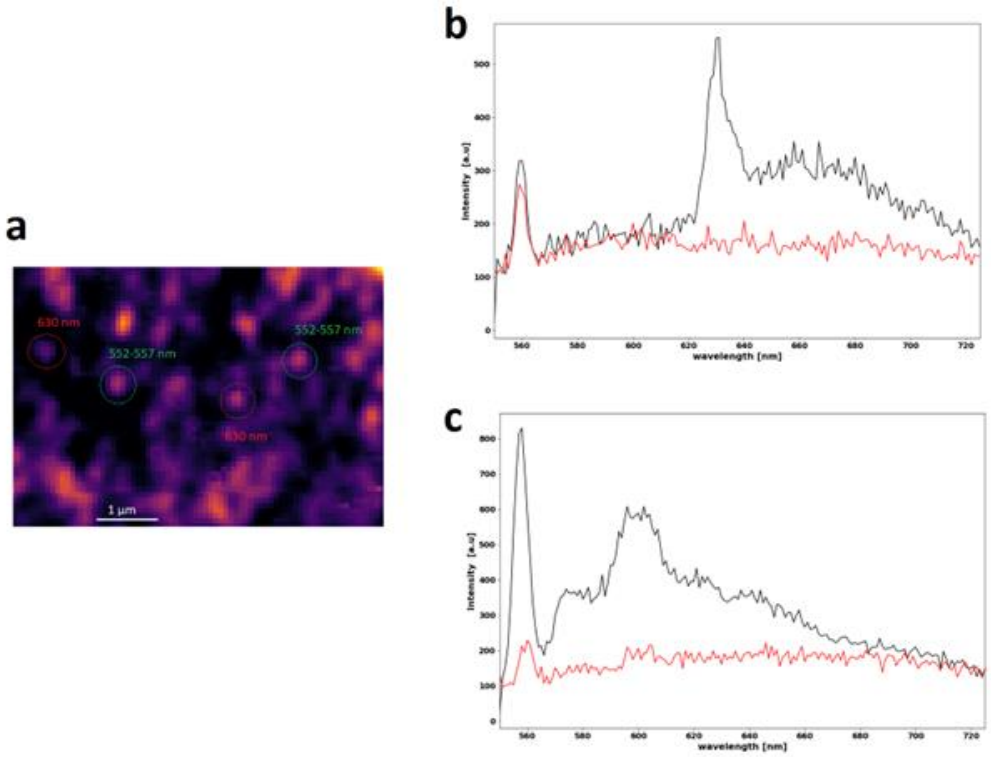


Figure 4.1.25 Room temperature analysis of single emitter under 520 nm excitation with an optical power of 1.2 mW. a) PL confocal map acquired at the edge of an implanted region. b) Spectra of the single emitter circled in a) with background overlaid with 552 and 557nm emission lines. c) spectra of 630 nm emitter and background overlaid. The small peak at 560 nm represents the First order Raman line.

The fitting curve to evaluate the lifetime of the radiative decay and the saturation curve for the PbV single emitter and the 630 nm feature are reported in Figure 4.1.26.

The HBT analysis stemmed a radiative lifetime of the excited state for the PbV defect (whose spectrum is reported in Figure 4.1.25b) to (3.57 ± 0.21) ns which is compatible with the reported values [88], [123], [128]. The saturation curve yielded (1.07 ± 0.08) Mcps for a saturation power of (1.27 ± 0.23) mW and such values are in line with ref [123], despite no quantitative comparison could be performed since the setup adopted is different from the case in ref [123].

Regarding the 630 nm feature, the excited state lifetime yielded a value of (9.33 ± 0.21) ns which is somehow coherent with the values observed for the defects reported in Chapter 1.3.2 but not comparable with ref [224]. The saturation parameters are the following: I_{sat} (0.84 ± 0.31) kcps and P_{sat} (0.93 ± 0.26) mW.

The discrepancy of the above mentioned value can be attributed to the diverse annealing procedure, in ref [49] it is reported that its intensity remains unchanged up to LPLT annealing while in this case study the HPHT might have promoted a more stable configuration, hence a difference in both the saturation parameters as

well as the excitetd state lifetime, as reported in ref [165]. The attribution of such optical feature as non related to the ion implantation is here further supported. It can be related to residual radiation damage of the crystal.

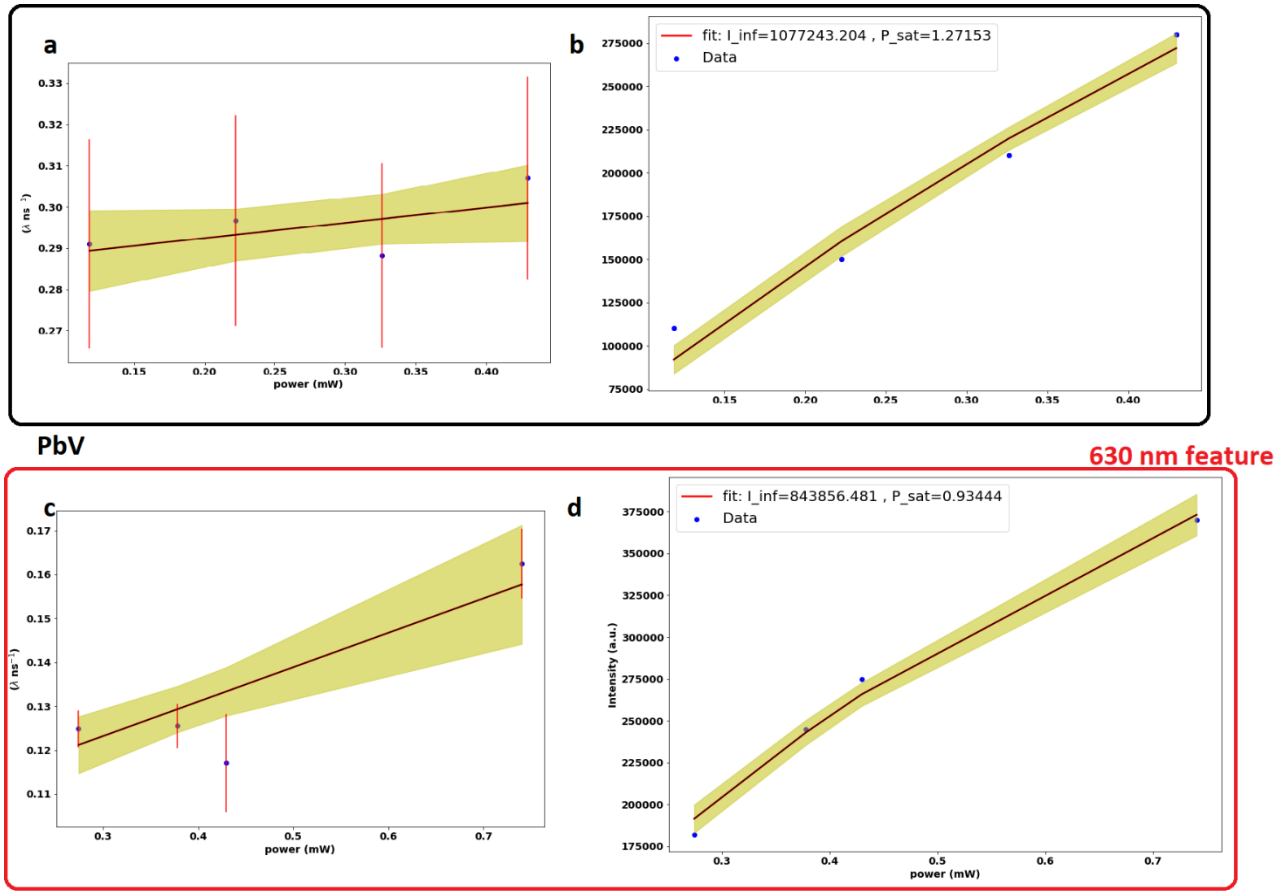


Figure 4.1.26 Excited state lifetime and saturation curve for the PbV defect (a and b) and for the 630 nm feature (c and d). The acquisition was taken under 520 nm excitation.

4.2 Emerging classes of colour centres

The need for diverse single-photon emitters displaying desirable opto-physical properties (high emission rate, narrow linewidth) is motivating the discovery and characterisation of alternative classes of optical defects in diamond with respect to the consolidated NV complex and group-IV related defects [76]. In this sense, Ion implantation represents a versatile tool to engineer different types of optically active defects, allowing for the fine control of key parameters as extensively discussed in Chapter 2 [79], [86].

The fabrication of novel colour centres in diamond and the systematic investigation represents a crucial tool to further improve the knowledge on such systems and possibly permitting the discovery of versatile colour centres for the different technological applications. Following the work from Lumhann et al [140], part of the research activities of the three years' PhD work was focussed on the discovery and characterisation of novel optically active defects in diamond. Particularly this Section is focussed on the results obtained on the Magnesium-based complex and the Fluorine-related defect in diamond.

4.2.1 Magnesium vacancy colour centre

Magnesium-related colour centre is of recent discovery [140]. Its first systematic optical characterisation was performed during the present PhD work and are here presented. The results are compared with the theoretical framework presented in ref [237]. The work here presented is the result of the collaboration with the group of Solid-State physics from KU Leuven and the Instituto Superior Técnico in Lisbon.

The work is divided in two sections: the first section is dedicated to the structural properties as well as the structural formation by the Emission Channelling technique; the second section is centred on the PL characterisation adopting different excitation energies (both at cryogenic and room temperature) to study its optical activity. The emission channelling analysis was performed by the researchers of the Group of Leuven and Lisbon at the ISOLDE facility at CERN. The results from the EC contributed to the understanding of the structural properties of the defect and corroborate the ab-inito model presented in ref [237] along with the optical characterisation, performed during the PhD.

4.2.1.1 Emission channelling and structural analysis

To experimentally evaluate the lattice location of the Mg ion in the crystal lattice, the Emission Channelling (EC) technique is adopted [178], [179], [238].

As mentioned in Chapter 2, the Emission Channelling (EC in the following) is a powerful technique that allows to probe a crystalline solid with a radioactive beam and collecting the characteristic emitted electrons from the β^- nuclear decay [178]. With a position sensitive detector, it is thus possible to reconstruct the angle dependent electron patterns in the host material.

In the following, the summary of the experimental methods as well as the physical discussion is reported. This technique is adopted to probe a single crystal <100> oriented from Element Six with Nitrogen concentration < 1 ppm. The implantation is performed both at room and higher temperature (800 °C for Mg [80]) with low fluence (< 10^{11} cm^{-2}) implantation.

For the Mg structural analysis, it was used a short lived ^{27}Mg (half-life of 9.45 minutes) produced at CERN's Isolde on-line isotope facility. A Ti target was bombarded with 1.4 GeV protons resulting in nuclear fragmentation reactions. Once the Ti target reaches 2000 °C it starts to out diffuse; Mg ions are ionised to Mg^+ by means of resonant lasers, accelerating at 30 keV and the ^{27}Mg is selected by a bending magnet.

The beam was focussed to 1 mm diameter spot and the β^- EC are measured with a 30x30 mm^2 detector placed at ~300 mm from the sample resulting in an angular resolution of ~0.1°. The $^{27}Mg^+$ ions are implanted at 2.1–5.5 × 10^{11} cm^{-2}, the resulting total fluence is estimated to be in the 10^{13} cm^{-2} range.

To evaluate the obtained EC patterns, the major lattice sites were fitted by combination of the theoretical ones [238] adopting the many-beam approach [238]. In Figure 4.2.1, the (100) plane of diamond is shown with the substitutional sites as well as the major lattice sites and finally the tentatively predicted lattice positions for the Mg complex. It is worth mentioning that the nomenclature regarding impurity-vacancy structures, for historical reason, originates from the Nitrogen Vacancy defect. The NV strucure is vacancy bonded with a nitrogen occupying a substitutional lattice site in diamond [116], it can be therefore seen as inserting a nitrogen atom in a double vacancy site, replacing the N with the vacancy. For the Mg complex, the EC analysis performed by the Solid-State group from KU Leuven and Centro de Ciências e Tecnologias Nucleares in Lisbon at the ISOLDE facility at CERN leads to attribute the defect to a split-vacancy configuration, referred with the EC nomenclature as Bond Centred (BC). The fitted patterns were evaluated to study substitutional (S) and interstitial sites in lattice structure. The yields were derived considering displacements of the S positions over the along ⟨111⟩, ⟨100⟩, or ⟨110⟩ directions.

Particularly, the nomenclature yields to the following complexes (as theoretically predicted by [237]):

- Mg + 1V correpsonds to MgV_S (S)
- Mg + 2V correpsonds to MgV (BC)

- Mg + 3V correpsonds to MgV_2 interstitial site close to the Split Position (SP) location in Fig. 1.2.1

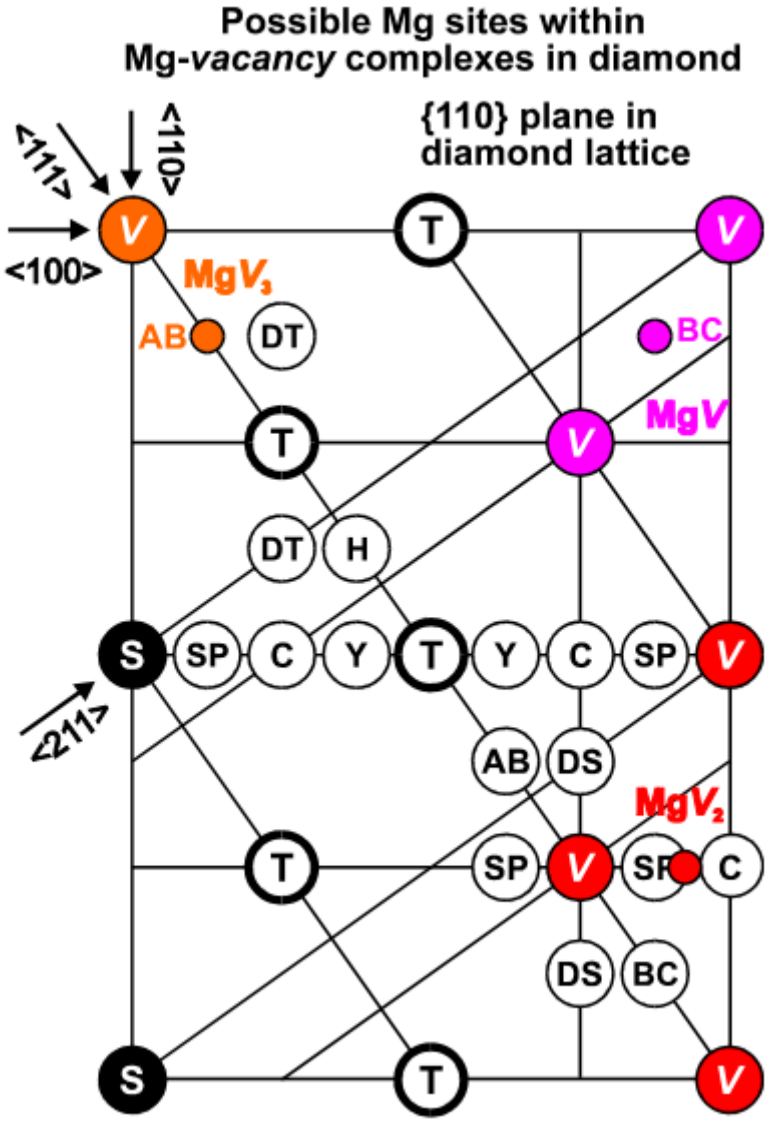


Figure 4.2.1 (100) cut of diamond lattice with possible positions of the substitutional and major interstitial sites in diamond. The interstitial sites here are the highest symmetry ones and they are obtained by displacements from substitutional sites from the S position along the bond-centred (BC), antibonding (AB), tetrahedral (T), and hexagonal (H); along , the split (SP) and the "Yb" (Y, named after Yb) and "C" (C, named after its C2v symmetry) sites; and along , i.e. the -split (DS). The potential lattice sites and structures for MgV, MgV_2, and MgV_3 systems are shown in violet, red, and orange.

Since the ^{27}Mg half-life is too short to perform in-situ annealing during the implantation, the analysis was carried by performing two implantation experiments at fixed room temperature and 800 °C, respectively. The obtained experimental and predicted patterns for the 2-temperature considered for the measurements are shown in Figure 4.2.2.

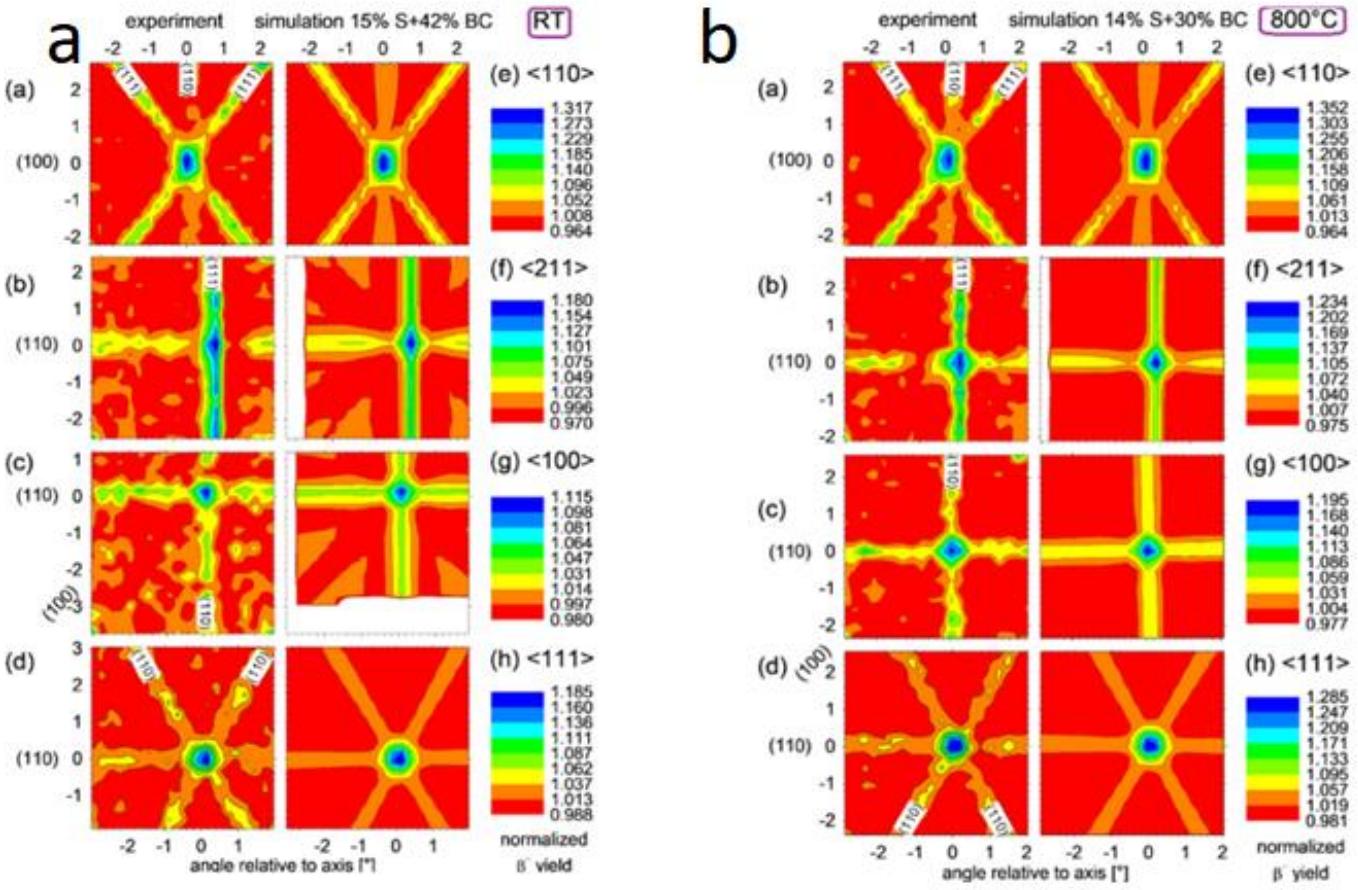


Figure 4.2.2 Experimental and simulated Emission Channelling maps from ^{27}Mg over the <110>, <211>,<100> and <111> crystal orientations acquired at (a) room temperature implantation and (b) at 800 °C implantation. Plots a to d are the experimental patterns; plots e to h are the simulated ones.

The fitted patterns along <110>, <211>, <100> are shown in Figure 4.2.2a for room temperature implantation and 1.2.2b for 800 °C in-situ annealing. At first glance, the anisotropies of the EC measured are weak, indicating that a significant fraction of the atoms occupies the sites with low crystal symmetry.

The analysis for both room temperature and 800 °C implantation showed that a large fraction of BC sites was occupied, respectively (30-42% depending on the adopted fitting procedure), at the expense of a limited fraction (14-15%) of substitutional sites. This result implicates that 30-40 % of implanted Mg ions are found actually at the lattice sites theoretically predicted in ref [237], hence forming the MgV complex in split vacancy configuration.

To further correlate the EC analysis with the spectroscopic investigation, different spectra were acquired on the samples implanted at ISOLDE. The spectra are reported in Figure 4.2.3. The spectra are acquired from the Room Temperature and in-situ annealing cases adopting a 532 nm laser excitation. The implantations are performed on a ultrapure single crystal sample "quantum grade" at Isolde facility with 30 keV ^{24}Mg at fluence of $1x10^{12}$ cm^{-2} on two different areas under two different conditions: at room temperature and under in-situ annealing at 800 °C. The room temperature implantation was the annealed for 20 minutes at 800 °C to promote the creation of optically active MgV defects, the in-situ annealed area did not underwent further annealing treatments. As depicted in the Figure, the spectra display identical features: sharp peak at 557 nm, intense peak at 572 nm originating from the Raman scattering with diamond and a set of smaller bands at 575 nm and 600 nm and 650 nm attributed as phononic replicas. A more detailed PL analysis is discussed in the following paragraph, the most relevant aspect of this discussion is the activation of MgV defects under the same experimental conditions of the EC analysis, hence directly linking with the EC structural characterisation with the PL signal originating from the Mg implantation.

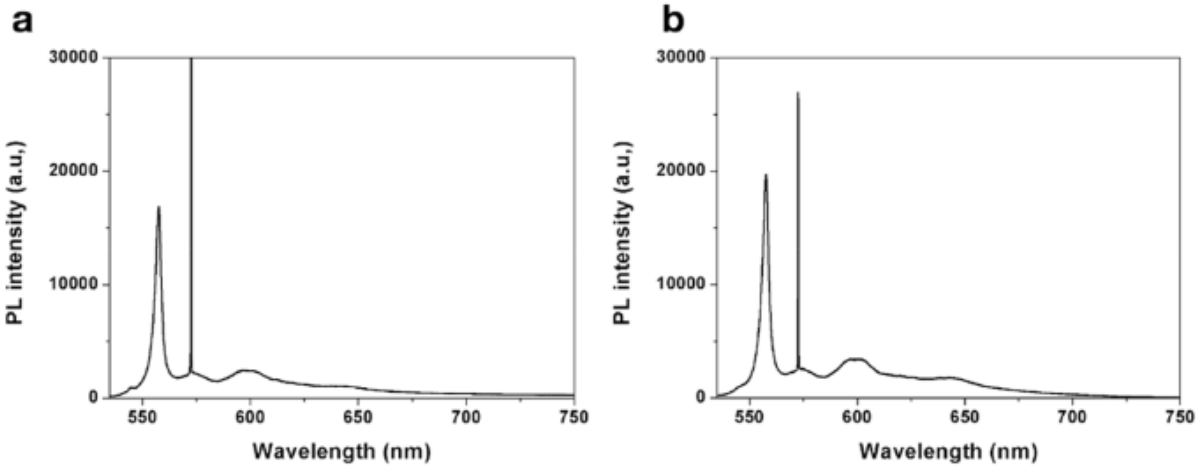


Figure 4.2.3 PL spectra acquired at room temperature with a 532 nm excitation laser from a ultrapure "electronic" grade sample. The implantation is performed at CERN Isolde facility with 30 keV ^{24}Mg with a fluence of $1x10^{12}$ cm^{-2} . a) room temperature implantation spectrum after 20 minutes annealing at 800 °C. b) Spectrum acquired on the in-situ annealing at 800 °C implantation.

4.2.1.2 Optical characterisation of MgV colour centre

A type IIa sample (labelled as sample 5) from ElementSix was adopted for the analysis of the MgV optical properties. Two regions 200x200 μm^2 are implanted with Mg^+ with fluencies of $1x10^9$ cm^{-2} and $1x10^{12}$ cm^{-2} at the IMBL Laboratory (KU Leuven). The sample underwent to 2 hours furnace thermal annealing firstly at 500 °C and secondly at 1200 °C and pressure < 10^{-6} mbar. After the thermal treatment, it was performed an oxygen plasma to remove eventual organic contaminants and graphite mixed phase from the surface. To perform the PL characterisation different CW lasers were adopted in the range from 405 nm to 532 nm. It was carried out a systematic ensemble analysis at room temperature and cryogenic temperature. Finally, the single emitter level analysis was performed to evaluate the opto-physical properties of the defect. Different custom confocal microscopes were used to perform the characterisation here presented. The analysis carried after the first annealing at 500 °C had the aim of understanding the proper thermal energy to activate the MgV defect. No single defects were observed after the first annealing, hence a second one at 1200 °C was performed. The PL spectra shows similar features: a first peak at 557 nm, a set of two small bands at 575 nm and 600 nm and a second peak at 741 nm corresponding to the GR1 peak (the neutral vacancy). The intensity of the main signals, i.e. 597 nm and GR1 peak, correlate as function of the fluence. The lower GR1 peak in the low fluence region with respect to the high fluence region signifies that a rather larger number of vacancies are present in the crystal and that the annealing temperature is not sufficient enough to restore completely the lattice (as expected for temperature lower than 700 °C [140]). The 597 nm signal correlates better in terms of intensity meaning that the temperature is sufficient to start activating the MgV complex, in fact for the low and high fluence cases, the relative intensity of the peak is identical.

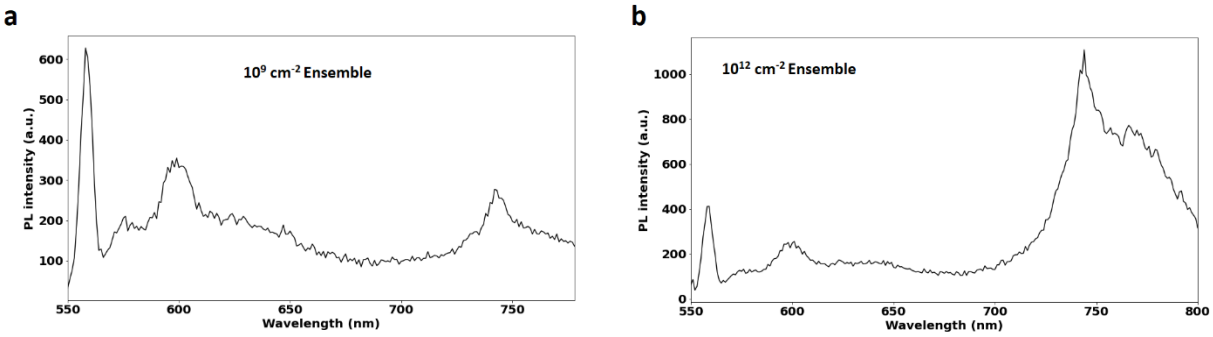


Figure 4.2.4 PL spectra acquired at the ensemble level in the low (10^9 cm^{-2}) and high (10^{12} cm^{-2}) fluence regions.

In Figure 4.2.5 it is reported a set of spectra acquired under different conditions and excitation wavelengths displaying the most relevant features observed for the MgV defect. Particularly, Figure 4.2.5a shows the PL spectrum at room temperature of the $1x10^{12}$ cm^{-2} ensemble under 532 nm excitation. In Figure 4.2.5b the spectra acquired under 522 nm excitation are shown in the temperature range from 5 K to 290 K.

The most relevant optical features are the following:

- A weak line at 544.8 nm (labelled as P_0). Such line is reported also in Mg-implanted diamond in ref [175], but is observed only in a sample region co-doped with P ions, while here it is observed for the undoped sample.
- A sharp line at 557.6 nm attributed as ZPL of the MgV defect [80], [140], [175], [237].
- A sharp line at 572.8 nm associated with the first order Raman scattering of diamond under 532 nm excitation.
- A set of smaller bands in the range 560 nm to 650 nm labelled as (P_1, P_2, P_3). These bands are attributed to phononic replicas of the MgV defect [237].
- A sharp peak at 608.3 nm (labelled as L_1). Such optical feature agrees with the theoretical report in ref [237] but it is only observable for low temperature (up to 200 K). The ab-initio model in ref [237] attributes such spectral line to a weakly-allowed transitions between the $^1A_{1u}$ to ^2E_g levels, as depicted in Figure 4.2.5c.
- A set of two smaller bands (labelled as L_2 and L_3) at 619.5 nm and 625.3 nm are tentatively attributed as phononic replicas of the L_1 feature.

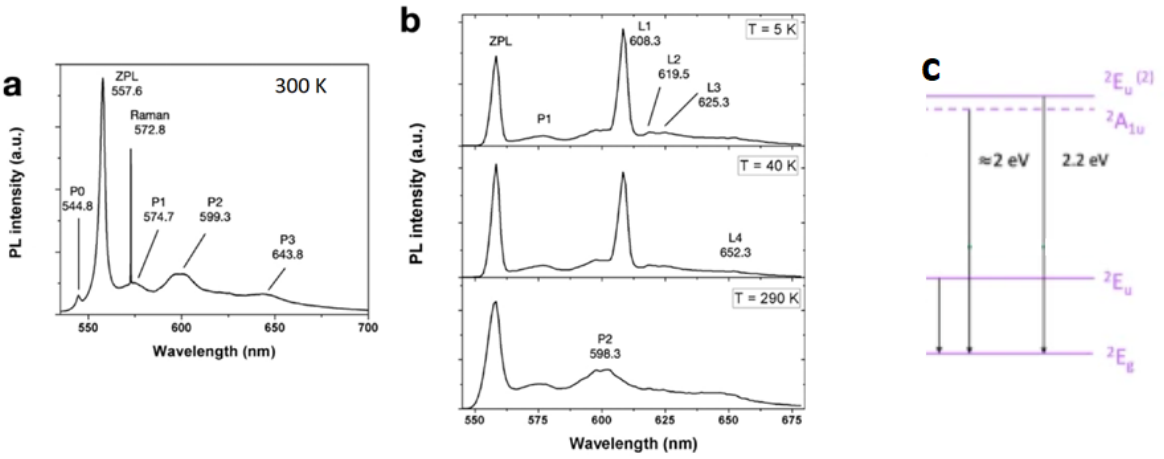


Figure 4.2.5 a) PL spectra acquired on the 10^{12} cm^{-2} implanted region under 532 nm excitation. b) cryogenic temperature analysis (5 K to room temperature) on the same ensemble of a) under 522 nm excitation. c) Energy diagram of the MgV defect from the ab-initio model from ref [237]*. The ZPL corresponds to the $^2E_u^{(2)}$ to ^2E_g levels, the L1 features corresponds to the $^1A_{1u}$ to ^2E_g levels.*

While the ZPL at 557 nm, along with the replicas $P_{1/3}$, were already reported in the scientific literature in refs [140], [175], [239], the L_1,L_2 and L_3 spectral lines observed at cryogenic temperature have not been reported in the scientific literature so far under any experimental framework and they are observed in this work for the first time. In ref [237] the L_1 spectral line is predicted by ab-inito models at an energy of ~2 eV, thus displaying good agreement with the experimental data. The expected transitions are between the $^1A_{1u}$ to ^2E_g levels. The lack of emission at room temperature of the L_1 line is explained by the fact that a weakly allowed transition. From the energy diagram reported in ref [237] it is calculated a shift of ~185 meV between the excited state of the ZPL and the L_1 transition (assuming the same ground state for both) and possibly the

quenching of the L_1 line is due to phonon-assisted processes at room temperature, similarly to the emission process involving the A and B lines of the group IV emitters [76], [87], [89], [118].

To further understand the optical properties of the MgV defect, Figure 4.2.6 displays the temperature dependence of the ZPL as function of the measurement temperature. The model describing the shift of the ZPL position is based on two assumptions [240]: thermal expansion of the lattice and electron-phonon interaction. Typically, it is expected a redshift of the emission line as function of the temperature [121], [239] as a consequence of the contraction of the lattice parameter with the temperature decrease, thus corresponding to a strengthening of the chemical bonds and therefore an increase of the photon energy [241], [242]. Contrarily, the MgV ZPL temperature dependency displays an unusual behaviour. In fact, as depicted in Figure 4.2.6, the ZPL behaviour in the range 5-290 K displays a blue-shift, meaning that the ZPL shifts towards lower wavelengths for higher measurement temperatures (from 558.4 nm at 5 K to 557.7 nm at 290 K). Such observation is in agreement with ref [239], where a dedicated study of the ZPL position of the MgV complex was performed from room temperature up to 320 K.

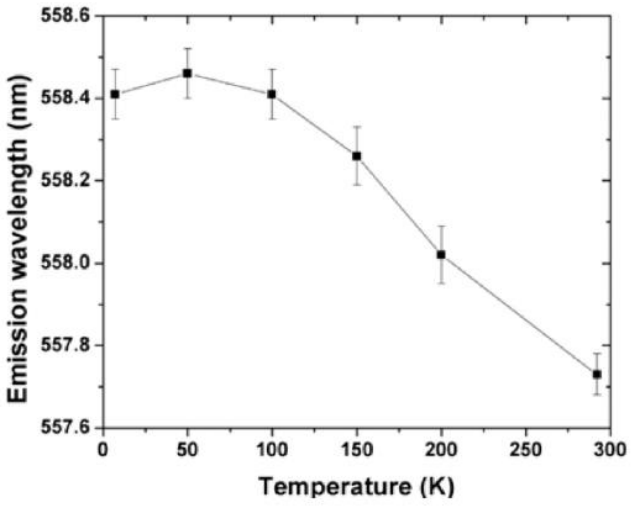


Figure 4.2.6 ZPL shift as function of the measuring temperature in the 5-290 K range.

The observed blue shift is tentatively explained owing to the ab-inito model in ref [237]. As depicted in Figure 4.2.5c, the ZPL is predicted to be an emission line doublet deriving from the ground state splitting (levels ^2E_u and ^2E_g). In Figure 4.2.7a it is reported from the ab-initio model of ref [237] the predicted energy levels within the diamond gap of the MgV defect. Figure 4.2.7b displays the predicted split of the ground state as function of strain. It indicates a decreasing separation in energy while augmenting compressive strain, hence at lower temperature. Such projection does not diverge with the FWHM of the ZPL displayed in Figure 4.2.5a (obtained at room temperature) of ∼3 nm which could be explained as a convoluted peak. High resolution cryogenic analysis as well as PLE spectroscopy are needed to further investigate such unusual behaviour.

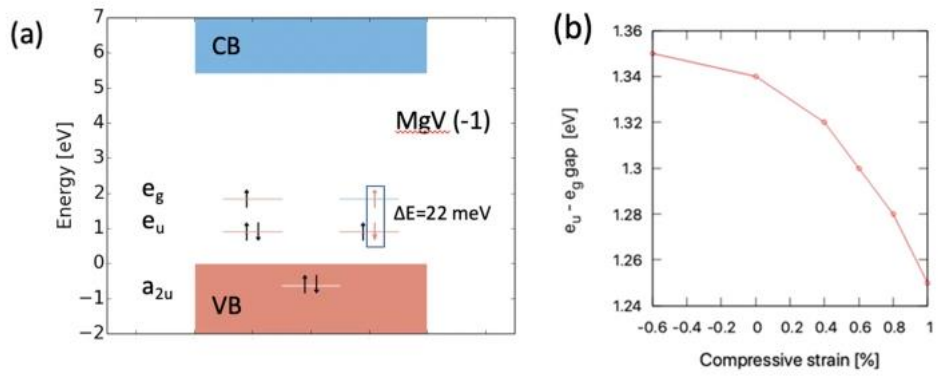


Figure 4.2.7 a) Band structure of the MgV complex in the diamond bandgap. b) Strain effects on the e_u-e_g levels.Figure from ref [237]

4.2.1.3 Ensemble characterisation: optical excitability of the MgV complex

To get further in details with the optical properties of the MgV complex, it was performed a systematic measurement campaign at the ensemble level. Four different CW excitation lasers were used, namely, 405 nm, 450 nm,490.5 nm, 509.5 nm, 522 nm and a PW supercontinuum white laser.

In Figure 4.2.5b three different datasets are reported: a) displays the optical analysis performed at the cryogenic temperature of 5 K under 405 nm, 490.5 nm and 522 nm excitation wavelengths; b) displays the identical analysis reported for a) at room temperature, with an additional laser excitation at 509.5 nm; c) in the graph a set of spectra are acquired under PW illumination ranging from 460 nm to 535 nm.

The reason for the choice of all the excitation lasers is two-folded. Firstly, a disambiguation in the observed spectral lines from the Raman-related features is needed. In this sense the occurrence of the ZPL, P_1-P_3 and the L_0-L_2 (at cryogenic temperature as discussed already above) under all the excitation adopted confirms the attribution of these spectral lines to Mg^+ implantation and disambiguate the lines from the Raman lines. In the following table, it is reported foreach adopted laser, the spectral filtering chosen to suppress the undesired spectral bands and the position of the first order Raman line.

The P_0 feature is mostly observed for shorter wavelengths excitation than 522, the reason behind this occurrence is the optical filtering adopted to suppress the laser line. In the case of the 509.5 nm laser, the P_0 feature is partially overlapped with the first order Raman. No direct comparison of the measured intensity of the ZPL was possible for the different lasers due to the different choice of the dichroic mirror employed for the 509.5 nm and for the 522 nm measurement (cutoff wavelength at 520nm/567 nm). Secondly, for 522 nm excitation the Raman line is partially overlapped with the ZPL and with the constraint of the spectroscopic system adopted (resolution 4 nm).

Secondly, the ionisation of the MgV complex could be probed with respect to probe excitation energy, offering in principle an attribution of the most relevant spectral lines to different emitting defects or charge states based on an excitation wavelength-dependent analysis. It is observed a decrease of the ZPL/L_0 ratio at increasing excitation wavelengths.

The decrease of the ZPL under excitation < 522 nm t is hypothesised to be related to a conversion of the charge states available for the MgV centre in the diamond gap towards optically inactive configurations [237]. The inability to observe isolated emitter in the range 405 nm-509.5 nm further validate this hypothesis.

To explore in more detail the optical excitability of the MgV defect, it was performed a non-resonant PLE measurement with a PW supercontinuum white laser in the wavelengths from 460 nm to 535 nm. The laser power is kept constant at 50 µW on the sample surface with a fixed bandwidth of 10 nm. Each acquired spectrum, shown in Figure 4.2.8a, is background subtracted (a spectrum is acquired in the pristine area of the sample under the same experimental conditions). The integral of ZPL confirms the higher excitability in the range of 520 nm as suggested by the above-mentioned measurement. The latter analysis indicates that the

522 nm excitation is the most suited to efficiently excite the MgV complex. The quasi-resonant Raman excitation is in perspective, a useful resource to boost the ZPL intensity of the MgV colour centre and coherently control the single emitters with cost effective laser diodes [243].

It was performed a non-resonant PLE analysis to evaluate the maximum excitability of the MgV complex. In Figure 4.2.8a it is reported the set of spectra acquired on the 10^{12} cm^{-2} ensemble under different excitation wavelengths. The spectra were acquired using a supercontinuum PW white laser tuned at wavelengths ranging from 460 nm to 535 nm. The spectra show clearly a decreasing trend for the whole emission. It was then fitted the ZPL with a Gaussian curve and plotted as function of excitation wavelength, as displayed in Figure 4.2.8b, to better evaluate the excitability of the MgV complex. From the Figure it is observable that a maximum appears at a wavelength of ~520 nm. It is worth remarking that due to the spectroscopic constraints (~ 4 nm resolution), the ZPL partially overlap with the first order Raman peak. Hence, the measurements were subtracted to the spectrum acquired in an implanted area to deconvolute the MgV signal from the Raman signal.

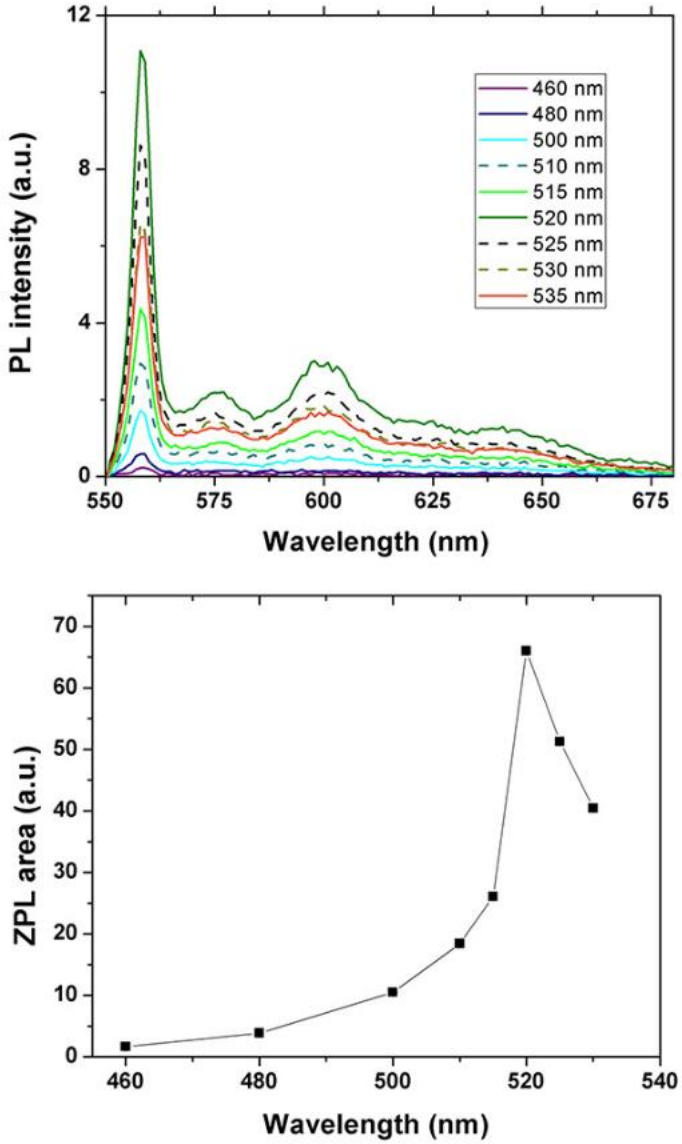


Figure 4.2.8 a) Non-resonant PLE spectroscopy of the MgV ensemble ranging from 460 nm to 535 nm. The spectra are acquired with an optical power of 50 µW on the sample surface. d) ZPL peak as function of excitation wavelength.

As final discussion, to validate the optical excitability performed at room temperature it was performed an analysis with a 450 nm laser the edges of the 10^{12} cm^{-2} ensemble to locate possible single emitters. In Figure 4.2.9 two confocal scans are reported. The same maps were acquired with an excitation wavelength of 450 nm and an optical power of 0.6 mW in a time interval of 10 minutes. It is indeed observable the ionisation of the defects and therefore no single emitter analysis was performed with other excitation than 522 nm. Such observation is in good agreement with what observed at ensemble level.

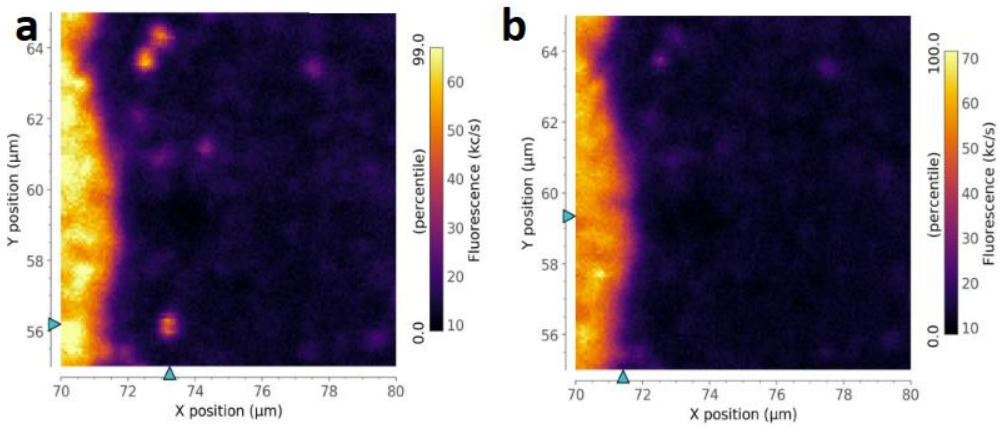


Figure 4.2.9 PL scan acquired under 450 nm excitation laser with an optical power of 0.6 mW. a) and b) are acquired within 10 minutes interval.

4.2.1.4 Single emitter analysis

The above-mentioned analysis suggested to perform the measurements at the single emitter level adopting the 522 nm excitation. The edges of the region implanted with a fluence of 10^{12} cm^{-2} were scanned to locate individual emitters both at room and cryogenic temperature. It was performed a systematic characterisation by means of a scanning system, the Hanbury-Brown & Twiss interferometer and finally, the PL spectrum of the candidate as single emitter is acquired.

Figure 4.2.10 displays the analysis performed on an individual emitter (circled in white). The PL spectrum (in Figure 4.2.10d) is background subtracted (i.e. it was subtracted the signal not originating from the emitter) and it matches with the ensemble characterisation performed previously. The second order autocorrelation function $g^2(t)$ is shown for various excitation power, it is visible a bunching behaviour indicating the defect can be described by a three level system. The $g^2(t)$ is background subtracted and for t -> 0 the minimum is well below 0.5 meaning that the emitter analysed is indeed single. The absence of datapoints in Figure 4.2.10b-c is due to the removal of the backflash peaks to correctly fit the experimental curve, as discussed in Chapter 3.4.

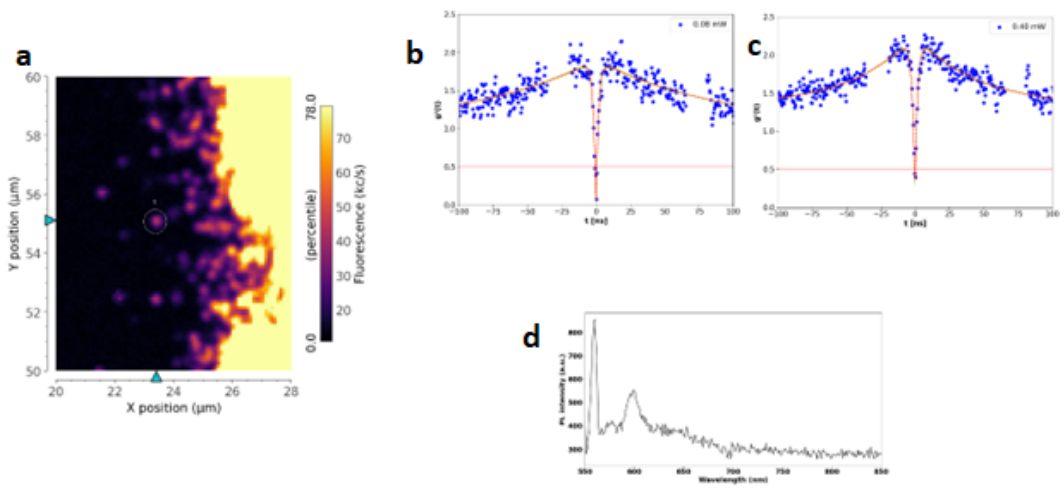


Figure 4.2.10 a) PL scan of the edges of the implanted region, the white circled spot represents the analysed emitter. b) and c) Second order autocorrelation functions for different optical power. The missing data points are due to the subtraction of the backflash peaks generated by the fiber coupled HBT interferometer c) Spectrum background corrected of the emitter circled in white. The measurements are acquired with an optical power of 80 and 400 µW respectively for a and b.

The plot in Figure 4.2.11 represents the fitting curve of the parameter λ which was obtained as discussed in Appendix I. The fitting procedure yields a value for the excited state lifetime (λ_1(P=0)) is (2.1 ± 0.3) ns, the fitting curve is shown in Figure 4.2.11

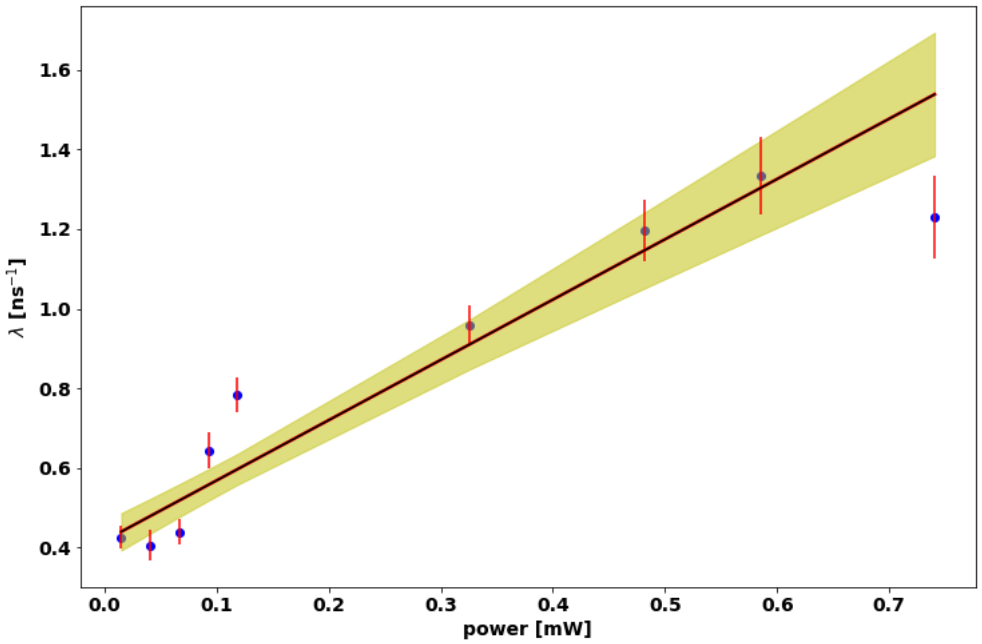


Figure 4.2.11 Linear fit of the λ parameter, the intercept represents the inverse of the excited state lifetime of the analysed defect.

Different emitters were characterised to perform a statistical analysis on the excited state lifetime as well as the saturation intensity and saturation power. This analysis is shown in Figure 4.2.12. Particularly, in Figure 4.2.12a the distribution obtained for 15 different emitters is shown, the mean value is in good agreement with what reported in literature [140], [237], i.e. ~2.4 ns. For each individual emitter analysed a different saturation curve was acquired, in Figure 4.2.12b it is displayed only a set of four curves that are a subset of

what obtained. Particularly, the curves reported shows a rather large variability of the fitted parameters. Due to the adopted experimental setup, the saturation intensity cannot be regarded as a reliable estimation of the proper intensity of the MgV^- colour centre. In fact, the ZPL was partially filtered out by the 567 nm cutoff dichroic mirror but despite this particular constraint, the brightness of the defect is ranged in the Mcps which makes this defect a promising candidate as SPS. Contrarily, the saturation power was estimated in the range comprised between (0.87 ± 0.09)–(2.7 ± 0.4) mW.

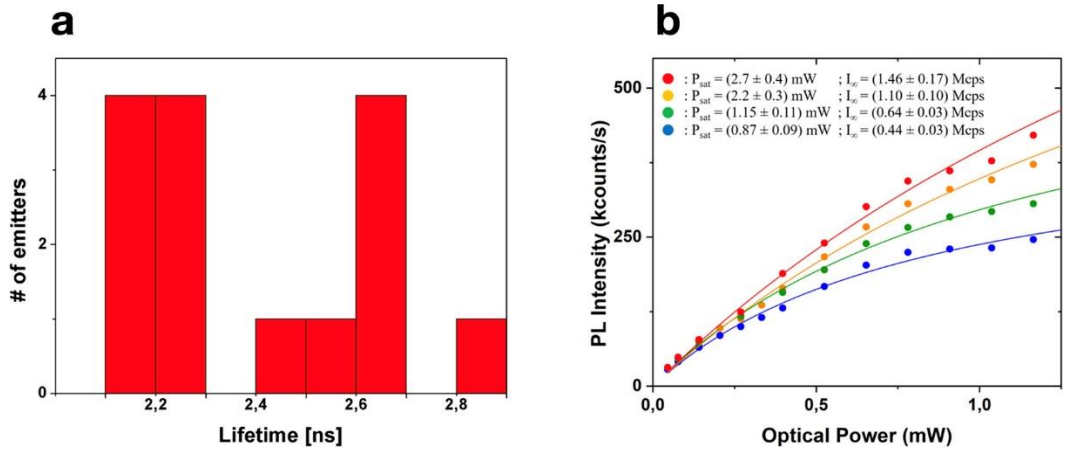


Figure 4.2.12 a) Distribution of the excited state lifetime of 15 different single emitters. b) Saturation curves for 4 emitters under the same experimental conditions. The background was subtracted for each of the presented curves. In the legend the fitting parameters are presented.

An identical characterisation at cryogenic temperature is reported here for a different exemplary emitter. In Figure 4.2.13 the main results of the optical characterisation are reported. From a spectral point of view, it was only observed the ZPL emission at 557 nm without the L_0 line was observed. The validation as single emitter of the analysed source is granted by the function $g^2(t)$. The obtained excited state lifetime is (2.8 ± 1.1 ns).

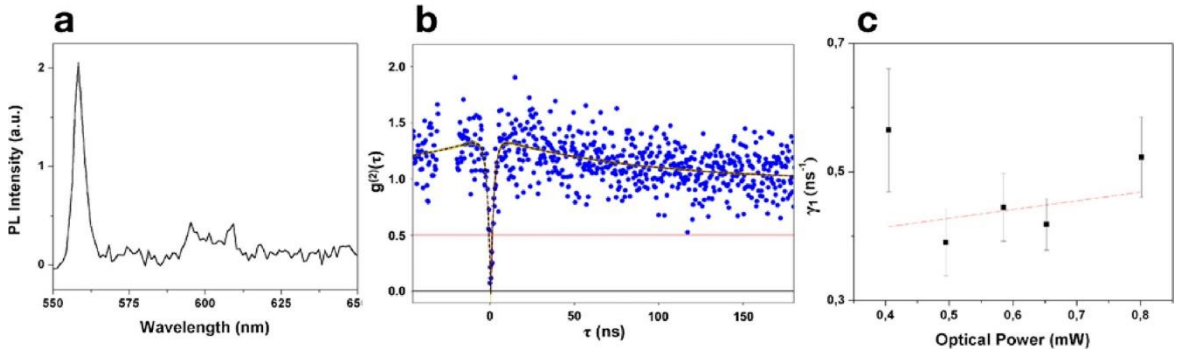


Figure 4.2.13 Cryogenic characterisation of a single emitter at 7 K. a) Pl spectrum (background subtracted) under 4.6 mW optical power. b) Second order autocorrelation function acquired for the same emitter (0.7 mW optical power). c) γ_1 parameter plot

4.2.2 Fluorine-based colour centre in diamond

As already mentioned in Chapter 1.3.2, Fluorine-based emitters in diamond are of recent discovery [140]. The F-related colour centre displays a rather intense PL ensemble spectrum ranging from 600-750 nm as shown in Figure 4.2.14a. The systematic PL characterisation of F-related ensembles is presented here both at room and cryogenic temperature under different excitation CW wavelengths. The cryogenic temperature measurement permits to reveal a structured sequence of lines in the range 600-670 nm (Figure 4.2.14b). Finally, the correlation as function of fluence strongly lead to unambiguously attribute the observed spectral feature to the F-related complex.

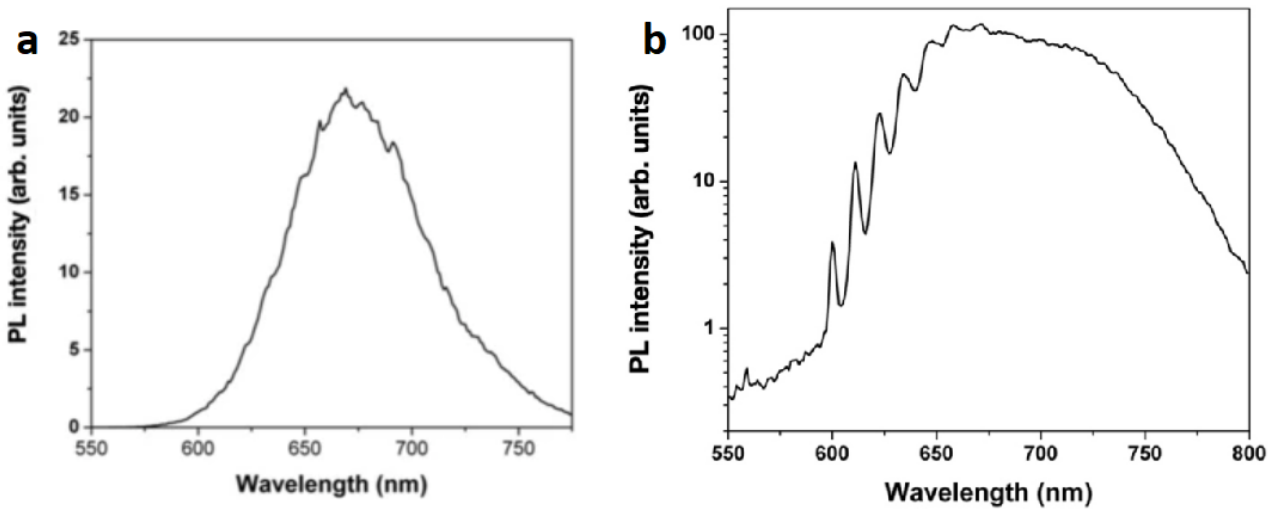


Figure 4.2.14 a) PL spectrum of 1.47 MeV F^{2+} ensemble region under 522 nm excitation. b) cryogenic PL spectrum acquired at 4.5 K under 490.5 nm excitation from the implanted ensemble at 5x10^{13} cm^{-2} with 50 keV energy. The optical power on the sample surface is 3.6 mW. Both spectra were acquired on sample 6.

4.2.2.1 Experimental

The sample (labelled as 6) adopted in this work is a "electronic grade" type IIa single crystal from Element Six. Sample 6 underwent Fluorine implantation at two different facilities: the university of Leipzig (for the keV implantations) and the Laboratory for Ion Beam Interactions of the Ruđer Bošković Institute (for the Mev implantation). Several regions with ~ 175 µm diameter were implanted with 50 keV F^- at different ion fluences, ranging from 5 x 10^{10} cm^{-2} to 5x10^{15} cm^{-2}, and an additional area was implanted with 1.47 MeV with F^{2+} ions at a fluence of 1 x 10^{13} cm^{-2}. A single region was implanted with C^- ions at a fluence of 5 × 10^{15} cm^{-2} with an energy of 35 keV.

Sample 6 underwent a furnace thermal annealing at 1200 °C for 2 hours in high vacuum regime (pressure < 5x10^6 mbar) and an oxygen plasma treatment to reduce possible fluorescent contaminants on the surface.

A second nominally identical control sample (sample 7 in the following) was implanted with Nitrogen at the ANSTO *Centre for Accelerator Science* with N^+ ions at an energy of 10 keV and a fluence of 1 x 10^{14} cm^{-2}; sample 7 underwent 2 hours at 950 °C annealing under the same pressure conditions of sample 1.

The spectral characterisation was performed using different setups: a micro-Raman confocal microscope equipped with 532 nm excitation laser; a custom single-photon sensitive confocal microscope equipped with three different excitation wavelengths (405-490.5-522 nm respectively). The spectral resolution of the custom confocal microscopes was estimated to be 4 nm based on the FWHM of the first order Raman peak measured. Finally, it was adopted a closed-cycle the same optical cryostat to characterise the PL ensemble over the 4-300 K range.

4.2.2.2 Room temperature characterisation

A PL analysis was performed acquiring with emphasis of the spectral emission at the ensembles level, aiming at correlating the observed spectral features for all the implanted regions. In Figure 4.2.16 it is reported a set of spectra showing the main spectral feature of the F-related implanted areas. Figure 4.2.16a shows the overlay of the different keV implanted ensembles: the black curve represents the pristine region of the sample while the other colours the different ensembles fabricated at increasing ion fluence. It is visible the increase in the PL intensity with the increase of the ion fluence, indicating that it is correlated with the concentration of F ions. In Figure 4.2.16b it is highlighted the comparison of the low fluence implanted (5×10^{10} cm^{-2}) area with a Carbon implanted region with the aim of unambiguously attribute the measured PL feature in Figure 4.2.16a to the Fluorine ion implantation.

The main signal from the F-related complex is an intense band ranging from 560 nm to 800 nm, in good agreement with ref [140]. No particular feature is observable in the spectra. To rule out an attribution of the PL spectrum to an intrinsic defect, it was implanted a region with 35 keV C^- at a fluence of $5x10^{15}$ cm^{-2}. In Figure 4.2.16b it is reported the overlay of the high fluence F region and the C region acquired under the same experimental constraints, the spectra are normalised over the first order Raman peak. Clearly visible for both spectra are the peaks related to the first and second order Raman, while the black curve displays a weak band centred at 640 nm the green curve shows an intense band centred at 670 nm. This comparison indicates that the F-related PL signal is not originated from the Nitrogen content of the sample or from residual damage due to ion implantation.

The F-related emission has significant overlap with the NV signal and to disambiguate the attribution to the latter, it was performed a characterisation of a second sample implanted with Nitrogen and directly compared the ensemble intensity. The comparison was made on the high fluences implanted regions of F-related ($5x10^{13}$ cm^{-2}) and the NV implanted region (10^{14} cm^{-2}) under the same experimental constraints, i.e. 490 nm excitation laser, 2 mW of optical power and spectral filtering with a long-pass 500 nm. The intensity of the F region was evaluated to be 5.4 Mcps and the NV region 3.2 Mcps. Despite the factor 10 in the fluence, the F region is 1.7 time brighter with respect to the NV one.

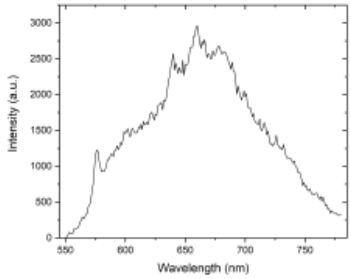


Figure 4.2.15 NV spectrum acquired on sample 7 under green excitation (522 nm) and an optical power of 10 mW.

Despite the assumptions, the result cannot be strictly related to the relative intensity of the individual Fluorine defect, the formation efficiency of such complex is not determined in this work and it is out of the scope as well. The brightness of the F region with respect to the NV region cannot be addressed directly since the N^+ region is implanted at a fluence close to the saturation [244]. Thus, considered that the F region is at saturation as well leads to an estimation of 1.7x brighter respect to the NV one. Conversely, if the assumption of a full linear dependence of the PL signal for both classes of defects is valid, the different fluences are to be taken into account and therefore the brightness ratio between the F and NV region reaches a value of ~15. In

a realistic frame, the estimation discussed here can be seen as boundary values for the brightness comparison.

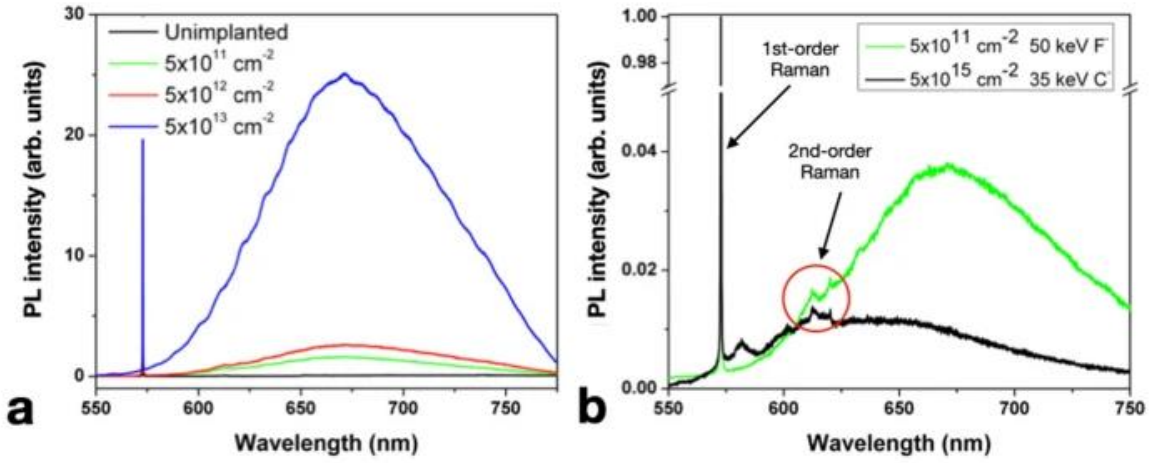


Figure 4.2.16 a) PL spectrum of the ensembles implanted with 50 keV F^- ions, the black curve represents the pristine region. The spectrum is acquired under 532 nm excitation and an optical power of 26.2 mW. b) Overlay of C^- and F^- implanted areas. In the legend the key parameters are reported such as fluence and energy. The spectra are normalised on the first order Raman peak and both the first and second order peaks are highlighted.

A zoom of the low intensity s reported in Figure 4.2.17. A weak but consistently visible peak at 558 nm is visible at fluences above 5×10^{12} cm^{-2}. The 558 nm feature is not observable in the C implanted test area, while it could be compatible with the 557 nm peak observed in cathodoluminescence from an electron irradiated sample and attributed to an interstitial-type defect [49], [245] it is reported to anneal out above 700 °C [246]while the analysed sample underwent 1200 °C thermal treatment. Moreover, no similar signature is reported in previously reported works on C-implanted areas [247]. A tentative attribution of the 558 nm feature is that to be related to the F ion implantation rather than other impurities despite no clear correlation is observed with the intense band centred at 670 m based on the available dataset.

It is worth mentioning that the ensemble characterisation at room temperature was also performed with the sample implanted with 1.47 MeV F^{2+} ions. As shown in Figure 4.2.14a, the PL signal displays the same spectral features of the keV implanted ensemble contributing to the attribution of the spectral features to be F-related. Moreover, it shows the possibility of fabricating both at keV and MeV regime the Fluorine complex with possible different creation yield (a purpose which is beyond the scope of the present work) and not to intrinsic lattice impurities related to the MeV implantation. It was not performed a comparison in the PL signal between the MeV and keV implanted ensembles since the PL spectrum in Figure 4.2.14a was acquired under different experimental conditions.

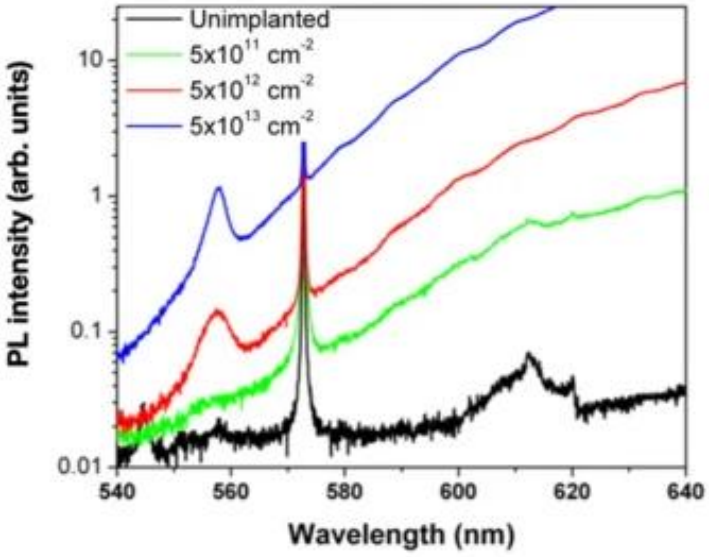


Figure 4.2.17 Zoom of the spectral range 540-640 nm to focus the attention on the 558 nm peak. The peak becomes more visible above the $5x10^{11}$ cm^{-2} implanted region.

4.2.2.3 Cryogenic characterisation

To further understand the structure and the emission lines convoluted in the broad emission band of the F-related complex, it was performed a systematic analysis at cryogenic temperature under different experimental conditions, namely excitation wavelengths over different temperatures.

Figure 4.2.14b displays the PL spectrum acquired on sample 6 at 4.5K under 490.5 nm illumination on the ensemble implanted at $5x10^{13}$ cm^{-2} with 50 keV energy. The spectrum displays a distinguishable set of peaks, namely: 600, 611, 623, 634, 647, 658 and 671 nm. The spectral resolution of the adopted setup is 4 nm and therefore the width of the signal are limited by this experimental constraint.

The lines are spaced in energy of (36 ± 5) meV. This observation enables one to consider the 600 nm line as ZPL of the F-related complex, thus, the energy shift is in agreement with an electron-phonon coupling falling in the 10-100 meV range [78]. It is worth mentioning the occurrence of the 558 nm peak also in the low temperature regime as shown in Figure 4.2.14b. Its attribution is again unclear since it cannot be attributed as ZPL of the emission band discussed here, since the energy difference with respect to the 600 nm is (150 ± 5)meV .

In Figure 4.2.18 two sets of spectra are reported for excitation wavelengths of 405 nm (acquired at 10 mW optical power), 490.58 nm (acquired at 2.1 mW optical power) and 522 nm (acquired at 2.4 mW optical power). The absence of datapoints above 700 nm for the spectra acquired under 405 nm illumination are due to filtering adopted to cut the fluorescence originating from the optical components of the confocal microscope. The spectra at cryogenic temperature are acquired at 4.5 K and they all show similar features, i.e. the same set of aforementioned emission peaks in the 600-650 nm range. The spectrum acquired under 488 nm illumination also displays a secondary band centred at 710 nm, not observed in the previous analysis under green excitation [140]. The observation of the same PL signatures between the 4.5 K and room temperature under the different illumination regimes are persistent and this indicates that the observed features are not Raman-related. The observed sequence of peaks in the 600-650 nm range cannot be attributed to particular interference processes originated from internal reflections since they are not visible

at room temperature and, moreover, the implanted fluence is low enough to avoid occurrence of such phenomenon [248].

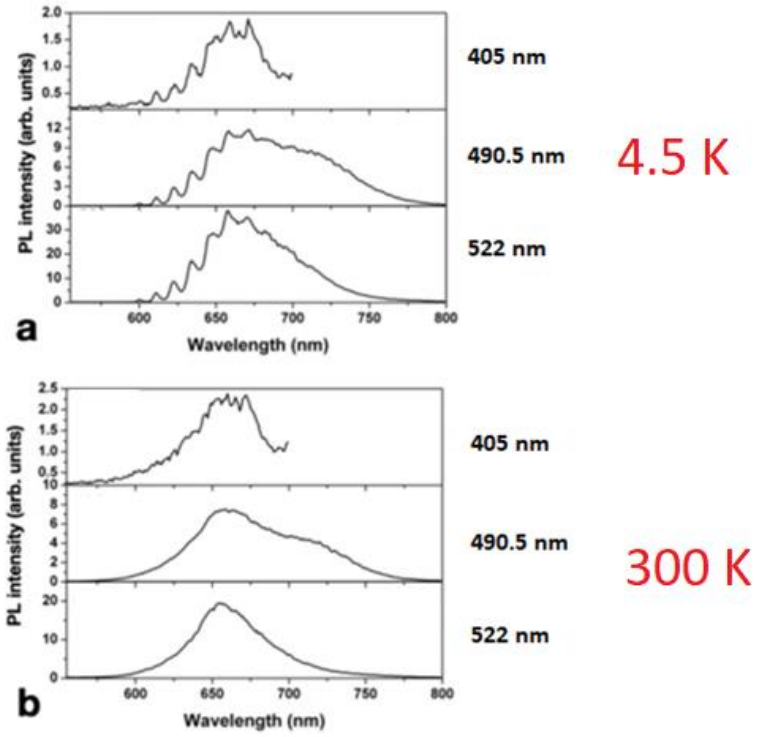


Figure 4.2.18 Ensemble PL spectra acquired under different excitation wavelengths as highlighted in the legend. a) 4.5 K dataset. b) room temperature dataset.

A systematic temperature-dependent analysis on the higher fluence keV ensemble was acquired under 490.5 nm excitation to further evaluate the presence of the secondary band centred at 710 nm observed in Figure 4.2.18. The aim of this analysis is to evaluate the occurrence of eventual optical distinguishable features originating from this band. The outcome of the analysis is reported in Figure 4.2.19, the temperature range is between 4.5 K and room temperature. No visible trend is observable between the two main bands object of this investigation, but it is clear the presence of the above-mentioned spectral lines in the range 600-650 nm. The widening of such features in the temperature range 4.5-160 K further confirm their attribution as phonon sidebands of the hypothesised ZPL at 600 nm. Further investigations are required to evaluate the internal structure of the secondary band located at 710 nm.

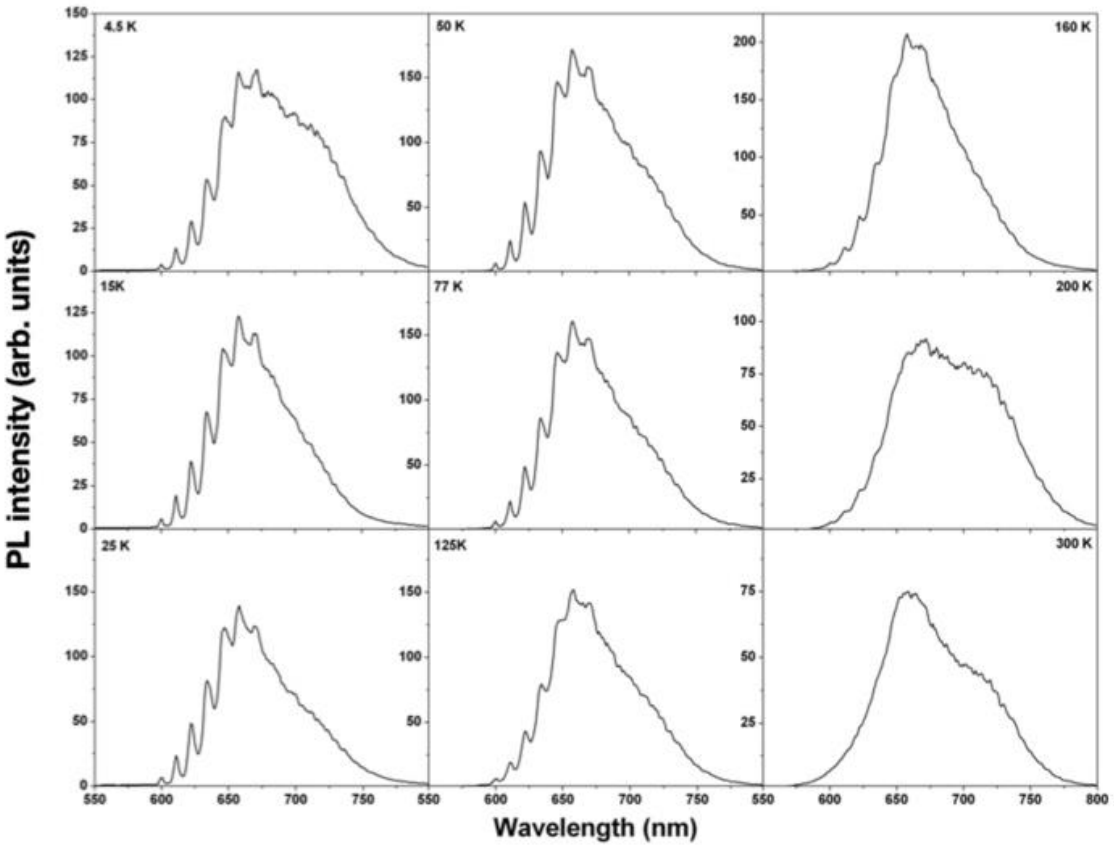


Figure 4.2.19 Temperature dependent PL spectra ranging from 4.5 K to 300 K of the F ensemble acquired under 490.5 nm excitation and an optical power of 2 mW from sample 7.

The inability of observing it under 405 nm excitation makes it not directly attributable to alternative different charge state, as for the NV centre. If otherwise confirmed, the secondary band would be associated to a higher excitation energy with respect to the main emission band stemming lower photon energy. This hypothesis would lead to the occurrence of indirect transitions or non-radiative processes in the deexcitation process that can be evaluated only at single photon emitter level.

5 Summary and discussion

The Dissertation was centred on the fabrication and more specifically characterisation of different colour centres in diamond, both alternative to what is reported in Literature so far (MgV and FV) as well as to further explore the known ones (SnV and PbV). The results obtained can be divided hence in 2 sections. The third section include the description of the installed ion implanter at the Department of Physics of Torino.

1. Characterisation and processing methods to explore the optical properties of group IV defects in diamond.

The fabrication of SnV and PbV defects in diamond was reported. The study at the single emitter level of both defects could pave the way for their practical implementation in Quantum Information Protocols (QIP), which is currently limited by different fabrication drawbacks. The present works contribute to a better understanding of the tunability of the SnV optical lines and the of the optical properties of defects related to large ion masses with ion implantations such as Pb. Furthermore, the formation mechanism related to defects involving large mass ions such as Sn, Pb via ion implantation is of crucial interest. Different fabrication strategies could be put in place to provide a thorough understanding of the optical properties of group-IV colour centres, including an unambiguous attribution of the optical lines associated between the ensemble and the single emitter level. In the dissertation, two different fabrication mechanisms were discussed. The main activity discussed is a robust optical characterisation at both ensemble and single emitter level.

The study on SnV defects reports the optical characterisation of SnV single emitter under different surface treatments conditions. More specifically, it was demonstrated the possibility to tune the main emission lines typically observable at ensemble level with oxygen functionalisation. Moreover, it was shown that the functionalisation could enhance the tunability of the 620 nm lines (referred as SnV^- in literature) with respect to no surface treatments (after O treatment, 40% of the lines shifted to 620 nm with respect to the as-annealed case where only 10% of the emitters had PL signal at 620 nm). It was demonstrated for the first time the compresence of multiple lines within the same single emitter level further improving the research towards a clearer understanding of the different spectral lines. Hence, the surface chemical functionalisation of bulk diamond was demonstrated to offer a useful method to tune the optical lines of SnV and Sn-related spectral lines, making the fabrication of devices simpler with respect to challenging thermal treatments such as HPHT annealing.

The research on the PbV defect was made under different thermal treatment conditions, firstly the optical lines associated to the PbO_2 implantation were analysed after LPLT annealing and under different experimental conditions (namely different excitation wavelength and both at room and cryogenic temperature). A set of single emitters were observed with no clear trend with respect to the ensemble spectral lines. Different emitters were observed having a clear counterpart in the ensemble characterisation and tentatively attributed as possible different charge state or different emitter associated to different configuration of Pb-related defects.

The HPHT treatment is still considered the best option to fabricate indistinguishable PbV^- colour centres [128], yet the attribution of optical transitions associated with the PbV defect as unique is still non-trivial. The second part of the work presented here provides a useful reference for the understanding of the optical lines associated PbO_2 ion implantation in diamond and investigates their origin as a function of the HPHT annealing. More specifically, it was observed a set of features (at 517 nm, 590 nm and 630 nm) already reported in literature, and further explored as function of various experimental conditions. The bulk sample was also analysed in the non-implanted regions to both understand the effects of the harsh HPHT treatment on the bulk itself and to disambiguate spectral lines reported in literature. In fact, different spectral features were observed in both the implanted ensemble and the non-implanted region enabling a clearer insight of the PB-related spectral lines with respect to other impurities. Afterwards, a robust single emitter characterisation was performed to evaluate the occurrence of these lines as single photon sources. As future step to fabricate

PbV defects, it would be necessary to explore the implantation under in-situ annealing. Heating the substrate during the implantation would be beneficiary to make the vacancies migrate while implanting, possibly enhancing the creation yield of the defects.

2. Characterisation of alternative defects in diamond

The exploration of novel colour centres in diamond is an ongoing quest. With the purpose of isolating single emitters displaying appealing QIP or sensing, two classes of emerging defects were characterised. In this Dissertation, namely Fluorine- and Magnesium- based ones.

Particularly, the MgV colour centre displays interesting properties, including a high Debye Waller factor, a theoretically predicted ZPL splitting which is compatible with its temperature-dependent blue-shift, short-excited state lifetime. The corroboration of the photoluminescence analysis carried here by a structural analysis with the EC technique permitted to evaluate the accuracy of the theoretical predictions from ab-initio model. A robust characterisation was performed under different experimental constraints (cryogenic to room temperature and various excitation wavelengths) with the aim of exploring the opto-physical properties of MgV defects. At cryogenic temperature it was reported a novel spectral feature predicted in ab-initio models (a spectral line at 607 nm with 2 phononic replicas at 619 nm and 625 nm) but only at ensemble level. Further dedicated study is necessary to evaluate their occurrence at single emitter level and evaluate their opto-physical properties. To further pursue a more complete understanding of such spectral line, it would be interesting to perform a characterisation at cryogenic temperature to isolate a single emitter with the abovementioned spectral line.

A solid optical classification of the Fluorine-related defect is reported for the first time in this Dissertation. The FV was studied under the same experimental constraints discussed for the MgV defect with the aim of distinguish the main optical features of the defect. No single emitter characterisation was possible due to the experimental constraints and moreover, to the similarity with respect to the NV defects. To unambiguously attribute the PL signal observed, different fluences were implanted in the keV energy regime and confirmed also at MeV energy. The technological interest of such defect is yet to be explored. As future investigation might be related to the study at single emitter level and possibly probe such defect to external electromagnetic fields to evaluate its use as sensor. In fact, the FV complex has a PL signal two-fold higher with respect to the NV and if it is indeed ODMR active could lead to higher signal and possibly sensitivity.

3. Development and setup of the 100 keV ion implanter

The development of the multi-elemental ion implanter performed during the PhD activities is of strategical importance for the pursue of fabricating colour centres in not only diamond, but also in other classes of materials such as Silicon, Silicon Carbide and wide band-gap semiconductors. Ion implantation offers a versatile method to incorporate different chemical species in semiconductors, hence enabling the fabrication of different classes of emitters. The fine tuning of the machine performed both at the hardware and software side, combined with the design and installation of a dedicated irradiation chamber, has the potential to become a strategical result for the achievement of deterministic ion implantation techniques. The construction started at the beginning of the second year of the PhD and the first beam extraction test was at the end of it. The full integration of the components and test the equipment and parameters (such as vacuum, perform the calibration of the mass spectrometry magnet, the building and development of the irradiation chamber) was an activity that was carried during the third year and therefore it was not possible to use the accelerator for the analysed samples. It was mainly employed for external users or collaborations that did not lead to any published scientific outcome at the moment of the writing of the dissertation. The goal now is to move towards a deterministic scheme of implantation via collimating masks adopting the IBIC technique for example (as discussed in Chapter 2.1.4). To achieve such aim, it is crucial to obtain an efficient method to count single ions within the target material and, via small aperture masks (diameters < 1 μm), to implant a specific number of ions per site to properly create single emitters in an organised pattern.

To summarise, this Thesis contributes to keep pushing the knowledge on opto-physical properties of quantum emitters in diamond, both on promising, yet widely investigated defects such as Group-IV based emitters, and on the discovery of the properties of novel classes of colour centres such as the MgV and the F-based systems. The fabrication of these classes of defects was achieved via ion implantation in different facilities. The installation and commissioning of a dedicated multi-elemental ion implanter at the Physics Department of the University of Torino, achieved with the contribution of the present PhD work, will perform dedicated studies on defect engineering at the solid state to perfect suitable fabrication strategies for different classes of SPSs.

6 Acknowledgements

As final step, I would like to thank the people that helped me and supported me both regarding the research and in general the activity that I carried during my PhD. I would like to thank Prof. Forneris for the opportunity and the support to achieve this Thesis, particularly for the patience regarding the correction of the different drafts and the teaching to improve my skills as scientific writer. Special thanks go to Dott. Ditalia Tchernij for the major help and the mentoring regarding the experimental activities along with the friendship outside the university walls. I thank Prof. Vittone for introducing me to the group suggesting me to pursue the research field of the diamond group led by Prof Olivero starting from my Master thesis and Prof. Picollo for teaching me some useful trick in the lab.

To my colleagues Elena, Vanna, Gabriele, Greta and Elisa goes my gratitude for listening to me and baring my thoughts both work-related as well as for the bond created outside the working environment.

Finally, I acknowledge my family and friends for the support during these years.

The project that funded the research activity performed during the PhD are here listed:

- “Departments of Excellence” (L. 232/2016), funded by the Italian Ministry of Education, University and Research (MIUR).
- The projects 20IND05 (QADeT) and 20FUN05 (SEQUME) leading to this publication have received funding from the EMPIR program co-financed by the Participating States and from the European Union’s Horizon 2020 research.
- “Ex post funding of research – 2021” of the University of Torino funded by the “Compagnia di San Paolo”.
- ROUGE and QUANTEP, funded by the 5th National Commission of the Italian National Institute for Nuclear Physics (INFN).
- Progetto IR-HPHT, funded by MIUR ex DM 737 /2021.
- Project “Piemonte Quantum Enabling Technologies” (PiQuET), funded by the Piemonte Region within the “Infra-P” scheme (POR-FESR 2014-2020 program of the European Union).

7 Appendix I

The mathematical details for the derivation of the experimental second order autocorrelation function are here discussed. Particularly, the emission characteristic of the emitting centres based on two and three levels system are discussed, to which a diamond-based emitter is assimilable. Particularly, the principal emission characteristics are the followings: decay time from the excited state to the ground state τ; the saturation power, the saturation intensity referred typically as emission rate.

7.1 Two level model

The two level model is the simplest to describe from an energetic perspective the emission of a colour centre. The assumption is that of an isolated molecule-like system within the gap of the considered semiconductor.

In Figure it is reported the schema of the two level model: the ground state is labelled as 1, the excited state is labelled as 2, the first excited vibronic states are also depicted.

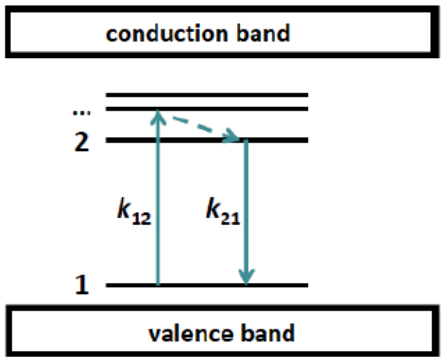


Figure 7.1.1 Schematic representation of the two level model. The energy levels are considered to be isolated from the edges of the energy ga.

The emission of a photon occurs through energy transitions between the levels. The transition of the system from the ground state to one of the excited levels occurs through the absorption of a photon and consequently it is not associated with the emission of light quanta. The system that is in a level 2 vibrational excited state relaxes knows non-radiatively in the ground state of the latter, and from this decays radiatively into the ground state, with the emission of a photon having energy equal to the difference between the two energy levels.

From a mathematical perspective, the above-mentioned discussion is modelled with rate equations of the time dependent population variation for the state 1 and 2: $n_1(t)$; $n_2(t)$.

The coefficients k_{12} and k_{21} depicted in Figure represent the terms proportional to the excitation from level 1 to 2 and to de-excitation from level 2 to ground state. The coefficient k_{12} is proportional to the excitation source and therefore to the optical power absorbed by the system itself: $k_{12} = \alpha P$, where P indicates the power pump. k_{21} is a constant related to the decay rate between levels 2 and 1, and a typical size of the system defined as $1/\tau$, more generally the coefficient k_{21} is defined as the sum of two coefficients related to channel decay radiative and for non-radiative channels: $k_{21} = k_{21}^{R} + k_{21}^{NR}$.

The rate equations for the system under analysis are therefore 2 and are reported in the system XXX. The temporal variation of the population of level 1 and proportional to the decrease in the level's population 1, due to the effect of the absorbed optical excitation which causes the system to transition to the excited one

and to the spontaneous decay from the excited level 2 towards the ground state. For the population of the excited level the following relations hold: complementary to those for level 1 as the population increases later to optical excitation and decreases by decay towards the ground state.

$$\begin{cases} \frac{dn(t)_1}{dt} = -k_{12}n(t)_1 + k_{21}n(t)_2 \\ \frac{dn(t)_2}{dt} = k_{12}n(t)_1 - k_{21}n(t)_2 \end{cases}$$

The constraint is that $n_1(t) + n_2(t) = 1$. At t =0 it follows that:

$$\begin{cases} n(t = 0)_1 = 1 \\ n(t = 0)_2 = 0 \end{cases}$$

The solution is then given by the following equation:

$$n(t)_2 = N_2\left[1 - e^{-\lambda t}\right]$$

$$N_2 = \frac{k_{12}}{k_{12} + k_{21}}$$
$$\lambda = k_{12} + k_{21}$$

N_2 represents the population the excited state in the stationary case, when the optical pump is on for a time interval greater than the emission of the single photon, hence when the system is on average in the excited state.

The aim of the discussion is to find the fitting curve using the second-order autocorrelation function. Therefore, since the intensity of the electromagnetic field is proportional to the number of emitted photons from a source, the latter equation can be rewritten adopting the following considerations.

When a photon is emitted the colour centre relaxes and returns at the fundamental level therefore $n_2(t)$ represents the probability of emission of a photon. From equation) we can therefore replace the component of Intensity at time $t + t_0$, where the t_0 component is due to the addition of a time delay in the acquisition chain, as follows:

$$I(t + t_0) = A\, n(t)_2$$

The intensity at time t0 can be rewritten as follows, in fact in in stationary conditions the average intensity of ow of photons is equal to finding the system in the excited state:

$$I(t_0) = A\, N_2$$

The constant A represents the proportional factor to k_{21}^R and the detector efficiency.

Hence, the second order autocorrelation function can be rewritten as follows:

$$g(t)^2 = \frac{< I(t)I(t + t_0) >}{|I(t_0)|^2} = \frac{A\, n(t)_2}{A\, N_2} = 1 - e^{-\lambda t}$$

It is worth noting that the second-order autocorrelation function is not dependent from the detector efficiency but it is dependent on the λ parameter which then depends on the optical power adopted to excite the electron from the ground to the excited state.

From an experimental perspective, to gain the information related to the excited state lifetime τ, it is needed to perform different autocorrelation measurements at various optical power since $\lambda = k_{12} + k_{21} = \alpha P + k_{21}$. The intercept obtained from the linear fit $\lambda(P)$ is then the inverse of the excited state lifetime.

The emission rate is linked to the probability of having the system in an excited state, to have the emission of a photon and the detection efficiency of the detector, the quantum efficiency Q defined as the ratio between the coefficient of radiative relaxation $k_{21}{}^{R}$ normalised over the cumulative relaxation coefficient k_{21}. Hence, the Rate can be written as:

$$R = N_2 \, {k_{21}}^R \eta^R = {k_{21}}^R \frac{{k_{21}}^R}{{k_{21}}^R + {k_{21}}^{NR}} \frac{\alpha P}{\alpha P + k_{21}} = I_\infty \frac{\alpha P}{\alpha P + k_{21}}$$

It can be hence obtained the decay time of system, the emission rate can be determined depending on the excitation power, as well as the saturation power (i.e. the maximum output power, beyond which it no longer increases increasing the input power).

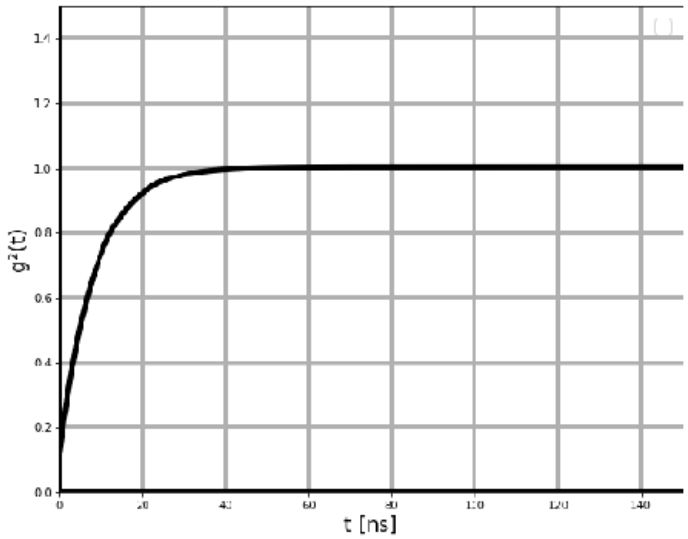


Figure 7.1.2 Second order autocorrelation function fitting curve for the two level model.

7.2 Three level model

The three-level model, schematized in Figure 1.3.7, is composed of the level 1 or ground state; a level 2 or excited level (responsible for the transition optics through ground state relaxation), and a third level (3) having intermediate energy, called shelving state.

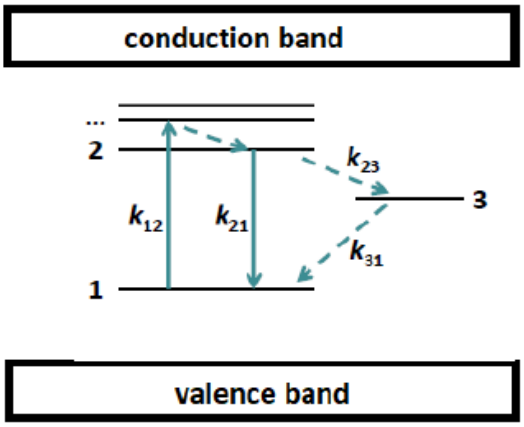


Figure 7.2.1 Schematic representation of the three level model. The energy levels are considered to be isolated from the edges of the energy gap.

As in the previous case, the excitation source promotes the system from level 1 to level 2. The system can now relax radiatively to the level 1 or relax with a non-radiative transition to level 3. This phenomenon is called *intersystem crossing* [249].

$$\begin{cases} \frac{dn(t)_1}{dt} = -k_{12}n(t)_1 + k_{21}n(t)_2 + k_{31}n(t)_3 \\ \frac{dn(t)_2}{dt} = -k_{12}n(t)_1 + k_{21}n(t)_2 - k_{23}n(t)_2 \\ \frac{dn(t)_3}{dt} = k_{23}n(t)_2 - k_{31}n(t)_3 \end{cases}$$

Similarly to the two level model, the constraint is that $n_1(t) + n_2(t) + n_3(t) = 1$. At t =0 it follows that:

$$\begin{cases} n(t=0)_1 = 1 \\ n(t=0)_2 = n(t=0)_3 = 0 \end{cases}$$

Analogously to the two level model, the solution to this system is the following:

$$n(t)_2 = N_2\left[1 - (1-a)e^{-\lambda_1 t} + ae^{-\lambda_2 t}\right]$$

With the parameters:

$$\lambda_{1/2} = A \pm \sqrt{A^2 - 4B}$$
$$A = k_{12} + k_{21} + k_{31} + k_{23}$$
$$B = k_{12}(k_{23} + k_{31}) + k_{31}(k_{21} + k_{23})$$
$$a = \frac{1 - \frac{k_{31}}{\lambda_2}}{k_{31}\left(\frac{1}{\lambda_2} - \frac{1}{\lambda_1}\right)}$$

Consequently, the second-order autocorrelation function becomes:

$$g(t)^2 = \frac{< I(t)I(t+t_0) >}{|I(t_0)|^2} = \frac{A\,n(t)_2}{A\,N_2} = 1 - (1-a)e^{-\lambda_1 t} + ae^{-\lambda_2 t}$$

The parameter λ_1 is always smaller than λ_2 and is responsible for the characteristic dip of the autocorrelation function at t=0 already observed for the two levels system. The second parameter generates the so-called bunching effect, due in the presence of the third energy level. The net effect of this parameter and that of forcing an emission with a precise time delay (statistically assimilable to a super-Poissonian component) with respect to the instant a which excitation occurs, following the characteristic relaxation time not radiative

through the shelving state. The centre emits in packets as it enters in a state of darkness and therefore does not resume the cycle of excitation and emission no until it returns to the ground state.

As regards the study of the emission rate, it can be introduced the approximation such that $k_{21} \gg k_{23} + k_{31}$. It immediately occurs, in analogy with the two-level model:

$$\lambda_1 = k_{12} + k_{31} = \alpha P + k_{31}$$
$$\lambda_2 = k_{31} + \frac{\alpha P k_{23}}{\alpha P k_{21}}$$

For $P \to \infty$ this parameter tends to the sum of the rates $k_{31} + k_{23}$. However, experimentally it is observed that this parameter grows linearly without reaching a saturation value. This phenomenon can be explained assuming that the transition from level 3 to level 1 depends on the power of excitation, and that it is not an electric dipole type transition, but which involves rather, phenomena of a more complex nature such as transitions of the electric quadrupole type or the Intersystem Crossing phenomenon [249].

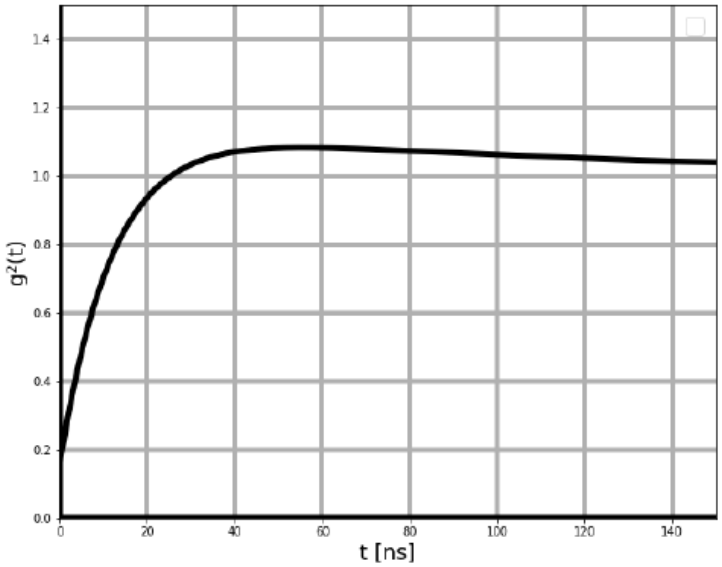


Figure 7.2.2 Second order autocorrelation function fitting curve for the three level model.

8 Appendix II

Part of the activity involved in the development and commissioning of the ion implanter was related to the development of the control software of the accelerator.

The software was written and developed in Labview from National Instruments. Two main software were written for the control of the beamline and the source area: the first operate the source area while the second the beamline and irradiation chamber. The mass spectrometry apparatus has a dedicated software as well as the irradiation chamber.

8.1 Source and beamline software

The two main software allow to control and to readout the instrumentation. The core of both the source area and the beamline consists of a control box (one for each section) that wire the instrumentation to different National Instruments card (type 6001) that are the main control source. The NI6001 cards consist of a multifunctional device with 24 channels: 8 analog inputs, 2 analog outputs, 13 digital channels, 1 5 V power supply.

The cards are then linked to the PC via usb cables for an active control of the instrumentation. The control box was partially built by the Solid-State laboratory but designed by the University of Lepizig, which was the main partner of the commissioning of the Ion Implanter. The activity carried out was then the debugging and testing of such control boxes and the fine tuning of the control parameters.

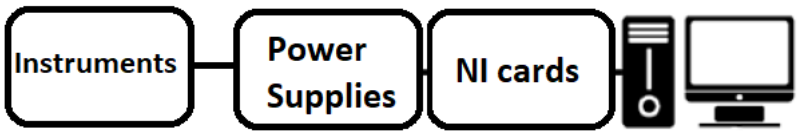


Figure 8.1.1 Building block schematics of the hardware to software interface for the source area and the beamline excluded the mass spectrometry system.

As specified Chapter 3.1.1, the source hardware is composed of 6 different power supplies: for the ionizer and the Line heater (the small pipe connecting the Cs reservoir to the main chamber) are current regulated; the extractor, cathode, focus and Cs oven are voltage driven. The software depicted in Figure 7.2.2allows to set the working parameters monitoring the instrument feedback to check for proper functioning of the source components. The controllers are monitored over time to evaluate the stability of the source area and perform irradiations of the sample with the most suited conditions.

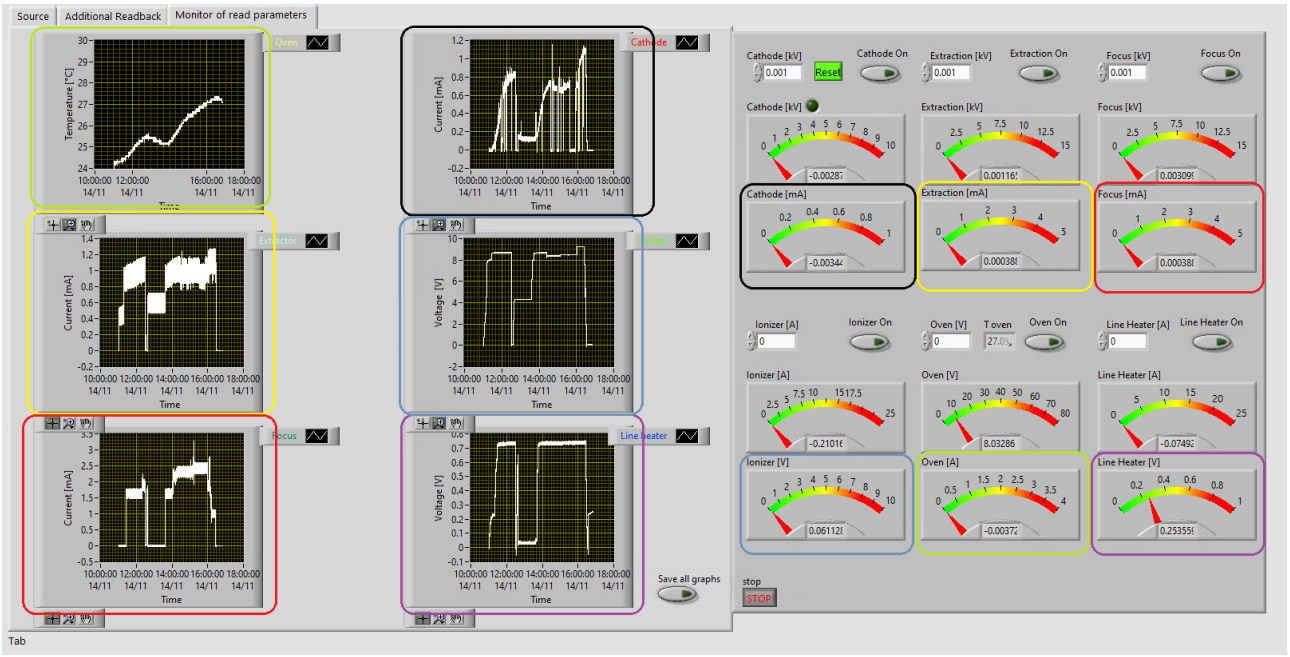


Figure 8.1.2 Picture of the LabView software that controls the Source area. The graphs on the left side represents the readout of the set parameters on the right side. The circles colours represent the readout of the instruments over time.

The software running the beamline is shown in, it is divided in different colours meaning different functions for the circled regions. The black circled region handles the vacuum controls (switching of the turbomolecular pumps) and the vacuometer reading, the opening vacuum valves control system (as well as an interlock system based on threshold of vacuum).

The control of the power supplies for the magnetic steerers (current controlled) is manoeuvred by the controls circled in purple. It is possible to modify the current injected in the devices to actively modify the beam size on the second faraday cup as well as on the sample holder. Two doublet quadrupoles and two magnetic steerers are handled by this system.

The yellow circled area permits to control the accelerating voltage of the terminal from 0 to a maximum of 100 kV.

The red circled area is used once the beam is focussed to the irradiation chamber and the desired beam current is obtained. The set up for the implantation scheme consists of the selection of the collimating area adopted for the implantation, the selection of the desired fluence. Depending on the timing for the implantation, two different paths were programmed: the *fast* and the *slow* implantation. The implantation can be both *Slow* (i.e., > 1s), enabling the faraday cup to be inserted when the proper timing is reached, as well as *fast* (i. e., 1 s < t < 0.3 s), with a proper switching off one of the magnetic steerers. The choice of *slow* or *fast* implantation depends on the beam current reaching the irradiation chamber as well as the desired fluence. It is possible to select the beam current and the aperture through which the beam is collimated, allowing for a precise definition of the implanted fluence.

Other tabs are present in Figure 8.2.8.1.3 but are related to additional readout and debugging of the whole control software.

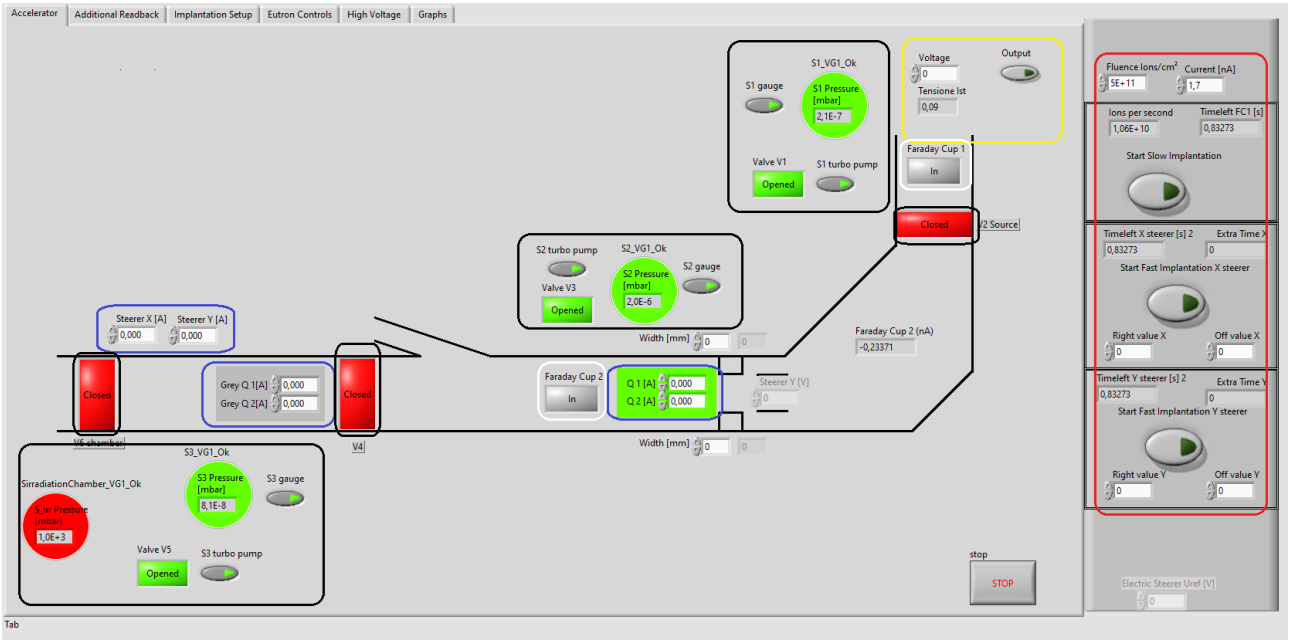


Figure 8.2.8.1.3 Picture of the LabView software that controls the beamline. The circled regions are divided in colours that represent the different purposes. The white circled regions allow to control the Faraday Cups insertion, the red circled region allow to perform the implantations, the black circled region allow for the vacuum control, the violet regions allow to control the electrostatic components.

8.2 Mass spectrometry software

The mass spectrometry software is displayed in Figure 8.2.8.1.3, it is divided in different circled coloured areas having each a different purpose. The red area represents the switches of the magnet power supplies as well as the readout from it. The black circled area displays the setting parameters from the user to perform the mass spectrum. It has two buttons allowing to start or stop the scan, 4 controls to select the desired starting and ending point (in terms of magnet current), the dwell time and the average to perform per step. The mass spectrum is then displayed in the purple area, the graph is shown I term of beam current as function of magnet current. The calibration, discussed in the previous paragraph, is performed with the orange circled area. Two controls are set to the adopted energy and to the selected peak in the main graph allowing to disambiguate the chemical species observed. The output displays the mass in a.m.u.. If it is desired to increase or decrease the beam current on the second faraday cup, it is possible to modify the optics steering or focussing capabilities both from the source and the beamline. To monitor the beam current behaviour over time, it is inserted also a time graph (depicted in green) to allow for a visual increase or decrease.

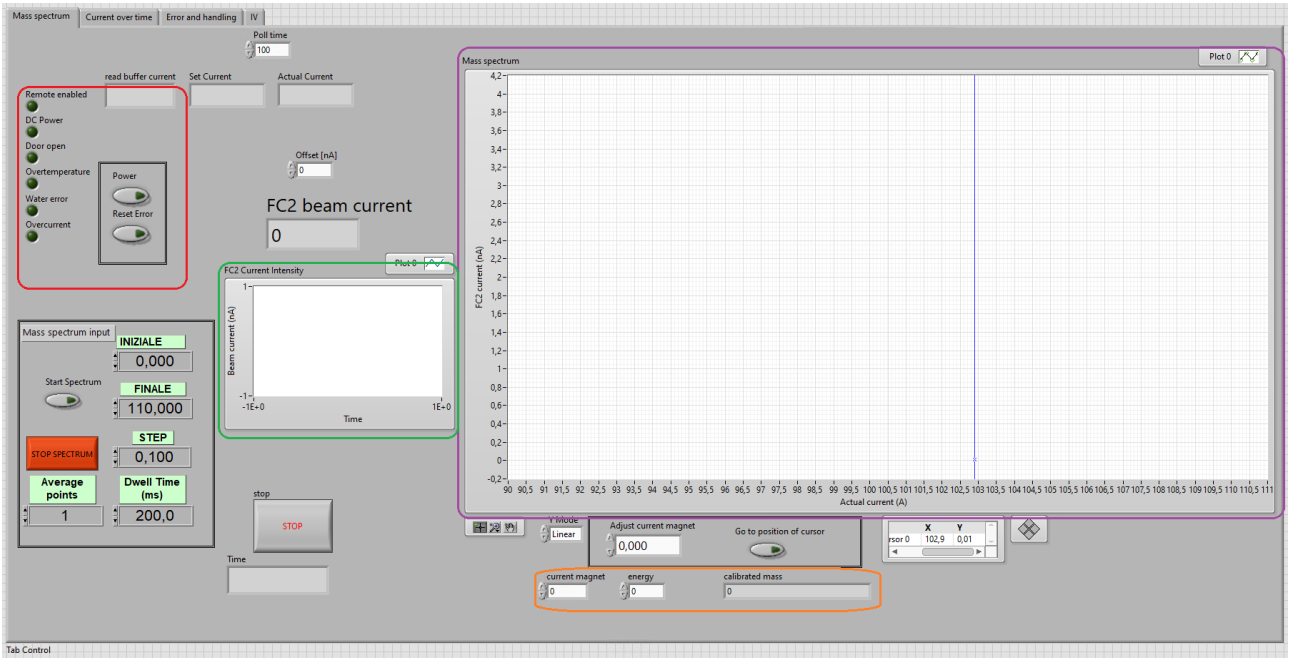


Figure 8.2.1 Software running the mass spectrometry system. The circled areas represent each a different control. The green one displays the beam current over time, the red one the controllers of the magnet power supply, the black one the parameters adopted for the scan, the purple one displays the main graph obtained from the magnetic field scan of the beam current, the orange one allows to calibrate the peaks of the main graph.

8.3 Irradiation chamber software

As for the other described sections of the ion implanter, it was developed a Labview code to run the irradiation chamber area. The most relevant features are regarding the movement of the positioners where the sample holder is mounted, the monitor of the beam current using a picoammeter (Model Keithley 6485) and as last feature a scanning system. The scanning system have a double purpose, firstly allow to perform scans to implant larger areas with respect to the beam size, secondly, to image the beam on the Faraday cup mounted on the sample holder. The imaging of the beam spot is typically performed by means of irradiating a PMMA coated substrate and observe the imprinted spot on it. During the development of finer tools to image the beam spot, the scanning of the positioners where the faraday cups is located was developed. The aperture of the cup is 1.5 mm and the beam typically ranges from 100 µm to 2 mm, the total scan area is then larger than the apertures of the collimating masks and faraday cup. In Figure 8.3.1 it is shown the Labview software that runs the irradiation chamber system. The red circled area represents the control of the positioners. The graph (circled in green) displays the beam current (in pA) read during the operation of the faraday cup. To perform scans it was conducted a scanning system that allow to move both x and y over the whole ranges of the positioners. Figure 8.3.2 displays the scanning software. The green circled areas represent the dwell time for the reading of the beam current and the Intensity plot obtained reading for each step of the scan the current. The red area permits to set the ranges for the scan and the resolution, meaning the size of the single pixel in terms of the step of the positioners. The purple area displays the scanning parameters to set for the implantation such as the fluence, the timing for a single scan, the number of iterations for multiple scans and the beam current (in nA).

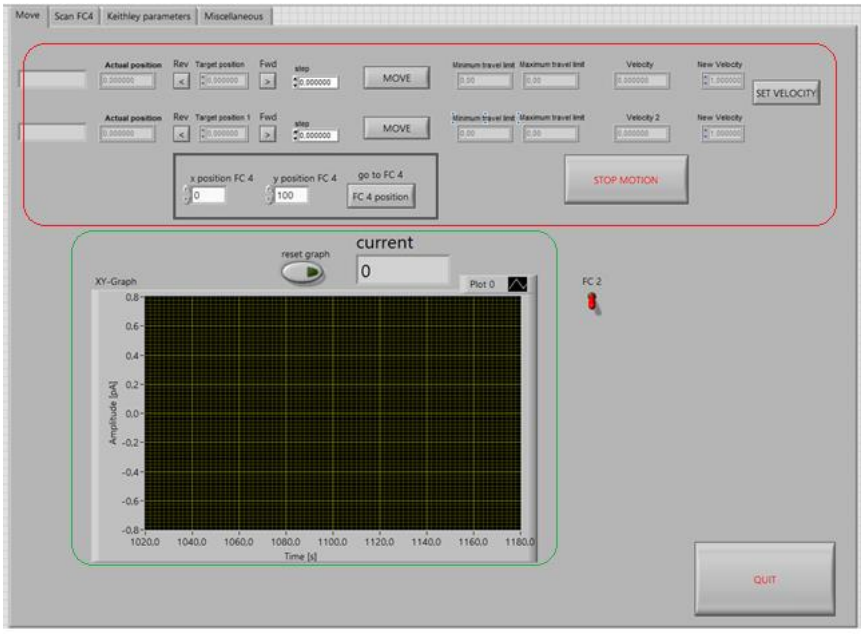


Figure 8.3.1 Main page of the software running the irradiation chamber system. The graph displays the beam current in pA over time. The top part allows to move the positioners to the desired positions.

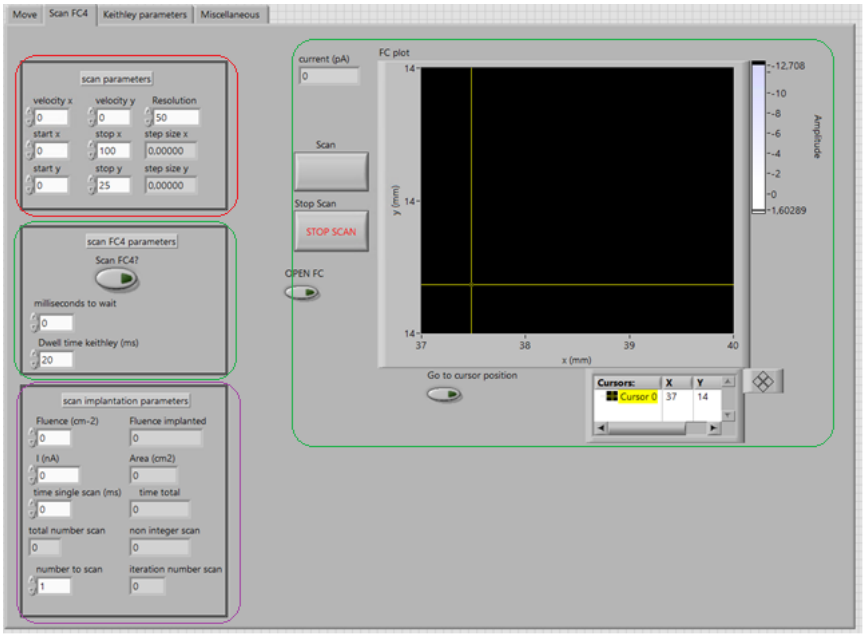


Figure 8.3.2 Scanning system. The graph displays the intensity plot of the beam across the faraday cup. The side parameters are related to the number of total scans, ranges, dwell time for the scan.

9 Bibliography

[1] J. P. Dowling and G. J. Milburn, 'Quantum technology: the second quantum revolution', *Philosophical Transactions of the Royal Society of London. Series A: Mathematical, Physical and Engineering Sciences*, vol. 361, no. 1809, pp. 1655–1674, Aug. 2003, doi: 10.1098/rsta.2003.1227.

[2] F. Flamini, N. Spagnolo, and F. Sciarrino, 'Photonic quantum information processing: a review', *Reports on Progress in Physics*, vol. 82, no. 1, p. 016001, Jan. 2019, doi: 10.1088/1361-6633/aad5b2.

[3] S. Pezzagna and J. Meijer, 'Quantum computer based on color centers in diamond', *Appl Phys Rev*, vol. 8, no. 1, Mar. 2021, doi: 10.1063/5.0007444.

[4] C. L. Degen, F. Reinhard, and P. Cappellaro, 'Quantum sensing', *Rev. Mod. Phys.*, vol. 89, no. September, pp. 1–39, 2017, doi: 10.1103/RevModPhys.89.035002.

[5] C. Couteau *et al.*, 'Applications of single photons in quantum metrology, biology and the foundations of quantum physics', *Nature Reviews Physics*, vol. 5, no. 6, pp. 354–363, May 2023, doi: 10.1038/s42254-023-00589-w.

[6] M. D. Eisaman, J. Fan, A. Migdall, and S. V Polyakov, 'Invited Review Article: Single-photon sources and detectors', *Review of Scientific Instruments*, vol. 82, no. 7, p. 71101, Jul. 2011, doi: 10.1063/1.3610677.

[7] I. Aharonovich, D. Englund, and M. Toth, 'Solid-state single-photon emitters', *Nat Photonics*, vol. 10, no. 10, pp. 631–641, Oct. 2016, doi: 10.1038/nphoton.2016.186.

[8] H. G. Barros *et al.*, 'Deterministic single-photon source from a single ion', *New J. Phys.*, vol. 11, 2009, doi: 10.1088/1367-2630/11/10/103004.

[9] E. Meyer-Scott, C. Silberhorn, and A. Migdall, 'Single-photon sources: Approaching the ideal through multiplexing', *Review of Scientific Instruments*, vol. 91, no. 4, Apr. 2020, doi: 10.1063/5.0003320.

[10] E. Giese, R. Fickler, W. Zhang, L. Chen, and R. W. Boyd, 'Influence of pump coherence on the quantum properties of spontaneous parametric down-conversion', *Phys Scr*, vol. 93, no. 8, p. 084001, Aug. 2018, doi: 10.1088/1402-4896/aace12.

[11] X. Ma and H.-K. Lo, 'Quantum key distribution with triggering parametric down-conversion sources', *New J Phys*, vol. 10, no. 7, p. 073018, Jul. 2008, doi: 10.1088/1367-2630/10/7/073018.

[12] M. Attia, A. Gueddana, and R. Chatta, 'Success Probability of Optical Quantum CNOT Gate Based on Probabilistic Single Photon Sources', *Journal of Nanoelectronics and Optoelectronics*, vol. 11, no. 4, pp. 441–449, Aug. 2016, doi: 10.1166/jno.2016.1831.

[13] A. Kiraz, M. Ehrl, Th. Hellerer, Ö. E. Müstecaplıoğlu, C. Bräuchle, and A. Zumbusch, 'Indistinguishable Photons from a Single Molecule', *Phys Rev Lett*, vol. 94, no. 22, p. 223602, Jun. 2005, doi: 10.1103/PhysRevLett.94.223602.

[14] S. Buckley, K. Rivoire, and J. Vučković, 'Engineered quantum dot single-photon sources', *Reports on Progress in Physics*, vol. 75, no. 12, p. 126503, Dec. 2012, doi: 10.1088/0034-4885/75/12/126503.

[15] P. Senellart, G. Solomon, and A. White, 'High-performance semiconductor quantum-dot single-photon sources', *Nat Nanotechnol*, vol. 12, no. 11, pp. 1026–1039, Nov. 2017, doi: 10.1038/nnano.2017.218.

[16] Y. Arakawa and M. J. Holmes, 'Progress in quantum-dot single photon sources for quantum information technologies: A broad spectrum overview', *Appl Phys Rev*, vol. 7, no. 2, Jun. 2020, doi: 10.1063/5.0010193.

[17] C. Bonato *et al.*, 'Strain tuning of quantum dot optical transitions via laser-induced surface defects', *Phys Rev B*, vol. 84, no. 7, p. 075306, Aug. 2011, doi: 10.1103/PhysRevB.84.075306.

[18] 'http://quantum-technologies.iap.uni-bonn.de/en/cavity-qed.html'.

[19] M. E. Bathen and L. Vines, 'Manipulating Single-Photon Emission from Point Defects in Diamond and Silicon Carbide', *Adv Quantum Technol*, vol. 4, no. 7, Jul. 2021, doi: 10.1002/qute.202100003.

[20] R. J. Glauber, 'Coherent and Incoherent States of the Radiation Field', *Physical Review*, vol. 131, no. 6, pp. 2766–2788, Sep. 1963, doi: 10.1103/PhysRev.131.2766.

[21] S. G. Lukishova and L. J. Bissell, 'Nanophotonic Advances for Room-Temperature Single-Photon Sources', 2019, pp. 103–178. doi: 10.1007/978-3-319-98402-5_4.

[22] D. Simin *et al.*, 'All-Optical dc Nanotesla Magnetometry Using Silicon Vacancy Fine Structure in Isotopically Purified Silicon Carbide', *Phys Rev X*, vol. 6, no. 3, p. 031014, Jul. 2016, doi: 10.1103/PhysRevX.6.031014.

[23] S. Hong *et al.*, 'Nanoscale magnetometry with NV centers in diamond', *MRS Bull*, vol. 38, no. 02, pp. 155–161, Jan. 2013, doi: 10.1557/mrs.2013.23.

[24] S. Choe *et al.*, 'Precise temperature sensing with nanoscale thermal sensors based on diamond NV centers', *Current Applied Physics*, vol. 18, no. 9, pp. 1066–1070, Sep. 2018, doi: 10.1016/j.cap.2018.06.002.

[25] G. Petrini *et al.*, 'Is a Quantum Biosensing Revolution Approaching? Perspectives in NV-Assisted Current and Thermal Biosensing in Living Cells', *Adv Quantum Technol*, vol. 3, no. 12, Dec. 2020, doi: 10.1002/qute.202000066.

[26] J. L. Webb *et al.*, 'Nanotesla sensitivity magnetic field sensing using a compact diamond nitrogen-vacancy magnetometer', *Appl Phys Lett*, vol. 114, no. 23, Jun. 2019, doi: 10.1063/1.5095241.

[27] D. Simin *et al.*, 'All-Optical dc Nanotesla Magnetometry Using Silicon Vacancy Fine Structure in Isotopically Purified Silicon Carbide', *Phys Rev X*, vol. 6, no. 3, p. 031014, Jul. 2016, doi: 10.1103/PhysRevX.6.031014.

[28] A. N. Anisimov *et al.*, 'Optical thermometry based on level anticrossing in silicon carbide', *Sci Rep*, vol. 6, no. 1, p. 33301, Sep. 2016, doi: 10.1038/srep33301.

[29] M. Alkahtani *et al.*, 'Tin-vacancy in diamonds for luminescent thermometry', *Appl Phys Lett*, vol. 112, no. 24, Jun. 2018, doi: 10.1063/1.5037053.

[30] J. Poizat *et al.*, 'Single Photon Quantum Cryptography', *Phys Rev Lett*, vol. 89, no. 18, Jan. 2002, doi: 10.1103/PhysRevLett.89.187901.

[31] C. H. Bennett and G. Brassard, 'Quantum cryptography: Public key distribution and coin tossing', *Theor Comput Sci*, vol. 560, no. P1, pp. 7–11, 2014, doi: 10.1016/j.tcs.2014.05.025.

[32] C. H. Bennett, F. Bessette, G. Brassard, L. Salvail, and J. Smolin, 'Experimental Quantum Cryptography', *Journal of Cryptology 9 1992 International Association for Cryptologic Research*, 1992.

[33] A. Carrasco-Casado, V. Fernández, and N. Denisenko, 'Free-Space Quantum Key Distribution', 2016, pp. 589–607. doi: 10.1007/978-3-319-30201-0_27.

[34] 'https://www.siqust.eu/'.

[35] J. C. Zwinkels, E. Ikonen, N. P. Fox, G. Ulm, and M. L. Rastello, 'Photometry, radiometry and "the candela": evolution in the classical and quantum world', *Metrologia*, vol. 47, no. 5, pp. R15–R32, Oct. 2010, doi: 10.1088/0026-1394/47/5/R01.

[36] T. Pohl, P. Meindl, U. Johannsen, D. Taubert, and L. Werner, 'Measurement of the absolute spectral responsivity in the mid-infrared based on the cryogenic electrical substitution radiometer and an optimized thermopile detector', *Journal of Sensors and Sensor Systems*, vol. 8, no. 1, pp. 195–205, May 2019, doi: 10.5194/jsss-8-195-2019.

[37] S. Welz, Y. Gogotsi, and M. J. McNallan, 'Nucleation, growth, and graphitization of diamond nanocrystals during chlorination of carbides', *J Appl Phys*, vol. 93, no. 7, pp. 4207–4214, Apr. 2003, doi: 10.1063/1.1558227.

[38] F. Gorrini *et al.*, 'On the thermodynamic path enabling a room-temperature, laser-assisted graphite to nanodiamond transformation', *Sci Rep*, vol. 6, no. 1, p. 35244, Jan. 2016, doi: 10.1038/srep35244.

[39] RIGAULT G, *INTRODUZIONE ALLA CRISTALLOGRAFIA*. LEVROTTO & BELLA, 2008.

[40] Karl E. Spear and John P. Dismukes, *Synthetic Diamond: Emerging CVD Science and Technology*. 1994.

[41] P. Pavone *et al.*, '*Ab initio* lattice dynamics of diamond', *Phys Rev B*, vol. 48, no. 5, pp. 3156–3163, Aug. 1993, doi: 10.1103/PhysRevB.48.3156.

[42] J. Barjon, N. Habka, C. Mer, F. Jomard, J. Chevallier, and P. Bergonzo, 'Resistivity of boron doped diamond', *physica status solidi (RRL) – Rapid Research Letters*, vol. 3, no. 6, pp. 202–204, Sep. 2009, doi: 10.1002/pssr.200903097.

[43] J. F. Prins, 'Ion implantation of diamond for electronic applications', *Semicond Sci Technol*, vol. 18, no. 3, pp. S27–S33, Mar. 2003, doi: 10.1088/0268-1242/18/3/304.

[44] M. Nesládek, K. Meykens, K. Haenen, L. M. Stals, T. Teraji, and S. Koizumi, 'Low-temperature spectroscopic study of *n* -type diamond', *Phys Rev B*, vol. 59, no. 23, pp. 14852–14855, Jan. 1999, doi: 10.1103/PhysRevB.59.14852.

[45] H. Sternschulte, K. Thonke, R. Sauer, and S. Koizumi, 'Optical evidence for 630-meV phosphorus donor in synthetic diamond', *Phys Rev B*, vol. 59, no. 20, pp. 12924–12927, 1999, doi: 10.1103/PhysRevB.59.12924.

[46] A. Zunger and A. J. Freeman, 'Ground-state electronic properties of diamond in the local-density formalism', *Phys Rev B*, vol. 15, no. 10, pp. 5049–5065, May 1977, doi: 10.1103/PhysRevB.15.5049.

[47] A. Dychalska, W. Koczorowski, M. Trzcinski, L. Mosińska, and M. Szybowicz, 'The Effect of Surface Treatment on Structural Properties of CVD Diamond Layers with Different Grain Sizes Studied by Raman Spectroscopy', *Materials*, vol. 14, no. 5, p. 1301, Mar. 2021, doi: 10.3390/ma14051301.

[48] F. Maier, M. Riedel, B. Mantel, J. Ristein, and L. Ley, 'Origin of Surface Conductivity in Diamond', *Phys Rev Lett*, vol. 85, no. 16, pp. 3472–3475, Oct. 2000, doi: 10.1103/PhysRevLett.85.3472.

[49] A. M. Zaitsev, 'Optical Properties of Diamond', 2001, doi: 10.1007/978-3-662-04548-0.

[50] J. M. King, J. E. Shigley, T. H. Gelb, S. S. Guhin, M. Hall, and W. Wang, 'Characterization and Grading of Natural-Color Yellow Diamonds', *Gems & Gemology*, vol. 41, no. 2, pp. 88–115, Jun. 2005, doi: 10.5741/GEMS.41.2.88.

[51] E. Corte *et al.*, 'Spectral Emission Dependence of Tin-Vacancy Centers in Diamond from Thermal Processing and Chemical Functionalization', *Adv. Photonics Res.*, vol. 3, no. 1, p. 2100148, Jan. 2022, doi: 10.1002/adpr.202100148.

[52] M. V Hauf *et al.*, 'Chemical control of the charge state of nitrogen-vacancy centers in diamond', *Phys Rev B Condens Matter Mater Phys*, no. 8, pp. 1–4, 2011, doi: 10.1103/PhysRevB.83.081304.

[53] S. Sturari *et al.*, 'A comprehensive study of the effect of thermally induced surface terminations on nanodiamonds electrical properties', *Surfaces and Interfaces*, vol. 38, p. 102831, Jun. 2023, doi: 10.1016/j.surfin.2023.102831.

[54] F. Picollo *et al.*, 'Synthesis and characterization of porphyrin functionalized nanodiamonds', *Diam Relat Mater*, vol. 91, 2019, doi: 10.1016/j.diamond.2018.11.001.

[55] H. A. Girard *et al.*, 'Hydrogenation of nanodiamonds using MPCVD: A new route toward organic functionalization', *Diam Relat Mater*, vol. 19, no. 7–9, pp. 1117–1123, Jul. 2010, doi: 10.1016/j.diamond.2010.03.019.

[56] A. Krueger and D. Lang, 'Functionality is Key: Recent Progress in the Surface Modification of Nanodiamond', *Adv Funct Mater*, vol. 22, no. 5, pp. 890–906, Mar. 2012, doi: 10.1002/adfm.201102670.

[57] L. Tang, C. Tsai, W. W. Gerberich, L. Kruckeberg, and D. R. Kania, 'Biocompatibility of chemical-vapour-deposited diamond', *Biomaterials*, vol. 16, no. 6, pp. 483–488, Jan. 1995, doi: 10.1016/0142-9612(95)98822-V.

[58] F. Picollo *et al.*, 'A New Diamond Biosensor with Integrated Graphitic Microchannels for Detecting Quantal Exocytic Events from Chromaffin Cells', *Advanced Materials*, vol. 25, no. 34, pp. 4696–4700, Jan. 2013, doi: 10.1002/adma.201300710.

[59] S. Spadaro, G. Conte, M. Pimpinella, and A. S. Guerra, 'Electrical and dosimetric characterization of a CVD diamond detector with high sensitivity', *Radiat Meas*, vol. 48, pp. 1–6, Jan. 2013, doi: 10.1016/j.radmeas.2012.11.017.

[60] J. Forneris *et al.*, 'Measurement and modelling of anomalous polarity pulses in a multi-electrode diamond detector', *EPL (Europhysics Letters)*, vol. 104, no. 2, p. 28005, Oct. 2013, doi: 10.1209/0295-5075/104/28005.

[61] G. Tomagra *et al.*, 'Diamond-based sensors for in vitro cellular radiobiology: Simultaneous detection of cell exocytic activity and ionizing radiation', *Biosens Bioelectron*, vol. 220, p. 114876, Jan. 2023, doi: 10.1016/j.bios.2022.114876.

[62] H. Sumiya, K. Harano, and K. Tamasaku, 'HPHT synthesis and crystalline quality of large high-quality (001) and (111) diamond crystals', *Diam Relat Mater*, vol. 58, pp. 221–225, Sep. 2015, doi: 10.1016/j.diamond.2015.08.006.

[63] F. Silva *et al.*, 'High quality, large surface area, homoepitaxial MPACVD diamond growth', *Diam Relat Mater*, vol. 18, no. 5–8, pp. 683–697, Jan. 2009, doi: 10.1016/J.DIAMOND.2009.01.038.

[64] Y. N. Palyanov, I. N. Kupriyanov, A. F. Khokhryakov, and Y. M. Borzdov, 'High-pressure crystallization and properties of diamond from magnesium-based catalysts', *CrystEngComm*, vol. 19, no. 31, pp. 4459–4475, 2017, doi: 10.1039/C7CE01083D.

[65] 'https://www.gemsngems.com/product-category/lab-created/lab-created-diamond/'.

[66] J. C. Angus, 'Diamond synthesis by chemical vapor deposition: The early years', *Diam Relat Mater*, vol. 49, pp. 77–86, Oct. 2014, doi: 10.1016/j.diamond.2014.08.004.

[67] M. Schwander and K. Partes, 'A review of diamond synthesis by CVD processes', *Diam Relat Mater*, vol. 20, no. 9, pp. 1287–1301, Oct. 2011, doi: 10.1016/j.diamond.2011.08.005.

[68] A. M. Edmonds *et al.*, 'Characterisation of CVD diamond with high concentrations of nitrogen for magnetic-field sensing applications', *Materials for Quantum Technology*, vol. 1, no. 2, p. 025001, Jun. 2021, doi: 10.1088/2633-4356/abd88a.

[69] J. Barjon *et al.*, 'Silicon incorporation in CVD diamond layers', *physica status solidi (a)*, vol. 202, no. 11, pp. 2177–2181, Sep. 2005, doi: 10.1002/pssa.200561920.

[70] S. Koizumi, T. Teraji, and H. Kanda, 'Phosphorus-doped chemical vapor deposition of diamond', *Diam Relat Mater*, vol. 9, no. 3–6, pp. 935–940, Apr. 2000, doi: 10.1016/S0925-9635(00)00217-X.

[71] M. Marton *et al.*, 'New chemical pathway for large-area deposition of doped diamond films by linear antenna microwave plasma chemical vapor deposition', *Diam Relat Mater*, vol. 126, p. 109111, Jun. 2022, doi: 10.1016/j.diamond.2022.109111.

[72] Christopher M. Breeding and James E. Shigley, 'THE "TYPE" CLASSIFICATION SYSTEM OF DIAMONDS AND ITS IMPORTANCE IN GEMOLOGY', *Gems and Gemology*, 2009.

[73] B. Dischler, 'Intrinsic Defects and Their Associates in Diamond', in *Handbook of Spectral Lines in Diamond*, Berlin, Heidelberg: Springer Berlin Heidelberg, 2012, pp. 269–302. doi: 10.1007/978-3-642-22215-3_8.

[74] Ashcroft and Mermin, *Solid State chemistry*. 1976.

[75] F. Jelezko and J. Wrachtrup, 'Single defect centres in diamond: A review', *physica status solidi (a)*, vol. 203, no. 13, pp. 3207–3225, Oct. 2006, doi: 10.1002/pssa.200671403.

[76] C. Bradac, W. Gao, J. Forneris, M. E. Trusheim, and I. Aharonovich, 'Quantum nanophotonics with group IV defects in diamond', *Nat Commun*, vol. 10, no. 1, p. 5625, Dec. 2019, doi: 10.1038/s41467-019-13332-w.

[77] G. Prestopino *et al.*, 'Photo-physical properties of He-related color centers in diamond', *Appl Phys Lett*, vol. 111, no. 11, pp. 1–6, 2017, doi: 10.1063/1.4996825.

[78] A. M. Zaitsev, 'Vibronic spectra of impurity-related optical centers in diamond', *Phys Rev B*, vol. 61, no. 19, pp. 12909–12922, Jan. 2000, doi: 10.1103/PhysRevB.61.12909.

[79] S. Pezzagna, D. Rogalla, D. Wildanger, J. Meijer, and A. Zaitsev, 'Creation and nature of optical centres in diamond for single-photon emission—overview and critical remarks', *New J Phys*, vol. 13, no. 3, p. 035024, Mar. 2011, doi: 10.1088/1367-2630/13/3/035024.

[80] E. Corte *et al.*, 'Magnesium-Vacancy Optical Centers in Diamond', *ACS Photonics*, vol. 10, no. 1, pp. 101–110, Jan. 2023, doi: 10.1021/acsphotonics.2c01130.

[81] M. Bähr, M. Jahn, C. Heinze, K. Neckermann, J. Meijer, and T. Ortlepp, 'Compact All-Optical Quantum Sensor Device Based on Nitrogen Vacancy Centers in Diamond', *physica status solidi (a)*, vol. 220, no. 4, Feb. 2023, doi: 10.1002/pssa.202200338.

[82] N. Mizuochi *et al.*, 'Electrically driven single-photon source at room temperature in diamond', *Nat Photonics*, vol. 6, no. 5, pp. 299–303, Jan. 2012, doi: 10.1038/nphoton.2012.75.

[83] A. Lohrmann *et al.*, 'Diamond based light-emitting diode for visible single-photon emission at room temperature', *Appl Phys Lett*, no. 25, Jan. 2011, doi: 10.1063/1.3670332.

[84] C. Bradac, W. Gao, J. Forneris, M. E. Trusheim, and I. Aharonovich, 'Quantum nanophotonics with group IV defects in diamond', *Nat Commun*, vol. 10, no. 1, p. 5625, Dec. 2019, doi: 10.1038/s41467-019-13332-w.

[85] V. Nadolinny, A. Komarovskikh, and Y. Palyanov, 'Incorporation of Large Impurity Atoms into the Diamond Crystal Lattice: EPR of Split-Vacancy Defects in Diamond', *Crystals (Basel)*, vol. 7, no. 8, p. 237, Jul. 2017, doi: 10.3390/cryst7080237.

[86] J. M. Smith, S. A. Meynell, A. C. Bleszynski Jayich, and J. Meijer, 'Colour centre generation in diamond for quantum technologies', *Nanophotonics*, vol. 8, no. 11. De Gruyter, pp. 1889–1906, Nov. 2019. doi: 10.1515/nanoph-2019-0196.

[87] T. Iwasaki *et al.*, 'Tin-Vacancy Quantum Emitters in Diamond', *Phys. Rev. Lett.*, vol. 119, no. 25, p. 253601, Dec. 2017, doi: 10.1103/PhysRevLett.119.253601.

[88] P. Wang, T. Taniguchi, Y. Miyamoto, M. Hatano, and T. Iwasaki, 'Low-Temperature Spectroscopic Investigation of Lead-Vacancy Centers in Diamond Fabricated by High-Pressure and High-Temperature Treatment', *ACS Photonics*, vol. 8, no. 10, pp. 2947–2954, 2021, doi: 10.1021/acsphotonics.1c00840.

[89] T. Iwasaki *et al.*, 'Germanium-Vacancy Single Color Centers in Diamond', *Sci Rep*, vol. 5, no. 1, p. 12882, Jan. 2015, doi: 10.1038/srep12882.

[90] S. Lai *et al.*, 'High-pressure high-temperature industrial preparation of micron-sized diamond single crystals with silicon-vacancy colour centres', *Int J Refract Metals Hard Mater*, vol. 105, p. 105806, Jun. 2022, doi: 10.1016/j.ijrmhm.2022.105806.

[91] S. G. Lyapin, A. A. Razgulov, A. P. Novikov, E. A. Ekimov, and M. V Kondrin, 'High pressure photoluminescence studies of diamond with GeV centers', *Nanosystems: Physics, Chemistry, Mathematics*, vol. 9, pp. 67–69, Feb. 2018, doi: 10.17586/2220-8054-2018-9-1-67-69.

[92] Y. N. Palyanov, I. N. Kupriyanov, and Y. M. Borzdov, 'High-pressure synthesis and characterization of Sn-doped single crystal diamond', *Carbon N Y*, vol. 143, pp. 769–775, Mar. 2019, doi: 10.1016/j.carbon.2018.11.084.

[93] M. A. Lobaev *et al.*, 'Investigation of silicon-vacancy center formation during the CVD diamond growth of thin and delta doped layers', *J Mater Chem C Mater*, vol. 9, no. 29, pp. 9229–9235, 2021, doi: 10.1039/D1TC01538A.

[94] K. Ohno *et al.*, 'Engineering shallow spins in diamond with nitrogen delta-doping', *Appl Phys Lett*, vol. 101, no. 8, p. 082413, Aug. 2012, doi: 10.1063/1.4748280.

[95] M. A. Lobaev *et al.*, 'Diamond p–i–n Diode with Nitrogen Containing Intrinsic Region for the Study of Nitrogen-Vacancy Center Electroluminescence', *physica status solidi (RRL) – Rapid Research Letters*, vol. 14, no. 11, Nov. 2020, doi: 10.1002/pssr.202000347.

[96] C. Osterkamp *et al.*, 'Engineering preferentially-aligned nitrogen-vacancy centre ensembles in CVD grown diamond', *Sci Rep*, vol. 9, no. 1, p. 5786, Apr. 2019, doi: 10.1038/s41598-019-42314-7.

[97] R. R. Gattass and E. Mazur, 'Femtosecond laser micromachining in transparent materials', *Nat Photonics*, vol. 2, no. 4, pp. 219–225, Apr. 2008, doi: 10.1038/nphoton.2008.47.

[98] S. M. Eaton *et al.*, 'Quantum Micro–Nano Devices Fabricated in Diamond by Femtosecond Laser and Ion Irradiation', *Adv Quantum Technol*, vol. 2, no. 5–6, Jun. 2019, doi: 10.1002/qute.201900006.

[99] Y. C. Chen *et al.*, 'Laser writing of coherent colour centres in diamond', *Nat. Photonics*, vol. 11, no. 2, pp. 77–80, 2016, doi: 10.1038/nphoton.2016.234.

[100] D. Farfurnik *et al.*, 'Enhanced concentrations of nitrogen-vacancy centers in diamond through TEM irradiation', *Appl Phys Lett*, vol. 111, no. 12, Sep. 2017, doi: 10.1063/1.4993257.

[101] C. A. McLellan, B. A. Myers, S. Kraemer, K. Ohno, D. D. Awschalom, and A. C. Bleszynski Jayich, 'Patterned Formation of Highly Coherent Nitrogen-Vacancy Centers Using a Focused Electron

Irradiation Technique', *Nano Lett*, vol. 16, no. 4, pp. 2450–2454, Apr. 2016, doi: 10.1021/acs.nanolett.5b05304.

[102] E. Losero *et al.*, 'Creation of NV Centers in Diamond under 155 MeV Electron Irradiation', *Advanced Physics Research*, Nov. 2023, doi: 10.1002/apxr.202300071.

[103] K. Ohno *et al.*, 'Three-dimensional localization of spins in diamond using 12C implantation', *Appl Phys Lett*, vol. 105, no. 5, Aug. 2014, doi: 10.1063/1.4890613.

[104] Z. Huang *et al.*, 'Diamond nitrogen-vacancy centers created by scanning focused helium ion beam and annealing', *Appl Phys Lett*, vol. 103, no. 8, p. 081906, Aug. 2013, doi: 10.1063/1.4819339.

[105] M. I. Current, 'Ion implantation of advanced silicon devices: Past, present and future', *Mater Sci Semicond Process*, vol. 62, pp. 13–22, May 2017, doi: 10.1016/j.mssp.2016.10.045.

[106] T. Lühmann, J. Meijer, and S. Pezzagna, 'Charge-Assisted Engineering of Color Centers in Diamond', *physica status solidi (a)*, vol. 218, no. 5, Mar. 2021, doi: 10.1002/pssa.202000614.

[107] S. Pezzagna *et al.*, 'Creation of colour centres in diamond by collimated ion-implantation through nano-channels in mica', *physica status solidi (a)*, vol. 208, no. 9, pp. 2017–2022, Sep. 2011, doi: 10.1002/pssa.201100455.

[108] Y. Zhou *et al.*, 'Direct writing of single germanium vacancy center arrays in diamond', *New J. Phys.*, vol. 20, no. 12, p. 125004, Dec. 2018, doi: 10.1088/1367-2630/aaf2ac.

[109] A. Gruber, A. Dräbenstedt, C. Tietz, L. Fleury, J. Wrachtrup, and C. von Borczyskowski, 'Scanning Confocal Optical Microscopy and Magnetic Resonance on Single Defect Centers', *Science (1979)*, vol. 276, no. 5321, pp. 2012–2014, Jun. 1997, doi: 10.1126/science.276.5321.2012.

[110] D. Propst, J. Kotakoski, and E. H. Åhlgren, 'Impurity atom configurations in diamond and their visibility via scanning transmission electron microscopy imaging', *Electronic Structure*, vol. 5, no. 3, p. 033004, Sep. 2023, doi: 10.1088/2516-1075/acf9d3.

[111] J. R. Maze *et al.*, 'Properties of nitrogen-vacancy centers in diamond: The group theoretic approach', *New J Phys*, vol. 13, no. 2, p. 25025, Feb. 2011, doi: 10.1088/1367-2630/13/2/025025.

[112] M. W. Doherty, N. B. Manson, P. Delaney, F. Jelezko, J. Wrachtrup, and L. C. L. L. Hollenberg, 'The nitrogen-vacancy colour centre in diamond', *Phys Rep*, vol. 528, no. 1, pp. 1–45, 2013, doi: 10.1016/j.physrep.2013.02.001.

[113] M. Ruf, N. H. Wan, H. Choi, D. Englund, and R. Hanson, 'Quantum networks based on color centers in diamond', *J Appl Phys*, vol. 130, no. 7, Aug. 2021, doi: 10.1063/5.0056534.

[114] G. Petrini *et al.*, 'Nanodiamond–Quantum Sensors Reveal Temperature Variation Associated to Hippocampal Neurons Firing', *Advanced Science*, vol. 10, no. 11, Apr. 2023, doi: 10.1002/advs.202301101.

[115] E. Bernardi *et al.*, 'A biocompatible technique for magnetic field sensing at (sub)cellular scale using Nitrogen-Vacancy centers', *EPJ Quantum Technol*, vol. 7, no. 1, p. 13, Dec. 2020, doi: 10.1140/epjqt/s40507-020-00088-2.

[116] Á. Gali, '*Ab initio* theory of the nitrogen-vacancy center in diamond', *Nanophotonics*, vol. 8, no. 11, pp. 1907–1943, Nov. 2019, doi: 10.1515/nanoph-2019-0154.

[117] C. Schreyvogel, M. Wolfer, H. Kato, M. Schreck, and C. E. Nebel, 'Tuned NV emission by in-plane Al-Schottky junctions on hydrogen terminated diamond', *Sci Rep*, vol. 4, pp. 1–6, 2014, doi: 10.1038/srep03634.

[118] G. Thiering and A. Gali, ‘Ab Initio Magneto-Optical Spectrum of Group-IV Vacancy Color Centers in Diamond’, *Phys Rev X*, vol. 8, no. 2, p. 21063, Jun. 2018, doi: 10.1103/PhysRevX.8.021063.

[119] Z.-H. Zhang, A. M. Edmonds, N. Palmer, M. L. Markham, and N. P. de Leon, ‘Neutral Silicon-Vacancy Centers in Diamond via Photoactivated Itinerant Carriers’, *Phys Rev Appl*, vol. 19, no. 3, p. 034022, Mar. 2023, doi: 10.1103/PhysRevApplied.19.034022.

[120] U. F. S. D’Haenens-Johansson *et al.*, ‘Optical properties of the neutral silicon split-vacancy center in diamond’, *Phys Rev B*, vol. 84, no. 24, p. 245208, Jan. 2011, doi: 10.1103/PhysRevB.84.245208.

[121] S. D. D. Tchernij *et al.*, ‘Single-Photon-Emitting Optical Centers in Diamond Fabricated upon Sn Implantation’, *ACS Photonics*, vol. 4, no. 10, pp. 2580–2586, Oct. 2017, doi: 10.1021/acsphotonics.7b00904.

[122] J. P. Goss, R. Jones, S. J. Breuer, P. R. Briddon, and S. Öberg, ‘The Twelve-Line 1.682 eV Luminescence Center in Diamond and the Vacancy-Silicon Complex’, *Phys Rev Lett*, vol. 77, no. 14, pp. 3041–3044, Sep. 1996, doi: 10.1103/PhysRevLett.77.3041.

[123] S. Ditalia Tchernij *et al.*, ‘Single-Photon Emitters in Lead-Implanted Single-Crystal Diamond’, *ACS Photonics*, vol. 5, no. 12, pp. 4864–4871, Dec. 2018, doi: 10.1021/acsphotonics.8b01013.

[124] M. Ruf, N. H. Wan, H. Choi, D. Englund, and R. Hanson, ‘Quantum networks based on color centers in diamond’, *J Appl Phys*, vol. 130, no. 7, Aug. 2021, doi: 10.1063/5.0056534.

[125] L. De Santis, M. E. Trusheim, K. C. Chen, and D. R. Englund, ‘Investigation of the Stark Effect on a Centrosymmetric Quantum Emitter in Diamond’, *Phys Rev Lett*, vol. 127, no. 14, p. 147402, Sep. 2021, doi: 10.1103/PhysRevLett.127.147402.

[126] A. E. Rugar *et al.*, ‘Quantum Photonic Interface for Tin-Vacancy Centers in Diamond’, *Phys Rev X*, vol. 11, no. 3, p. 031021, Jul. 2021, doi: 10.1103/PhysRevX.11.031021.

[127] J. Görlitz *et al.*, ‘Coherence of a charge stabilised tin-vacancy spin in diamond’, *npj Quantum Inf*, vol. 8, no. 1, p. 45, Apr. 2022, doi: 10.1038/s41534-022-00552-0.

[128] P. Wang *et al.*, ‘Transform-Limited Photon Emission From a Lead-Vacancy Center in Diamond Above 10 K’, Aug. 2023.

[129] R. Sandstrom *et al.*, ‘Optical properties of implanted Xe color centers in diamond’, *Opt Commun*, vol. 411, pp. 182–186, 2018, doi: 10.1016/J.OPTCOM.2017.11.064.

[130] D. W. Drumm, M. C. Per, S. P. Russo, and L. C. L. Hollenberg, ‘Thermodynamic stability of neutral Xe defects in diamond’, *Phys Rev B*, vol. 82, no. 5, Jan. 2010, doi: 10.1103/PhysRevB.82.054102.

[131] V. A. Martinovich and A. A. Gorokhovsky, ‘Laser-induced luminescence of xenon implanted natural diamond’, *J Lumin*, vol. 107, no. 1–4, pp. 261–265, May 2004, doi: 10.1016/j.jlumin.2003.12.003.

[132] V. D. V. D. Tkachev, A. M. Zaitsev, and V. D. V. D. Tkachev, ‘Chemical Activity of Noble Gases in Diamond’, *physica status solidi (b)*, vol. 129, no. 1, pp. 129–133, Jan. 1985, doi: 10.1002/pssb.2221290112.

[133] G. Prestopino *et al.*, ‘Photo-physical properties of He-related color centers in diamond’, *Appl Phys Lett*, vol. 111, no. 11, pp. 1–6, 2017, doi: 10.1063/1.4996825.

[134] I. Aharonovich *et al.*, ‘Enhanced single-photon emission in the near infrared from a diamond color center’, *Phys Rev B*, vol. 79, no. 23, p. 235316, Jun. 2009, doi: 10.1103/PhysRevB.79.235316.

[135] I. Aharonovich *et al.*, ‘Chromium single-photon emitters in diamond fabricated by ion implantation’, *Phys Rev B*, vol. 81, no. 12, p. 121201, Mar. 2010, doi: 10.1103/PhysRevB.81.121201.

[136] D. Steinmetz, E. Neu, J. Meijer, W. Bolse, and C. Becher, 'Single photon emitters based on Ni/Si related defects in single crystalline diamond', *Applied Physics B*, vol. 102, no. 3, pp. 451–458, Mar. 2011, doi: 10.1007/s00340-011-4402-x.

[137] I. Aharonovich, S. Castelletto, D. A. Simpson, A. D. Greentree, and S. Prawer, 'Photophysics of chromium-related diamond single-photon emitters', *Phys Rev A (Coll Park)*, Jan. 2010, doi: 10.1103/PhysRevA.81.043813.

[138] T. Müller *et al.*, 'Wide-range electrical tunability of single-photon emission from chromium-based colour centres in diamond', *New J Phys*, vol. 13, no. 7, p. 75001, Jan. 2011, doi: 10.1088/1367-2630/13/7/075001.

[139] S. Castelletto, I. Aharonovich, B. C. Gibson, B. C. Johnson, and S. Prawer, 'Imaging and Quantum-Efficiency Measurement of Chromium Emitters in Diamond', *Phys Rev Lett*, vol. 105, no. 21, p. 217403, Nov. 2010, doi: 10.1103/PhysRevLett.105.217403.

[140] T. Lühmann *et al.*, 'Screening and engineering of colour centres in diamond', *J Phys D Appl Phys*, vol. 51, no. 48, p. 483002, Dec. 2018, doi: 10.1088/1361-6463/aadfab.

[141] D. E. Groom and S. R. Klein, 'Passage of particles through matter', *The European Physical Journal C*, vol. 15, no. 1–4, pp. 163–173, Mar. 2000, doi: 10.1007/BF02683419.

[142] J.W Mayer, L. Eriksson, and J.A. Davies, *Ion Implantation in Semiconductors*. New York: Academic, 1970.

[143] J. F. Ziegler, J. P. Biersack, and U. Littmark, *The stopping and range of ions in solids*. New York: Pergamon, 1985.

[144] J. F. Ziegler, M. D. Ziegler, and J. P. Biersack, 'SRIM – The stopping and range of ions in matter (2010)', *Nucl Instrum Methods Phys Res B*, vol. 268, no. 11–12, pp. 1818–1823, Jun. 2010, doi: 10.1016/j.nimb.2010.02.091.

[145] K. Nordlund *et al.*, 'Primary radiation damage: A review of current understanding and models', *Journal of Nuclear Materials*, vol. 512, pp. 450–479, Dec. 2018, doi: 10.1016/j.jnucmat.2018.10.027.

[146] R. Smith, *Atomic and ion collisions in solids and at surfaces. Theory, simulation and applications*. Loughborough Univ. of Technology (United Kingdom), 1997.

[147] 'https://commons.wikimedia.org/wiki/File:Heatspikecollisioncascade.png'.

[148] S. Was Gary, *Fundamentals of Radiation Materials Science*. Berlin, Heidelberg: Springer Berlin Heidelberg, 2007. doi: 10.1007/978-3-540-49472-0.

[149] M. Moneta and J. Czerbniak, 'Electronic stopping power of atoms for ions', *Nucl Instrum Methods Phys Res B*, vol. 90, no. 1–4, pp. 67–71, May 1994, doi: 10.1016/0168-583X(94)95514-X.

[150] D. Liljequist, 'A simple calculation of inelastic mean free path and stopping power for 50 eV-50 keV electrons in solids', *J Phys D Appl Phys*, vol. 16, no. 8, pp. 1567–1582, Aug. 1983, doi: 10.1088/0022-3727/16/8/023.

[151] J. P. Biersack, 'Calculation of projected ranges—analytical solutions and a simple general algorithm', *nuclear instruments and methods*, no. 182, pp. 199–206, 1981.

[152] M.O. El- Ghossain, 'Calculations of Stopping Power, and Range of Ions Radiation (Alpha Particles) Interaction with Different Materials and Human Body Parts', *International Journal of Physics*, vol. 5, no. 3, pp. 92–98, 2017.

[153] A. E. Rugar *et al.*, 'Generation of Tin-Vacancy Centers in Diamond via Shallow Ion Implantation and Subsequent Diamond Overgrowth', *Nano Lett*, vol. 20, no. 3, pp. 1614–1619, Mar. 2020, doi: 10.1021/acs.nanolett.9b04495.

[154] S. Pezzagna *et al.*, 'Creation of colour centres in diamond by collimated ion-implantation through nano-channels in mica', *Physica Status Solidi (A) Applications and Materials Science*, vol. 208, no. 9. John Wiley & Sons, Ltd, pp. 2017–2022, Sep. 2011. doi: 10.1002/pssa.201100455.

[155] W. Wu and S. Fahy, 'Molecular-dynamics study of single-atom radiation damage in diamond', *Phys Rev B*, vol. 49, no. 5, pp. 3030–3035, Jan. 1994, doi: 10.1103/PhysRevB.49.3030.

[156] D. Saada, J. Adler, and R. Kalish, 'Computer simulation of damage in diamond due to ion impact and its annealing', *Phys Rev B*, vol. 59, no. 10, pp. 6650–6660, Jan. 1999, doi: 10.1103/PhysRevB.59.6650.

[157] P. Olivero *et al.*, 'Direct fabrication of three-dimensional buried conductive channels in single crystal diamond with ion microbeam induced graphitization', *Diam Relat Mater*, vol. 18, no. 5–8, pp. 870–876, May 2009, doi: 10.1016/j.diamond.2008.10.068.

[158] D. Das, A. Kandasami, and M. S. Ramachandra Rao, 'Realization of highly conducting *n* -type diamond by phosphorus ion implantation', *Appl Phys Lett*, vol. 118, no. 10, Mar. 2021, doi: 10.1063/5.0039909.

[159] F. Picollo *et al.*, 'Fabrication and electrical characterization of three-dimensional graphitic microchannels in single crystal diamond', *New J Phys*, vol. 14, no. 5, p. 53011, May 2012, doi: 10.1088/1367-2630/14/5/053011.

[160] R. Kalish and S. Prawer, 'Graphitization of diamond by ion impact: Fundamentals and applications', *Nucl. Inst. Methods Phys. Res. B*, vol. 106, no. 1–4, pp. 492–499, Jan. 1995, doi: 10.1016/0168-583X(95)00758-X.

[161] T. Yamamoto *et al.*, 'Extending spin coherence times of diamond qubits by high-temperature annealing', *Phys. Rev. B*, vol. 88, no. 7, p. 75206, Aug. 2013, doi: 10.1103/physrevb.88.075206.

[162] V. P. Popov, L. N. Safronov, O. V Naumova, D. V Nikolaev, I. N. Kupriyanov, and Y. N. Palyanov, 'Conductive layers in diamond formed by hydrogen ion implantation and annealing', *Nucl. Instruments Methods Phys. Res. Sect. B Beam Interact. with Mater. Atoms*, vol. 282, pp. 100–107, 2012, doi: 10.1016/j.nimb.2011.08.050.

[163] P. Baeri and E. Rimini, 'Laser annealing of silicon', *Mater Chem Phys*, vol. 46, no. 2–3, pp. 169–177, Nov. 1996, doi: 10.1016/S0254-0584(97)80010-7.

[164] S. Ditalia Tchernij *et al.*, 'Fluorine-based color centers in diamond', *Sci Rep*, vol. 10, no. 1, pp. 1–7, Dec. 2020, doi: 10.1038/s41598-020-78436-6.

[165] E. Nieto Hernández *et al.*, 'Efficiency Optimization of Ge-V Quantum Emitters in Single-Crystal Diamond upon Ion Implantation and HPHT Annealing', *Adv Quantum Technol*, vol. 6, no. 8, Aug. 2023, doi: 10.1002/qute.202300010.

[166] P. Räcke, L. Pietzonka, J. Meijer, D. Spemann, and R. Wunderlich, 'Vacancy diffusion and nitrogen-vacancy center formation near the diamond surface', *Appl Phys Lett*, vol. 118, no. 20, p. 204003, May 2021, doi: 10.1063/5.0046031.

[167] J. O. Orwa *et al.*, 'An upper limit on the lateral vacancy diffusion length in diamond', *Diam Relat Mater*, vol. 24, pp. 6–10, Apr. 2012, doi: 10.1016/j.diamond.2012.02.009.

[168] R. Kingi, Y. Wang, S. J. Fonash, O. Awadelkarim, and J. Mehlhaff, 'Comparison Between Rapid Thermal and Furnace Annealing for A-Si Solid Phase Crystallization', *MRS Proceedings*, vol. 424, p. 237, Feb. 1996, doi: 10.1557/PROC-424-237.

[169] P. Acosta Alba *et al.*, 'Nanosecond Laser Annealing for Phosphorous Activation in Ultra-Thin Implanted Silicon-On-Insulator Substrates', in *2016 21st International Conference on Ion Implantation Technology (IIT)*, IEEE, Sep. 2016, pp. 1–4. doi: 10.1109/IIT.2016.7882896.

[170] A. L. Robinson, 'Femtosecond Laser Annealing of Silicon', *Science (1979)*, vol. 226, no. 4672, pp. 329–330, Oct. 1984, doi: 10.1126/science.226.4672.329.

[171] J. Engel *et al.*, 'Combining femtosecond laser annealing and shallow ion implantation for local color center creation in diamond', *Appl Phys Lett*, vol. 122, no. 23, Jun. 2023, doi: 10.1063/5.0143922.

[172] E. Murray, 'Quantum photonics hybrid integration platform', *Appl. Phys. Lett.*, vol. 107, p. 171108, 2015.

[173] A. Sipahigil, 'An Integrated Diamond Nanophotonics Platform for Quantum Optical Networks', in *Conference on Lasers and Electro-Optics*, Washington, D.C.: OSA, 2017, p. FTh3H.4. doi: 10.1364/CLEO_QELS.2017.FTh3H.4.

[174] D. Kim, M. I. Ibrahim, C. Foy, M. E. Trusheim, R. Han, and D. R. Englund, 'A CMOS-integrated quantum sensor based on nitrogen–vacancy centres', *Nat Electron*, vol. 2, no. 7, pp. 284–289, Jul. 2019, doi: 10.1038/S41928-019-0275-5.

[175] T. Lühmann, R. John, R. Wunderlich, J. Meijer, and S. Pezzagna, 'Coulomb-driven single defect engineering for scalable qubits and spin sensors in diamond', *Nat Commun*, vol. 10, no. 1, p. 4956, Oct. 2019, doi: 10.1038/s41467-019-12556-0.

[176] B. N. Murdin, N. Cassidy, D. Cox, R. Webb, and R. J. Curry, 'Error Rates in Deterministic Ion Implantation for Qubit Arrays', *physica status solidi (b)*, vol. 258, no. 6, Jun. 2021, doi: 10.1002/pssb.202000615.

[177] E. N. Hernandez *et al.*, 'Efficient fabrication of high-density ensembles of color centers via ion implantation on a hot diamond substrate', Oct. 2023.

[178] H. Hofsäss and G. Lindner, 'Emission channeling and blocking', *Phys Rep*, vol. 201, no. 3, pp. 121–183, Mar. 1991, doi: 10.1016/0370-1573(91)90121-2.

[179] U. Wahl *et al.*, 'Position-sensitive Si pad detectors for electron emission channeling experiments', *Nucl Instrum Methods Phys Res A*, vol. 524, no. 1–3, pp. 245–256, May 2004, doi: 10.1016/j.nima.2003.12.044.

[180] T. Schröder *et al.*, 'Scalable focused ion beam creation of nearly lifetime-limited single quantum emitters in diamond nanostructures', *Nat Commun*, vol. 8, no. 1, p. 15376, May 2017, doi: 10.1038/ncomms15376.

[181] B. J. M. Hausmann *et al.*, 'Single-color centers implanted in diamond nanostructures', *New J Phys*, vol. 13, no. 4, p. 45004, Jan. 2011, doi: 10.1088/1367-2630/13/4/045004.

[182] K. Groot-Berning *et al.*, 'Deterministic Single-Ion Implantation of Rare-Earth Ions for Nanometer-Resolution Color-Center Generation', *Phys Rev Lett*, vol. 123, no. 10, p. 106802, Sep. 2019, doi: 10.1103/PhysRevLett.123.106802.

[183] T. Matsukawa, T. Fukai, S. Suzuki, K. Hara, M. Koh, and I. Ohdomari, 'Development of single-ion implantation — controllability of implanted ion number', *Appl Surf Sci*, vol. 117–118, pp. 677–683, Jun. 1997, doi: 10.1016/S0169-4332(97)80163-8.

[184] D. N. Jamieson *et al.*, 'Controlled shallow single-ion implantation in silicon using an active substrate for sub-20-keV ions', *Appl Phys Lett*, vol. 86, no. 20, p. 202101, May 2005, doi: 10.1063/1.1925320.

[185] C. Sahin, P. Geppert, A. Müllers, and H. Ott, 'A high repetition deterministic single ion source', *New J Phys*, vol. 19, no. 12, p. 123005, Dec. 2017, doi: 10.1088/1367-2630/aa9461.

[186] R. Hellborg, Ed., *Electrostatic Accelerators*. Berlin, Heidelberg: Springer Berlin Heidelberg, 2005. doi: 10.1007/b138596.

[187] I. Ahmad and W. Akram, 'Introductory Chapter: Introduction to Ion Implantation', in *Ion Implantation - Research and Application*, InTech, 2017. doi: 10.5772/intechopen.68785.

[188] 'https://elearning.iaea.org/m2/mod/scorm/player.php?a=2110&currentorg=Beam_transport_ORG&scoid=5238'.

[189] B. Zhou, H. Zhang, P. Zhang, W. Li, and S. An, 'Design and optimization study of a duoplasmatron ion source for high-intensity proton beam', *Nucl Instrum Methods Phys Res A*, vol. 1010, p. 165550, Sep. 2021, doi: 10.1016/j.nima.2021.165550.

[190] 'https://www.cmam.uam.es/facilities/accelerator/duoplasmatron-ion-source/'.

[191] Roy Middleton, *A Negative-Ion Cookbook*. Philadelphia, 1989.

[192] G. T. Caskey, R. A. Douglas, H. T. Richards, and H. Vernon Smith, 'A simple negative-ion sputter source', *Nuclear Instruments and Methods*, vol. 157, no. 1, pp. 1–7, Nov. 1978, doi: 10.1016/0029-554X(78)90581-5.

[193] 'https://en.wikipedia.org/wiki/Einzel_lens'.

[194] 'https://www.orsayphysics.com/what-is-fib#:~:text=The%20Focused%20Ion%20Beam%20(FIB,sample%20in%20a%20vacuum%20chamber.'

[195] L. Bischoff, P. Mazarov, L. Bruchhaus, and J. Gierak, 'Liquid metal alloy ion sources—An alternative for focussed ion beam technology', *Appl Phys Rev*, vol. 3, no. 2, p. 021101, Jun. 2016, doi: 10.1063/1.4947095.

[196] M. Wortmann, A. Ludwig, J. Meijer, D. Reuter, and A. D. Wieck, 'High-resolution mass spectrometer for liquid metal ion sources', *Review of Scientific Instruments*, vol. 84, no. 9, Sep. 2013, doi: 10.1063/1.4822275.

[197] J P Gauyacq and A G Borisov, 'Charge transfer in atom–surface collisions: effect of the presence of adsorbates on the surface', *J. Phys.: Condens. Matter*, vol. 10, pp. 6585–6619, 1998.

[198] G. Huszka and M. A. M. Gijs, 'Super-resolution optical imaging: A comparison', *Micro and Nano Engineering*, vol. 2, pp. 7–28, Mar. 2019, doi: 10.1016/j.mne.2018.11.005.

[199] *Encyclopedia of Optical Engineering*. Taylor & Francis, 2011. doi: 10.1081/E-EOE.

[200] R. H. Webb, 'Confocal optical microscopy', *Reports on Progress in Physics*, vol. 59, no. 3, pp. 427–471, 1996, doi: 10.1088/0034-4885/59/3/003.

[201] 'http://www.physicsbootcamp.org/section-circular-aperture-and-angular-resolution-light.html'.

[202] 'https://www.micro-shop.zeiss.com/en/us/shop/objectives/422392-9961- 000/Objective-EC-Epiplan-Neofluar-100x-0.90-BD-DIC-M27'.

[203] C. J. R. Sheppard, 'Resolution and super-resolution', *Microsc Res Tech*, vol. 80, no. 6, pp. 590–598, Jun. 2017, doi: 10.1002/jemt.22834.

[204] S. Astner and M. Ulrich, 'Konfokale Laserscan-Mikroskopie', *Der Hautarzt*, vol. 61, no. 5, pp. 421–428, May 2010, doi: 10.1007/s00105-009-1878-y.

[205] M. Alkahtani *et al.*, 'Tin-vacancy in diamonds for luminescent thermometry', *Appl Phys Lett*, vol. 112, no. 24, p. 241902, Jun. 2018, doi: 10.1063/1.5037053.

[206] H. Wang, M. E. Trusheim, L. Kim, H. Raniwala, and D. R. Englund, 'Field programmable spin arrays for scalable quantum repeaters', *Nat Commun*, vol. 14, no. 1, Dec. 2023, doi: 10.1038/s41467-023-36098-8.

[207] S. Ditalia Tchernij *et al.*, 'Spectral features of Pb-related color centers in diamond – a systematic photoluminescence characterization', *New J Phys*, vol. 23, no. 6, p. 63032, Jun. 2021, doi: 10.1088/1367-2630/ac038a.

[208] H. Yamano *et al.*, 'Charge state stabilization of shallow nitrogen vacancy centers in diamond by oxygen surface modification', *Jpn J Appl Phys*, vol. 56, no. 4S, p. 04CK08, Apr. 2017, doi: 10.7567/JJAP.56.04CK08.

[209] L. Rondin *et al.*, 'Surface-induced charge state conversion of nitrogen-vacancy defects in nanodiamonds', *Phys Rev B Condens Matter Mater Phys*, vol. 82, no. 11, pp. 1–5, Jan. 2010, doi: 10.1103/PhysRevB.82.115449.

[210] S. Szunerits and R. Boukherroub, 'Different strategies for functionalization of diamond surfaces', *Journal of Solid State Electrochemistry*, vol. 12, no. 10, pp. 1205–1218, Jan. 2008, doi: 10.1007/s10008-007-0473-3.

[211] H. Ma, N. Sheng, M. Govoni, and G. Galli, 'First-principles studies of strongly correlated states in defect spin qubits in diamond', *Physical Chemistry Chemical Physics*, vol. 22, no. 44, pp. 25522–25527, 2020, doi: 10.1039/D0CP04585C.

[212] E. A. Ekimov, S. G. Lyapin, and M. V. Kondrin, 'Tin-vacancy color centers in micro- and polycrystalline diamonds synthesized at high pressures', *Diam Relat Mater*, vol. 87, pp. 223–227, Aug. 2018, doi: 10.1016/j.diamond.2018.06.014.

[213] J. Görlitz *et al.*, 'Spectroscopic investigations of negatively charged tin-vacancy centres in diamond', *New J Phys*, vol. 22, no. 1, p. 013048, Jan. 2020, doi: 10.1088/1367-2630/ab6631.

[214] M. E. Trusheim *et al.*, 'Transform-Limited Photons From a Coherent Tin-Vacancy Spin in Diamond', *Phys Rev Lett*, vol. 124, no. 2, p. 023602, Jan. 2020, doi: 10.1103/PhysRevLett.124.023602.

[215] T. Lühmann, J. Küpper, S. Dietel, R. Staacke, J. Meijer, and S. Pezzagna, 'Charge-State Tuning of Single SnV Centers in Diamond', *ACS Photonics*, vol. 7, no. 12, pp. 3376–3385, 2020, doi: 10.1021/acsphotonics.0c01123.

[216] H. Pinto *et al.*, 'First-principles studies of the effect of (001) surface terminations on the electronic properties of the negatively charged nitrogen-vacancy defect in diamond', *Phys Rev B*, vol. 86, no. 4, p. 045313, Jul. 2012, doi: 10.1103/PhysRevB.86.045313.

[217] S. J. Sque, R. Jones, and P. R. Briddon, 'Structure, electronics, and interaction of hydrogen and oxygen on diamond surfaces', *Phys Rev B*, vol. 73, no. 8, p. 085313, Feb. 2006, doi: 10.1103/PhysRevB.73.085313.

[218] C. Su and J.-C. Lin, 'Thermal desorption of hydrogen from the diamond C(100) surface', *Surf Sci*, vol. 406, no. 1–3, pp. 149–166, May 1998, doi: 10.1016/S0039-6028(98)00107-1.

[219] V. L. Kuznetsov, I. L. Zilberberg, Yu. V. Butenko, A. L. Chuvilin, and B. Segall, 'Theoretical study of the formation of closed curved graphite-like structures during annealing of diamond surface', *J Appl Phys*, vol. 86, no. 2, pp. 863–870, Jul. 1999, doi: 10.1063/1.370816.

[220] M. M. Hassan and K. Larsson, 'Effect of Surface Termination on Diamond (100) Surface Electrochemistry', *The Journal of Physical Chemistry C*, vol. 118, no. 40, pp. 22995–23002, Oct. 2014, doi: 10.1021/jp500685q.

[221] R. E. Thomas, R. A. Rudder, and R. J. Markunas, 'Thermal desorption from hydrogenated and oxygenated diamond (100) surfaces', *Journal of Vacuum Science & Technology A: Vacuum, Surfaces, and Films*, vol. 10, no. 4, pp. 2451–2457, Jul. 1992, doi: 10.1116/1.577983.

[222] J. M. Binder *et al.*, 'Qudi: A modular python suite for experiment control and data processing', *SoftwareX*, vol. 6, pp. 85–90, 2017, doi: 10.1016/j.softx.2017.02.001.

[223] E. Neu, M. Agio, and C. Becher, 'Photophysics of single silicon vacancy centers in diamond: implications for single photon emission', *Opt Express*, vol. 20, no. 18, p. 19956, Jan. 2012, doi: 10.1364/OE.20.019956.

[224] A. Yu. Neliubov *et al.*, 'Enigmatic color centers in microdiamonds with bright, stable, and narrow-band fluorescence', *Phys Rev B*, vol. 107, no. 8, p. L081406, Feb. 2023, doi: 10.1103/PhysRevB.107.L081406.

[225] M. E. Trusheim *et al.*, 'Lead-Related Quantum Emitters in Diamond', in *Conference on Lasers and Electro-Optics*, Washington, D.C.: OSA, 2018, p. FTu4H.2. doi: 10.1364/CLEO_QELS.2018.FTu4H.2.

[226] E. I. Rosenthal *et al.*, 'Microwave Spin Control of a Tin-Vacancy Qubit in Diamond', *Phys Rev X*, vol. 13, no. 3, p. 031022, Aug. 2023, doi: 10.1103/PhysRevX.13.031022.

[227] A. E. Rugar, C. Dory, S. Sun, and J. Vučković, 'Characterization of optical and spin properties of single tin-vacancy centers in diamond nanopillars', *Phys Rev B*, vol. 99, no. 20, p. 205417, May 2019, doi: 10.1103/PhysRevB.99.205417.

[228] S. Blakley *et al.*, 'Fiber-Optic Quantum Thermometry with Germanium-Vacancy Centers in Diamond', *ACS Photonics*, vol. 6, no. 7, pp. 1690–1693, 2019, doi: 10.1021/acsphotonics.9b00206.

[229] T. Müller *et al.*, 'Optical signatures of silicon-vacancy spins in diamond', *Nat Commun*, vol. 5, no. 1, p. 3328, 2014, [Online]. Available: http://www.nature.com/articles/ncomms4328

[230] B. Pingault *et al.*, 'Coherent control of the silicon-vacancy spin in diamond', *Nat Commun*, vol. 8, no. 1, p. 15579, May 2017, doi: 10.1038/ncomms15579.

[231] L. J. Rogers *et al.*, 'Electronic structure of the negatively charged silicon-vacancy center in diamond', *Phys Rev B*, no. 23, Jan. 2014, doi: 10.1103/PhysRevB.89.235101.

[232] C. T. Nguyen *et al.*, 'All-optical nanoscale thermometry with silicon-vacancy centers in diamond', *Appl. Phys. Lett.*, vol. 112, no. 20, pp. 3–7, Jan. 2018, doi: 10.1063/1.5029904.

[233] M. E. Trusheim *et al.*, 'Lead-related quantum emitters in diamond', *Phys Rev B*, vol. 99, no. 7, p. 75430, Feb. 2019, doi: 10.1103/PHYSREVB.99.075430.

[234] N. Aslam, G. Waldherr, P. Neumann, F. Jelezko, and J. Wrachtrup, 'Photo-induced ionization dynamics of the nitrogen vacancy defect in diamond investigated by single-shot charge state detection', *New J Phys*, vol. 15, no. 1, p. 13064, Jan. 2013, doi: 10.1088/1367-2630/15/1/013064.

[235] C. X. Li *et al.*, 'UV-induced charge-state conversion from the negatively to neutrally charged nitrogen-vacancy centers in diamond', *J Appl Phys*, vol. 132, no. 21, Dec. 2022, doi: 10.1063/5.0125286.

[236] S. Häußler *et al.*, 'Photoluminescence excitation spectroscopy of SiV− and GeV− color center in diamond', *New J Phys*, vol. 19, no. 6, p. 63036, Jul. 2017, doi: 10.1088/1367-2630/AA73E5.

[237] A. Pershin, G. Barcza, Ö. Legeza, and A. Gali, 'Highly tunable magneto-optical response from magnesium-vacancy color centers in diamond', *npj Quantum Inf*, vol. 7, no. 1, p. 99, Jun. 2021, doi: 10.1038/s41534-021-00439-6.

[238] U. Wahl, *Advances in electron emission channeling measurements in semiconductors*, vol. 129. 2000. doi: 10.1023/A:1012697429920.

[239] E. Osmic, S. Pezzagna, T. Lühmann, W. Böhlmann, and J. Meijer, 'Unusual temperature dependence of the photoluminescence emission of MgV centers in diamond', *Appl Phys Lett*, vol. 121, no. 8, Aug. 2022, [Online]. Available: https://pubs.aip.org/aip/apl/article-abstract/121/8/084101/2834246/Unusual-temperature-dependence-of-the?redirectedFrom=fulltext

[240] Y. P. Varshni, 'Temperature dependence of the energy gap in semiconductors', *Physica*, vol. 34, no. 1, pp. 149–154, Jan. 1967, doi: 10.1016/0031-8914(67)90062-6.

[241] B. Dong *et al.*, 'Temperature dependence of optical centers in Ib diamond characterized by photoluminescence spectra', *Diam Relat Mater*, vol. 116, Jun. 2021, doi: 10.1016/J.DIAMOND.2021.108389.

[242] M. W. Doherty *et al.*, 'Temperature shifts of the resonances of the <math> <msup> <mi mathvariant="normal">NV</mi> <mo>−</mo> </msup> </math> center in diamond', *Phys Rev B*, vol. 90, no. 4, p. 41201, Jul. 2014, doi: 10.1103/PhysRevB.90.041201.

[243] J. N. Becker *et al.*, 'Ultrafast all-optical coherent control of single silicon vacancy colour centres in diamond', *Nat. Commun.*, vol. 7, p. 13512, Nov. 2016, doi: 10.1038/ncomms13512.

[244] S. Pezzagna, B. Naydenov, F. Jelezko, J. Wrachtrup, and J. Meijer, 'Creation efficiency of nitrogen-vacancy centres in diamond', *New J Phys*, vol. 12, no. 6, p. 65017, Jun. 2010, doi: 10.1088/1367-2630/12/6/065017.

[245] D. G. Monticone *et al.*, 'Native NIR-emitting single colour centres in CVD diamond', *New J. Phys.*, vol. 16, no. 5, pp. 1–18, Jan. 2014, doi: 10.1088/1367-2630/16/5/053005.

[246] J. W. Steeds, T. J. Davis, S. J. Charles, J. M. Hayes, and J. E. Butler, '3H luminescence in electron-irradiated diamond samples and its relationship to self-interstitials', *Diam Relat Mater*, vol. 8, no. 10, pp. 1847–1852, Oct. 1999, doi: 10.1016/S0925-9635(99)00144-2.

[247] J. Forneris *et al.*, 'Electrical control of deep NV centers in diamond by means of sub-superficial graphitic micro-electrodes', *Carbon N Y*, vol. 113, pp. 76–86, 2017, doi: 10.1016/j.carbon.2016.11.031.

[248] P. Olivero *et al.*, 'Characterization of three-dimensional microstructures in single-crystal diamond', *Diam Relat Mater*, vol. 15, no. 10, pp. 1614–1621, Jan. 2006, doi: 10.1016/J.DIAMOND.2006.01.018.

[249] M. L. Goldman *et al.*, 'State-selective intersystem crossing in nitrogen-vacancy centers', *Phys Rev B*, vol. 91, no. 16, p. 165201, Apr. 2015, doi: 10.1103/PhysRevB.91.165201.

10 Publications

The research activity performed during the PhD contributed to 6 papers. The first 4 papers are those explained with detail in Chapter 4, in particular my role in each publication was primarily related to the optical characterisation. In detail, the following list report the title of the publication and the role:

- Fluorine-based color centers in diamond: my role was related to the optical characterisation of the MeV implanted sample and to the research of single emitters, finally not reported in the final manuscript.
- Spectral features of Pb-related color centers in diamond – a systematic photoluminescence characterization: my role was associated to the characterisation of the single emitter level under blue light illumination and the data analysis of the latter.
- Spectral Emission Dependence of Tin-Vacancy Centers in Diamond from Thermal Processing and Chemical Functionalization. My role was dual, the partial data acquisition and analysis along with the annealing and surface functionalisation.
- Magnesium-Vacancy optical center in diamond: my role was centred on the annealing steps along with the data acquisition and analysis of the room temperature characterisation, both at ensemble and single emitter level.

Additional work was carried out during the PhD that led to publications, namely:

- Engineering Multicolor Radiative Centers in hBN Flakes by Varying the Electron Beam Irradiation Parameters. The main activity carried is centred on the optical characterisation at the confocal microscope.

- Efficiency Optimization of Ge-V Quantum Emitters in Single-Crystal Diamond upon Ion Implantation and HPHT Annealing. I primarily characterise at ensemble level the Ge implanted regions after the HPHT annealing and contributed to the data analysis. Secondly, I performed at the University of Leipzig the ion implantation on the LPLT annealed sample with Ge ions.

scientific reports

Check for updates

OPEN

Fluorine-based color centers in diamond

S. Ditalia Tchernij[1,2,3], T. Lühmann[4], E. Corte[1,2], F. Sardi[1], F. Picollo[1,2], P. Traina[3], M. Brajković[5], A. Crnjac[5], S. Pezzagna[4], Ž. Pastuović[6], I. P. Degiovanni[3,2], E. Moreva[3], P. Aprà[1,2], P. Olivero[1,2,3], Z. Siketić[5], J. Meijer[4], M. Genovese[3,2] & J. Forneris[1,2,3]✉

We report on the creation and characterization of the luminescence properties of high-purity diamond substrates upon F ion implantation and subsequent thermal annealing. Their room-temperature photoluminescence emission consists of a weak emission line at 558 nm and of intense bands in the 600–750 nm spectral range. Characterization at liquid He temperature reveals the presence of a structured set of lines in the 600–670 nm spectral range. We discuss the dependence of the emission properties of F-related optical centers on different experimental parameters such as the operating temperature and the excitation wavelength. The correlation of the emission intensity with F implantation fluence, and the exclusive observation of the afore-mentioned spectral features in F-implanted and annealed samples provides a strong indication that the observed emission features are related to a stable F-containing defective complex in the diamond lattice.

Diamond has been widely investigated as an appealing material for quantum optics and quantum information processing applications, due to the availability of several classes of optically active defects (usually referred to as "color centers") that can be suitably engineered in its crystal structure[1–3]. To date, the most prominent type of defect is the so-called negatively-charged nitrogen-vacancy center (NV^-), due to several key features of this system, namely: photo-stability at room temperature, high quantum efficiency and most importantly unique spin properties with great potential for applications in quantum sensing and computing[4–9].

The need for single-photon emitters displaying desirable opto-physical properties (high emission rate, narrow linewidth) has also motivated the discovery and characterization of several classes of optical centers in diamond alternative to the NV complex, based (among others) on group-IV impurities[10] (Si[11,12], Ge[13,14], Sn[15,16], Pb[17,18]) and noble gases (He, Xe[19–21]). In this context, ion implantation represents a powerful and versatile tool to engineer a broad range of different types of color centers, allowing for the fine control of key parameters such as ion species and energy, as well as irradiation fluence to determine the type and density of defect complexes[22,23].

Up to now though, the number of the emitters characterized by a reproducible fabrication process is fairly limited, and a systematic investigation in this field is still to be finalized. Thus, the fabrication of novel luminescent defects with desirable properties upon the implantation of selected ion species still represents a crucial strategy to achieve further advances in the field. Following from a previous report with preliminary results on this system[24], in this work we report on the systematic characterization in photoluminescence (PL) under different optical excitation wavelengths of F-related color centers in diamond created upon ion implantation and subsequent annealing.

Experimental

The characterization of F-related emission here presented was performed on a type-IIa single-crystal diamond sample (*Sample #1*) produced by ElementSix with Chemical Vapor Deposition technique, namely a $2\times2\times0.5$ mm^3 "electronic grade" substrate having nominal concentrations of both substitutional nitrogen and boron impurities below the 5 ppb level.

The sample was implanted with 50 keV F^- ions at the low-energy accelerator of the University of Leipzig. Several circular regions of ~ 175 μm diameter were irradiated at varying fluences in the 5×10^{10}–5×10^{15} cm^{-2} range by the use of a custom beam collimator. An additional region was implanted with 1.47 MeV F^{2+} ions (1×10^{13} cm^{-2} fluence) at the Laboratory for Ion Beam Interactions of the Ruđer Bošković Institute. The sample

[1]Physics Department, University of Torino, 10125 Turin, Italy. [2]Istituto Nazionale Di Fisica Nucleare (INFN), Sezione Di Torino, 10125 Turin, Italy. [3]Istituto Nazionale Di Ricerca Metrologica (INRiM), 10135 Turin, Italy. [4]Applied Quantum Systems, Felix-Bloch Institute for Solid-State Physics, Universität Leipzig, 04103 Leipzig, Germany. [5]Laboratory for Ion Beam Interactions, Ruđer Bošković Institute, 10000 Zagreb, Croatia. [6]Centre for Accelerator Science, Australian Nuclear Science and Technology Organisation, New Illawarra Road, Lucas Heights, NSW 2234, Australia. ✉email: jacopo.forneris@unito.it

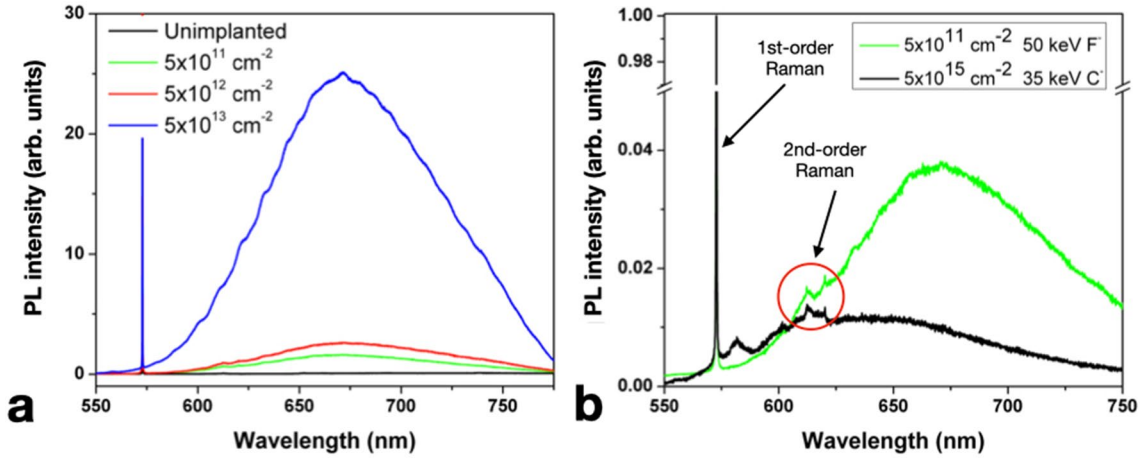


Figure 1. (**a**) PL spectra acquired under 532 nm laser excitation wavelength from regions implanted with different 50 keV F- ion fluences in the 5×10^{11}–1×10^{13} cm^{-2} range. The PL spectrum of a pristine region of the sample is included for the sake of comparison (black line). (**b**) Comparison of the PL spectrum acquired from the region implanted with 5×10^{11} cm^{-2} 50 keV F-ion fluence (green line) with a sample region irradiated with 35 keV C$^-$ ions at 5×10^{15} cm^{-2} fluence (black line). Both curves are normalized to the first-order Raman peak. The first-order and second-order Raman features of diamond are highlighted.

was then processed with a high-temperature thermal annealing (1200 °C, 4 h in vacuum at ~ 10^{-6} mbar pressure) and a subsequent oxygen plasma treatment, with the purpose of minimizing the background fluorescence from surface contaminations. To compare the luminescence intensity of F-related ensembles with the well-known emission properties of the NV center, a nominally identical sample (Sample #2) was implanted at the ANSTO *Centre for Accelerator Science* with 10 keV N^+ ions at a fluence of 10^{14} ions cm^{-2}. The implanted sample was then annealed at 950 °C for 2 h.

A preliminary PL characterization was performed using a Horiba Jobin–Yvon HR800 micro-Raman spectrometer equipped with a CW excitation laser at 532 nm wavelength.

Temperature-dependent PL measurements were performed using a custom-made cryogenic single-photon confocal microscope exploiting a closed-cycle optical cryostat operating in the 4–300 K temperature range. Optical excitation was provided through a 100 × air objective (0.85 NA) by a set of CW laser diodes with emission wavelengths of 405 nm, 488 nm and 520 nm. A suitable set of optical filters enabled the detection of PL emission at wavelengths larger than 550 nm. The PL spectra were acquired using a single-grating monochromator (1200 grooves mm^{-1}, 600 nm blaze) fiber-coupled to a Si-single-photon detector operating in Geiger mode. The spectral resolution of the apparatus was estimated to be ≤ 4 nm.

Results

PL emission at room temperature. Ensemble PL spectra acquired at room temperature are presented in Fig. 1 for different F implantation fluences.

The emission spectra reported in Fig. 1a were acquired from the implanted regions under 532 nm laser excitation (26.2 mW laser power) and exhibit a broad, intense and apparently unstructured PL band in the 600–800 nm spectral region (fluorine-related band, FB1, in the following), with a maximum centered at ~ 670 nm. Although not particularly characteristic in its spectral features, the observation of this band is consistent with what reported in Ref.[24] under 488 nm excitation, where a broad emission band in the 590–800 was formed upon F implantation at a 5×10^{14} cm^{-2} ion fluence and a subsequent thermal annealing at 1600 °C.

It is worth mentioning that the FB1 band is partially spectrally overlapping with the emission of the NV^0 and NV^-center in diamond (i.e. PL bands in the 575–650, and 638–750 nm range, respectively, typically observed together in ensemble PL spectra[4]).

In order to benchmark the PL intensity of the F-related emission with respect to the one from NV centers, the photon count rate of the region implanted at 1×10^{13} cm^{-2} fluence was compared with that of Sample #2 (10 keV N^+ implantation at 1×10^{14} cm^{-2} fluence) under the same experimental conditions (i.e.: 488 nm laser excitation at 2 mW optical power, long-pass 500 nm spectral filtering, and 488 nm and 520 nm notch filters to remove the laser line and the first-order Raman scattering).

Despite the F ion implantation fluence being 10 times smaller, the measured ensemble PL emission intensity from F-related centers of 5.4 Mcps was ~ 1.7 times higher with respect to what measured (3.2 Mcps) from the NV-centers ensemble. It is worth stressing that this result cannot be explicitly related to the brightness of individual F-related centers, since the efficiency in the formation of the active optical complex has yet to be determined. In this sense, the more intense PL emission at the ensemble level might be also caused by a higher formation efficiency with respect to the NV center. A direct comparison of the formation efficiency for the two types of color centers could not be performed, due to the fact that the dependence of the NV-ensemble PL emission intensity from the N^+ implantation fluence is close to saturation at the considered value of 1×10^{14} cm^{-2} [25]. If the PL emission intensities from ensembles of both types are assumed to have reached a saturation with respect to

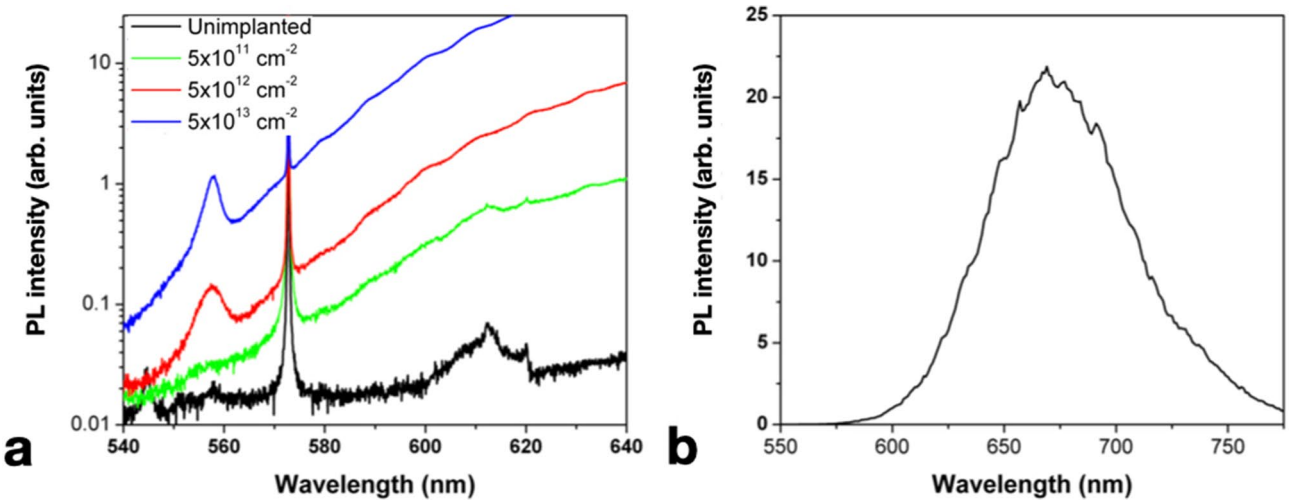


Figure 2. (**a**) Inset of Fig. 1a in the 540–660 nm spectral range. The axes are rescaled to highlight the PL emission peak at 558 nm. (**b**) PL spectrum acquired under 520 nm laser excitation from a sample region implanted with 1.47 MeV F^{2+} ions at 1×10^{13} cm^{-2} fluence.

irradiation fluence, then F-related centers would be estimated to be $5.4/3.2 \cong 1.7$ times brighter than NV centers. In the opposite case, if a full linear dependence of the ensemble PL emission intensity from ion irradiation fluence can still be assumed for both types of color centers, then the different fluence values should be taken into account, leading to a ~ 15 brightness increase estimation. Realistically, the most accurate estimation of the brightness increase can be assumed to be comprised between these boundary values. It is worth remarking that the higher PL emission intensity from the F-related ensemble is in line with the observation in Ref.[26] on the increased conversion efficiency of NV centers in N-implanted diamond upon the introduction of dopants with high-electron affinity such as S, O. According to this scheme, the optical activation of defects based on halogen impurities might follow a similar thermodynamic pathway.

In addition to the above discussion, to further rule out the possibility that the observed spectral feature can be attributed to NV-related emission, a pristine region of the same sample was irradiated with C^- ions at 35 keV energy (5×10^{15} cm^{-2} f1uence) and processed alongside the F-implanted region with the same annealing parameters. The PL spectrum from this test area, acquired under the same excitation conditions, is reported in Fig. 1b for the sake of comparison. It displays a significantly weaker band centered at 640 nm, whose intensity is comparable with the second-order Raman scattering of diamond observed at ~ 620 nm (corresponding to a 2664 cm^{-1} Raman shift), while not exhibiting any features similar to those observed for the FB1 band. This observation is indicative of the fact that the FB1 band is neither related to the formation of NV centers upon the introduction of lattice vacancies in a N-containing diamond substrate, nor to generic ion-induced structural damage.

In addition, the substantial increase (Fig. 1a) of the FB1 intensity at increasing F implantation fluences supports our attribution of this spectral feature to a stable F-containing defect in the diamond lattice.

Figure 2a displays a zoom-in in the 540–640 nm spectral range of the PL data reported in Fig. 1a. A weak PL peak at 558 nm appears in the regions implanted with F ions at fluences higher than 5×10^{12} cm^{-2}. This peak was consistently observed in all of the room-temperature measurements performed on the F-implanted regions, while being absent from the test spectrum reported in Fig. 1b. While the peak position might be compatible with a 557 nm feature observed in cathodoluminescence from electron-irradiated diamonds that was previously attributed to an interstitial-type defect (ITD in the following)[19,27], a different interpretation is suggested by the persistence of the peak upon 1200 °C annealing (ITD is reported to anneal out at 700 °C[28]). Furthermore, it is worth remarking that this spectral feature was not reported in a previous PL characterization of C-implanted diamond[29], and analogously has not been observed in our measurements in nominally identical samples implanted with a wide range of different ion species. Based on these considerations, a tentative attribution of the 558 nm line as related to an F-containing defect is made, although its relationship with the FB1 band is unclear on the basis of the available dataset.

Finally, Fig. 2b shows a PL spectrum acquired under 520 nm laser excitation (5.6 mW power, 565 nm long-pass filter) from the region implanted with 1.47 MeV F^{2+} ions at 1×10^{13} cm^{-2} fluence. Since the spectrum was acquired with the cryogenic single-photon confocal microscope rather than with the micro-Raman spectrometer, the PL intensity scale cannot be quantitatively compared with that of the previously discussed measurements. However, it is worth noting that Fig. 2b displays the same spectral features reported in Fig. 1a. This observation further corroborates the attribution of the emission spectrum to a F-containing lattice defect, and indicates that such optical center can be fabricated upon the implantation of fluorine ions of both keV and MeV energies (possibly with different creation yields, whose investigation is beyond the scope of this work), thus ruling out its possible attribution to intrinsic lattice defects related to high-energy irradiation effects.

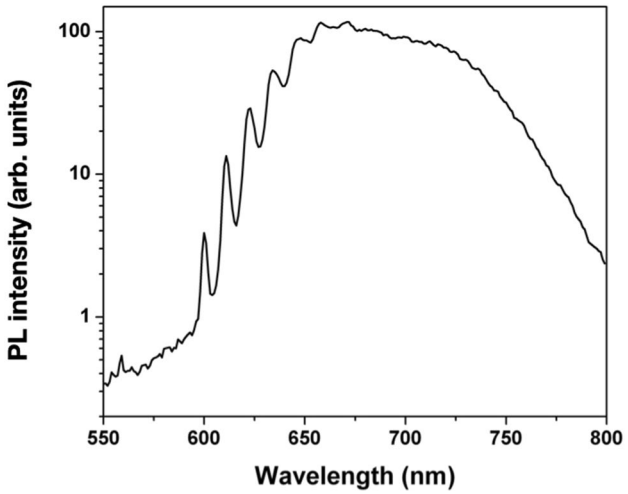


Figure 3. PL spectrum acquired at 4.5 K temperature under 488 nm laser excitation from the region of sample #1 implanted with at 5×10^{13} cm^{-2} fluence.

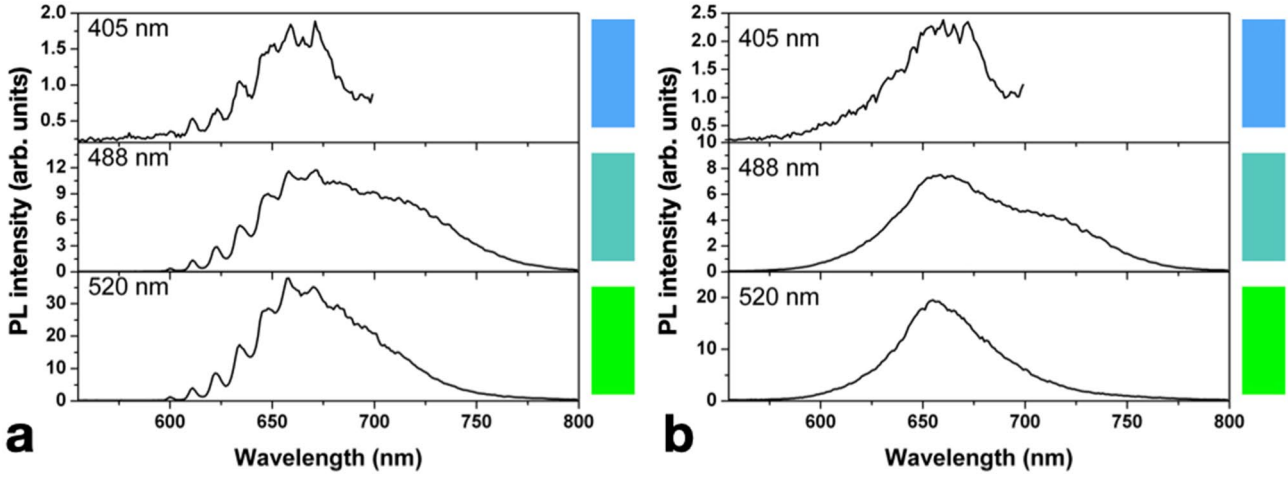


Figure 4. Ensemble PL spectra acquired at 4.5 K (**a**) and room temperature (**b**) from the region of sample #1 implanted at a fluence of 5×10^{13} cm^{-2} under different excitation wavelenghts.

PL emission at variable temperatures. In order to gain a deeper insight into the spectral features of F-related color centers with respect to the aforementioned results and the previous report in Ref.[24], low-temperature PL measurements were performed at different excitation wavelengths. Figure 3 displays an ensemble PL spectrum acquired at 4.5 K under 488 nm excitation (3.6 mW laser power) from a region implanted at 5×10^{13} cm^{-2} fluence. At the reported temperature, the FB1 band reveals an articulated structure of different emission lines, the most prominent being located at 600, 611, 623, 634, 647, 658 and 671 nm. The linewidth estimation is limited by the spectral resolution (~4 nm) of the measurement system. In Fig. 4, PL spectra acquired from the same region both at 4.5 K and at room temperature are reported for different laser excitation wavelengths, including 405 nm (10 mW laser power) and 520 nm (2.4 mW). It is worth noting that the spectra acquired using the 405 nm laser were limited to the 500–700 nm spectral range due to the luminescence of optical elements employed in the confocal microscopy setup at higher wavelengths. The persistence of the emission lines at the same wavelengths under different excitation sources indicates that they cannot be attributed to Raman scattering. Furthermore, they can hardly be attributed to any interference process due to multiple internal reflections within the irradiated sample, firstly because they are visibly temperature-dependent, and most importantly because (differently from what is reported in Ref.[30]) the implantation fluence is low enough to avoid the presence of a reflective layer below the sample surface. Within a ~4 nm limit due to the spectral resolution of the experimental apparatus, all of the aforementioned lines are uniformly spaced in energy of $\Delta E = (36 \pm 5)$ meV. If the 600 nm emission line corresponds, as assumed here, to the zero-phonon line (ZPL) of the F-related center, such energy shift value is compatible with an electron–phonon coupling, as it falls in the energy range (10–100 meV) related to quasi-local vibrations[19].

Remarkably, the 558 nm line reported in Fig. 2a is also visible in Fig. 3, although its relative intensity with respect to the FB1 band maximum is further decreased with respect to room-temperature conditions. Such

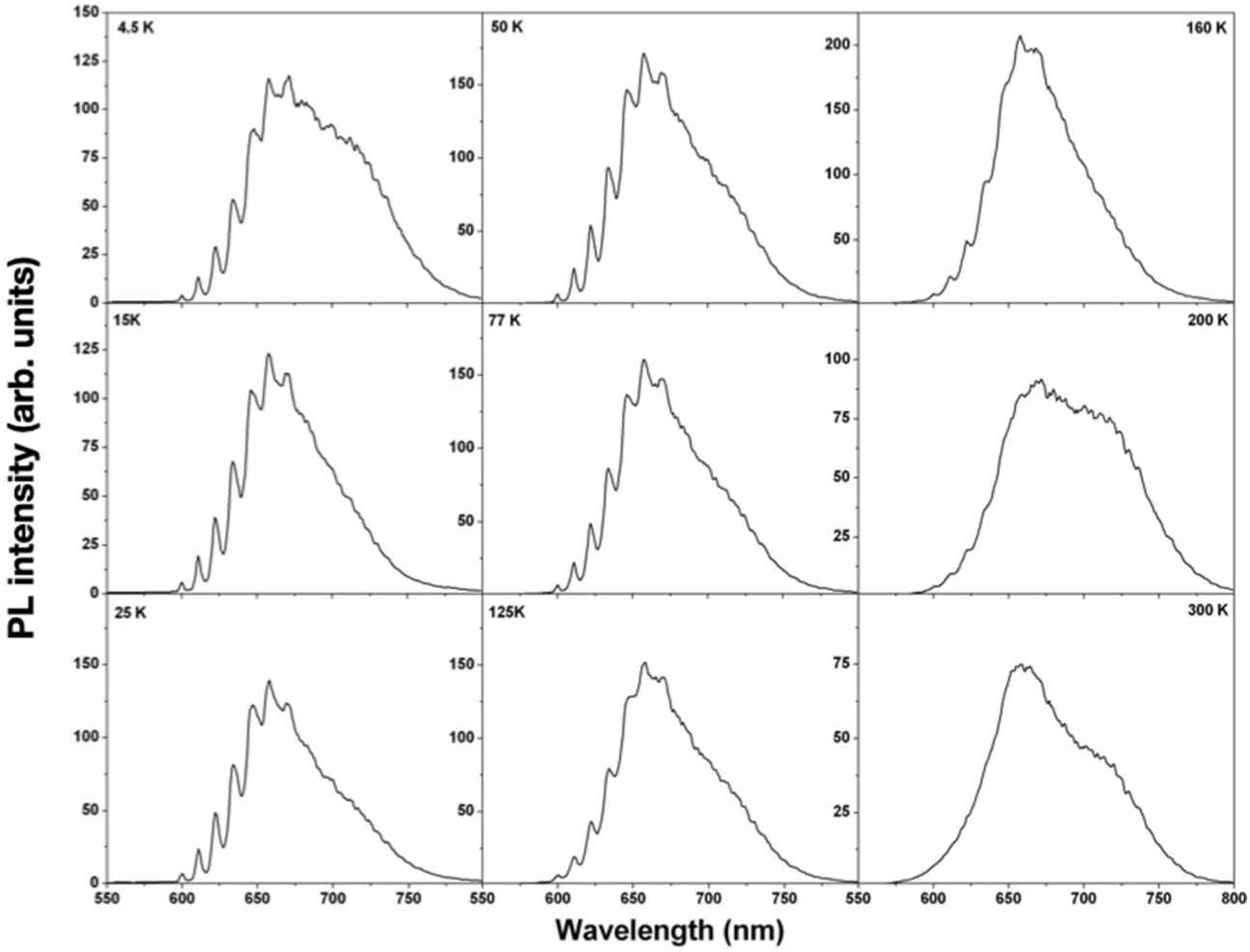


Figure 5. Ensemble PL emission from the region of sample #1 implanted at a fluence of 5×10^{13} cm^{-2} under 488 nm excitation as a function of temperature.

observation is indicative of the fact that the 558 nm emission can hardly be attributed to the ZPL of the FB1 band. This interpretation is further supported by the 155 meV energy separation with respect to its closest emission line at 600 nm. Therefore, the available experimental data are not sufficient to justify any reasonable attribution of the observed peak.

While no significant differences were observed among the PL peaks reported in Fig. 4, a comparison among the spectra reveals an additional emission band (FB2 in the following), which is visible (both at 4.5 K and 300 K) under 488 nm excitation only. This component appears as a second band centered at ~ 710 nm, not observed in the previous report on F-implanted diamond[24]. The emergence of the FB2 band cannot be determined under 405 nm excitation as it lies outside of the available spectral range. If confirmed, its observation could lead to the attribution of FB1 and FB2 as different charge states of the same defect, in a similar fashion to the well-established interpretation of the emission bands of the neutral and negative charge states of the nitrogen-vacancy complex. In this case, FB2 would be related to a higher excitation energy (> 2.39 eV) with respect to FB1 despite resulting a lower photon energy. This might indicate the presence of indirect transitions or non-radiative processes involved in the luminescence mechanism, to be further assessed at the single-photon emitter level.

Figure 5 shows the PL spectra at various temperatures in the 4.5–300 K temperature range, under 488 nm excitation. The assessment of a trend in the relative intensity of the FB1 and FB2 bands was not possible due to slightly different focusing conditions. Nevertheless, the progressive broadening of the set of lines in the 600–670 nm range is clearly visible up to temperatures as high as 160 K, thus providing a further confirmation of their attribution as phonon sidebands of the 600 nm ZPL emission. Conversely, the absence of any distinguishable internal structure of the FB2 band even at 4.5 K temperature cannot be understood without a specific interpretative model, and thus will require further investigations.

Discussion and conclusions

In this work we reported on the fabrication by means of ion beam implantation and thermal annealing of a new class of color centers based on F impurities. The ensemble PL characterization showed several peculiar spectral features that, to the best of the authors' knowledge, were not reported so far at the state of the art, namely: a weak

emission peak at 558 nm, two bands centered at ~ 670 nm (FB1) and ~ 710 nm (FB2), the latter being visible under 488 nm excitation but not under 520 nm. At cryogenic temperatures, the FB1 band exhibited an articulated structure of separate emission lines, whose arrangement is compatible with the attribution of the 600 nm spectral features to the ZPL emission of the center, coupled to a set of six phonon replica spaced by a (36 ± 5) meV energy attributed to quasi-local vibrations. The weak 558 nm emission could not be related to the FB1, nonetheless it is not implausible that it originates from a different F-containing lattice defect.

The results discussed in this work, although limited to the study of ensembles of emitters, offer the first extensive characterization of F-related defects, thus confirming the claim on their optical activity presented in Ref.[24], where their characterization at the single-photon emitter level was challenging due to the strong similarity in both the spectral signatures and the excited state radiative lifetime with respect to those of the NV center[4]. A further study will be beneficial to assess the photoemission dynamics of the center and its brightness for potential use as single-photon source. A systematic investigation on individual centers will also be necessary in order to clarify the attribution of the 558 nm emission line and the nature of the FB2 band.

Preliminary ab initio simulations by J.P Goss and colleagues identified a stable neutral charge state of the fluorine-vacancy (F-V) complex with a ground state C_{2v} symmetry[31]. The evidence collected in this report leads to attribute the luminescence in F-implanted diamond to such complex. While the afore-mentioned work was not aimed at the identification of the center, the transitions from positive (neutral) to neutral (negative) charge states were calculated as $E_{0/+}$=3.0 eV and $E_{-/0}$ = 1.9 eV, respectively. The experimental observation of a significant decrease in the FB1 PL emission under 405 nm laser (~ 3.07 eV) with respect to higher excitation wavelengths might be compatible with the transition of the defect between two different charge states. In particular, the FB1 band might be attributed to its neutral charge state. This interpretation might be supported by future refined numerical simulations of the optical transitions of the defect, as well as by the observation of different spectral features under > 650 nm excitation wavelength (1.9 eV), at which the transition to the negative charge state is predicted to occur. On the other hand, such model does not suggest an interpretation for the FB2 band, which was observed under 488 nm excitation only.

The observation of optical activity from a F-V defect in diamond might also unveil further appealing practical applications in quantum technologies[4–9,32] and in particular in quantum sensing and quantum computation, since the theoretical model in Ref.[31] suggests a ground state electronic spin configuration similar to that of the NV center (S = 1/2, and S = 1 for neutrally- and negatively-charged impurity-vacancy defects, respectively). If confirmed by EPR experiments, such property could pave the way to the utilization of F-related centers in diamond for quantum information processing applications, taking advantage of the non-zero nuclear spin of the naturally occurring ^{19}F for hyperfine interactions for defects control and coupling[31].

Received: 31 July 2020; Accepted: 5 November 2020
Published online: 09 December 2020

References

1. Schröder, T. *et al.* Quantum nanophotonics in diamond. *J. Opt. Soc. Am. B* **33**(4), B65 (2016).
2. Aharonovic, I., Englund, D. & Toth, M. Solid-state single-photon emitter. *Nat. Photonics* **10**, 631 (2016).
3. Chen, D., Zheludev, N. & Gao, W. Building blocks for quantum network based on group-iv split-vacancy centers in diamond. *Adv. Quantum Technol.* **3**, 1900069 (2020).
4. Doherty, M. W. *et al.* The nitrogen-vacancy colour centre in diamond. *Phys. Rep.* **528**, 1 (2013).
5. Staudacher, T. *et al.* Nuclear magnetic resonance spectroscopy on a (5-nanometer) 3 sample volume. *Science* **339**, 561 (2013).
6. Dolde, F. *et al.* Nanoscale detection of a single fundamental charge in ambient conditions using the NV− center in diamond. *Phys. Rev. Lett.* **112**, 097603 (2014).
7. Sipahigil, A. *et al.* Quantum interference of single photons from remote nitrogen-vacancy centers in diamond. *Phys. Rev. Lett.* **108**, 143601 (2012).
8. Le Sage, D. *et al.* Efficient photon detection from color centers in a diamond optical waveguide. *Phys. Rev. B* **85**, 121202 (2012).
9. Schirhagl, R., Chang, K., Loretz, M. & Degen, C. L. Nitrogen-vacancy centers in diamond: nanoscale sensors for physics and biology. *Ann. Rev. Phys. Chem.* **65**, 83 (2014).
10. Bradac, C., Gao, W., Forneris, J., Trusheim, M. E. & Aharonovich, I. Quantum nanophotonics with group IV defects in diamond. *Nat. Commun.* **10**, 5625 (2019).
11. Wang, C., Kurtsiefer, C., Weinfurter, H. & Burchard, B. Single photon emission from SiV centres in diamond produced by ion implantation. *J. Phys. B* **39**, 37 (2006).
12. Müller, T. *et al.* Optical signatures of silicon-vacancy spins in diamond. *Nat. Commun.* **5**, 3328 (2014).
13. Palyanov, Y. N., Kupriyanov, I. N., Borzdov, Y. M. & Surovtsev, N. V. Germanium: a new catalyst for diamond synthesis and a new optically active impurity in diamond. *Sci. Rep.* **5**, 14789 (2015).
14. Iwasaki, T. *et al.* Germanium-vacancy single color centers in diamond. *Sci. Rep.* **5**, 12882 (2015).
15. Ditalia Tchernij, S. *et al.* Single-photon-emitting optical centers in diamond fabricated upon sn implantation. *ACS Photonics* **4**, 2580 (2017).
16. Iwasaki, T. *et al.* Tin-vacancy quantum emitters in diamond. *Phys. Rev. Lett.* **119**, 253601 (2017).
17. Ditalia Tchernij, S. *et al.* Single-photon emitters in lead-implanted single-crystal diamond. *ACS Photonics* **5**, 4864 (2018).
18. Trusheim, M. *et al.* Lead-related quantum emitters in diamond. *Phys. Rev. B* **99**, 075430 (2019).
19. Zaitsev, A. M. *Optical Properties of Diamond: Data Handbook* (Springer, Berlin, 2001).
20. Forneris, J. *et al.* Creation and characterization of He-related color centers in diamond. *J. Lumin.* **179**, 59 (2016).
21. Sandstrom, R. *et al.* Optical properties of implanted Xe color centers in diamond. *Optics Commun.* **411**, 182–186 (2018).
22. Pezzagna, S., Rogalla, D., Wildanger, D., Meijer, J. & Zaitsev, A. Creation and nature of optical centres in diamond for single-photon emission—overview and critical remarks. *New J. Phys.* **13**, 035024 (2011).
23. Orwa, J. *et al.* Fabrication of single optical centres in diamond—a review. *J. Lumin.* **130**, 1646 (2010).
24. Lühmann, T. *et al.* Screening and engineering of colour centres in diamond. *J. Phys. D Appl. Phys.* **51**, 483002 (2018).
25. Pezzagna, S., Naydenov, B., Jelezko, F., Wrachtrup, J. & Meijer, J. Creation efficiency of nitrogen-vacancy centres in diamond. *New J. Phys.* **12**, 065017 (2010).
26. Lühmann, T., John, R., Wunderlich, R., Meijer, J. & Pezzagna, S. Coulomb-driven single defect engineering for scalable qubits and spin sensors in diamond. *Nat. Commun.* **10**, 4956 (2019).

27. Gatto Monticone, D. *et al.* Native NIR-emitting single colour centres in CVD diamond. *New J. Phys.* **16**, 053005 (2014).
28. Steeds, J. W., Davis, T. J., Charles, S. J., Hayes, J. M. & Butler, J. E. 3H luminescence in electron-irradiated diamond samples and its relationship to self-interstitials. *Diam. Relat. Mater.* **8**, 1847 (1999).
29. Forneris, J. *et al.* Electrical control of deep NV centers in diamond by means of sub-superficial graphitic micro-electrodes. *Carbon* **113**, 76–86 (2017).
30. Olivero, P. *et al.* Characterization of three-dimensional microstructures in single-crystal diamond. *Diam. Relat. Mater.* **15**, 1614 (2006).
31. Goss, J. P., Briddon, P. R., Rayson, M. J., Sque, S. J. & Jones, R. Vacancy-impurity complexes and limitations for implantation doping of diamond. *Phys. Rev. B* **72**, 035214 (2005).
32. Petrini, G., Moreva, E., Bernardi, E., Traina, P., Tomagra, G., Carabelli, V., Degiovanni, I. P. & Genovese, M., Is a quantum biosensing revolution approaching? Perspectives in NV-assisted current and thermal biosensing in living cells. *Adv. Quantum Technol.* 2000066 (2020).

Acknowledgements

This work was supported by the following projects: Coordinated Research Project "F11020" of the International Atomic Energy Agency (IAEA); Project "Piemonte Quantum Enabling Technologies" (PiQuET), funded by the Piemonte Region within the "Infra-P" scheme (POR-FESR 2014-2020 program of the European Union); "Departments of Excellence" (L. 232/2016), funded by the Italian Ministry of Education, University and Research (MIUR); "Ex post funding of research" of the University of Torino funded by the "Compagnia di San Paolo"; FET OPEN Pathos. The project 17FUN06 (SIQUST) leading to this publication has received funding from the EMPIR programme co-financed by the Participating States and from the European Union's Horizon 2020 research and innovation programme. T.L., S.P and J.M. acknowledge the support of the ASTERIQS program of the European Commission. S.D.T. and J.F. gratefully acknowledge the EU RADIATE Project (proposal 19001744) for granting transnational access to the Laboratories of the Ruđer Bošković Institute.

Author contributions

J.F., P.O. M.G., S.D.T, designed the experiments. T.L., J.M. and S.P. performed keV F implantations; A.C., M.B., and Z.S., S.D.T performed MeV F ion implantations. Z.P. performed keV N implantations. F.S., P.A., F. P., E.C. contributed with post-implantation sample processing, room-temperature ensemble measurements, and micro-Raman photoluminescence spectroscopy. J. F., E.M. I.P.D., and P.T. developed a cryogenic confocal microscopy setup and acquired PL spectra at varying temperatures. J.F., S.D.T, P.O. performed the analyses and wrote the manuscript. All authors contributed to revise the manuscript.

Competing interests

The authors declare no competing interests.

Additional information

Correspondence and requests for materials should be addressed to J.F.

Reprints and permissions information is available at www.nature.com/reprints.

Publisher's note Springer Nature remains neutral with regard to jurisdictional claims in published maps and institutional affiliations.

Open Access This article is licensed under a Creative Commons Attribution 4.0 International License, which permits use, sharing, adaptation, distribution and reproduction in any medium or format, as long as you give appropriate credit to the original author(s) and the source, provide a link to the Creative Commons licence, and indicate if changes were made. The images or other third party material in this article are included in the article's Creative Commons licence, unless indicated otherwise in a credit line to the material. If material is not included in the article's Creative Commons licence and your intended use is not permitted by statutory regulation or exceeds the permitted use, you will need to obtain permission directly from the copyright holder. To view a copy of this licence, visit http://creativecommons.org/licenses/by/4.0/.

© The Author(s) 2020

New Journal of Physics
The open access journal at the forefront of physics

Deutsche Physikalische Gesellschaft DPG IOP Institute of Physics

PAPER • OPEN ACCESS

Spectral features of Pb-related color centers in diamond – a systematic photoluminescence characterization

To cite this article: Sviatoslav Ditalia Tchernij *et al* 2021 *New J. Phys.* **23** 063032

View the article online for updates and enhancements.

You may also like

- Numerical study of silicon vacancy color centers in silicon carbide by helium ion implantation and subsequent annealing
Yexin Fan, Ying Song, Zongwei Xu et al.
- 2022 Roadmap on integrated quantum photonics
Galan Moody, Volker J Sorger, Daniel J Blumenthal et al.
- 2023 roadmap for materials for quantum technologies
Christoph Becher, Weibo Gao, Swastik Kar et al.

This content was downloaded from IP address 130.192.98.148 on 13/05/2024 at 10:14

New Journal of Physics
The open access journal at the forefront of physics

Deutsche Physikalische Gesellschaft DPG
IOP Institute of Physics

Published in partnership with: Deutsche Physikalische Gesellschaft and the Institute of Physics



OPEN ACCESS

RECEIVED
2 February 2021

REVISED
15 May 2021

ACCEPTED FOR PUBLICATION
20 May 2021

PUBLISHED
14 June 2021

Original content from this work may be used under the terms of the Creative Commons Attribution 4.0 licence.

Any further distribution of this work must maintain attribution to the author(s) and the title of the work, journal citation and DOI.



PAPER

Spectral features of Pb-related color centers in diamond – a systematic photoluminescence characterization

Sviatoslav Ditalia Tchernij[1,2,3], Emilio Corte[1,2], Tobias Lühmann[4], Paolo Traina[3], Sébastien Pezzagna[4], Ivo Pietro Degiovanni[2,3], Georgios Provatas[5], Ekaterina Moreva[3], Jan Meijer[4], Paolo Olivero[1,2,3], Marco Genovese[2,3] and Jacopo Forneris[1,2,3,*]

[1] Physics Department, University of Torino, Torino 10125, Italy
[2] Istituto Nazionale di Fisica Nucleare (INFN), sezione di Torino, Torino 10125, Italy
[3] Istituto Nazionale di Ricerca Metrologica (INRiM), Torino 10135, Italy
[4] Applied Quantum Systems, Felix-Bloch Institute for Solid-State Physics, Universität Leipzig, Leipzig 04103, Germany
[5] Laboratory for Ion Beam Interactions, Ruđer Bošković Institute , Zagreb 10000, Croatia
[*] Author to whom any correspondence should be addressed.

E-mail: jacopo.forneris@unito.it

Keywords: diamond, ion implantation, single photon emitters, luminescent centers, Pb-related color center

Abstract

We report on the systematic characterization of the optical properties of diamond color centers based on Pb impurities. An ensemble photoluminescence analysis of their spectral emission was performed at different excitation wavelengths in the 405–520 nm range and at different temperatures in the 4–300 K range. The series of observed spectral features consist of different emission lines associated with Pb-related defects. Finally, a room-temperature investigation of single-photon emitters under 490.5 nm laser excitation is reported, revealing different spectral signatures with respect to those already reported under 514 nm excitation. This work represents a substantial progress with respect to previous studies on Pb-related color centers, both in the attribution of an articulated series of spectral features and in the understanding of the formation process of this type of defect, thus clarifying the potential of this system for high-impact applications in quantum technologies.

1. Introduction

Diamond color centers have been extensively studied in the last decades as appealing systems for applications in quantum optics and quantum information processing, ranging from the use as single photon emitters to quantum sensing of magnetic and electric fields and of temperature, pressure and strain [1–7]. Despite the increasing interest of these systems among the scientific community, only a fairly limited number of emitters related to impurities incorporated in the diamond lattice has been demonstrated so far [6, 8, 9], and most of the preliminary practical demonstrations of diamond-based quantum technologies rely on the peculiar spin properties of the negatively-charged nitrogen-vacancy color center (NV) [10–15].

Indeed, even if NV centers present several interesting properties, they are also subject to significant drawbacks, such as broad spectral emission, charge state blinking, relatively low emission rate [16, 17], thus prompting for the search of alternative new centers overcoming this limits and/or presenting complementary properties.

Besides the already consolidated color centers related to group-IV impurities such as SiV, GeV, and SnV complexes [6, 18–27], two independent works have recently demonstrated the creation of optically-active defects in diamond upon Pb ion implantation and subsequent annealing, and have reported their characterization at the single-photon emitter level [28, 29].

The Pb-related defects exhibited appealing emission properties for quantum information processing applications, with room temperature photoluminescence (PL) emission rates exceeding 10^6 photons s^{-1} [28], an emission mainly concentrated in the zero phonon line (ZPL) due to the low phonon coupling and a

© 2021 The Author(s). Published by IOP Publishing Ltd on behalf of the Institute of Physics and Deutsche Physikalische Gesellschaft

large ground-state splitting predicted by numerical simulations [29, 30], with potentially disruptive implications towards the achievement of long spin coherence for quantum memories and optical quantum networks [6].

On the other hand, the currently available reports evidenced the presence of several spectral lines of uncertain attribution. Furthermore, discrepancies in the observation of some emission peaks (namely: 520–525 nm doublet, 538 nm doublet, 715 nm line) emerged and were attributed to different experimental conditions such as excitation wavelength and operating temperatures [28, 29].

We report here on a systematic investigation of Pb-related centers under varying excitation wavelengths in the 405–520 nm range and temperature between 4 K and 300 K. Our results address and discuss the aforementioned discrepancies by providing systematic information on the relative emission intensities of these spectral features as a function of the measurement temperature, thus paving the way to the practical application of these centers. Finally, a comprehensive discussion summarizing the currently available results is presented, including the possible attribution of the observed emission lines and their relation with the theoretical models proposed in the literature.

2. Experimental

The experiments were performed on a single-crystal IIa diamond substrate produced by ElementSix. The sample has a 'detector grade' quality (i.e. substitutional N and B concentration: $[N_S] < 5$ ppb, $[B_S] < 5$ ppb). Pb-related centers were created upon the implantation of 35 keV PbO_2^- ions at different fluences, namely 5×10^{11} cm^{-2} and 2×10^{13} cm^{-2}. The sample underwent a thermal annealing process at 1200 °C for 2 h in high vacuum ($<5 \times 10^{-6}$ mbar) to promote the formation of the centers, as discussed in a previous report [28]. It is worth remarking that the implantation of PbO_2^- ions was motivated by the higher extraction efficiency and stability with respect to the technically challenging acceleration of a Pb^- beam [31]. At the same time, a control sample was implanted with 9 MeV O^{4+} ions at 4×10^{13} cm^{-2} fluence and annealed under the same experimental conditions, in order to explicitly assess the contribution of optically-active O-related defects to the PL spectra acquired in the considered wavelength range [28]. After annealing, an oxygen plasma cleaning process was performed to ensure the removal of the surface graphitic phases and optically-active contaminants.

The processed substrate was characterized using different PL single-photon sensitive confocal microscopy setups. A cryogenic setup operating based on a liquid helium closed-cycle optical cryostat [32] (100x air objective, 0.85 NA) operating in the 4–300 K temperature range was employed for the measurements reported in section 3.1. The latter apparatus was not equipped with nano-positioners, thus preventing the investigation of individual emitters at cryogenic temperatures. For this reason, an additional confocal microscope operating at room temperature (100x air objective, 0.95 NA), equipped with closed-loop nano-positioners was used for the identification of individual emitters (measurements reported in section 3.2). In both setups, the optical excitation was provided by a set of CW laser diodes with emission wavelengths of 405 nm, 490.5 nm and 520 nm. The PL spectra were acquired using a single-grating monochromator (1200 grooves mm^{-1}, 600 nm blaze, ~4 nm spectral resolution) that was fiber-coupled to a single-photon avalanche detector (SPAD). The room-temperature setup was equipped with a Hanbury-Brown & Twiss (HBT) interferometer, allowing the assessment of single-photon emitters via the measurement of the second-order autocorrelation function. The HBT interferometer was implemented by connecting two independent SPAD to the output of a multimode fiber-integrated 50:50 beam-splitter. A third confocal microscope (60x oil objective 1.35 N.A.) equipped with an SPAD outcoupled in open air was used to characterize the spectral emission from individual spots under 532 nm laser excitation (measurements reported in section 3.3). In this latter setup, the PL spectra were acquired using a Peltier-cooled CCD array camera with a spectral resolution of ~2 nm, as determined by the first-order Raman peak (572 nm) FWHM width.

3. Results

3.1. Ensemble-level PL characterization

Following preliminary reports on the formation and the optical properties of Pb-related color centers [28, 29], we performed the first extensive PL characterization of this class of defects at an ensemble level (2×10^{13} cm^{-2} implantation fluence) under different excitation wavelengths in a temperature range of 4–300 K. Figure 1 shows the PL spectra acquired at 4 K, 77 K and 300 K under 405 nm (figures 1(a)), 490.5 nm (figures 1(b)) and 520 nm (figure 1(c)) excitations, respectively. The main results of this set of measurements can be summarized as follows.

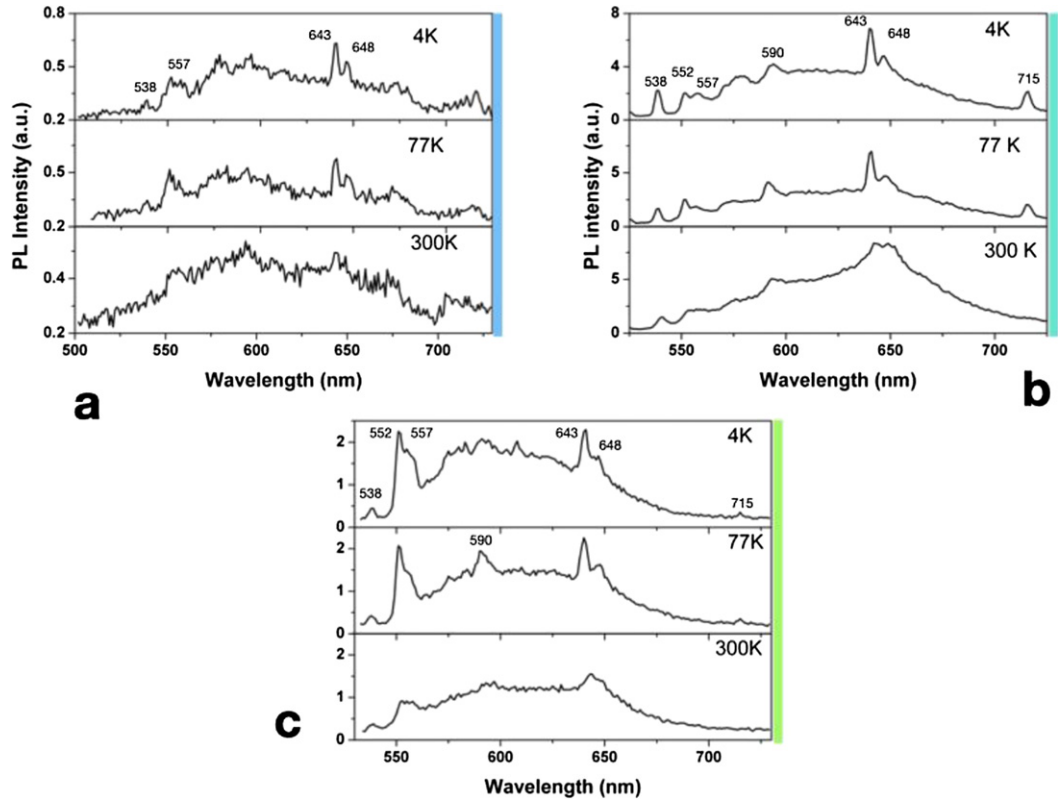


Figure 1. PL spectra acquired at different temperatures (4 K, 77 K, 300 K) from the region implanted with PbO_2^- ions at 2×10^{13} cm^{-2} fluence. The reported spectra were acquired under the following optical excitation wavelengths: (a) 405 nm (b) 490.5 nm (c) 520 nm.

405 nm excitation. The spectra acquired under 405 nm laser excitation (10 mW optical power) are reported in figure 1(a). All spectra were acquired using along-pass filter with 500 nm cutoff wavelength. The spectra were limited to wavelengths shorter than 720 nm due to the observation of fluorescence at larger wavelengths from the optical components of the confocal microscope. The most evident spectral features, mainly visible at lower temperatures, consist of a small peak at 538 nm, a band centered at ∼557 nm, and a broad band in the 570–670 nm range. Additional sharp peaks at 643 nm and 648 nm are visible only at 4 K and 77 K temperatures. At 300 K temperature, the above-listed peaks convolve into a broader emission band centered at 645 nm. Considering the ∼3 nm spectral resolution of the apparatus and the spectral blue-shifting at decreasing temperatures (already reported in reference [28]), these lines are compatible with the weak emission lines at 640.4 nm and 649.8 nm observed under the same excitation wavelength in reference [28].

490.5 nm excitation. Spectra were acquired at 3.5 mW excitation power, using a laser diode with 490.5 nm emission wavelength. The spectra were acquired using a 500 nm long-pass filter and a (514 ± 15) nm notch filter to prevent the observation of the first-order Raman line (expected at 524.8 nm based on the 1332 cm^{-1} Raman shift of diamond). The main PL emission features (figure 1(b)) consist of peaks located respectively at 538 nm, 552 nm and 557 nm, together with an additional wide band at ∼590 nm, consistently with what reported in reference [28] under 532 nm excitation. The emission lines at 643 nm and 648 nm are also visible under 490.5 nm laser excitation. Finally, a PL peak is observed at 715 nm at 4 K and 77 K temperatures, while this spectral line could not be resolved at room temperature.

A PL spectrum (figure 2) of the O-implanted control sample was acquired under the same experimental conditions to address the contribution of oxygen-related defects to the emission properties observed in reference [28]. Notably, the low-temperature O-related emission exhibits a ZPL at 590 nm, which is qualitatively in line with what reported in reference [8], although its prominence with respect to the baseline is non-negligible only at low temperatures. Based on this observation, we cannot rule out that the 590 nm band could be attributed to O-related impurities, although it was observed on a sample implanted with elemental Pb only in reference [28].

Furthermore, a band centered at 650 nm was visible at low temperatures, although it did not display a doublet and exhibited a limited prominence with respect to the baseline. The band broadened at higher wavelengths emitting in the whole 650–700 nm range. The limited spectral prominence and the difference

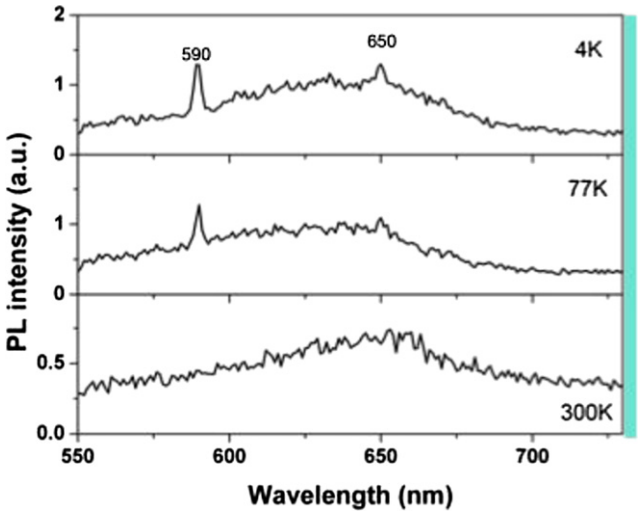


Figure 2. PL spectra acquired 490.5 nm optical excitation wavelengths at different temperatures (4 K, 77 K, 300 K) from the region implanted with O^{4+} ions at 2×10^{13} cm^{-2} fluence.

in the spectral position (643 nm vs 650 nm) suggest that the 643 nm line observed in Pb (references [28, 29]) and PbO_2 (reference [28] and present work) implanted samples could not be attributed to O-related impurities.

520 nm excitation. The PL spectra (figure 1(c)) were acquired using a 50:50 beam-splitter instead of a long-pass dichroic mirror, with the purpose of allowing the collection of the spectral features at wavelengths shorter than 567 nm, corresponding to the cutoff wavelength of the available dichroic mirror. Since the above-mentioned dichroic mirror was not employed, a (514 ± 15) nm notch filter and a long-pass filter with 530 nm cutoff wavelength were used instead, in order to filter out the laser excitation light.

The prominence of the PL peaks at 538 nm, 552 nm and 557 nm is significantly higher with respect to the other spectral features, if compared with the results obtained at shorter excitation wavelengths. The substantial intensity decrease of the 557 nm feature at increasing temperature suggests that the emission line should be attributed to PL from the Pb-related center, rather than to the first-order Raman emission of diamond (expected at 558.7 nm wavelength), more so considering that this emission line is also visible under different excitation wavelength. Therefore, in our interpretation the first-order Raman line is strongly convoluted with the PL emission feature, while being characterized by a significantly lower emission intensity. The 590 nm band is visible in the spectra, regardless of the measurement temperature. Similarly to what observed under 490.5 nm excitation, the 643 nm peak and the less intense 648 nm peak tend to convolve into a broad emission band at room temperature, although their intensities with respect to the emission doublet at 552 nm and 557 nm is weaker if compared with the PL spectra acquired at lower excitation wavelengths. The emission peak at 715 nm is also barely visible at 4 K temperature, differently from the case of 490.5 nm laser excitation.

3.2. Single-center-level photon emission characterization

We report on the room-temperature characterization of isolated quantum emitters resulting from ions scattered outside of the region implanted at 5×10^{11} cm^{-2} fluence, as reported in the confocal microscopy map [33] shown in figure 3(a). Differently from the data reported in references [28, 29] under 450 nm and 520 nm laser excitations, respectively, the characterization was performed at room temperature under 490.5 nm excitation (2.8 mW excitation power). In this case, an additional 520 nm notch filter was used to minimize the background emission due to the first-order Raman peak of diamond (expected at 521.8 nm). We discuss the properties of a typical emitter exhibiting a narrow ZPL at 643 nm and a low intensity phonon sideband, as reported in figure 3(b). The attribution of such spectral line to a Pb-related defect was justified by the observation of the 643 nm emission in both reference [27] as well as in section 3.1 of the present work at the ensemble level, and in reference [28] from individual spots, although without a systematic characterization at the single-photon emission level.

The emission properties of the center were studied by means of HBT interferometry [34, 35]. Figure 4(a) shows second-order auto-correlation chronograms collected under different excitation powers and background-subtracted following the procedure described in reference [28]. The <0.5 values observed in correspondence of zero delay time under all excitation power values is indicative of the fact that the

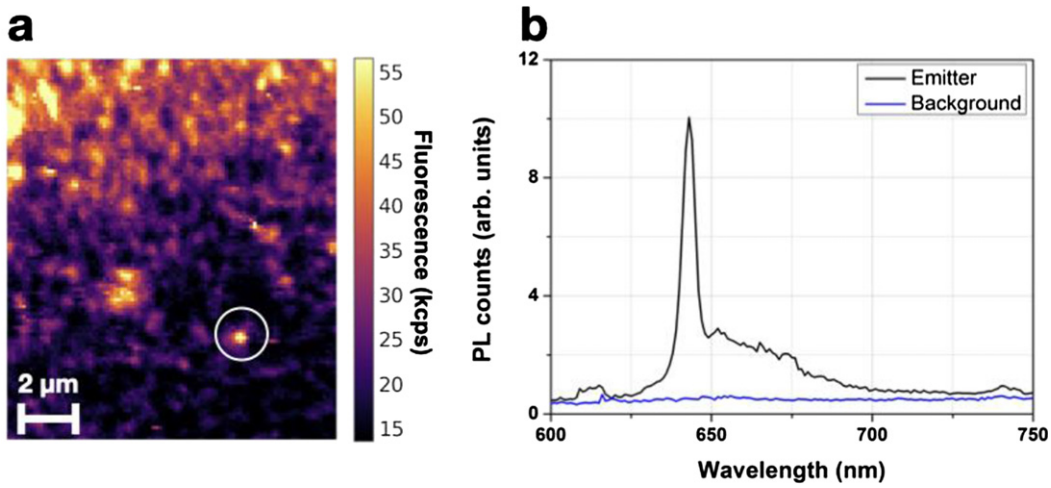


Figure 3. Room-temperature single-photon emission of an individual Pb-related defect under 490.5 nm laser excitation. (a) PL confocal map acquired at the edge of region implanted with 5×10^{11} cm^{-2} PbO_2^- ions; (b) PL emission spectrum acquired from the circled spot in (a).

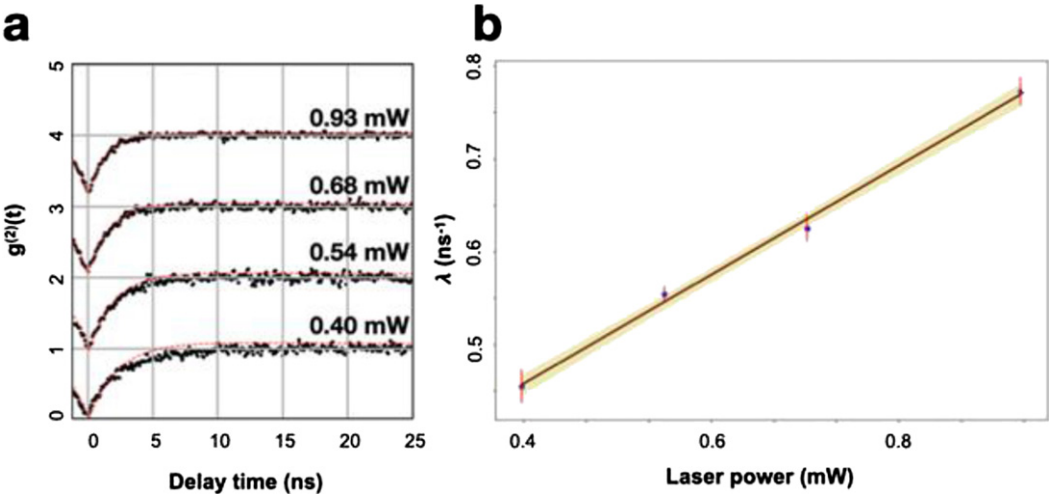


Figure 4. (a) Background-corrected second-order auto-correlation chronograms acquired at increasing optical powers from the emitter circled in white in figure 3(a). Each chronogram is translated by a unit step along the vertical axis for the sake of readability. (b) Linear fit of the exponential constant value λ extracted from figure 4(a) as a function of the excitation power. The reciprocal of the intercept value defines the emission lifetime.

emission originates from an individual optical center [36]. A fitting procedure of the anti-correlation dip around zero delay time was carried on the basis of the two-level system model, using the $g^{(2)}(t) = 1 - \exp[-\lambda t]$ functional expression, as discussed in reference [24]. The time constant $\tau = \lambda^{-1}$ was estimated at each excitation power. The λ values obtained from the above-mentioned exponential fitting procedure as a function of excitation power P were linearly interpolated with the $\lambda(P) = {\tau_0}^{-1} + \alpha P$ function (figure 4(b)), thus allowing the estimation of the radiative lifetime of the center's excited state as $\tau_0 = (4.5 \pm 0.3)$ ns. This value is compatible with the value predicted by means of DFT calculations in reference [30], as well as comparable with what observed for both the 552 nm emission line under 520 nm laser excitation [28]and multiple emission lines (520, 552, 555, 575, 648 nm, see **table** 1) under 450 nm excitation [29]. The emission rate of the defect (1.8×10^5 s^{-1} at ~0.93 mW excitation power) was not directly comparable with the previous results under 520 nm laser excitation (i.e. >1 Mcps [28]), since the confocal microscopy setup adopted there was coupled into open air, and was thus characterized by a higher photon detection efficiency. It is worth noting that the emission line discussed in this analysis could not be clearly detected under the same temperature conditions at the ensemble level, due to the convolution of the 643 nm peak with additional spectral feature at room-temperature (figure 3(b)). This observation suggests that the ensemble emission is composed of different types of optical transitions originating from different types of lattice defects. Particularly, this observation suggests that the room-temperature band centered at 650 nm is

Table 1. Summary of the emission lines related to Pb ion implantation in diamond. Comments: ∗ might be superimposed to first-order Raman under 520 nm excitation; ∗∗ extremely weak emission under 520 nm excitation; ○ observed from the same emitter under 450 nm excitation; § observed from the same emitter under 490.5 nm excitation.

Emission wavelength (nm)	Excitation wavelength (nm)	Temperature (K)	Interpretation	Notes
517–520	450	4	ZPL doublet, DFT calculations [29, 30]	○
538	405, 490.5, 520, 532	4–300	Possible attribution as PbV ZPL [28]	
552	450, 490.5, 520, 532	4–300	Possible attribution as PbV ZPL [28]	○
557	405, 450, 490.5, 520∗, 532	4–300	Phonon replica of the 538/552 nm ZPL [28]	○, ∗
565	450	4		
575	450, 520, 490.5	4–300	NV^0 center ZPL [28, 29]	○
590	405, 490.5, 520, 532	4–300	Phonon sideband of the 552 nm ZPL [28], O-related emission in PbO_2 implanted diamond	
639–643	405, 450, 490.5, 520	4–300	NV^- center under extreme strain [29], alternative PbV charge state ZPL [28, 29]	§
648	405, 450, 490.5, 520	4–300	Phonon replica of the 643 nm ZPL	§
655–659	450, 490.5	4–300		
715	490.5, 520, 532	4–77		∗∗

the convolution of several different spectra of individual defects, each emitting at a specific set of wavelengths. To further qualify this point, a broader room-temperature investigation on the spectral emission properties of a set of individual luminescent spots is presented in the following section.

3.3. Additional emission lines from isolated emission spots

An additional study was performed to characterize individual emitters in Pb-implanted diamond. Figures 5(a)–(j) display a set of PL spectra acquired at room temperature under 532 nm excitation from the corresponding individual spots highlighted in the confocal map in figure 5(k), that was acquired in correspondence of the outer edge of a PbO_2^--implanted region (5×10^{11} cm^{-2} fluence). For the sake of comparison, the ensemble PL spectrum acquired at the center of the implanted region under the same experimental conditions is reported in figure 5(l). In these measurements, the use of a 550 nm long-pass filter prevented the detection of the possible occurrence of the Pb-related 552 nm line.

It is worth noting that the individual spots investigated in this analysis were not assessed by means of HBT interferometry, and thus that the observed emission spectra do not necessarily correspond to PL emission at the single-photon level.

The emission features reported in figure 5 can be grouped into few well-defined emission lines. Among them, the PL peaks at 557 nm and 643 nm (figure 5(e)) were already observed at the ensemble level (figure 5(l)), and can thus be safely attributed to Pb-related defects. It is worth mentioning that these two lines concurrently appear in the same spectrum, thus not ruling out that they may originate from the very same defect. Secondly, these lines do not appear concurrently with other Pb-related features discussed in the previous works, such as the 575 nm line or the 590 nm band.

An additional emission line observed in figure 5 is located at 554 nm (figure 5(g)). In consideration of the spectral resolution of the apparatus, this line is compatible with both the 552 nm and 557 nm lines that were attributed to Pb-related defects, and thus its attribution is not straightforward. The line could result from a lattice strain-induced shift of either the afore-mentioned PL peaks, but it is also compatible with the 555 nm emission reported in previous works from proton and neutron irradiated diamond [37, 38].

In addition, a recurring set of spectral lines, not observed at the ensemble level, is visible in figure 5, namely: 564 nm (figures 5(c), (f) and (g)), 567 nm (figures 5(b), (i) and (j)), 581 nm (figures 5(a)), 605 nm (figure 5(a)), 651 nm (figures 5(d) and (i), 655 nm (figure 5(d)) and 658 nm (figures 5(a), (b), (d), (g) and (j)). There is no apparent correlation between any of these peaks, whose occurrence in the spectra reported in figures 5(a)–(j) is independent from all of the other observed spectral features.

This observation suggests that these emission lines are associated to different types of luminescent defects. Furthermore, the absence of such spectral features in the ensemble PL spectrum in figure 5(l) could be compatible with two possible interpretations. On one hand, the lines might be associated either to radiation-induced defects which are not directly related to Pb impurities. This attribution may be justified by previous reports of emission lines in irradiated diamond at 563 nm [37, 39] and 656 nm [37]. On the other hand, some of the afore-mentioned PL peaks might be related to alternative Pb-containing defects, whose formation in high concentrations is not favored by the thermal processing adopted in the present work.

It is also worth mentioning that the 564 nm, 567 nm, 651 nm and 658 nm peaks have been observed from isolated spots at 4 K temperature (450 nm excitation wavelength) in reference [29]. In this work, their

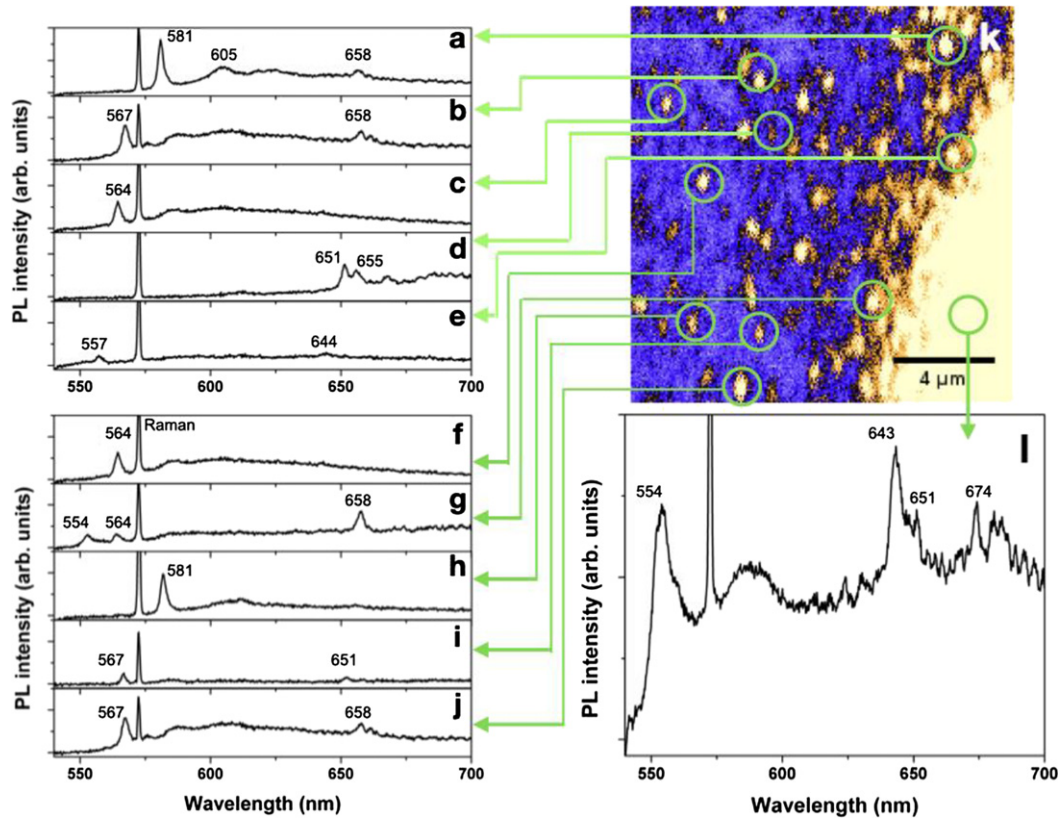


Figure 5. (a)–(j) PL spectra acquired from the corresponding isolated spots circled in figure 5(k). (k) Confocal microscopy map acquired under 532 nm excitation wavelength at the edge of the region implanted with 5×10^{11} cm^{-2} PbO_2^-. (l) Ensemble PL spectrum acquired at the center of the implanted region under the same experimental conditions.

occurrence was significantly less frequent with respect to the main emission lines (520 nm, 525 nm, 552 nm, 575 nm, 590 nm, 638 nm) that were attributed to Pb-related defects, therefore an attribution of these emission lines was not suggested. It is therefore worth remarking that our observation is in line with the results obtained in reference [29], despite the adoption of a different excitation wavelength (i.e. 450 nm).

4. Discussion

In order to clarify the compatibility of the reported results with respect to previous works, the results of PL characterization at ensemble level of PbO_2^--implanted diamond is discussed more extensively in this section. The reported emission lines are summarized in table 1 and sorted by increasing emission wavelength, in the context of the relevant spectral features that have been reported so far. A direct comparison with the previous works [28, 29] is made possible by the fact that both of them relied on the fabrication of defects by ion implantation, as well as on the same annealing temperature (i.e. 1200 °C), implying the same conditions for the formation of optical centers in diamond. The findings are also discussed in the framework of the currently available DFT theoretical predictions [27, 30]. The following discussion is limited to the spectral features that were unambiguously observed at the ensemble level or directly attributed to Pb-related defects in the previous reports.

517–520 nm. This line was experimentally observed under 450 nm excitation at 4 K temperature in reference [28] from individual emission spots together with the 552 nm, 557 nm, 575 nm and 648 nm emission lines. A 2.4 eV emission is theoretically predicted to be the ZPL of the Pb-V center [29, 30]. However, in our experiment we were not able to observe it under any operating condition of excitation wavelength and measurement temperature. In figure 6 we report the PL spectra in the 510–600 nm range acquired under different excitation wavelengths (i.e. 405 nm and 488 nm) at 4 K temperature from the region implanted with PbO_2^- ions at 2×10^{13} cm^{-2} PbO_2^- fluence. The fact that the peak was not visible under 405 nm laser excitation (figure 6, blue line) could be explained by assuming that the energy of the laser light might be too high to efficiently excite this emission or alternatively the occurrence of a partial ionization of the center. Furthermore, the 490.5 nm laser excitation determines the first-order 1332 cm^{-1}

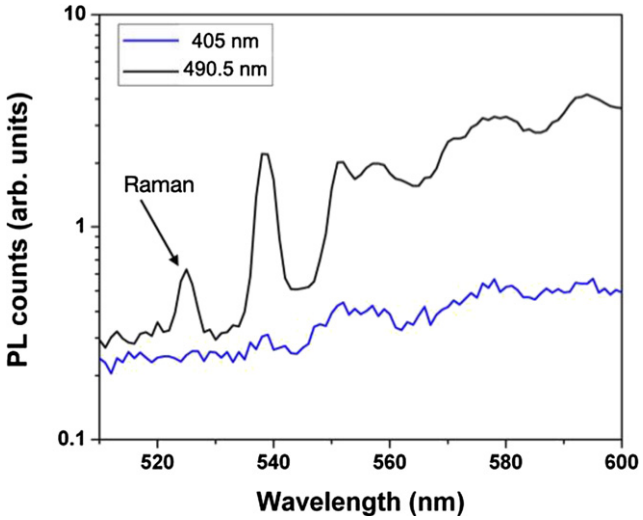


Figure 6. Photoluminescence spectra in the 520–600 nm range acquired from the region implanted with a fluence of 2×10^{13} cm^{-2} at 4 K temperature under 405 nm (blue line) and 490.5 nm excitation wavelengths (black line). The 525 nm peak corresponds to the first-order Raman shift of diamond under the 490.5 nm laser excitation.

Raman shift to be spectrally located at 524.8 nm: in this context, in this study a 490.5 nm laser excitation was adopted to allow the full deconvolution of Raman and PL spectral features across the 517–520 nm range. However, the PL spectrum collected under 409.5 nm excitation reported in figure 6 (black line) did not exhibit any spectral feature in the region of interest, with the exception of the 525 nm Raman line. Finally, the 520 nm laser could not be adopted to investigate this line under near-resonant excitation and therefore its possible occurrence under these excitation conditions could not be assessed.

525 nm. This line was observed under 450 nm excitation at 4 K from an individual spot together with the 552 nm, 557 nm, 575 nm and 648 nm lines [29]. However, it was not visible under 405 nm excitation in the 4–300 K temperature range and could not be assessed under 490.5 nm excitation due to the overlapping first-order Raman emission at 1332 cm^{-1} shift.

538 nm, 552 nm, 557 nm. These emission peaks were observed in reference [28] under 514 nm and 532 nm excitations, as well as in reference [29] under 450 nm excitation with the exception of the 538 nm line. Their observation is confirmed in the present work under 405 nm, 490.5 nm and 520 nm excitation. The highest prominence with respect to the spectral baseline was achieved under 520 nm excitation. These emission lines were concurrently observed from isolated spots under 450 nm excitation [28], although in combination with additional lines at 525 nm and 648 nm. Also, they were observed from single-photon emitters under 532 nm excitation concurrently with the 590 nm band [28]. These results strongly suggest that all of the above-listed emission lines originate from the same type of Pb-related impurity. The 552 nm and 557 nm lines were tentatively interpreted as possible ZPL candidates for the PbV center in reference [28], although without the support of a comprehensive theoretical modelling.

575 nm. This emission line is observed in this work as a minor peak under all operating conditions. The peak is visible in the whole 4–300 K temperature range under 405 nm, 450 nm, 490.5 nm, 514 nm, 520 nm and 532 nm laser excitation [28, 29]. Both of the above-cited works attributed the emission to the neutrally-charged NV center, although its systematic occurrence over a number of high-quality samples characterized by a low concentration of substitutional N (∼ppb) is worth being remarked.

590 nm. This emission band was consistently observed in all experimental reports on the Pb-related defects in the 4–300 K temperature range under 514 nm [28] and 532 nm [28, 29] excitation. This work confirms its occurrence under 405 nm, 490.5 nm and 520 nm excitation in all of the considered measurement temperature ranges. The band was also observed concurrently with the 538 nm, 552 nm and 557 nm lines at the single-photon emitter level, and thus tentatively interpreted as an optical-photon-mediated emission process [28]. However, the identification in this work of a 590 nm emission line in O-related ensembles suggests that this latter attribution could not be ruled out.

639 nm–660 nm. PL emission in this spectral region was observed in reference [29] at 4 K, under both 450 nm and 532 nm excitations, and it was tentatively attributed to NV centers. The observation of different lines (640 nm and 650 nm, in the 143–300 K temperature range) in reference [28] under 405 nm laser excitation poses questions about this attribution, since it has been previously observed that the NV$^-$ emission is quenched by ionization processes at excitation energies larger than 2.6 eV [40]. In this

sense, a possible, tentative attribution to a different charge state of the PbV center could not be entirely ruled out on the basis of the available data. This interpretation is mentioned in reference [29], where the spectral switching between the 520 nm ZPL and this set of lines could be attributed to the PbV charge state instability. It is also worth considering the recent attribution of a 639 nm PL line to interstitial-related lattice defects [41]. The plausibility of the latter interpretation is based on the large density of radiation-induced vacancies generated in diamond by the impact of an individual Pb ion.

In the present work an intense doublet was observed at the ensemble level at 643–648 nm under all experimental conditions (the highest prominence with respect to the baseline being observed under 490.5 nm), although at room temperature they were strongly convoluted into a broader emission band. The temperature-dependent results shown here offer an unambiguous link between the clear observation of the lines reported in reference [29] and their broadened, weak emission discussed in the reference [28]. The fact that the 643 nm line is more intense and narrower than the 648 nm line (figure 1) might support the interpretation of the former as a ZPL which is associated to its first phonon replica at a larger wavelength. Notably, the ∼18 meV spectral separation between the two peaks is in line with the expected value for quasi-local vibrations involving a Pb atom in the diamond lattice (i.e. ∼21.5 meV [28]). Moreover, room-temperature single-photon emission was observed with a ZPL of 643 nm, as reported in figure 3(b) under 490.5 nm laser excitation. In this case the possible phonon sideband (648 nm) is broadened at room temperature over a band in the 645–680 nm range.

The ∼650 nm band observed from ensembles at room temperature does not directly correspond to the spectral features of a single-photon emitter, for which the emission line is confirmed to be narrow. The band could therefore be attributed to a broadening of the ensemble emission of a set of individual emitters as a function of temperature. Conversely, a band centered at 650 nm was also observed in this work at low temperatures in O-implanted diamond, although it did not display a doublet and exhibited a limited prominence with respect to the baseline. The limited spectral prominence and the difference in the spectral position (643 nm vs 650 nm) suggest that the 643 nm line observed in Pb (references [28, 29]) and PbO_2 (reference [28] and present work) implanted samples could not be attributed to O-related impurities.

655–659 nm. Some emission lines in this spectral range are reported in reference [29] under 450 nm excitation at 4 K temperature, however their attribution is not discussed in details. PL peaks in the 651–658 nm range were also observed at room temperature in the present work from isolated spots under 532 nm excitation, although without displaying any correlation with spectral lines related to Pb-containing defects. Our tentative attribution of these lines, due to their absence from ensemble PL spectra, is therefore of radiation-induced defects. However, it cannot be ruled out that the emission originates from a Pb-containing defect characterized by a lower formation efficiency under the thermodynamic conditions adopted both in the present study and in the previous experimental efforts [28, 29].

670 nm. A relatively weak emission line at this wavelength is reported in reference [28] from room-temperature measurements carried under 405 nm laser excitation. Its observation however was not confirmed by the measurements performed in the present work under different experimental conditions (excitation wavelength, measurement temperature).

715 nm. A peak appearing at this wavelength was reported in reference [28] at a 4 K temperature. Particularly, it was observable under 532 nm laser excitation, while it could not be detected under a 450 nm excitation. Moreover, it was not observed at room temperature in reference [28] under 514 nm and 532 nm excitations. In the present work we observe that the emission line can be excited under 490.5 nm and 520 nm wavelengths at 4 K and 77 K (see figure 1), and that its intensity significantly drops at increasing temperature until it is not visible at room temperature. This observation harmonizes the results reported references [28, 29], indicating that the ionization of the involved emitter occurs at excitation wavelengths across the 450–490.5 nm range, and that the line visibility is suppressed in the 77–300 K temperature range. To the best of our knowledge, no apparent interpretation of this emission lines are currently available in literature.

5. Conclusions

We reported on the creation of Pb-related color centers in diamond by means of PbO_2^- ion implantation and subsequent thermal annealing, and their optical characterization. The measurements were performed by adopting three different excitation wavelengths, namely 405 nm, 490.5 nm and 520 nm, at different temperatures in the 4–300 K range. The results of the systematic investigation of an articulated set of PL emission peaks provide a solid interpretational framework that substantially expands the understanding of this defective complex. Moreover, both of the most prominent doublets observed at 552–557 nm and 643–648 nm [28, 29] were also observed at the single photon emitter level: while the former was already

reported in reference [28] under 532 nm excitation, the latter was characterized in the present work for the first time, under 490.5 nm excitation. A dedicated study on the photochromism [16] of individual defects is needed to clarify whether the striking resemblance of the two observed doublets could stem from their attribution to the ZPLs of Pb-related defects in different charge states.

The observation of several additional emission lines has also been studied under different experimental conditions. Particularly, the observation of the 715 nm line in reference [29] has been confirmed by our observations under 490.5 nm and 520 nm laser excitations at $T \leqslant 77$ K, while the emission could not be observed at room temperature.

Additionally, the ZPL at 517–520 nm observed in reference [29] and predicted in reference [30] was not observed in this work under any excitation wavelength and measurement temperature conditions.

Finally, a set of additional lines, not visible at the ensemble level, were observed from isolated spots at the edge of Pb-implanted regions. Their attribution was not conclusive and it cannot be ruled out that their lack of visibility in ensemble PL spectra might originate from a sub-optimal activation under the adopted thermal processing conditions. The high damage density introduced in the diamond lattice by the implantation of a heavy ion such as Pb might indeed require more effective processing methods to promote the formation of the PbV center, such as HPHT annealing [25], or alternative fabrication methods such as the incorporation of impurities during the crystal synthesis [26]. Future experimental studies on the defect formation based on such techniques could contribute to fully disambiguate the nature of the spectral features associated with Pb implantation in diamond.

These results clarify the potential of the PbV center for its high-impact application in quantum technologies. Besides the clear advantage offered by a bright and narrowband emitter for on-demand single-photon generation [42] or labeling in biological environments [43], the long spin coherence stemming from the predicted large ground-state splitting of the PbV^- center prospects a promising tool for the practical realization of multi-qubit quantum network nodes.

Acknowledgments

This work was supported by the following projects: Coordinated Research Project 'F11020' of the International Atomic Energy Agency (IAEA); Project 'Piemonte Quantum Enabling Technologies' (PiQuET), funded by the Piemonte Region within the 'Infra-P' scheme (POR-FESR 2014–2020 program of the European Union); 'Departments of Excellence' (L. 232/2016), funded by the Italian Ministry of Education, University and Research (MIUR); 'Ex post funding of research' of the University of Torino funded by the 'Compagnia di San Paolo'; FET OPEN Pathos; 'Intelligent fabrication of QUANTum devices in DIAmond by Laser and Ion Irradiation' (QuantDia) project funded by the Italian Ministry for Instruction, University and Research within the 'FISR 2019' program; 'Training on LASer fabrication and ION implantation of DEFects as quantum emitters' (LasIonDef) project funded by the European Research Council under the 'Marie Skłodowska-Curie Innovative Training Networks' program. The projects 17FUN06 (SIQUST), 17FUN01 (BeCOMe) and 20FUN05 (SEQUME) leading to this publication have received funding from the EMPIR programme co-financed by the Participating States and from the European Union's Horizon 2020 Research and Innovation Programme. TL, SP and JM acknowledge the support of the ASTERIQS program of the European Commission. SDT and JF gratefully acknowledge the EU RADIATE Project (proposal 19001744) for granting transnational access to the Laboratories of the Ru đer Bošović Institute.

Data availability statement

The data that support the findings of this study are available upon reasonable request from the authors.

ORCID iDs

Sviatoslav Ditalia Tchernij https://orcid.org/0000-0002-2639-5229
Ivo Pietro Degiovanni https://orcid.org/0000-0003-0332-3115
Georgios Provatas https://orcid.org/0000-0001-9471-1572
Paolo Olivero https://orcid.org/0000-0002-7512-6295
Marco Genovese https://orcid.org/0000-0001-9186-8849
Jacopo Forneris https://orcid.org/0000-0003-2583-7424

References

[1] Doherty M W, Manson N B, Delaney P, Jelezko F, Wrachtrup J and Hollenberg L C L 2013 The nitrogen-vacancy colour centre in diamond *Phys. Rep.* **528** 1–45
[2] Childress L and Hanson R 2013 Diamond NV centers for quantum computing and quantum networks *MRS Bull.* **38** 134–8
[3] Nelz R *et al* 2019 Toward wafer-scale diamond nano- and quantum technologies *APL Mater.* **7** 011108
[4] Metsch M H *et al* 2019 Initialization and readout of nuclear spins via negatively charged silicon-vacancy center in diamond *Phys. Rev. Lett.* **122** 190503
[5] Schröder T, Mouradian S L, Zheng J, Trusheim M E, Walsh M, Chen E H, Li L, Bayn I and Englund D 2016 Quantum nanophotonics in diamond (Invited) *J. Opt. Soc. Am.* B **33** B65–83
[6] Bradac C, Gao W, Forneris J, Trusheim M and Aharonovich I 2019 Quantum nanophotonics with group IV defects in diamond (arXiv:1906.10992)
[7] Petrini G, Moreva E, Bernardi E, Traina P, Tomagra G, Carabelli V, Degiovanni I P and Genovese M 2020 Is a quantum biosensing revolution approaching? Perspectives in NV-assisted current and thermal biosensing in living cells *Adv. Quantum Technol.* **3** 2000066
[8] Lühmann T *et al* 2018 Screening and engineering of colour centres in diamond *J. Phys. D: Appl. Phys.* **51** 483002
[9] Eaton S M *et al* 2019 Quantum micro-nano devices fabricated in diamond by femtosecond laser and ion irradiation *Adv. Quantum Technol.* **2** 1900006
[10] Barry J F, Turner M J, Schloss J M, Glenn D R, Song Y, Lukin M D, Park H and Walsworth R L 2016 Optical magnetic detection of single-neuron action potentials using quantum defects in diamond *Proc. Natl Acad. Sci.* **113** 14133–8
[11] Hensen B *et al* 2015 Loophole-free Bell inequality violation using electron spins separated by 1.3 kilometres *Nature* **526** 682
[12] Breeze J D, Salvadori E, Sathian J, Alford N M and Kay C W M 2018 Continuous-wave room-temperature diamond maser *Nature* **555** 493
[13] Webb J L, Clement J D, Troise L, Ahmadi S, Johansen G J, Huck A and Andersen U L 2019 Nanotesla sensitivity magnetic field sensing using a compact diamond nitrogen-vacancy magnetometer *Appl. Phys. Lett.* **114** 231103
[14] Zhou H *et al* 2020 Quantum metrology with strongly interacting spin systems *Phys. Rev.* X **10** 31003
[15] Unden T *et al* 2018 Coherent control of solid state nuclear spin nano-ensembles *npj Quantum Inf.* **4** 39
[16] Gaebel T *et al* 2006 Photochromism in single nitrogen-vacancy defect in diamond *Appl. Phys.* B **82** 243–6
[17] Bradac C *et al* 2010 Observation and control of blinking nitrogen-vacancy centres in discrete nanodiamonds *Nat. Nanotechnol.* **5** 345–9
[18] Becker J N *et al* 2016 Ultrafast all-optical coherent control of single silicon vacancy colour centres in diamond *Nat. Commun.* **7** 13512
[19] Görlitz J *et al* 2020 Spectroscopic investigations of negatively charged tin-vacancy centres in diamond *New J. Phys.* **22** 013048
[20] Sukachev D D *et al* 2017 Silicon-vacancy spin qubit in diamond: a quantum memory exceeding 10 ms with single-shot state readout *Phys. Rev. Lett.* **119** 223602
[21] Iwasaki T *et al* 2015 Germanium-vacancy single color centers in diamond *Sci. Rep.* **5** 12882
[22] Siyushev P *et al* 2017 Optical and microwave control of germanium-vacancy center spins in diamond *Phys. Rev.* B **96** 081201
[23] Meng X, Liu S, Dadap J I and Osgood R M Jr 2017 Plasmonic enhancement of a silicon-vacancy center in a nanodiamond crystal *Phys. Rev. Mater.* **1** 015202
[24] Ditalia Tchernij S *et al* 2017 Single-photon-emitting optical centers in diamond fabricated upon Sn implantation *ACS Photonics* **4** 2580
[25] Iwasaki T, Miyamoto Y, Siyushev P, Jelezko F, Taniguchi T, Metsch M and Hatano M 2017 Tin-vacancy quantum emitters in diamond *Phys. Rev. Lett.* **119** 253601
[26] Palyanov Y N, Kupriyanov I N and Borzdov Y M 2019 High-pressure synthesis and characterization of Sn-doped single crystal diamond *Carbon* **143** 769
[27] Trusheim M E *et al* 2020 Transform-limited photons from a coherent tin-vacancy spin in diamond *Phys. Rev. Lett.* **124** 023602
[28] Ditalia Tchernij S *et al* 2018 Single-photon emitters in lead-implanted single-crystal diamond *ACS Photonics* **5** 4864
[29] Trusheim M E *et al* 2019 Lead-related quantum emitters in diamond *Phys. Rev.* B **99** 075430
[30] Thiering G and Gali A 2018 *Ab initio* magneto-optical spectrum of group-IV vacancy color centers in diamond *Phys. Rev.* X **021063** 2–17
[31] Middleton R A 1990 *Negative Ion Cookbook* (Philadelphia: University of Pennsylvania)
[32] Gozzelino L *et al* 2011 Magnetic characterization of MgB_2 bulk superconductor for magnetic field mitigation solutions *J. Supercond. Nov. Magnetism* **24** 307–12
[33] Binder J M *et al* 2017 Qudi: a modular python suite for experiment control and data processing *SoftwareX* **6** 85
[34] Brouri R, Beveratos A, Poizat J-P and Grangier P 2000 Photon antibunching in the fluorescence of individual color centers in diamond *Opt. Lett.* **25** 1294
[35] Chunnilall C J, Degiovanni I P, Kück S, Müller I and Sinclair A G 2014 Metrology of single-photon sources and detectors: a review *Opt. Eng.* **53** 081910
[36] Eisaman M D, Fan J, Migdall A and Polyakov S V 2011 Invited review article: single-photon sources and detectors *Rev. Sci. Instrum.* **82** 071101
[37] Zaitsev A M 2001 *Optical Properties of Diamond* (Berlin: Springer)
[38] Field J E 1992 *The Properties of Natural and Synthetic Diamond* (New York: Academic)
[39] Forneris J *et al* 2017 Electrical control of deep NV centers in diamond by means of sub-superficial graphitic micro-electrodes *Carbon* **113** 76–86
[40] Aslam N, Waldherr G, Neumann P, Jelezko F and Wrachtrup J 2013 Photo-induced ionization dynamics of the nitrogen vacancy defect in diamond investigated by single-shot charge state detection *New J. Phys.* **15** 013064
[41] Zhang Y, Wang K, Chang S, Tian Y and Li J 2020 Photoluminescence studies of the 640 nm center in electron irradiated IIa diamond *Spectrosc. Lett.* **53** 580
[42] Sipahigil A *et al* 2016 An integrated diamond nanophotonics platform for quantum-optical networks *Science* **354** 847–50
[43] Simpson D A, Morrisroe E, McCoey J M, Lombard A H, Mendis D C, Treussart F, Hall L T, Petrou S and Hollenberg L C L 2017 Non-neurotoxic nanodiamond probes for intraneuronal temperature mapping *ACS Nano* **11** 12077

ADVANCED PHOTONICS RESEARCH
Open Access
www.adpr-journal.com

Spectral Emission Dependence of Tin-Vacancy Centers in Diamond from Thermal Processing and Chemical Functionalization

Emilio Corte, Selene Sachero, Sviatoslav Ditalia Tchernij, Tobias Lühmann, Sébastien Pezzagna, Paolo Traina, Ivo Pietro Degiovanni, Ekaterina Moreva, Paolo Olivero, Jan Meijer, Marco Genovese, and Jacopo Forneris**

A systematic photoluminescence (PL) investigation of the spectral emission properties of individual optical defects fabricated in diamond upon ion implantation and annealing is reported. Three spectral lines at 620, 631, and 647 nm are identified and attributed to the SnV center due to their occurrence in the PL spectra of the very same single-photon emitting defects. It is shown that the relative occurrence of the three spectral features can be modified by oxidizing the sample surface following thermal annealing. The relevant emission properties of each class of individual emitters, including the excited state emission lifetime and the emission intensity saturation parameters are reported.

1. Introduction

Diamond-based color centers are appealing candidates as solid-state single-photon sources for applications in emerging fields of quantum technologies, such as quantum computing, quantum information, and quantum sensing.[1–5] A class of group-IV-related quantum emitters, fabricated upon Sn ion implantation, thermal annealing, and surface oxidation was recently discovered.[6,7] These color centers exhibit intriguing opto-physical properties, such as high emission rate, narrow spectral width, and emission concentrated in the zero-phonon line (ZPL), thus sparking the interest of the scientific community toward practical applications in the field of quantum technologies,[4] including quantum sensing,[8] nanophotonics,[9] and spintronics.[10,11]

The characteristic spectral feature of the optical activity of the SnV center consists of a strong room-temperature ZPL emission at 620 nm, which is widely attributed to the negative charge state of the defect (SnV^-) based on the convincing support of independent theoretical works based on ab initio simulations.[6,11,12] In addition, multiple works have independently observed additional emission lines at 593 nm,[6,7,13,14] 631 nm,[7,14,15] 647 nm,[6–8,13–15] and 663 nm.[12,14,15]

While the 663-nm line has been convincingly interpreted as a radiation-induced defect,[12,15] the attribution of the remaining photoluminescence (PL) peaks is still uncertain and requires further disambiguation. DFT simulations have highlighted the possibility to observe the SnV center in different charge states,[11,16] however a conclusive model of the experimental findings according to this interpretation has not been achieved yet. Recent reports on this subject suggest that the aforementioned emission lines are originating from different Sn-containing lattice complexes.[6,8,9] In these works the defects are created by ion irradiation, and different experimental conditions (ion implantation energy, annealing temperature and duration, and chemical termination of the latter) are explored. In particular, it is worth noting that the ion irradiation parameters result in different depth distributions of the defects, as well as their distance from the surface. Remarkably, high-pressure/high-temperature annealing processing performed without specific additional surface treatments resulted in the observation of the sole 620 nm emission line.[6] Moreover, the excitability of the 647 nm line under 633 nm laser excitation provided a strong experimental indication that such spectral feature cannot be attributed to the negative charge state of the SnV defect (620 nm ZPL).[15]

Finally, the electrical control of the Fermi level of an O-terminated p-i-p diamond junction has shown that all the

E. Corte, S. Ditalia Tchernij, P. Olivero, J. Forneris
Dipartimento di Fisica, Università degli Studi di Torino, Istituto Nazionale di Fisica Nucleare (INFN), Sez. Torino
Istituto Nazionale di Ricerca Metrologica (INRiM)
via P. Giuria 1, 10125 Torino, Italy
E-mail: sviatoslav.ditaliatchernij@unito.it; jacopo.forneris@unito.it

S. Sachero
Dipartimento di Fisica
Università degli Studi di Torino
via P. Giuria 1, 10125 Torino, Italy

T. Lühmann, S. Pezzagna, J. Meijer
Applied Quantum Systems, Felix-Bloch Institute for Solid-State Physics
Universität Leipzig
Linnéstraße 5, 04103 Leipzig, Germany

P. Traina, I. P. Degiovanni, E. Moreva, M. Genovese
Division of Quantum Metrology and Nanotechnologies
Istituto Nazionale di Ricerca Metrologica (INRiM)
Strada delle Cacce 91, 10135 Torino, Italy

The ORCID identification number(s) for the author(s) of this article can be found under https://doi.org/10.1002/adpr.202100148.

© 2021 The Authors. Advanced Photonics Research published by Wiley-VCH GmbH. This is an open access article under the terms of the Creative Commons Attribution License, which permits use, distribution and reproduction in any medium, provided the original work is properly cited.

DOI: 10.1002/adpr.202100148

26999293, 2022, 1, Downloaded from https://onlinelibrary.wiley.com/doi/10.1002/adpr.202100148 by Universita Di Torino, Wiley Online Library on [13/05/2024]. See the Terms and Conditions (https://onlinelibrary.wiley.com/terms-and-conditions) on Wiley Online Library for rules of use; OA articles are governed by the applicable Creative Commons License

620, 631, and 647 nm could be identified at the single-photon emitter level, but those spectral features were observed only from separate defects.[14]

In this work, we compare the room-temperature properties of single emitters in a Sn-ion-implanted diamond sample following different post-implantation processing treatments. Particularly, we report the concurrent observation di of the 620, 631, and 647 nm from the same individual emitter after a thermal annealing process that was not followed by a chemical functionalization of the diamond surface. We also discuss the variation in the relative population of the emission lines in a discrete set of single centers upon the subsequent O-termination of the sample surface by means of plasma treatments. Finally, we report a characterization of the aforementioned lines at the single-photon emitter level. These results offer promising perspectives towards the chemical control of the emission properties of Sn-related defects in diamond.

2. Results

2.1. Sn-Related Emitters Formed upon Thermal Annealing

We report in this section the characterization of the emitters upon the sole thermal annealing, that is, without any further surface functionalization. **Figure 1**a shows a typical PL map ($13 \times 13\,\mu m^2$ area, 60 μW excitation power) acquired from the region under investigation,[29] showing a density of $\leq 1\,\mu m^{-2}$ bright luminescent spots, whose emission was investigated individually. The discussion in the following text is focused on those sole spots (≈30), where HBT interferometry confirmed a second-order auto-correlation function $g^{(2)}(t=0) < 0.25$ after background correction.[7] Consistently with what observed in the reports discussed in Section 1, three main groups of spectral lines were observed, corresponding to the emission at 620 nm (S1), 631 nm (S2), and 647 nm (S3). Selected spectra are reported in **Figure 1**b, highlighting that the S1–S3 emission lines could be observed both separately (i–iii) as the sole spectral feature of the considered center, as well as concurrently in the emission spectra of the same individual single-photon emitter. Particularly, Figure 1b-iv, v, and vi show the spectra of single-photon emitters exhibiting both the "S1 and S2", "S1 and S3," "S2 and S3" spectral features at the same time, respectively. **Figure 2**a (grey dots refer to the as-annealed sample) shows the spectral position of the emission lines acquired during the PL characterization, evidencing a non-negligible (i.e., ≈25%) occurrence of multiple emission lines among the S1–S3 set from the same point defect. The reported peaks were identified using a spectral analysis routine relying on first derivative analysis. A threshold for noise discrimination was set to select only those peaks having a prominence with respect to the baseline higher than 10% the prominence of the most intense peak.

To provide further insight into the aforementioned discussion, we report in **Figure 3**a the PL spectrum of an individual emitter concurrently exhibiting the S1 and S3 emission peaks. Figure 3b shows the $g^{(2)}(t)$ acquired from the center under 0.27 mW laser excitation. The antibunching at $t=0$ (background-corrected $g^{(2)}(0)=0.11 \pm 0.11$, considering a signal-to-background ratio[6,7] of $\rho = 0.49 \pm 0.05$) indicates that the emission originates from an individual lattice defect.[30]

Conversely in Figure 3c we report the PL spectrum of a diffraction-limited spot where both the S2 and S3 line could be observed. The antibunching behavior was denoted by a value of $g^{(2)}(0) = 0.04 \pm 0.09$ upon background subtraction ($\rho = 0.55 \pm 0.07$), confirming that also in this case the emission originates from the very same emitter.

Based on this analysis, the concurrent observation of the pairs of spectral features (S1 and S3; S2 and S3) individual emitters suggests that all the three emission lines are to be referred to the same localized lattice defect.

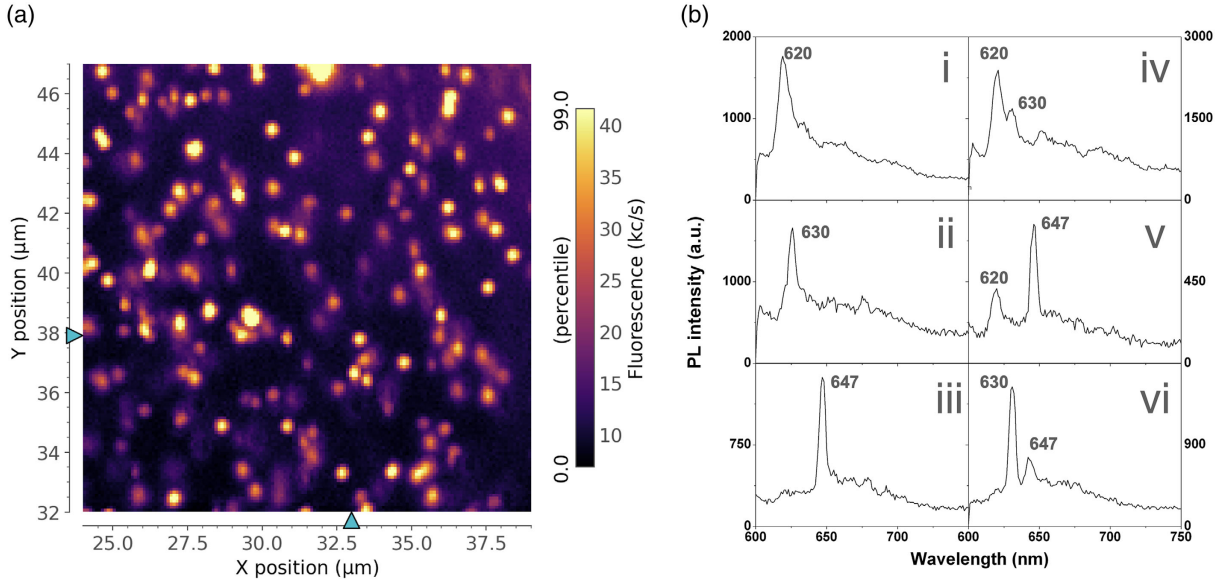


Figure 1. a) Typical confocal PL map acquired under 520 nm laser excitation (60 μW power on the sample) from the Sn-implanted region of interest of the sample. b) PL spectra from individual emitters exhibiting emission lines at: i) 620 nm, ii) 631 nm, iii) 647 nm, iv) 620 and 631 nm; v) 620 and 647 nm, and vi) 631 and 647 nm.

© 2021 The Authors. Advanced Photonics Research published by Wiley-VCH GmbH

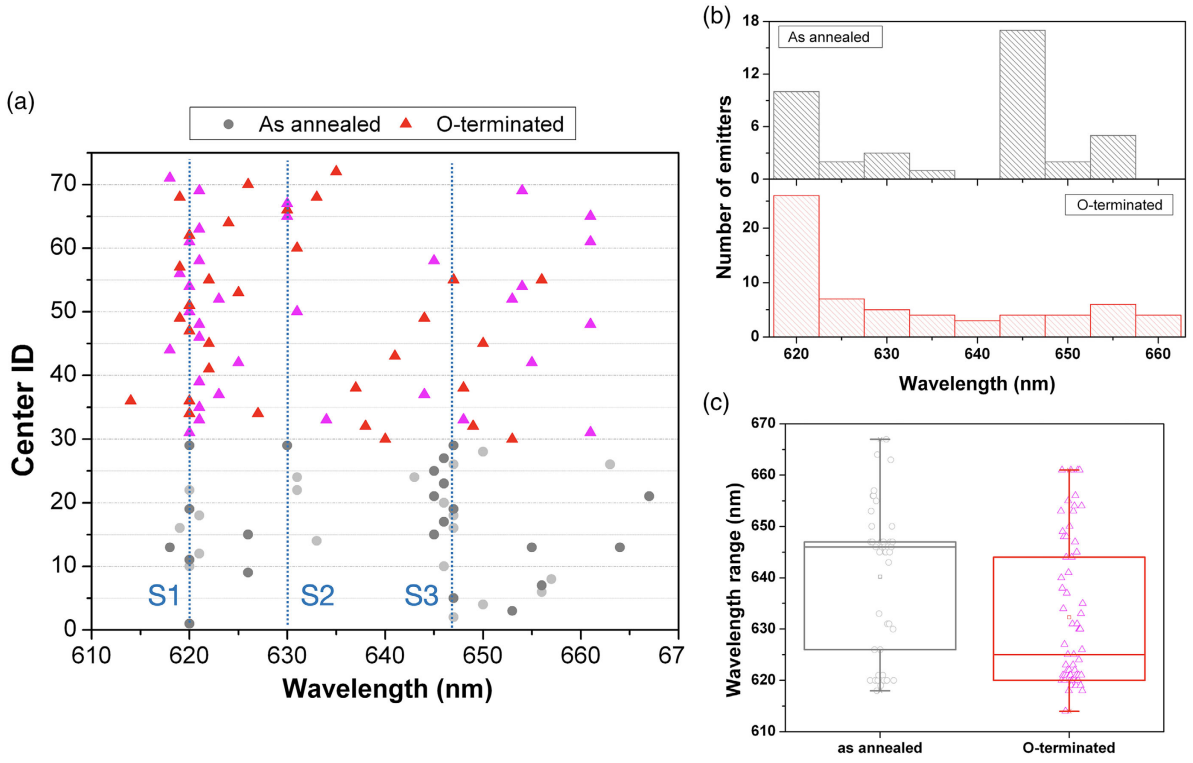


Figure 2. a) Summary of the spectral position of the main emission lines acquired from a set of individual diffraction-limited emitting spots in the Sn-implanted region of the sample. Both light and dark grey dots refer to the as-annealed sample; the alternate color code is chosen to highlight the occurrence of multiple emission lines from individual emitting spots. Red and magenta dots refer to emitters observed in the sample upon oxygen plasma treatment. b) Histograms of the occurrence of emission lines relative to the dataset shown in a). Grey and red bars refer to the as-annealed and oxygen-terminated sample, respectively. c) Box chart of the emission lines distribution extracted from the datasets in a).

2.2. Sn-Related Emitters Characterization upon Surface O-Termination

We report the PL characterization of the emitters in the region of interest of the sample following the O_2 plasma treatment described in Section 2. The O-termination of the sample required to unmount the sample from the confocal microscope. After this process the same region of the sample was investigated, but a study of the very same emitters studied in the previous experimental campaigns could not be performed. The interpretation of the data therefore rely on the assumption that the occurrence of the spectral lines is homogeneous in the whole region of interest, provided that the same density of centers per surface unit was observed. Additional characterizations performed after an O_2 plasma treatment performed at a higher microwave power (40 W) provided results statistically comparable with those reported here. Figure 2a shows the spectral position of the PL lines observed over a set of ≈40 emitters upon O-termination of the surface (red scatter data). The data indicate an apparent increase in the relative population of the S1 emission line, concurrently with a significant decrease in that of the S2 peak. This observation is further corroborated by the histogram shown in Figure 2b showing the occurrence of the spectral lines as a function of the emission wavelength observed after thermal annealing (gray bars) and after plasma treatment (red).

The "as annealed" sample reveals a prevalence of the S3 line (≈40% of the total amount of the observed lines) with respect to the S1 (25%). Such distribution is completely reversed in the O-terminated configuration, in which S1 becomes the most observed spectral feature (≈40%), the S3 emission being associated to a mere 6% of the counts. Such observation is more evidenced by the box chart shown in Figure 2c. Here, the median of the "as annealed" sample ZPL distribution (gray) coincides with the S3 emission line, while the range of spectra features compatible with the S1 line define the Q2–Q1 interquartile for the "O-terminated" data (red).

These data, together with the concurrent observation of both S1 and S3 lines from the very same individual defect, might be suggestive of their attribution to different charge states of the same defect. Particularly, the S1 line has been unambiguously attributed to the negative charge state of the tin-vacancy center SnV^-.[6,11] The prevalence of this line upon O-termination of the diamond surface is also in line with what already reported for the nitrogen-vacancy center (NV), whose negative charge state is stabilized upon chemical functionalization by elements with positive electron affinity.[31] However, a direct comparison with the charge state population of NV centers could not be performed due to the scarce amount of these defects in the sample under investigation. Furthermore, previous attempts to dynamically switch the S1 and S3 emission upon the electrical tuning of

© 2021 The Authors. Advanced Photonics Research published by Wiley-VCH GmbH

26999293, 2022, 1, Downloaded from https://onlinelibrary.wiley.com/doi/10.1002/adpr.202100148 by Universita Di Torino, Wiley Online Library on [13/05/2024]. See the Terms and Conditions (https://onlinelibrary.wiley.com/terms-and-conditions) on Wiley Online Library for rules of use; OA articles are governed by the applicable Creative Commons License

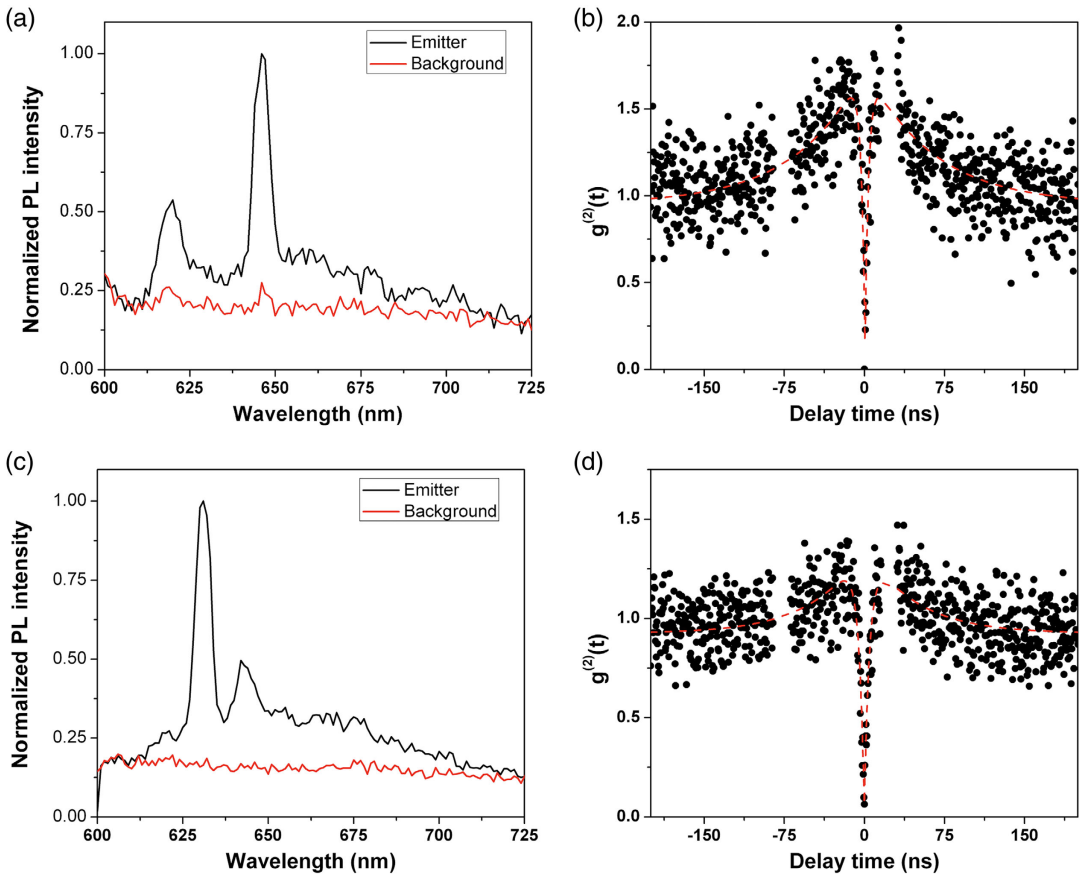


Figure 3. a) Emission spectrum from a diffraction-limited emission spot (black line) showing the S1 and S3 lines. The red line indicates the background emission spectrum acquired from a low-intensity emission spot placed in closed proximity of the probed emitter. The black line does not take into account background subtraction. b) Corresponding background-corrected second-order autocorrelation function $g^{(2)}(t)$. c) Emission spectrum from a diffraction-limited emission spot (black line) showing the S2 and S3 lines, and d) corresponding background-corrected $g^{(2)}(t)$ function. Both $g^{(2)}(t)$ functions were measured under 520 nm laser excitation (0.27 mW power). The missing datapoint around −75 and +20 ns delay time correspond to the backflash peaks of the HBT interferometer,[40] which were removed for ease of view.

the diamond Fermi level down to 4.6 eV below the conduction band[14] suggest that S3 line might not be identified with the SnV^0 charge state. Therefore, the attribution of the S3 line to the interaction of the SnV center with surrounding defects resulting from an incomplete annealing of the crystal lattice upon ion implantation, could not be disregarded under the parameters adopted for the sample processing.[6]

Photon count rate blinking could not be adopted as a criterion to discriminate among these two possible attributions. On the one hand, indeed, blinking is often linked with both charge state conversion and non-resonant energy transfer to surrounding defects.[32,33] On the other hand, count rate blinking (few to tens of seconds time scales) was indeed observed even from several defects exhibiting one spectral line only upon sufficiently high excitation power (>200 μW). Conversely, several diffraction-limited spots exhibiting multiple spectral components showed stable count rates over tens of seconds of observation. Finally, the spectral measurements were acquired using a scanning monochromator, so that the simultaneous monitoring over time of the three main emission lines was not possible due to the given constraints of the experimental setup.

The histogram shown in Figure 2b does not reveal urther significant spectral components, neither in the as-annealed sample, nor following the subsequent surface oxidization. Both the S2 and the 660 nm lines are observed, although their occurrence is significantly smaller than that of the S1 and S3 spectral features (S2: 7% as-annealed, 8% O-terminated; 660 nm: 12% as annealed, 9% O-terminated).

It is also worth mentioning that 7% of the identified emission lines in the as-annealed sample does not correspond to the S1 or S3 lines, but occur in the spectral range comprised between 620 and 635 nm. Such fraction increases to 35% if the lines in the 625–655 nm range are considered for the O-terminated sample. This observation might not be incompatible with the hypothesis that the SnV center is not fully formed under the adopted low-pressure high-temperature annealing process,[5,6] or with the interpretation of the ZPL spectral diffusion as a consequence of the radiation-induced local strain interacting with the defects.

© 2021 The Authors. Advanced Photonics Research published by Wiley-VCH GmbH

26999293, 2022, 1, Downloaded from https://onlinelibrary.wiley.com/doi/10.1002/adpr.202100148 by Universita Di Torino, Wiley Online Library on [13/05/2024]. See the Terms and Conditions (https://onlinelibrary.wiley.com/terms-and-conditions) on Wiley Online Library for rules of use; OA articles are governed by the applicable Creative Commons License

26999293, 2022, 1, Downloaded from https://onlinelibrary.wiley.com/doi/10.1002/adpr.202100148 by Universita Di Torino, Wiley Online Library on [13/05/2024]. See the Terms and Conditions (https://onlinelibrary.wiley.com/terms-and-conditions) on Wiley Online Library for rules of use; OA articles are governed by the applicable Creative Commons License

2.3. Characterization of Emitters with S1, S2, and S3 Spectral Features

Individual Sn-related centers evidencing a single emission line were studied systematically to assess the respective emission properties in the "as annealed" sample. The properties observed at the single-photon emitter level did not reveal significant differences upon O-termination of the surface, in addition to the occurrence of each spectral line.

We report the results acquired from individual emitters exhibiting only one spectral feature, that is, the S1, S2, and S3 line only, respectively.

Each of these defects was characterized by acquiring the second-order auto-correlation function curve at different optical excitation powers. Each of these curves underwent a fitting procedure according to a three-level system based on the following equation[7,34]:

$$g^{(2)}(t) = 1 - a_1 \exp(-|t|\lambda_1) + a_2 \exp(-|t|\lambda_2) \quad (1)$$

where the term proportional to a_1 describes the nonclassical antibunching signature of quantum emitters. The λ_1 parameter was fitted against the excitation power P according to a linear model to infer the lifetime of the excited state as $\tau = [\lambda_1(P=0)]^{-1}$.

We also studied the emission intensity I of the defect as a function of the optical excitation power, to establish a preliminary comparison of the relevant emission properties of the three spectral components on the basis of those, already discussed in the literature, of the S1 line. The emission intensity was modelled after the expression[7,35]

$$I(P) = I_{sat} \cdot P/(P + P_{sat}) \quad (2)$$

where I_{sat} and P_{sat} are the saturation intensity and the saturation excitation power, respectively.

2.3.1. S1—620 nm Emission Line

The characterization of the defect emitting at 620 nm ZPL (from whom the PL spectrum "i" reported in Figure 1b was acquired) is shown in **Figure 4**. $g^{(2)}(t)$ curves acquired in the 0.27–0.43 mW excitation power range (Figure 4a) are reported as an example. The linear fitting of the λ_1 parameter (Figure 4b) resulted in an estimation of the radiative emission lifetime of $\tau = (6.0 \pm 0.8)$ ns, a value fully compatible with what reported in previous works and attributed to the ZPL of the SnV^- center.[6,7,36] Similarly, the center's deshelving lifetime was estimated by a linear regression of the dependence of λ_2 on the laser excitation power (Figure 4c) as $\tau_2 = \lambda_2\ (0)^{-1} = (68 \pm 9)$ ns. The analysis upon background subtraction of the emission intensity saturation curve (Figure 4d) resulted in an excitation saturation power $P_{sat} = (0.32 \pm 0.07)$ mW. This value is compatible with what reported in ref. [7], considering that the (1.11 ± 0.01) mW value reported there quantified the laser power

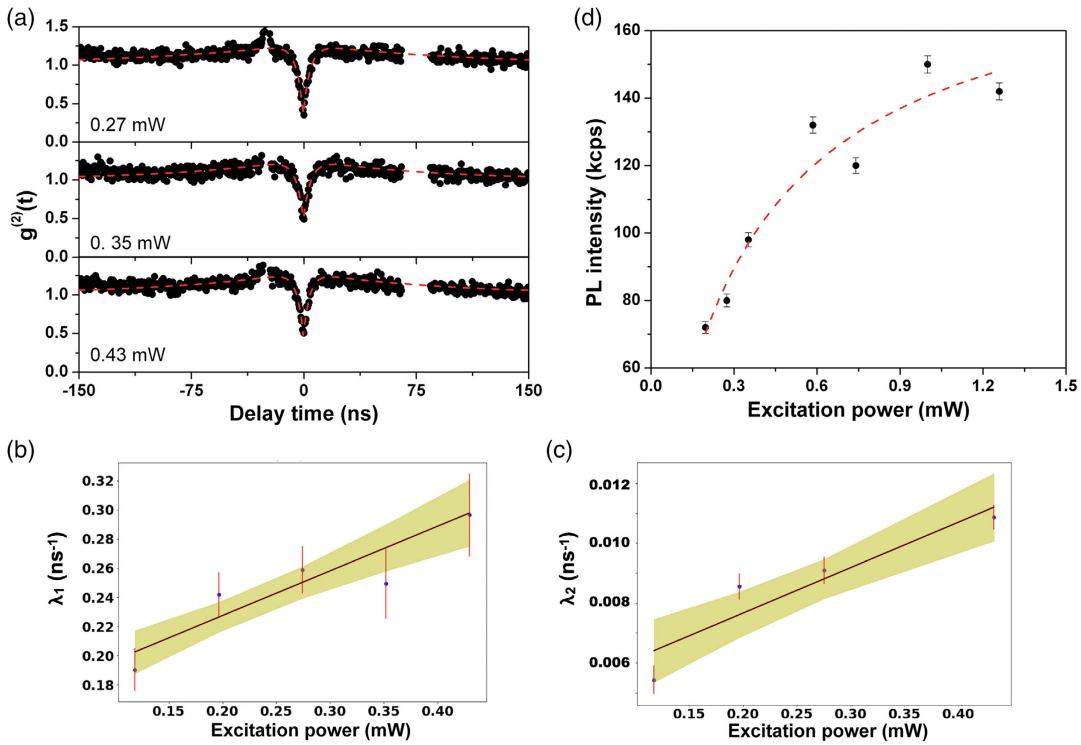


Figure 4. Characterization of the single-photon emission properties of an individual Sn-related defect emitting at the S1 line (620 nm), corresponding to the PL spectrum iii in Figure 1b. a) Second-order auto-correlation functions ($g^{(2)}(t)$ curves shown without background-correction) acquired under 0.27, 0.35, and 0.43 mW laser excitation power. b) Linear fit of the decay constant λ_1 extracted from the function fit of the $g^{(2)}(t)$ curves as a function of the excitation power. Red lines represent the fitting curves. c) Linear fit of the deshelving state lifetime parameter as a function of the laser excitation power. d) Background-subtracted emission rate as a function of the laser excitation power. The red dashed line represents the fitting curve.

© 2021 The Authors. Advanced Photonics Research published by Wiley-VCH GmbH

incident on the microscope objective. A decrease of ≈60% in the power transmitted to the sample was observed in the confocal microscope adopted in this work. The saturation emission intensity $I_{sat} = (186 \pm 15)$ kcps was an order of magnitude lower than what reported in the previous characterization of this emission line.[7] This discrepancy is ascribed to the fiber-coupling of the source in the confocal microscope adopted for the present study, to be compared with the adoption of a higher-efficiency air-coupling of single-photon detectors in the referenced work. While a direct comparison between the two experiments cannot be performed without a metrological calibration of the two experimental apparatuses, the value obtained in this work could be used as a reference to assess the relative intensity of the S2 and S3 emission lines with respect to the bright[6,7] emission of the 620 nm peak.

2.3.2. S2—631 nm Emission Line

A defect emitting at 631 nm (PL spectrum "ii" in Figure 1b) was characterized against the same emission properties (**Figure 5**). The acquisition of $g^{(2)}(t)$ curves in the 0.27–0.59 mW excitation power range (Figure 5a) enabled a preliminary estimation of the center lifetime as $\tau_1 = \lambda_1 (0)^{-1} = (4.8 \pm 1.7)$ ns (Figure 5b). Despite the value being compatible with that of the S1 line, the saturation emission intensity (Figure 5c) displayed a significantly higher value of $I_{sat} = (300 \pm 40)$ kcps achieved at a compatible excitation saturation power $P_{sat} = (0.42 \pm 0.08)$ mW.

2.3.3. S3—647 nm Emission Line

The $g^{(2)}(t)$ curves relative to the 647 nm emission of a defect associated with the PL spectrum "iii" in Figure 1b are shown in **Figure 6**a for the 0.27–0.59 mW excitation power range. The measurements enabled to quantify the center's excited state lifetime as $\tau_1 = (7.4 \pm 1.0)$ ns (Figure 6b).

It is also worth noting that the λ_2 parameter (Figure 6c) exhibits a decreasing trend at increasing excitation power, a behavior which is not usually observed in diamond quantum emitters.[37,38] The deshelving lifetime was estimated from the intercept parameter of the linear regression in Figure 6b as $\tau_2 = \lambda_1 (0)^{-1} = (68 \pm 9)$ ns.

The unusual behavior observed for the emitter can be tentatively attributed to the power-dependent depletion of the shelving state in favor of a fourth, excited state.[37] This interpretation would be in line with the attribution of the S3 emission to the interaction of the SnV center with a surrounding radiation-induced defect. However, an unambiguous attribution of this phenomenon, such as the identification of the additional fourth level with the conduction band (thus indicating a charge-state conversion process) or its attribution to resonant energy transfer with surrounding lattice defects will require systematic dedicated studies.

The saturation emission intensity (Figure 5d) displayed a value of $I_{sat} = (450 \pm 70)$ kcps, suggesting that the center is twice as bright as the SnV^- ZPL. Conversely, the optical power required to achieve the saturation ($P_{sat} = (1.0 \pm 0.3)$ mW) is twice as higher.

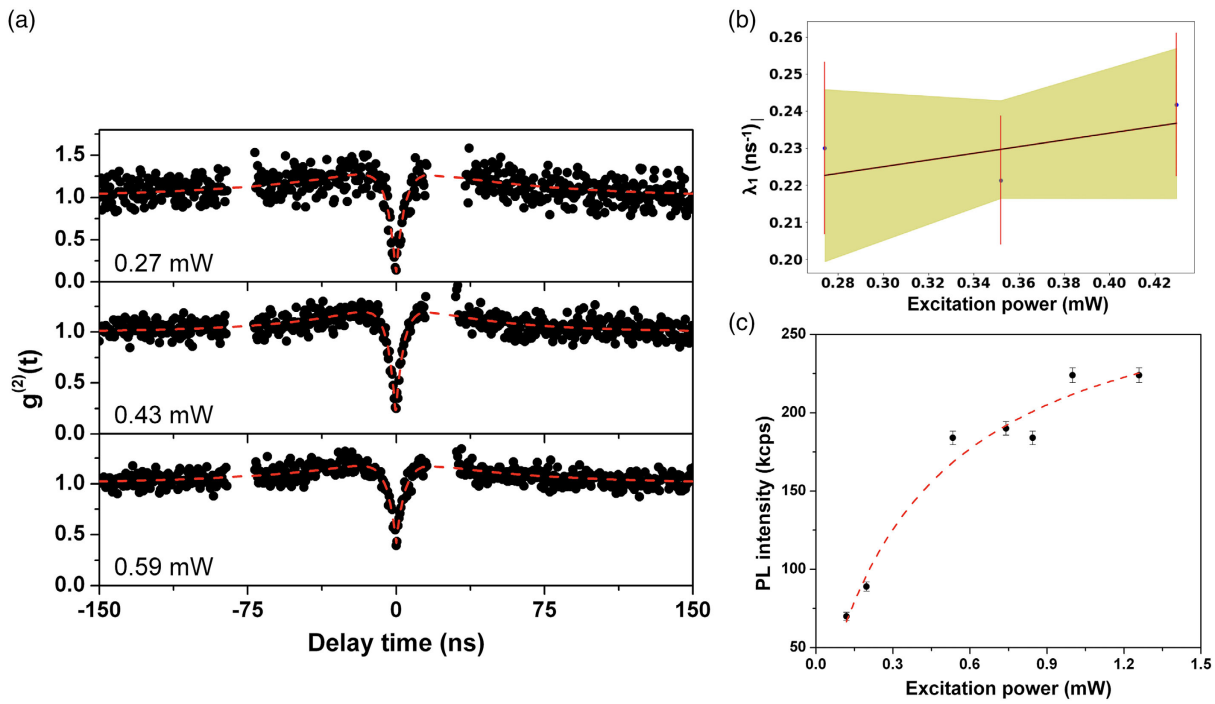


Figure 5. Characterization of the single-photon emission properties of an individual Sn-related defect emitting at the S2 line (631 nm, corresponding to the PL spectrum ii in Figure 1b. a) Second-order auto-correlation functions ($g^{(2)}(t)$ curves shown without background-correction) acquired under 0.27, 0.43, and 0.59 mW laser excitation power. b) Linear fit of the decay constant λ_1 extracted from the function fit of the $g^{(2)}(t)$ curves as a function of the excitation power. c) Background-subtracted emission rate as a function of the laser excitation power. The red dashed line represents the fitting curve.

© 2021 The Authors. Advanced Photonics Research published by Wiley-VCH GmbH

26999293, 2022, 1, Downloaded from https://onlinelibrary.wiley.com/doi/10.1002/adpr.202100148 by Universita Di Torino, Wiley Online Library on [13/05/2024]. See the Terms and Conditions (https://onlinelibrary.wiley.com/terms-and-conditions) on Wiley Online Library for rules of use; OA articles are governed by the applicable Creative Commons License

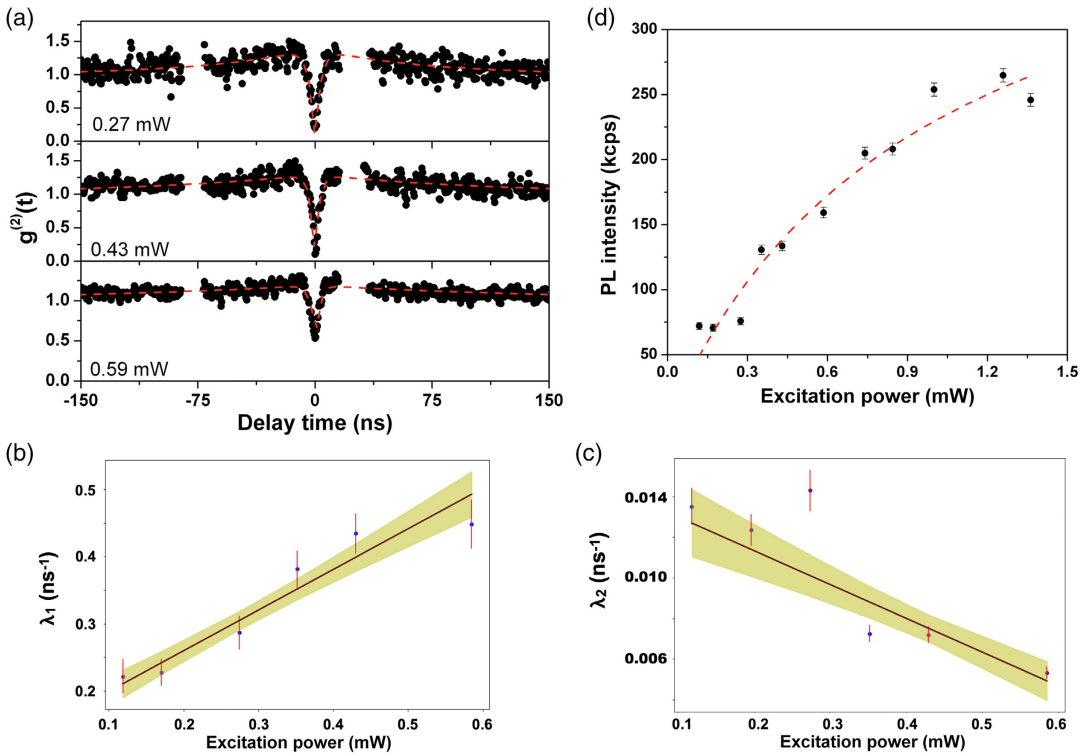


Figure 6. Characterization of the single-photon emission properties of an individual Sn-related defect emitting at the S3 line (647 nm), corresponding to the PL spectrum iii in Figure 1b. a) Second-order auto-correlation functions ($g^{(2)}(t)$ curves shown without background-correction) acquired under 0.27, 0.43, and 0.59 mW laser excitation power. b) Linear fit of the decay constant λ_1 extracted from the function fit of the $g^{(2)}(t)$ curves as a function of the excitation power. c) Linear fit of the deshelving state lifetime parameter as a function of the laser excitation power. d) Background-subtracted emission rate as a function of the laser excitation power. The red dashed line represents the fitting curve.

Table 1. Summary of the emission properties of individual defects in Sn-implanted diamond.

Wavelength [nm]	Emission saturation intensity [kcps]	Emission saturation power [mW]	Excited state lifetime [ns]	Deshelving transition lifetime [ns]
620	186 ± 15	0.32 ± 0.07	6.0 ± 0.8	220 ± 60
631	300 ± 40	0.42 ± 0.08	4.8 ± 1.7	NA
647	450 ± 70	1.0 ± 0.3	7.4 ± 1.0	68 ± 9

A summary of the relevant characterization parameters is reported in **Table 1** for ease of comparison.

3. Conclusions

In this work, we reported the observation of multiple spectral emission lines at 620 nm (S1), 631 nm (S2), and 647 nm (S3) from individual defects formed upon Sn ion implantation in diamond and subsequent annealing, all of which were consistently observed in multiple previous reports.[6–8,12,14] The data presented here show for the first time the concurrent observation of all these three spectral contributions from the very same, single-photon emitting defect, suggesting among the possible explanations their attribution to the same defect complex, that is, the SnV center.

We also investigated the occurrence of the S1–S3 lines as a function of the sample processing. The as-annealed substrate exhibited a prevalence of the S3 spectral feature among the spectral emission of ≈40 individual centers. Conversely, the S3 population density decreased in favor of the S1 emission line upon O-termination of the sample surface. This observation, in combination with the observation of both lines from the very same defect and of different emission lifetimes and intensity excitation saturation parameters, might suggestive of the attribution of the 647 nm PL peak to a different charge state of the defect, possibly neutral charge state of the SnV complex (SnV^0), which has not been observed so far in other promising group-IV-related centers such as the GeV and the PbV.[4] This interpretation seems however to be ruled out by the findings recently reported in ref. [14], where the dynamical tuning of the diamond Fermi level by means of a p-i-p junction enabled to modulate the occurrence of the S1 emission line, but not that of the S3 spectral feature.

Conversely, the observation of a decreasing deshelving lifetime parameter τ_2 as a function of the laser excitation power suggests that the S3 emission might be related to a four-level system, a hypothesis that would not be in contrast with an energy transfer process involving the SnV center and surrounding radiation-induced defects generated upon ion implantation. This attribution will require a confirmation on centers fabricated upon

© 2021 The Authors. Advanced Photonics Research published by Wiley-VCH GmbH

26999293, 2022, 1, Downloaded from https://onlinelibrary.wiley.com/doi/10.1002/adpr.202100148 by Universita Di Torino, Wiley Online Library on [13/05/2024]. See the Terms and Conditions (https://onlinelibrary.wiley.com/terms-and-conditions) on Wiley Online Library for rules of use; OA articles are governed by the applicable Creative Commons License

chemical vapor deposition synthesis or ion implantation followed by HPHT annealing, to rule out the role of local strains in the emergence of the 647 nm line. Conversely, its investigation as a function of the laser excitation wavelength will provide additional insight on charge state conversion mechanisms involved in the aforementioned emission. If confirmed, in analogy with what reported for the SiV^0 center,[39] a neutrally charged SnV complex might display strong insensitivity to environmental noise and therefore offer further increased spin coherence times and higher brightness, thus proving to be a natural candidate for the implementation of long-lived quantum memories.

4. Experimental Section

The measurements were performed on a high-purity single-crystal IIa diamond substrate with <100> orientation, denoted as "electronic grade" due to the <5 ppb concentration of both substitutional B and N impurities. A $200 \times 200\ \mu m^2$ region was implanted using a collimated 60 keV Sn^- ions at $2 \times 10^{10}\ cm^{-2}$ fluence. The implantation was performed through a collimating steel mask placed at a ≈5 mm distance from the sample surface. This configuration allowed the implantation of stray ions at a lower fluence at the outer edge of the implanted region. This outer region was selected to observe and investigate Sn-related emitters at the individual level. The ions penetration range—estimated as 23 nm according to SRIM (stopping range of ions in matter) simulations[17]—was sufficiently close to the sample surface to consider the chemical terminations to be effective at tuning possible charge states of the lattice defects.[18]

The sample was subsequently annealed for 2 h in vacuum at 1200 °C to promote the formation of optically active defects. After the annealing process, residual surface conductivity was removed by an oxygen plasma treatment.

The PL characterization of individual defects was then performed under two different functionalization conditions of the sample surface: "as annealed," that is, without any functionalization following a subsequent thermal annealing process (2 h, 950 °C), and after a plasma treatment in O_2 (experimental parameters: 60 Pa pressure, 0.5 sccm O_2 flux, 30 min duration, 23 W microwave power).

As mentioned earlier, the sample surface has a (100) orientation. It is broadly recognized that its chemical termination has a major effect on the local surface charge density of diamond, which in turn results in substantial variations on the charge state of color centers, as extensively investigated for the nitrogen-vacancy complex.[19] As widely ascertained in previous works, the as-CVD-grown (i.e., as-implanted) surface of the diamond sample is characterized by a hydrogen termination and is characterized by a negative electron affinity of 1.7 eV.[20] Thermal annealing in vacuum at temperatures exceeding 1000 °C results in the desorption of hydrogen from the sample surface[21] and in the rearrangement of carbon atoms at the surface involving the formation sp^2 bonds.[22] After this annealing process, once the sample surface is exposed to the environmental atmosphere, water contamination typically results in electron affinity values which are still negative.[23] Conversely, the exposure to oxygen plasma results in the oxygen termination of the surface, which is then characterized by a positive electron affinity of 2.4 eV.[24–26]

The PL emission of individual SnV centers was characterized by means of a fiber-coupled single-photon sensitive room-temperature confocal microscope already presented in previous works.[27] The confocal microscope was operated using a 520 nm CW laser excitation. A 600 nm long-pass filter enabled the minimization of the background associated with the Raman scattering (567 nm); at the same time, it prevented the investigation of the 593 nm emission line reported in previous works.[6,7,13,14] The spectral features of the emitters were analyzed using a single-grating monochromator (1200 grooves mm^{-1}, 600 nm blaze, and ≈4 nm spectral resolution) fiber-coupled to a single-photon avalanche detector.[28]

Acknowledgements

This work was supported by the following projects: Coordinated Research Project "F11020" of the International Atomic Energy Agency (IAEA); "Piemonte Quantum Enabling Technologies" (PiQuET) project funded by the Piemonte Region within the "Infra-P" scheme (POR-FESR 2014-2020 program of the European Union); "Departments of Excellence" (L. 232/2016), funded by the Italian Ministry of Education, University and Research (MIUR); "Ex post funding of research" project of the University of Torino funded by the "Compagnia di San Paolo"; "Intelligent fabrication of QUANTum devices in DIAmond by Laser and Ion Irradiation" (QuantDia) project funded by the Italian Ministry for Instruction, University and Research within the "FISR 2019" program; "Training on LASer fabrication and ION implantation of DEFects as quantum emitters" (LasIonDef) project funded by the European Research Council under the "Marie Skłodowska-Curie Innovative Training Networks" program; CSN5 "PICS4ME" experiment funded by the Italian National Institute of Nuclear Physics (INFN). The following projects leading to this publication have received funding from the EMPIR programme co-financed by the Participating States and from the European Union's Horizon 2020 research and innovation programmes "Single-photon sources as new quantum standards" project: 17FUN06 SIQUST; "Beyond classical optical metrology" project: 17FUN01 (BeCOMe); "Single- and entangled-photon sources for quantum metrology" project 20FUN05 (SEQUME); "Quantum sensors for metrology based on single-atom-like device technology" project 20IND05 (QADeT). TL, SP and JM acknowledge the funding from the European Union's Horizon 2020 research and innovation programme under grant agreement No 820394 (ASTERIQS).

Conflict of Interest

The authors declare no conflict of interest.

Data Availability Statement

The data that support the findings of this study are available from the corresponding author upon reasonable request.

Keywords

annealing, charge, diamond, ion implantation, quantum, single-photon source, tin

Received: May 27, 2021
Revised: September 14, 2021
Published online: November 5, 2021

[1] S. Prawer, *Quantum Information Processing with Diamond: Principles and Applications*, Woodhead Publishing, Cambridge **2014**.
[2] I. Aharonovich, D. Englund, M. Toth, *Nat. Photonics* **2016**, *10*, 631.
[3] T. Schröder, S. L. Mouradian, J. Zheng, M. E. Trusheim, M. Walsh, E. H. Chen, L. Li, I. Bayn, D. Englund, *J. Opt. Soc. Am. B* **2016**, *33*, B65.
[4] C. Bradac, W. Gao, J. Forneris, E. Trusheim, I. Aharonovich, *Nat. Commun.* **2019**, *10*, 5625.
[5] G. Petrini, E. Moreva, E. BErnardi, P. Traina, G. Tomagra, V. Carabelli, I. P. Degiovanni, M. Genovese, *Adv. Quantum Tech.* **2020**, *2*, 2000066.
[6] T. Iwasaki, Y. Miyamoto, T. Taniguchi, P. Siyushev, M. H. Metsch, F. Jelezko, M. Hatano, *Phys. Rev. Lett.* **2017**, *119*, 253601.
[7] S. Ditalia Tchernij, T. Herzig, J. Forneris, J. Küpper, S. Pezzagna, P. Traina, E. Moreva, I. P. Degiovanni, G. Brida, N. Skukan,

© 2021 The Authors. Advanced Photonics Research published by Wiley-VCH GmbH

26999293, 2022, 1, Downloaded from https://onlinelibrary.wiley.com/doi/10.1002/adpr.202100148 by Universita Di Torino, Wiley Online Library on [13/05/2024]. See the Terms and Conditions (https://onlinelibrary.wiley.com/terms-and-conditions) on Wiley Online Library for rules of use; OA articles are governed by the applicable Creative Commons License

M. Genovese, M. Jaksic, J. Meijer, P. Olivero, *ACS Photonics* **2017**, *4*, 2580.
[8] M. Alkahtani, I. Cojocaru, X. Liu, T. Herzig, J. Meijer, J. Küpper, T. Lühmann, A. V. Akimov, P. Hemmer, *Appl. Phys. Lett.* **2018**, *112*, 241902.
[9] A. E. Rugar, C. Dory, S. Sun, J. Vučković, *Phys. Rev. B* **2019**, *99*, 205417.
[10] M. E. Trusheim, B. Pingault, N. H. Wan, M. Gündogan, L. De Santis, R. Debroux, D. Gangloff, C. Purser, K. C. Chen, M. Walsh, J. J. Rose, J. N. Becker, B. Lienhard, E. Bersin, I. Paradeisanos, G. Wang, D. Lyzwa, A. R.-P. Montblanch, G. Malladi, H. Bakhru, A. C. Ferrari, I. A. Walmsley, M. Atatüre, D. Englund, *Phys. Rev. Lett.* **2020**, *124*, 023602.
[11] G. Thiering, A. Gali, *Phys. Rev. X* **2018**, *8*, 021063.
[12] E. A. Ekimov, S. G. Lyapin, M. V. Kondrin, *Diam. Relat. Mater.* **2018**, *87*, 223.
[13] T. Lühmann, R. John, R. Wunderlich, J. Meijer, S. Pezzagna, *Nat. Commun.* **2019**, *10*, 4956.
[14] T. Lühmann, J. Küpper, S. Dietel, R. Staacke, J. Meijer, S. Pezzagna, *ACS Photonics* **2020**, *7*, 3376.
[15] A. E. Rugar, H. Lu, C. Dory, S. Sun, P. J. McQuade, Z.-X. Shen, N. A. Melosh, J. Vuckovic, *Nano Lett.* **2020**, *20*, 1614.
[16] G. Thiering, A. Gali, *A., NPJ Computational Materials* **2019**, *5*, 18.
[17] J. F. Ziegler, M. D. Ziegler, J. P. Biersack, *Nucl. Instr. Meth. B* **2010**, *268*, 1818.
[18] H. Yamano, S. Kawai, K. Kato, T. Kageura, M. Inaba, T. Okada, I. Higashimata, M. Haruyama, T. Tanii, K. Yamada, S. Onoda, W. Kada, O. Hanaizumi, T. Teraji, J. Isoya, H. Kawarada, *Jap. J. Appl. Phys.* **2017**, *56*, 04CK08.
[19] H. Pinto, R. Jones, D. W. Palmer, J. P. Goss, A. K. Tiwari, P. R. Briddon, N. G. Wright, A. B. Horsfall, M. J. Rayson, S. Öberg, *Phys. Rev. B* **2012**, *86*, 045313.
[20] S. J. Sque, R. Jones, P. R. Briddon, *Phys. Rev. B* **2006**, *73*, 085313.
[21] C. Su, J.-C. Lin, *Surf. Sci.* **1998**, *406*, 149.
[22] V. L. Kuznetsov, I. L. Zilberberg, Y. V. Butenko, A. L. Chuvilin, *J. Appl. Phys.* **1999**, *86*, 863.
[23] X. Gao, L. Liu, D. Qi, S. Chen, A. T. S. Wee, T. Ouyang, K. P. Loh, X. Yu, H. O. Moser, *J. Phys. Chem. C* **2008**, *112*, 2487.
[24] M. M. Hassan, K. Larsson, *J. Phys. Chem. C* **2014**, *118*, 22995.
[25] J.-P. Chou, A. Gali, *MRS Commun.* **2017**, *7*, 551.
[26] V. Petráková, A. Taylor, I. Kratochvilova, F. Fendrych, J. Vacik, J. Kucka, J. Stursa, P. Cicler, M. Ledvina, A. Fiserova, P. Kneppo, M. Nesladek, *Adv. Funct. Mater.* **2012**, *22* 812.
[27] G. Prestopino, M. Marinelli, E. Milani, C. Verona, G. Verona-Rinati, P. Traina, E. Moreva, I. P. Degiovanni, M. Genovese, S. Ditalia Tchernij, F. Picollo, P. Olivero. J. Forneris, *Appl. Phys. Lett.* **2017**, *111*, 111105.
[28] S. Ditalia Tchernij, E. Corte, T. Lühmann, P. Traina, S. Pezzagna, I. P. Degiovanni, G. Provatas, E. Moreva, J. Meijer, P. Olivero, M. Genovese, J. Forneris, *New J. Phys.* **2021**, *23*, 063032.
[29] J. M. Binder, A. Stark, N. Tomek, J. Scheuer, F. Frank, K. D. Jahnke, C. Müller, S. Schmitt, M. H. Metsch, T. Unden, T. Gehring, A. Huch, U. L. Andersen, L. J. Rogers, F. Jelezko, *Software X* **2017**, *6*, 85.
[30] A. Beveratos, R. Brouri, T. Gacoin, J.-P. Poizat, P. Grangier, *Phys. Rev. A* **2001**, *64*, 061802.
[31] M. V. Hauf., B. Grotz, B. Naydenov, M. Dankerl, S. Pezzagna, J. Meijer, F. Jelezko, J. Wrachtrup, M. Stutzmann, F. Reinhard, J. A. Garrido, *Phys. Rev. B* **2011**, *83*, 081394.
[32] D. Gatto Monticone, P. Traina, E. Moreva, J. Forneris, P. Olivero, I. P. Degiovanni, F. Taccetti, L. Giuntini, G. Brida, G. Amato, M. Genovese, *New J. Phys* **2014**, *16*, 053005.
[33] Z. Mu, Y. Zhou, D. Chen, J. E. Fröch, J. Tang, X. Li, I. Aharonovich, W.-B. Gao, *Adv. Opt. Mater.* **2020**, *8*, 2000495.
[34] S. C. Kitson, P. Jonsson, J. G. Rarity, P. R. Tapster, *Phys. Rev. A* **1998**, *58*, 620.
[35] T. Iwasaki, F. Ishibashi, Y. Miyamoto, Y. Doi, S. Kobayashi, T. Miyazaki, K. Tahara, K. D. Jahnke, L. J. Rogers, B. Naydenov, F. Jelezko, S. Yamasaki, S. Nagamachi, T. Inubushi, N. Mizuochi, M. Hatano, *Sci. Rep.* **2015**, *5*, 12882.
[36] J. Görlitz, D. Herrman, G. Thiering, P. Fuchs, M. Gandil, T. Iwasaki, T. Taniguchi, M. Kieschnick, J. Meijer, M. Hatano, *New J. Phys.* **2020**, *22*, 13048.
[37] E. Neu, M. Agio, C. Becher, *Opt. Express* **2012**, *20*, 19956.
[38] M. Nahra, D. Alshamaa, R. Deturche, V. Davydov, L. Kulikova, V. Agafonov, C. Couteau, *AVS Quant. Sci.* **2021**, *3*, 012001.
[39] B. C. Rose, D. Huang, Z.-H. Zhang, P. Stevenson, A. M. Tryshkin, S. Sangtawesin, S. Srinivasan, L. Loudin, M. Markham, A. M. Edmonds, D. J. Twitchen, S. A. Lyon, N. P. de Leon, *Science* **2018**, *63*, 60.
[40] A. Meda, I. P. Degiovanni, A. Tosi, Z. Yuan, G. Brida, M. Genovese, *Light* **2017**, *6*, 1626.

© 2021 The Authors. Advanced Photonics Research published by Wiley-VCH GmbH

26999293, 2022, 1, Downloaded from https://onlinelibrary.wiley.com/doi/10.1002/adpr.202100148 by Universita Di Torino, Wiley Online Library on [13/05/2024]. See the Terms and Conditions (https://onlinelibrary.wiley.com/terms-and-conditions) on Wiley Online Library for rules of use; OA articles are governed by the applicable Creative Commons License

ACS Photonics

Open Access

This article is licensed under CC-BY-NC-ND 4.0

pubs.acs.org/journal/apchd5

Article

Magnesium-Vacancy Optical Centers in Diamond

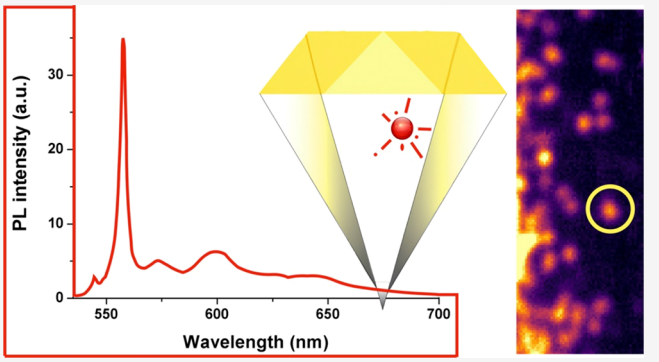
Emilio Corte,[▽] Greta Andrini,[▽] Elena Nieto Hernández, Vanna Pugliese, Ângelo Costa, Goele Magchiels, Janni Moens, Shandirai Malven Tunhuma, Renan Villarreal, Lino M. C. Pereira, André Vantomme, João Guilherme Correia, Ettore Bernardi, Paolo Traina, Ivo Pietro Degiovanni, Ekaterina Moreva, Marco Genovese, Sviatoslav Ditalia Tchernij, Paolo Olivero, Ulrich Wahl,* and Jacopo Forneris*

Cite This: *ACS Photonics* 2023, 10, 101−110

Read Online

ACCESS | Metrics & More | Article Recommendations | Supporting Information

ABSTRACT: We provide the first systematic characterization of the structural and photoluminescence properties of optically active centers fabricated upon implantation of 30−100 keV Mg^+ ions in synthetic diamond. The structural configurations of Mg-related defects were studied by the electron emission channeling technique for short-lived, radioactive ^{27}Mg implantations at the CERN-ISOLDE facility, performed both at room temperature and 800 °C, which allowed the identification of a major fraction of Mg atoms (∼30 to 42%) in sites which are compatible with the split-vacancy structure of the MgV complex. A smaller fraction of Mg atoms (∼13 to 17%) was found on substitutional sites. The photoluminescence emission was investigated both at the ensemble and individual defect level in the 5−300 K temperature range, offering a detailed picture of the MgV-related emission properties and revealing the occurrence of previously unreported spectral features. The optical excitability of the MgV center was also studied as a function of the optical excitation wavelength to identify the optimal conditions for photostable and intense emission. The results are discussed in the context of the preliminary experimental data and the theoretical models available in the literature, with appealing perspectives for the utilization of the tunable properties of the MgV center for quantum information processing applications.



KEYWORDS: *diamond, ion implantation, magnesium, color centers, emission channeling, lattice location*

Downloaded via UNIV DEGLI STUDI DI TORINO on May 13, 2024 at 09:14:43 (UTC).
See https://pubs.acs.org/sharingguidelines for options on how to legitimately share published articles.

1. INTRODUCTION

Diamond is a promising material platform for photonic quantum technologies, which offers single-photon sources for quantum information processing and sensing schemes based on the optical activity of lattice defects. These systems, commonly known as "color centers", can be engineered upon the controlled introduction of impurities in the diamond crystal structure by ion implantation.[1−3] Besides the well-known and widely investigated negatively charged nitrogen-vacancy center (NV^-), offering unique photophysical properties (photo-stability at room temperature, high quantum efficiency, and optically addressable spin properties) for quantum sensing and computing applications,[4−9] additional single-photon-emitting color centers with appealing features have emerged in the last decade, including group-IV impurities,[10−18] noble gases,[19−21] and other impurity-related defects.[22−24]

Particularly, recent work has shown a preliminary demonstration of the optical activity of Mg-related color centers in diamond. The available experimental data suggested the formation of an optically active defect (magnesium-vacancy center, MgV in the following) upon Mg ion implantation and annealing, denoted by a sharp emission line at 557.4 nm, low phonon coupling denoted by a high Debye−Waller factor, high (>0.5 Mcps) emission intensity, and 2−3 ns radiative lifetime.[25] Furthermore, these results fed the deployment of a detailed numerical ab initio study of the color center's structure,[26] offering an intriguing insight in its opto-physical properties, including the prediction of a large and tunable and spin-dependent ground-state splitting, thus offering an appealing tool for quantum information processing purposes.

In this work, we report on a systematic investigation of the MgV color center in diamond. The analysis covers both its structural properties and efficiency of structural formation, as evidenced from the determination of the lattice sites of implanted Mg by the emission channeling technique, and the optical emission properties, studied in the photoluminescence

Received: July 20, 2022
Published: December 13, 2022



© 2022 The Authors. Published by American Chemical Society

(PL) regime at the ensemble and single-photon emitter level, as a function of temperature and excitation wavelength. The present results extend the preliminary findings available in the scientific literature and offer contextual evidence to support the theoretical model predicted in ref 26.

2. RESULTS

2.1. Structural Properties of Mg-Related Defects in Diamond. For lattice location determination of Mg in diamond, the electron emission channeling (EC) technique from radioactive isotopes was adopted[27−30] (Figure S1 of the Supporting Information). The EC method allows probing the sites of radioactive isotopes in single-crystalline samples and was recently applied to identify the split-vacancy configuration of implanted ^{121}Sn inside the SnV complex in diamond.[31] The split vacancy configuration can be pictured as the impurity atom in the center of a divacancy, occupying a position which corresponds to the bond center (BC) site in an unperturbed lattice. The radioactive probe atoms are implanted at low fluences, and the emitted β^- particles are guided by the crystal potential on their way out of the crystal. A two-dimensional position-sensitive detector (PSD)[28,29] is used to measure the angle-dependent emission yield of electrons in the vicinity of major crystallographic directions, providing patterns which are characteristic for the probe atom lattice location in the sample. In the case of Mg, we used the short-lived ^{27}Mg ($t_{1/2}$ = 9.45 min), which was produced at CERN's ISOLDE on-line isotope separator facility by means of bombarding Ti targets with 1.4 GeV protons, followed by out-diffusion, resonant laser ionization and mass separation. More experimental details regarding EC experiments with ^{27}Mg can be found in refs[32,33] and in the Supporting Information. The major lattice sites can be identified by fitting the experimentally observed emission yields by linear combinations of theoretical patterns[28,29,34] calculated for specific positions of the emitter atoms in the lattice. For that purpose, the many-beam approach[27,28] was used to calculate the expected emission yields for substitutional (S) as well as around 250 interstitial sites in the diamond structure, which are obtained by displacing from the S position along ⟨111⟩, ⟨100⟩, or ⟨110⟩ directions in steps of around 0.04 Å (Figure S3 of the Supporting Information).

The sample used for the EC studies was a ⟨100⟩ oriented single crystal from ElementSix, termed "SC plate CVD", of size 3.0 × 3.0 × 0.25 mm^3, with a nitrogen concentration [N] < 1 ppm. Implantations were performed with 30 keV into a 1-mm diameter beam spot, simultaneously with the measurement of β^- EC effects by a 30 × 30 mm^2 PSD placed at a distance of 301 mm from the sample, resulting in an angular resolution of ∼0.1° (standard deviation). The fluences used to measure single EC patterns were around 2.1−5.5 × 10^{11} cm^{-2}, while the total accumulated fluence at the end of the experiment was 1.1 × 10^{13} cm^{-2}.

The half-life of ^{27}Mg is too short to perform annealing at high temperatures; with regard to thermal treatment of the sample, the only feasible option is varying the implantation temperature. The experimental emission patterns around ⟨110⟩, ⟨211⟩, ⟨100⟩, and ⟨111⟩ directions during room-temperature (RT) implantation are shown in Figure 1a−d, and those for 800 °C implantation (<10^{-5} hPa pressure) in Figure 2a−d. As a first qualitative observation, we notice that the anisotropies of the EC effects measured from ^{27}Mg are relatively weak in comparison to effects from other elements implanted under similar conditions into diamond, e.g., those of

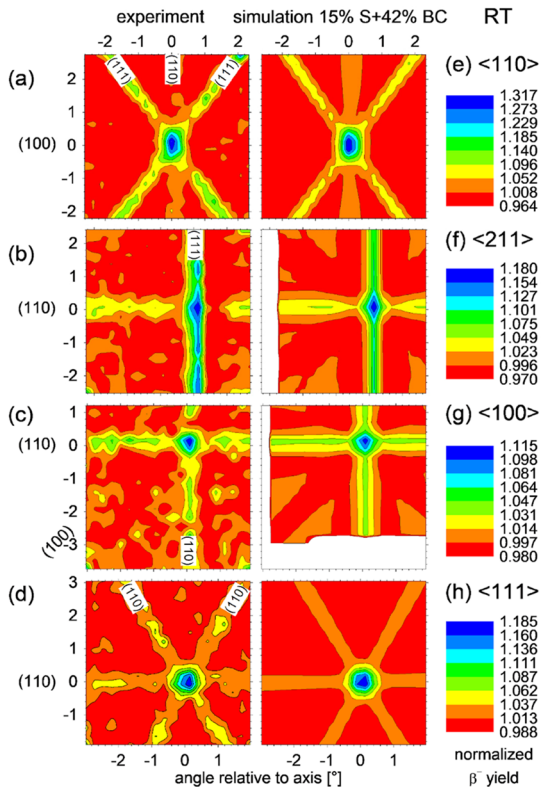


Figure 1. (a−d) Experimental β^- EC patterns from ^{27}Mg in diamond around the ⟨110⟩, ⟨211⟩, ⟨100⟩, and ⟨111⟩ directions during RT implantation. The panels show the number of detected electrons (normalized intensity indicated by the color scales) as a function of the angle relative to the respective crystal axis. These patterns are a signature for the exact location of the probe atom in the diamond lattice. The plots (e−h) are simulated theoretical patterns considering 15% on ideal substitutional and 42% on ideal BC sites. Note that during the RT ⟨211⟩ and ⟨100⟩ measurements, the sample was not yet oriented in such a way that the calculated patterns [±3.0°] cover the whole range of measured angles. The areas in the simulated patterns (f,g) which are not covered, are shown in white.

^{121}Sn.[31] This indicates that a considerable fraction of emitter atoms occupies lattice sites of relatively low crystal symmetry. In a first approach for the analysis, the experimental patterns were fitted by allowing two fractions ("2-site fits") of emitter atoms, one on ideal substitutional S and another on ideal BC sites, plus a flat contribution, which always needs to be considered in the analysis of EC patterns (the theoretical emission patterns for S and BC sites are shown in Figure S4 of the Supporting Information). The resulting best fit patterns for ⟨110⟩, ⟨211⟩, and ⟨100⟩ are shown in Figures 1e−g and 2e−g. As was outlined previously,[31] in the case of the ⟨111⟩ direction, the patterns from S and BC sites have qualitatively similar features, which results in the corresponding site fractions of the best fits being unstable. The theoretical patterns included for the ⟨111⟩ direction in Figures 1h and 2h are hence not those for the best fit results of that direction but for relative contributions from S and BC sites that were fixed to the ratios derived from the analysis of the other three directions (cf. Supporting Information). In all cases, the simulated patterns satisfactorily match the experimental results; the ⟨111⟩ measurements are also compatible with the results from the other directions. Compared to 1-site fits using either S or BC positions, the 2-site fits with S and BC significantly improved

https://doi.org/10.1021/acsphotonics.2c01130
ACS Photonics 2023, 10, 101−110

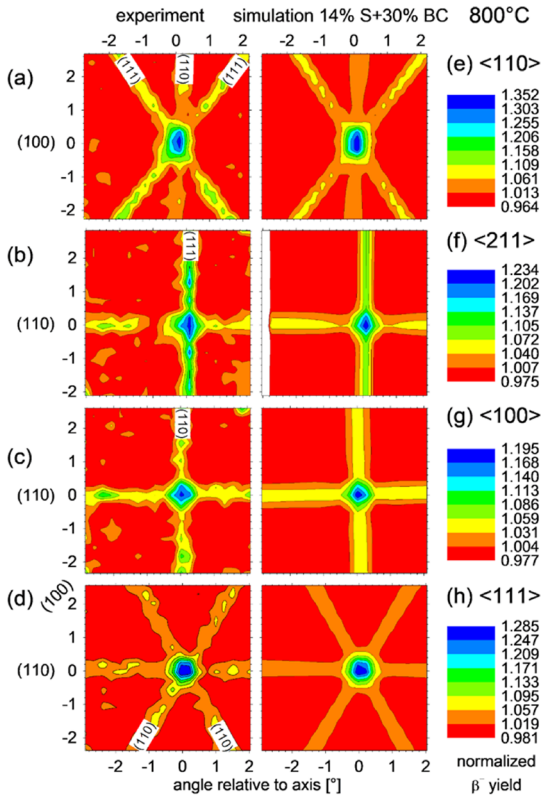


Figure 2. (a–d) Experimental β^- EC patterns from ^{27}Mg in diamond around the ⟨110⟩, ⟨211⟩, ⟨100⟩, and ⟨111⟩ directions during 800 °C implantation. The plots (e–h) are simulated theoretical patterns considering 14% on ideal substitutional and 30% on ideal BC sites.

the chi square of the fit by 19–42% and by 17–53%, respectively, while for the ⟨111⟩ directions, the improvement was much smaller, 1–3% only.

For both implantation temperatures, the largest fitted fractions were on BC sites (42% at RT; 30% at 800 °C), while smaller fractions were assigned to the substitutional positions (15% at RT; 14% at 800 °C). The result implies that 30–40% of implanted Mg atoms are found on sites which are compatible with the theoretically predicted Mg position within the MgV defect in the split-vacancy configuration of D_{3d} symmetry.[26] From a comparison of fluorescence intensity and implanted fluence, the formation efficiency of optically active MgV centers had been estimated to be 2–3% in undoped diamond implanted at RT and annealed to 800 °C.[35] Our results show that the structural efficiency of formation of the split-vacancy configuration in undoped diamond is certainly much higher than a few percent only, suggesting that a large part of the MgV centers are optically inactive. The fact that significantly higher optical activation was observed in P-doped diamond, reaching values as high as 48% following 1200 °C annealing,[35] indicates that co-doping with the *n*-type dopant *P* may transform an inactive form of MgV into optically active MgV centers.

Within the scope of the 2-site fit analysis of the EC experimental data, relatively large fractions of emitter atoms (43% at RT; 56% at 800 °C) were assigned to flat contributions to the emission patterns, the so-called "random sites". The assignment of random sites cannot be the consequence of significant radiation damage or amorphization of the sample, since for the light mass of ^{27}Mg at the applied fluences, the effect of damage should be negligible in diamond, especially for an implantation temperature of 800 °C. The most likely interpretation is that the random fraction represents additional ^{27}Mg sites of relatively low crystal symmetry, which only produce weak anisotropies in the angular-dependent electron emission yields. Two defect configurations, which could be responsible for such Mg lattice sites, are Mg inside a triple vacancy or inside a quadruple vacancy, which corresponds to the so-called MgV_2 or MgV_3 complexes (possible structures for these complexes are shown in Figure S3 of the Supporting Information). MgV_2 was theoretically considered,[26] and it was found to have a somewhat higher energy of formation than MgV, which was predicted to be the thermodynamically most stable Mg defect, followed by substitutional Mg. We note, however, that in the case of ion implantation, the energy for vacancy creation in the sample is provided by the implantation process; hence, the fact that MgV exhibits the lowest defect formation energy may not be the single determining factor which regulates the abundance of complexes formed, and thus, also Mg centers requiring triple or quadruple vacancies might be commonly found. The MgV_2 center was predicted to have a similar configuration to MgV, with an additional vacancy "attached from the side" and a symmetry lowering to C_1 (although no detailed Mg coordinates were published).[26] From simple geometrical arguments, one might expect the structure of MgV_2 as a central vacancy with two additional nearest-neighbor single vacancies within a (110) plane and hence with the Mg atom displaced along a ⟨100⟩ direction from an *S* site (Figure S3). In the case of MgV_3, there exist no predictions for its structure or formation energy in the literature. From simple geometric arguments, for Mg inside a quadruple vacancy consisting of one missing C atom with three additional nearest-neighbor single vacancies, one would tentatively expect trigonal symmetry with the Mg atom located close to the so-called antibonding position (Figure S3).

Having these intuitive structures of MgV_2 and MgV_3 in mind, and considering the possible existence of isolated interstitial Mg, we performed 3-site fits where, besides Mg on *S* and BC sites, the position of a third fraction of Mg probes was varied. We did not find any indication for the existence of (isolated) tetrahedral interstitial Mg (T_d symmetry), which supports the theoretical prediction that this configuration has a high formation energy, making it particularly unstable in vacancy-rich ion-implanted diamond. However, while the chi square of the ⟨110⟩ and ⟨211⟩ pattern fits improved if Mg sites displaced along ⟨100⟩ from *S* sites were considered, this result could not be confirmed by the ⟨100⟩ patterns. The identification of a third fraction of Mg probes in highly symmetric lattice sites, in particular displaced from *S* along ⟨100⟩ directions, was hence not conclusive. In the future, attempt will be made to resolve further Mg lattice sites by means of EC experiments using an enhanced angular resolution of 0.05°.

2.2. Optical Properties of MgV Centers. *2.2.1. Spectral Features of Ensemble Photoluminescence.* The detailed optical characterization of MgV centers was performed on a set of 2 × 2 × 0.5 mm^3 IIa single-crystal diamond plates produced by ElementSix by a chemical vapor deposition method. The crystals were denoted as "electronic grade" by the supplier, according to the nominal substitutional N and B concentrations below 5 ppb. The sample was implanted with 100 keV $^{24}Mg^+$ ions at the IMBL laboratory (KU Leuven). Several

https://doi.org/10.1021/acsphotonics.2c01130
ACS Photonics 2023, 10, 101–110

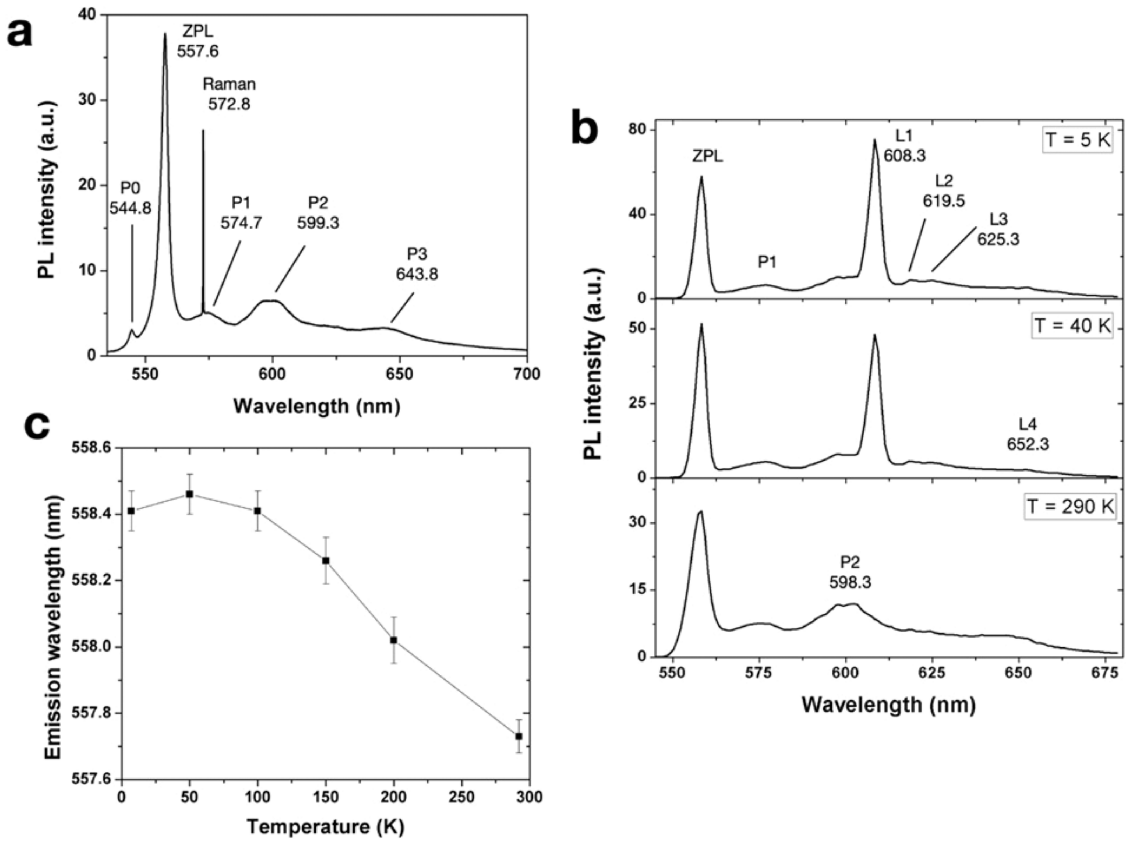


Figure 3. (a) RT spectrum of the MgV ensemble (5×10^{12} cm^{-2} implantation fluence) upon 532 nm laser excitation. (b) Ensemble spectra acquired under 522 nm excitation (3.7 mW) at a temperature of 5, 40, and 290 K. (c) Nominal position of the MgV ZPL dependence on temperature.

squared regions of ~200 × 200 μm^2 size were irradiated at different fluences in the 5×10^9–5×10^{12} cm^{-2} range through the utilization of a custom Al implantation mask (~15 μm thickness). The sample was then processed with high-temperature annealing (1200 °C, 2 h at ~10^{-6} hP pressure) and a subsequent oxygen plasma treatment, with the purpose of minimizing the background fluorescence originating from surface contaminants. The RT PL emission spectrum of the highest-fluence Mg-implanted diamond (5×10^{12} cm^{-2}) was acquired using a confocal micro-Raman setup under 532 nm excitation wavelength (21.6 mW optical power, <0.1 nm resolution, Figure 3a). The ensemble emission highlighted the following spectral features:

- A sharp line at 572.8 nm corresponding to the first-order Raman scattering of diamond (1332 cm^{-1} shift).
- An intense emission peak at 557.6 nm (2.224 eV; 3 nm FWHM), whose prominence with respect to all the remaining spectral features is in agreement with the early reports on its attribution to the zero-phonon line (ZPL) of the MgV defect[25,35] and its theoretical prediction as the main emission of the color center in its negative charge state.[26]
- A set of significantly less intense PL peaks centered at 574.7 nm (2.158 eV, denoted as "P1" in the following), 599.3 nm (2.069 eV, P2), and 643.8 nm (1.926 eV, P3). The wavelength of these three bands is compatible with the phonon sideband spectrum of the MgV center predicted in ref 26.
- An additional emission line at 544.8 nm (2.28 eV, "P0" in the following) exhibits a higher emission energy with respect to the MgV ZPL. The origin of such a feature is not clear. Its correlation with Mg-related emission in *n*-type diamond[35] is questioned by its observation in this work in undoped, highly pure substrates. Furthermore, no explicit observation in irradiated or ion-implanted diamond is present in the scientific literature to support its attribution to an intrinsic radiation-induced defect. The peak could thus be interpreted either as a Mg–vacancy complex different from the MgV center, in analogy with the 593.5 nm line in Sn-implanted diamond,[15] or, less likely, to the predicted ground-state splitting of the MgV defect.[26] In the latter case, however, the observed splitting (~52 meV) would greatly exceed the expected value of 22 meV.

A further temperature-dependent study on PL spectra (5–300 K range, 522 nm excitation, Figure 3b) from the same MgV ensemble offered two additional insights in the optical activity of such a lattice complex.

First, the MgV ZPL spectral shift exhibited a wavelength increase at decreasing temperatures. This effect is shown in Figure 3c, which reports the central wavelength of the ZPL (whose uncertainty of ~0.2 nm was estimated from the uncertainty associated with the Gaussian centroid fitting parameter) as a function of temperature. The shift was quantifiable as ~1 nm (558.4 nm) at 5 K with respect to the 557.6 nm emission at RT. This observation, to the best of the authors' knowledge, is unprecedented for a solid-state color

https://doi.org/10.1021/acsphotonics.2c01130
ACS Photonics 2023, 10, 101–110

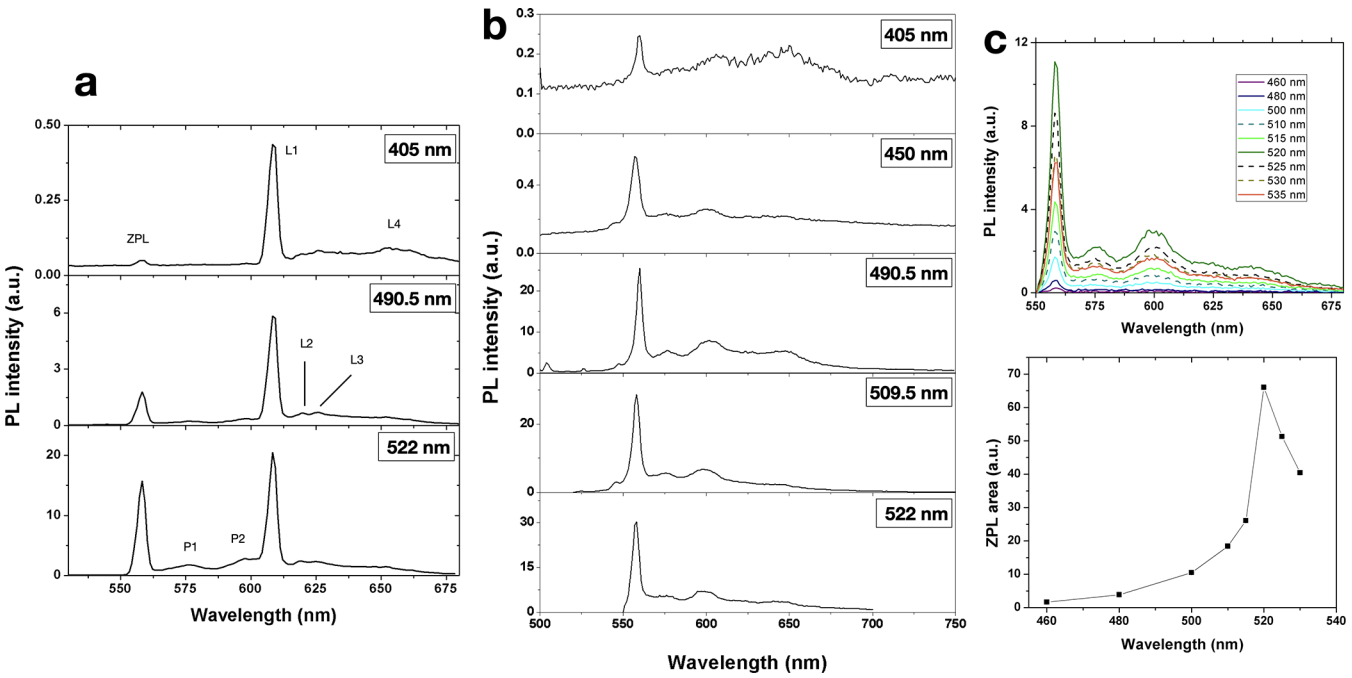


Figure 4. Ensemble spectra acquired: (a) at 5 K temperature under 405 nm (3.6 mW optical power), 490.5 nm (4.0 mW), and 522 nm (3.6 mW) excitation wavelengths; (b) at RT under (b) 405 nm (8 mW), 450 nm (2.2 mW), 490.5 nm (2.3 mW), 509.5 nm (2.2 mW), and 522 nm excitation wavelengths (0.3 mW). The spectra are normalized to the optical excitation power. (c) Background subtracted spectra acquired under 50 μW pulsed laser excitation (80 MHz repetition rate). (d) Excitation wavelength dependence of the 556.7 nm ZPL peak area extracted from the spectra in Figure 4c.

center, where the lattice parameter contraction at decreasing temperatures typically corresponds to a strengthening of the chemical bonds and thus an increase in the photon energy.[36−39]

This observation can be understood on the basis of the ab initio model in ref 26, which predicts that the MgV ZPL is an emission doublet originating from a ground-state splitting and that it exhibits decreasing energy separation at increasing compressive strain, hence at decreasing temperature. This prediction is not in contrast with the rather large ∼3 nm ZPL peak FWHM measured in the high-resolution PL spectra reported in Figure 3a, which could be interpreted as the convolution of the predicted emission doublet. The blue-shift then would be justified by an increased occupation probability of the ^4E_u state. High-resolution spectroscopy at cryogenic temperatures will be needed to further assess this hypothesis.

Second, the low-temperature emission becomes dominated by a new set of spectral features, namely, an intense peak at 608.3 nm (2.038 eV, "L1" in the following), exhibiting an intensity comparable with that of the MgV ZPL, accompanied by a set of weak bands at 619.5 nm (2.001 eV, L2), 625.3 nm (1.983 eV, L3), and 652.3 nm (1.901 eV) which can be tentatively interpreted as L1 phonon replicas.

The L1 line energy is compatible with its attribution to the $^2A_{1u} \rightarrow {}^2E_g$ transition, predicted at ∼2 eV in ref 26. The lack of observation of this line at RT is compatible with the fact that it is a weakly allowed transition. The ∼185 meV energy difference between the $^2A_{1u}$ and the $^2E_u{}^2$ states (i.e., the excited states of the ZPL and L1 transitions, for which the same final state ^2E_g is assumed[26] might be sufficient to favor the population of the latter upon RT phonon-assisted processes, thus quenching the L1 emission line.

2.2.2. Optical Excitability. The ensemble spectral emission of the same Mg-implanted region was investigated under different laser excitation wavelengths (Figure 4a−d), namely, 405, 450, 490.5, 509.5 (2.2 mW), and 522 nm, using a fiber-coupled single-photon-sensitive confocal microscope (details on optical filtering and the position of the Raman scattering lines are given in the Supporting Information).

All the above-mentioned excitation wavelengths highlighted the occurrence of the ZPL and P2−P3 emission lines, thus confirming their attribution to PL features in Mg-implanted diamond rather than Raman-related features of the implanted host material. Differently with respect to the other laser sources, for which a 505 nm long pass filter was used, the excitation spectrum under 522 nm excitation (Figure 4b) was acquired using a 567 nm long-pass dichroic mirror. In this case, the ∼50% transmittance of the filter at 560 nm[40] was sufficient to observe the ZPL of the MgV center but partially suppressed its emission intensity. Moreover, in the case of 522 nm excitation, the first-order Raman scattering occurs at 561 nm wavelength and thus partially overlaps with the ZPL of the MgV center under the given resolution (∼4 nm) of the spectrometry setup. Based on these considerations, a direct comparison in the ZPL intensity acquired under a 522 nm laser and that observed at other excitation wavelengths was not possible. It is however worth mentioning that the overall prominence of the MgV ZPL with respect to the baseline under laser excitation in the 405−510 nm range (for which the same optical setup was employed) decreases at increasing excitation energy, suggesting a progressive conversion between the charge state configurations available within the energy gap of diamond.[26] This hypothesis is further supported by the inability to detect single-photon emission under <510 nm excitation in regions where an abundance of individual centers was identified at longer wavelengths.

A further investigation of the dependence of the Mg-related PL on the excitation energy was performed using a dedicated

https://doi.org/10.1021/acsphotonics.2c01130
ACS Photonics 2023, 10, 101−110

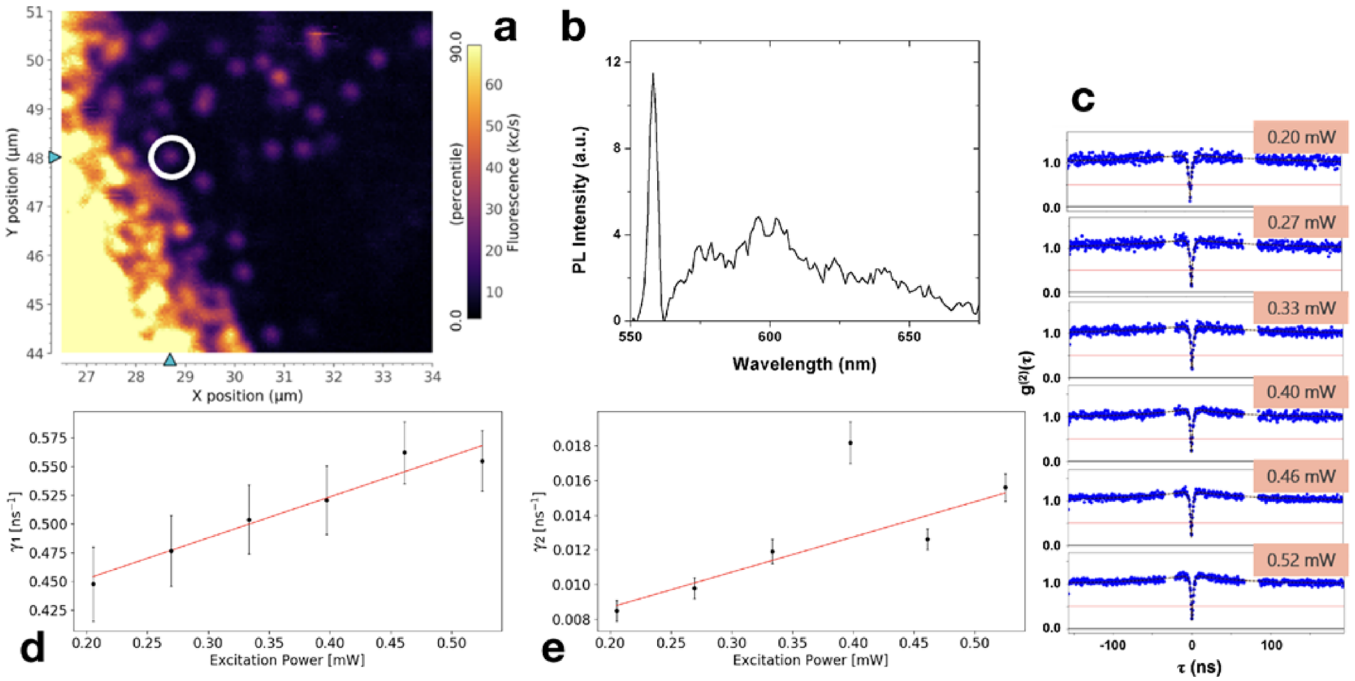


Figure 5. RT single-photon emission from MgV centers: (a) confocal microscopy map acquired under 522 nm laser excitation (1.0 mW) at the outer edge of a region implanted with Mg^+ ions at a 5×10^{12} cm^{-2} fluence. (b) Background-subtracted PL spectrum acquired from the individual emitter circled in white in Figure 5a. (c) Second-order auto-correlation function measurements of the same emitter under different optical excitation powers (0.2−0.52 mW range). The missing data points correspond to the backflash peaks originating from the fiber-coupled HBT interferometer, which were removed for clarity. (d) Dependence of the γ_1 emission parameters on the optical excitation power. (e) Dependence of the γ_2 emission fitting parameter on the optical excitation power.

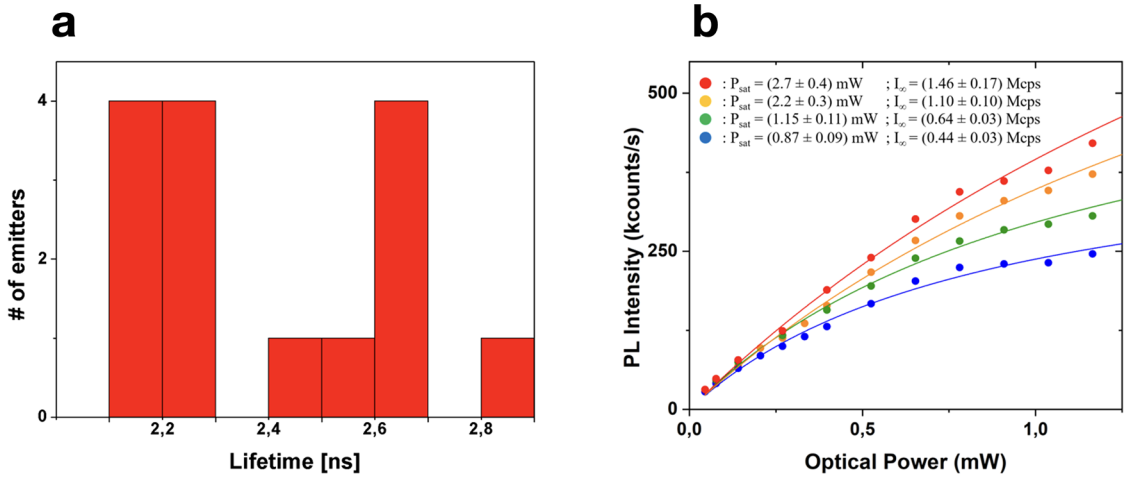


Figure 6. (a) Distribution of the excited-state lifetime of 15 individual MgV centers at RT. (b) Background-subtracted emission rate as a function of the optical excitation power (522 nm wavelength). The colored curves correspond to an exemplary subset of the emitters studied in Figure 5a. The legend indicates the fitting parameters obtained according to eq 2.

supercontinuum laser source filtered to offer an emission bandwidth of 10 nm with central wavelength in the range 460−535 nm (see the Supplementary Information for further details). The different ensemble spectra in Figure 4c were acquired with 50 μW fixed optical power (the data are background-subtracted; the background was measured by acquiring spectra in a pristine region of the sample to remove the contribution originating from Raman scattering). The area subtended by the ZPL peaks, reported in Figure 4d, confirms that the maximum excitability of the MgV emission is at 522 nm, as suggested also by Figure 4a,b. This feature indicates that the chosen wavelength is an effective tool to provide Raman-resonant excitation of the MgV center, thus enabling, in perspective, an efficient resource to maximize its emission intensity and optically address and coherently control individual emitters[41] using readily available and cost-effective laser diodes.

2.2.3. Single-Photon Emission Analysis. PL measurements on individual MgV centers were performed under 522 nm excitation at the outer edge of a region implanted at a 5×10^{12} cm^{-2} fluence. Figure 5a shows a 7×8 μm^2 map of such a region, acquired in confocal microscopy (1 mW excitation power), where the formation of individual luminescent spots of ~ 1 μm^{-2} density is clearly recognizable. A systematic analysis

https://doi.org/10.1021/acsphotonics.2c01130
ACS Photonics 2023, 10, 101−110

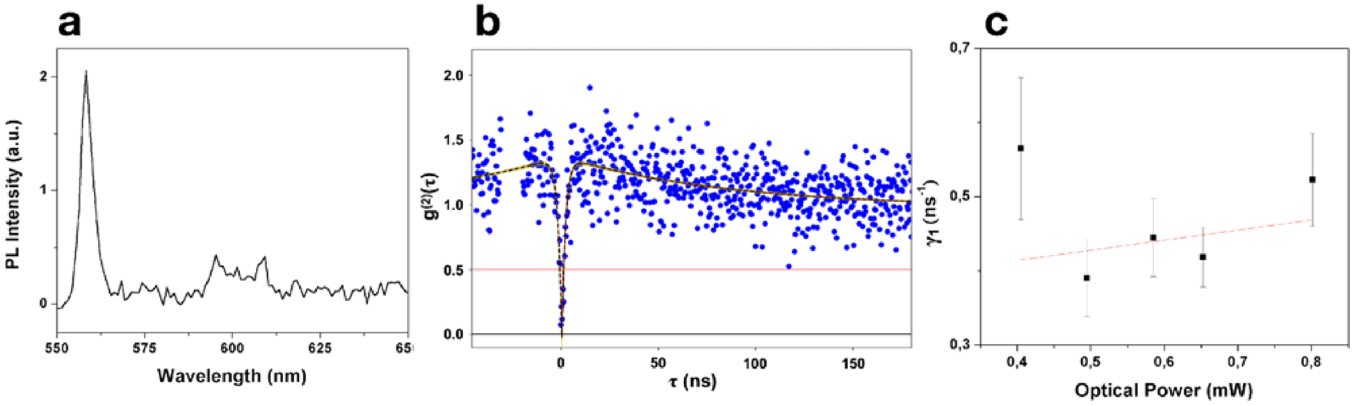


Figure 7. Investigation of single-photon emission from MgV centers at 7 K temperature: (a) background-subtracted PL spectrum acquired from an individual emitter under 522 nm optical excitation (4.6 mW); (b) second-order autocorrelation function acquired from the same emitter under 0.7 mW excitation power; (c) dependence of the γ_1 emission parameters on the optical excitation power. The excited lifetime for the emitter was estimated to be (2.8 ± 1.1) ns according to eq 1.

on such individual luminescent spots via Hanbury-Brown & Twiss (HBT) interferometry enabled us to identify and analyze single-emitting defects, whose RT characterization was performed in terms of their spectral properties, radiative lifetime of the excited state, and intensity saturation emission.

As an example, the individual emitter highlighted in Figure 5a by a white circle exhibits the emission spectrum shown in Figure 5b, which was acquired upon subtraction of the background emission acquired in the same experimental conditions from an unimplanted region of the sample. The measurement of the second-order autocorrelation function $g^{(2)}(\tau)$, presented in Figure 5c, was performed under different optical power excitations (0.20−0.52 mW range) highlighting a strong antibunching at a null delay time. This behavior, which indicates the occurrence of nonclassical emission, resulted in a background-subtracted value of $g^{(2)}(\tau = 0)$ well below 0.5 (0.15 ± 0.10 at 0.27 mW excitation power), which is regarded as the threshold for single-photon emitter discrimination. A bunching effect also became visible at increasing excitation powers, suggesting the presence of a shelving state involved in the emission dynamics of the center. The background-subtracted $g^{(2)}(\tau)$ curves were fitted (black dashed lines in Figure 5c) according to the $g^{(2)}(\tau)$ model corresponding to a three-level system:

$$g^{(2)}(\tau) = 1 - (1 + a)\cdot\exp(-|\tau|\cdot\gamma_1) + a\cdot\exp(-|\tau|\cdot\gamma_2) \quad (1)$$

where γ_1 and γ_2 are the reciprocals of the characteristic times associated with the de-excitation of the excited state and the shelving state, respectively.[42] The radiative lifetime of the center was finally estimated, by a linear fit of the γ_1 parameter against the excitation power P, as $\tau = [\gamma_1(P = 0)]^{-1} = (2.7 \pm 0.3)$ ns (Figure 5d).[43] A statistical analysis based on 15 individual emitters acquired from the same region (Figure 6a) revealed a relatively small dispersion of the data with a weighted average lifetime of (2.4 ± 0.2) ns, in good agreement with the preliminary data reported in ref 25. The fitting function in eq 1 enabled us also to investigate the dependence of the γ_2 parameter on the power of the optical excitation. Figure 5e shows the data acquired for the same emitter considered in Figure 5c,d. Notably, a clear increasing trend was observed, and the behavior was consistent for all the 15 emitters analyzed in this work, confirming that the emitter is adequately described by a three-level model.[43,44] The emission intensity of individual MgV centers was also studied as a function of the optical power of the laser excitation. Figure 6b displays the large variability (up to 50% of the distribution average) of the background-subtracted emission rate in the saturation regime for an exemplary subset of the emitters analyzed in Figure 6a. The data points were fitted according to the saturation model[11,45,46]

$$I(P) = I_{sat}\cdot P/(P + P_{sat}) \quad (2)$$

in which I is the emission rate and P is the laser excitation power. The saturation intensity I_{sat} cannot be regarded as a reliable estimate of the brightness of the MgV center, since a significant part of its ZPL emission is filtered by the 567 nm long-pass dichroic mirror adopted for the confocal microscope implementation. Even without considering the 50% transmittance of the latter at 560 nm, the PL count rate at saturation ranges between (0.44 ± 0.03) and (1.46 ± 0.17) Mcps (blue and red data in Figure 6b, respectively). If the dichroic mirror losses are taken into account, these results suggest RT emission rates above 2 Mcps, previously unreported for a solid-state quantum emitter without coupling to emission-enhancing cavities. Conversely, the saturation power under 522 nm excitation was estimated in the range (0.87 ± 0.09)−(2.7 ± 0.4) mW. In general, a qualitative trend correlating increasing emission intensity and saturation power could be observed.

The single-photon emission was also investigated at cryogenic temperatures. Figure 7 shows the typical results obtained for individual color centers at 7 K under 522 nm excitation. The identification of single MgV emitters was validated by the measurement of the PL spectra (Figure 7a), the evaluation of the $g^{(2)}(0)$ parameter (Figure 7b) (nominally, 0.05 ± 0.01 upon background removal[17]), and the excited-state lifetime evaluation (Figure 7c) (2.8 ± 1.1 ns). We underline that these results are compatible with those observed in the measurements we carried out at RT. Interestingly, the intense L1 emission feature observed from ensemble measurements at cryogenic temperatures could not be identified at the single-photon emitter level. Conversely, dedicated studies at varying excitation wavelengths did not succeed at isolating individual color centers, thus confirming the analysis on the excitation wavelength dependence presented at the ensemble level in Figure 4.

https://doi.org/10.1021/acsphotonics.2c01130
ACS Photonics 2023, 10, 101−110

3. CONCLUSIONS

This work offers a first systematic experimental analysis of the structural and photo-physical properties of MgV centers fabricated upon ion implantation, following the first report on their optical activity[25] and the development of a first theoretical model.[26]

The EC analysis of ^{27}Mg-implanted diamond revealed a high fraction of Mg (30−42%) in sites that are compatible with the split-vacancy configuration proposed as the structure of the relevant optically active center. This indicates the very efficient structural formation of MgV, which appears comparable to that of the SnV defect.[31]

The spectral features of MgV centers at both RT and cryogenic temperatures also confirmed the signature of the ZPL at 557.6 nm attributed to the $^2E_u{}^2 \rightarrow {}^2E_g$ optical transition. The temperature dependence of this emission line showed a peculiar, counter-intuitive blue-shift, which is unprecedented in the landscape of solid-state quantum emitters. This effect was interpreted in terms of an increased occupation probability of the ^4E_u state.

The analysis also showed previously unexplored emission properties, including the occurrence of a previously unreported line at 608.3 nm at cryogenic temperatures, compatible with the $^2A_{1u} \rightarrow {}^2E_g$ transition predicted in ref 26, and the persistence of the 544.8 nm emission under all the considered excitation wavelengths in undoped substrates (in disagreement with the results in ref 35).

Finally, the single-photon emitter analysis of MgV centers suggests an appealing excited-state radiative lifetime (2.7 ± 0.3) ns, paired with a bright emission rate in reaching, in the saturation regime, up to (1.46 ± 0.17) Mcps under (2.7 ± 0.4) mW Raman-resonant excitation power, despite a large variability in the data distribution. The highest measured emission intensity at saturation is larger than those of the most intense group-IV impurity-related defects (SnV and PbV),[15,17] at >1 Mcps rates, and tops them by a factor of two under resonant excitation if the specific spectral transmittance of the experiment is taken into account. The results presented here on the intense emission, the efficient structural formation of the defect exploiting ion implantation, and the high Debye−Waller factor, combined with the enticing spin-dependent properties for the center's ground state,[26] offer an enticing perspective of practical applications of the MgV center in quantum technologies as a bright qubit for quantum sensing and quantum information processing.

■ ASSOCIATED CONTENT

Supporting Information

The Supporting Information is available free of charge at https://pubs.acs.org/doi/10.1021/acsphotonics.2c01130.

Additional information on EC experimental parameters and data analysis, including implementation of "many-beam" simulations for the diamond structure, considered lattice sites, theoretical emission patterns for substitutional and BC sites, comparison of implantation conditions; PL of a RT vs 800 °C ISOLDE ^{24}Mg implanted sample, as well as experimental details on optical characterization (PDF)

■ AUTHOR INFORMATION

Corresponding Authors

Ulrich Wahl − *Centro de Ciências e Tecnologias Nucleares, Departamento de Engenharia e Ciências e Engenharias Nucleares, Instituto Superior Técnico, Universidade de Lisboa, 2695-066 Bobadela LRS, Portugal*; Email: uwahl@ctn.tecnico.ulisboa.pt

Jacopo Forneris − *Physics Department, University of Torino, Torino 10125, Italy; Istituto Nazionale di Fisica Nucleare (INFN), Sezione di Torino, Torino 10125, Italy; Istituto Nazionale di Ricerca Metrologica (INRiM), Torino 10135, Italy*; orcid.org/0000-0003-2583-7424; Email: jacopo.forneris@unito.it

Authors

Emilio Corte − *Physics Department, University of Torino, Torino 10125, Italy; Istituto Nazionale di Fisica Nucleare (INFN), Sezione di Torino, Torino 10125, Italy; Istituto Nazionale di Ricerca Metrologica (INRiM), Torino 10135, Italy*

Greta Andrini − *Dipartimento di Elettronica e Telecomunicazioni, Politecnico di Torino, Torino 10129, Italy; Istituto Nazionale di Fisica Nucleare (INFN), Sezione di Torino, Torino 10125, Italy; Istituto Nazionale di Ricerca Metrologica (INRiM), Torino 10135, Italy*

Elena Nieto Hernández − *Physics Department, University of Torino, Torino 10125, Italy; Istituto Nazionale di Fisica Nucleare (INFN), Sezione di Torino, Torino 10125, Italy; Istituto Nazionale di Ricerca Metrologica (INRiM), Torino 10135, Italy*

Vanna Pugliese − *Physics Department, University of Torino, Torino 10125, Italy*

Ângelo Costa − *KU Leuven, Quantum Solid State Physics, 3001 Leuven, Belgium*

Goele Magchiels − *KU Leuven, Quantum Solid State Physics, 3001 Leuven, Belgium*; orcid.org/0000-0003-3186-4883

Janni Moens − *KU Leuven, Quantum Solid State Physics, 3001 Leuven, Belgium*

Shandirai Malven Tunhuma − *KU Leuven, Quantum Solid State Physics, 3001 Leuven, Belgium*; orcid.org/0000-0001-7423-9661

Renan Villarreal − *KU Leuven, Quantum Solid State Physics, 3001 Leuven, Belgium*; orcid.org/0000-0003-2162-7083

Lino M. C. Pereira − *KU Leuven, Quantum Solid State Physics, 3001 Leuven, Belgium*

André Vantomme − *KU Leuven, Quantum Solid State Physics, 3001 Leuven, Belgium*; orcid.org/0000-0001-9158-6534

João Guilherme Correia − *Centro de Ciências e Tecnologias Nucleares, Departamento de Engenharia e Ciências e Engenharias Nucleares, Instituto Superior Técnico, Universidade de Lisboa, 2695-066 Bobadela LRS, Portugal*

Ettore Bernardi − *Istituto Nazionale di Ricerca Metrologica (INRiM), Torino 10135, Italy*

Paolo Traina − *Istituto Nazionale di Ricerca Metrologica (INRiM), Torino 10135, Italy*

Ivo Pietro Degiovanni − *Istituto Nazionale di Ricerca Metrologica (INRiM), Torino 10135, Italy; Istituto Nazionale di Fisica Nucleare (INFN), Sezione di Torino, Torino 10125, Italy*

Ekaterina Moreva − *Istituto Nazionale di Ricerca Metrologica (INRiM), Torino 10135, Italy*

Marco Genovese − *Istituto Nazionale di Ricerca Metrologica (INRiM), Torino 10135, Italy; Istituto Nazionale di Fisica Nucleare (INFN), Sezione di Torino, Torino 10125, Italy*

Sviatoslav Ditalia Tchernij − *Istituto Nazionale di Fisica Nucleare (INFN), Sezione di Torino, Torino 10125, Italy; Physics Department, University of Torino, Torino 10125, Italy; Istituto Nazionale di Ricerca Metrologica (INRiM), Torino 10135, Italy*

Paolo Olivero − *Physics Department, University of Torino, Torino 10125, Italy; Istituto Nazionale di Fisica Nucleare (INFN), Sezione di Torino, Torino 10125, Italy; Istituto Nazionale di Ricerca Metrologica (INRiM), Torino 10135, Italy;* orcid.org/0000-0002-7512-6295

Complete contact information is available at: https://pubs.acs.org/10.1021/acsphotonics.2c01130

Author Contributions

[▽]E.C. and G.A. contributed equally to the work.

Funding

Italian Ministry for Instruction, University and Research: project "Intelligent fabrication of QUANTum devices in DIAmond by Laser and Ion Irradiation" (QuantDia) within the "FISR 2019" program and program "Departments of Excellence" (L. 232/2016); European Research Council: project "Training on LASer fabrication and ION implantation of DEFects as quantum emitters" (LasIonDef) funded under the "Marie Skłodowska-Curie Innovative Training Networks" program; Italian National Institute for Nuclear Physics (INFN), 5th National Commission: experiments ROUGE and QUANTEP; Piemonte Region: project "Piemonte Quantum Enabling Technologies" (PiQuET) within the "Infra-P" scheme (POR-FESR 2014−2020 program of the European Union); Compagnia di San Paolo: Project "Ex post funding of research − 2021" of the University of Torino; EMPIR program co-financed by the Participating States and from the European Union's Horizon 2020 research and innovation program: projects 20IND05 (QADeT) and project 20FUN05 (SEQUME); European Commission: project RADIATE (grant ID 824096; proposal 20,002,351-ST); EU Horizon 2020 Framework: Grant Agreement No. 654002 (ENSAR2); KU Leuven and the Research Foundation − Flanders (FWO, Belgium); Portuguese Foundation for Science and Technology (Fundação para a Ciência e a Tecnologia FCT): project CERN/FIS-TEC/0003/2019.

Notes

The authors declare no competing financial interest.

■ ACKNOWLEDGMENTS

This work was supported by the following projects: "Intelligent fabrication of QUANTum devices in DIAmond by Laser and Ion Irradiation" (QuantDia) project funded by the Italian Ministry for Instruction, University and Research within the "FISR 2019" program; "Training on LASer fabrication and ION implantation of DEFects as quantum emitters" (LasIonDef) project funded by the European Research Council under the "Marie Skłodowska-Curie Innovative Training Networks" program; experiments ROUGE and QUANTEP, funded by the 5th National Commission of the Italian National Institute for Nuclear Physics (INFN); Project "Piemonte Quantum Enabling Technologies" (PiQuET), funded by the Piemonte Region within the "Infra-P" scheme (POR-FESR 2014-2020 program of the European Union); "Departments of Excellence" (L. 232/2016), funded by the Italian Ministry of Education, University and Research (MIUR); and "Ex post funding of research − 2021" of the University of Torino funded by the "Compagnia di San Paolo". The projects 20IND05 (QADeT) and 20FUN05 (SEQUME) leading to this publication have received funding from the EMPIR program co-financed by the Participating States and from the European Union's Horizon 2020 research and innovation program. J.F. gratefully acknowledges the EU RADIATE Project (grant ID 824096; proposal 20002351-ST) for granting transnational access to the IMBL laboratory at KU Leuven. A.C., G.M., J.M., S.M.T., R.V., A.V., and L.M.C.P. acknowledge support from the KU Leuven and the Research Foundation − Flanders (FWO, Belgium). We appreciate the support of the ISOLDE Collaboration and technical teams. This work was funded by the Portuguese Foundation for Science and Technology (Fundação para a Ciência e a Tecnologia FCT, CERN/FIS-TEC/0003/2019). The EU Horizon 2020 Framework supported ISOLDE beam times through Grant Agreement No. 654002 (ENSAR2). The authors would like to express their gratitude to Optoprim Srl and nLight for their collaboration and technical support.

■ REFERENCES

(1) Schröder, T.; Mouradian, S. L.; Zheng, J.; Trusheim, M. E.; Walsh, M.; Chen, E. H.; Li, L.; Bayn, I.; Englund, D. Quantum nanophotonics in diamond. *J. Opt. Soc. Am. B* **2016**, *33*, B65.

(2) Aharonovic, I.; Englund, D.; Toth, M. Solid-state single-photon emitters. *Nat. Photonics* **2016**, *10*, 631.

(3) Chen, D.; Zheludev, N.; Gao, W. Building Blocks for Quantum Network Based on Group-IV Split-Vacancy Centers in Diamond. *Adv. Quantum Technnol.* **2020**, *3*, No. 1900069.

(4) Doherty, M. W.; Manson, N. B.; Delaney, P.; Jelezko, F.; Wrachtrup, J.; Hollenberg, L. C. L. The nitrogen-vacancy colour centre in diamond. *Phys. Rep.* **2013**, *528*, 1.

(5) Tsurumoto, K.; Kuroiwa, R.; Kano, H.; Sekiguchi, Y.; Kosaka, H. Quantum teleportation-based state transfer of photon polarization into a carbon spin in diamond. *npj Commun. Phys.* **2019**, *2*, 74.

(6) Dolde, F.; Doherty, M. W.; Michl, J.; Jakobi, I.; Naydenov, B.; Pezzagna, S.; Meijer, J.; Neumann, P.; Jelezko, F.; Manson, N. B.; Wrachtrup, J. Nanoscale detection of a single fundamental charge in ambient conditions using the NV^- center in diamond. *Phys. Rev. Lett.* **2014**, *112*, No. 097603.

(7) Sipahigil, A.; Goldman, M. L.; Togan, E.; Chu, Y.; Markham, M.; Twitchen, D. J.; Zibrov, A. S.; Kubanek, A.; Lukin, M. D. Quantum interference of single photons from remote nitrogen-vacancy centers in diamond. *Phys. Rev. Lett.* **2012**, *108*, No. 143601.

(8) Pezzagna, S.; Meijer, J. Quantum computer based on color centers in diamond. *Appl. Phys. Rev.* **2021**, *8*, No. 011308.

(9) Petrini, G.; Tomagra, G.; Bernardi, E.; Moreva, E.; Traina, P.; Marcantoni, A.; Picollo, F.; Kvakova, K.; Cigler, P.; Degiovanni, I. P.; Carabelli, V.; Genovese, M. Nanodiamond quantum sensors reveal temperature variation associated to hippocampal neurons firing. *Adv. Sci.* **2022**, *9*, No. 2202014.

(10) Bradac, C.; Gao, W.; Forneris, J.; Trusheim, M. E.; Aharonovich, I. Quantum nanophotonics with group IV defects in diamond. *Nat. Commun.* **2019**, *10*, 5625.

(11) Wang, C.; Kurtsiefer, C.; Weinfurter, H.; Burchard, B. Single photon emission from SiV centres in diamond produced by ion implantation. *J. Phys. B* **2006**, *39*, 37.

(12) Müller, T.; Hepp, C.; Pingault, B.; Neu, E.; Gsell, S.; Schreck, M.; Sternschulte, H.; Steinmüller-Nethl, D.; Becher, C. Optical signatures of silicon-vacancy spins in diamond. *Nat. Commun.* **2014**, *5*, 3328.

(13) Palyanov, Y. N.; Kupriyanov, I. N.; Borzdov, Y. M.; Surovtsev, N. V. Germanium: a new catalyst for diamond synthesis and a new optically active impurity in diamond. *Sci. Rep.* **2015**, *5*, 14789.

(14) Iwasaki, T.; Ishibashi, F.; Miyamoto, Y.; Doi, Y.; Kobayashi, S.; Miyazaki, T.; Tahara, K.; Jahnke, K. D.; Rogers, L. J.; Naydenov, B.; Jelezko, F.; Yamasaki, S.; Nagamachi, S.; Inubushi, T.; Mizuochi, N.; Hatano, M. Germanium-Vacancy Single Color Centers in Diamond. *Sci. Rep.* **2015**, *5*, 12882.
(15) Ditalia Tchernij, S.; Herzig, T.; Forneris, J.; Küpper, J.; Pezzagna, S.; Traina, P.; Moreva, E.; Degiovanni, I. P.; Brida, G.; Skukan, N.; Genovese, M.; Jakšic, M.; Meijer, J.; Olivero, P. Single-Photon-Emitting Optical Centers in Diamond Fabricated upon Sn Implantation. *ACS Photonics* **2017**, *4*, 2580.
(16) Iwasaki, T.; Miyamoto, Y.; Taniguchi, T.; Siyushev, P.; Metsch, M. H.; Jelezko, F.; Hatano, M. Tin-Vacancy Quantum Emitters in Diamond. *Phys. Rev. Lett.* **2017**, *119*, No. 253601.
(17) Ditalia Tchernij, S.; Lühmann, T.; Herzig, T.; Küpper, J.; Damin, A.; Santonocito, S.; Signorile, M.; Traina, P.; Moreva, E.; Celegato, F.; Pezzagna, S.; Degiovanni, I. P.; Olivero, P.; Jakšć, M.; Meijer, J.; Genovese, M.; Forneris, J. Single-Photon Emitters in Lead-Implanted Single-Crystal Diamond. *ACS Photonics* **2018**, *5*, 4864.
(18) Trusheim, M. E.; Wan, H. N.; Chen, K. C.; Ciccarino, C. J.; Flick, J.; Sundararaman, R.; Malladi, G.; Bersin, E.; Walsh, M.; Lienhard, B.; Bakhru, H.; Narang, P.; Englund, D. Lead-related quantum emitters in diamond. *Phys. Rev. B* **2019**, *99*, No. 075430.
(19) Zaitsev, A. M.*Optical Properties of Diamond − Data Handbook*; Springer: Berlin, Heidelberg, 2001.
(20) Prestopino, G.; Marinelli, M.; Milani, E.; Verona, C.; Verona-Rinati, G.; Traina, P.; Moreva, E.; Degiovanni, I. P.; Genovese, M.; Ditalia Tchernij, S.; Picollo, F.; Olivero, P.; Forneris, J. Photo-physical properties of He-related color centers in diamond. *Appl. Phys. Lett.* **2017**, *111*, 111105.
(21) Sandstrom, R.; Ke, L.; Martin, A.; Wang, Z.; Kianinia, M.; Green, B.; Gao, W.; Aharonovich, I. Optical properties of implanted Xe color centers in diamond. *Opt. Commun.* **2018**, *411*, 182−186.
(22) Aharonovich, I.; Castelletto, S.; Johnson, B. C.; McCallum, J. C.; Simpson, D. A.; Greentree, A. D.; Prawer, S. Chromium single-photon emitters in diamond fabricated by ion implantation. *Phys. Rev. B* **2010**, *81*, No. 121201.
(23) Gaebel, T. T.; Popa, I.; Gruber, A.; Domhan, M.; Jelezko, F.; Wrachtrup, J. Stable single-photon source in the near infrared. *New J. Phys.* **2004**, *6*, 98.
(24) Ditalia Tchernij, S.; Lühmann, T.; Corte, E.; Sardi, F.; Picollo, F.; Traina, P.; Brajković, M.; Crnjac, A.; Pezzagna, S.; Pastuović, Ž.; Degiovanni, I. P.; Moreva, E.; Aprà, P.; Olivero, P.; Siketić, Z.; Meijer, J.; Genovese, M.; Forneris, J. Fluorine-based color centers in diamond. *Sci. Rep.* **2020**, *10*, 21537.
(25) Lühmann, T.; Raatz, N.; John, R.; Lesik, M.; Rödiger, J.; Portail, M.; Wildanger, D.; Kleißler, F.; Nordlund, K.; Zaitsev, A.; Roch, J.-F.; Tallaire, A.; Meijer, J.; Pezzagna, S. Screening and engineering of colour centres in diamond. *J. Phys. D: Appl. Phys.* **2018**, *51*, 483002.
(26) Pershin, A.; Barcza, G.; Legeza, Ö.; Gali, A. Highly tunable magneto-optical response from magnesium-vacancy color centers in diamond. *npj Quantum Inf.* **2021**, *7*, 99.
(27) Hofsäss, H.; Lindner, G. Emission channeling and blocking. *Phys. Rep.* **1991**, *201*, 121.
(28) Wahl, U. Advances in electron emission channeling measurements in semiconductors. *Hyperfine Interact.* **2000**, *129*, 349.
(29) Wahl, U.; Correia, J. G.; Czermak, A.; Jahn, S.; Jalocha, P.; Marques, J.; Rudge, A.; Schopper, F.; Soares, J. C.; Vantomme, A.; Weilhammer, P. Position-sensitive Si pad detectors for electron emission channeling experiments. *Nucl. Instrum. Methods Phys. Res., Sect. A* **2004**, *524*, 245.
(30) Pereira, L. M. C.; Vantomme, A.; Wahl, U.Characterizing defects with ion beam analysis and channeling techniques. In *Characterisation and Control of Defects in Semiconductors*, Tuomisto, F., Eds.; Institution of Engineering and Technology: Stevenage, UK, 2019, Chap. 11, pp 501−563.
(31) Wahl, U.; Correia, J. G.; Villarreal, R.; Bourgeois, E.; Gulka, M.; Nesládek, M.; Vantomme, A.; Pereira, L. M. C. Direct structural identification and quantification of the split-vacancy configuration for implanted Sn in diamond. *Phys. Rev. Lett.* **2020**, *125*, No. 045301.
(32) Wahl, U.; Amorim, L. M.; Augustyns, V.; Costa, A.; David-Bosne, E.; Lima, T. A. L.; Lippertz, G.; Correia, J. G.; da Silva, M. R.; Kappers, M. J.; Temst, K.; Vantomme, A.; Pereira, L. M. C. Lattice Location of Mg in GaN: A Fresh Look at Doping Limitations. *Phys. Rev. Lett.* **2017**, *118*, No. 095501.
(33) Wahl, U.; Correia, J. G.; Costa, A. R. G.; David-Bosne, E.; Lima, T. A. L.; Lippertz, G.; Vantomme, A.; da Silva, M. R.; Kappers, M. J.; Pereira, L. M. C. Lattice location studies of the amphoteric nature of implanted Mg in GaN. *Adv. Electron. Mater.* **2021**, *7*, No. 2100345.
(34) David-Bosne, E.; Wahl, U.; Correia, J. G.; Lima, T. A. L.; Vantomme, A.; Pereira, L. M. C. A generalized fitting tool for analysis of two-dimensional channeling patterns. *Nucl. Instrum. Methods Phys. Res., Sect. B* **2020**, *462*, 102.
(35) Lühmann, T.; John, R.; Wunderlich, R.; Meijer, J.; Pezzagna, S. Coulomb-driven single defect engineering for scalable qubits and spin sensors in diamond. *Nat. Commun.* **2019**, *10*, 4956.
(36) Razgulov, A. A.; Lyapin, S. G.; Novikov, A. P.; Ekimov, E. A. Low-temperature photoluminescence study of SnV centers in HPHT diamond. *Diamond Relat. Mater.* **2021**, *116*, No. 108379.
(37) Doherty, M. W.; Acosta, V. M.; Jarmola, A.; Barson, M. S. J.; Manson, N. B.; Budker, D.; Hollenberg, L. C. L. Temperature shifts of the resonances of the NV− center in diamond. *Phys. Rev. B* **2014**, *90*, No. 041201.
(38) Dong, B.; Shi, C.; Xu, Z.; Wang, K.; Luo, H.; Sun, F.; Wang, P.; Wu, E.; Zhang, K.; Liu, J.; Song, Y.; Fan, Y. Temperature dependence of optical centers in Ib diamond characterized by photoluminescence spectra. *Diamond Relat. Mater.* **2021**, *116*, No. 108389.
(39) Fan, J.-W.; Cojocaru, I.; Becker, J.; Fedotov, I. V.; Hassan, M.; Alkahtani, A.; Alajlan, A.; Blakley, S.; Rezaee, M.; Lyamkina, A.; Palyanov, Y. N.; Borzdov, Y. M.; Yang, Y.-P.; Zheltikov, A.; Hemmer, P.; Akimov, A. V. Germanium-Vacancy Color Center in Diamond as a Temperature Sensor. *ACS Photonics* **2018**, *5*, 765.
(40) Thorlabs Longpass Dichroic Mirrors/Beamsplitters website. Long-pass dichroic mirror, model DMLP567. https://www.thorlabs.com/newgrouppage9.cfm?objectgroup_id=3313. (accessed 2022-10-25).
(41) Becker, J. N.; Görlitz, J.; Arend, C.; Markham, M.; Becher, C. Ultrafast all-optical coherent control of single silicon vacancy colour centres in diamond. *Nat. Commun.* **2016**, *7*, 13512.
(42) Kitson, S. C.; Jonsson, P.; Rarity, J. G.; Tapster, P. R. Intensity fluctuation spectroscopy of small numbers of dye molecules in a microcavity. *Phys. Rev. A* **1998**, *58*, 620.
(43) Corte, E.; Sachero, S.; Ditalia Tchernij, S.; Lühmann, T.; Pezzagna, S.; Traina, P.; Degiovanni, I. P.; Moreva, E.; Olivero, P.; Meijer, J.; Genovese, M.; Forneris, J. Spectral Emission Dependence of Tin-Vacancy Centers in Diamond from Thermal Processing and Chemical Functionalization. *Adv. Photonics Res.* **2021**, *3*, No. 2100148.
(44) Kurtsiefer, C.; Mayer, S.; Zarda, P.; Weinfurter, H. Stable Solid-State Source of Single Photons. *Phys. Rev. Lett.* **2000**, *85*, 290.
(45) Aharonovich, I.; Castelletto, S.; Simpson, D. A.; Stacey, A.; McCallum, J.; Greentree, A. D.; Prawer, S. Two-Level Ultrabright Single Photon Emission from Diamond Nanocrystals. *Nano Lett.* **2009**, *9*, 3191.
(46) Neu, E.; Steinmetz, D.; Riedrich-Möller, J.; Gsell, S.; Fischer, M.; Schreck, M.; Becher, C. Single photon emission from silicon-vacancy colour centres in chemical vapour deposition nano-diamonds on iridium. *New J. Phys.* **2011**, *13*, No. 025012.

https://doi.org/10.1021/acsphotonics.2c01130
ACS Photonics 2023, 10, 101−110

nanomaterials

MDPI

Article

Engineering Multicolor Radiative Centers in hBN Flakes by Varying the Electron Beam Irradiation Parameters

Federica Bianco [1,*], Emilio Corte [2], Sviatoslav Ditalia Tchernij [2], Jacopo Forneris [2] and Filippo Fabbri [1,*]

[1] NEST Laboratory, Istituto Nanoscienze-CNR and Scuola Normale Superiore, Piazza San Silvestro 12, 56127 Pisa, Italy
[2] Physics Department, University of Torino and Istituto Nazionale di Fisica Nucleare Sez. Torino, Via P. Giuria 11, 10125 Torino, Italy
* Correspondence: federica.bianco@nano.cnr.it (F.B.); filippo.fabbri@nano.cnr.it (F.F.); Tel.: +39-050-509378 (F.B.); +39-050-509525 (F.F.)

Abstract: Recently, hBN has become an interesting platform for quantum optics due to the peculiar defect-related luminescence properties. In this work, multicolor radiative emissions are engineered and tailored by position-controlled low-energy electron irradiation. Varying the irradiation parameters, such as the electron beam energy and/or area dose, we are able to induce light emissions at different wavelengths in the green–red range. In particular, the 10 keV and 20 keV irradiation levels induce the appearance of broad emission in the orange–red range (600–660 nm), while 15 keV gives rise to a sharp emission in the green range (535 nm). The cumulative dose density increase demonstrates the presence of a threshold value. The overcoming of the threshold, which is different for each electron beam energy level, causes the generation of non-radiative recombination pathways.

Keywords: hexagonal boron nitride; electron irradiation; photoluminescence; defect-related light emission

check for updates

Citation: Bianco, F.; Corte, E.; Ditalia Tchernij, S.; Forneris, J.; Fabbri, F. Engineering Multicolor Radiative Centers in hBN Flakes by Varying the Electron Beam Irradiation Parameters. *Nanomaterials* **2023**, *13*, 739. https://doi.org/10.3390/nano13040739

Academic Editor: Tilmar Kümmell

Received: 16 January 2023
Revised: 10 February 2023
Accepted: 13 February 2023
Published: 15 February 2023

Copyright: © 2023 by the authors. Licensee MDPI, Basel, Switzerland. This article is an open access article distributed under the terms and conditions of the Creative Commons Attribution (CC BY) license (https://creativecommons.org/licenses/by/4.0/).

1. Introduction

Electron irradiation has been an interesting tool for engineering layered materials and tailoring their properties [1–3]. It is possible to consider two main classes of electron irradiation process: low-energy irradiation, where the electron beam energy is compatible with a scanning electron microscope (SEM) or a transmission electron microscope (TEM), i.e., 5–300 keV, and high-energy bombardment that is a process involving electrons with energy beyond 1 MeV.

Among two-dimensional (2D) materials, graphene was the first one in which electron-irradiation-induced defects were studied both experimentally and theoretically [4–9]. The interaction of the electrons with the graphene lattice can induce profound structural modifications. The graphene can suffer a decrease of its crystallinity in favor of a nanocrystalline or amorphous nature, depending on the irradiation doses. This can be obtained even at beam energy in the low-energy range [6,7,10–13]. Importantly, electron-induced defects in graphene have already demonstrated an enhancing of its chemical reactivity, leading to graphene chemical functionalization [14–16]. In addition, electron-irradiation-induced defects have been employed in the engineering of graphene electronic properties [17–21] and, more generally, in sensing applications [22–29]. In the case of high-energy electron irradiation, graphene has been mainly employed in composites for radiation shielding applications [30], therefore structural defects induced by MeV electrons in graphene sheets have been very poorly studied [31,32].

Transition metal dichalcogenides (TMDs) are another class of layered materials, where the effect of the interaction with electron beams has been widely explored for tuning their structural and optical properties [2]. In terms of structural properties, molybdenum-based TMDs, namely MoS_2 and $MoTe_2$, undergo a transition from the semiconducting phase (2H for MoS_2 and 1H for $MoTe_2$) to the metallic phase (1T for MoS_2 and 1T′ for $MoTe_2$), under

electron bombardment inside a TEM [33–36]. In addition, the formation of Mo nanoparticles has been demonstrated by massive desulfurization due to high-dose electron showering of multilayer MoS_2 flakes [37]. Meanwhile, in terms of optical properties, electron irradiation of TMDs has been used to induce below-bandgap radiative transitions, attributed to the generation of chalcogen vacancy [38–40]. Recently, 100 keV electron irradiation has been demonstrated to increase emission yield of quantum emitters in strained WSe_2 sandwiched in hBN flakes, by increasing the concentration of defects [41]. In the case of high-dose [37,42] or high-energy [43] electron bombardment, the formation of non-radiative recombination pathways causes the quenching of the excitonic light emission of TMDs.

In the case of hexagonal boron nitride (hBN), electron irradiation has been mainly used to tailor the optical properties by the controlled generation of radiative color centers. Recently, the color center generation in hBN has focused on the isolation of point defects with single photon emitter (SPE) characteristics. In particular, two recent works have demonstrated the position-controlled generation of blue-emitting (435 nm) SPE centers by low-energy electron impinging [44,45]. Meanwhile, employing low-energy electron beam irradiation in the presence of water vapor has shown the appearance of multicolor SPE centers in the 565–775 nm range [46,47]. These experiments have been carried out with electron beam energy compatible with scanning electron microscopes, i.e., 5–15 keV.

Additionally, high-energy electron bombardment (2 MeV) has been used to demonstrate the controlled generation of color centers with SPE characteristics in multilayer hBN flakes; in this particular case, the color centers present an intense sharp emission at 590 nm [48] or a broad emission at 810 nm [49] as consequence of the formation of single boron vacancy.

In this work, we investigate the engineering and tailoring of radiative recombination in hBN flakes by a patterned electron irradiation process. Firstly, we evaluate light emission energy and intensity of the generated color center as a function of the electron beam energy, by sub-bandgap excitation photoluminescence (PL) spectroscopy. We demonstrate that 10 keV and 20 keV beam energies cause a broad complex emission around 660 nm, while 15 keV irradiation induces the appearance of a sharp band at 535 nm. Meanwhile, the hBN crystalline disorder induced by the electron beam irradiation is evaluated by Raman spectroscopy. The eventual trade-off between the electron-energy-related penetration depth and the thickness of the hBN flakes is evaluated by means of Monte Carlo simulations of the scattering events caused by the impinging of the primary electron beam. Then, we report the effect of the interaction of a single irradiation spot and area dose using irradiation patterns, varying the distance among the different impinging sites. In this case, the monochromatic photoluminescence maps allow us to clarify the interaction of the different irradiation spots in the pattern and the threshold evaluation of the cumulative dose density, leading to possible non-radiative pathways in the highly damaged areas.

2. Materials and Methods

We obtained the hBN flakes via standard micromechanical exfoliation from bulk single crystals provided by HQ Graphene. The 300 nm SiO_2/Si exfoliation substrate was cleaned by oxygen plasma prior to deposition of the tape, while the samples were cleaned overnight in organic solvents to remove possible glue residuals.

Defects were induced in part of the hBN flakes by irradiating with electrons accelerated at different electron beam energies, varying from 10 keV up to 20 keV. The areas to be damaged were precisely targeted by a Zeiss SEM driven by a Raith pattern generator. The patterns consisted of square arrays of spots with increasing spacing. The e-beam was set to output a current of about 0.6 nA. The e-beam delivered a spot dose of ~3.5 nC, resulting in a dwell time of 6 s. The electron beam spot size was 10 nm. Three different spot spacings were employed, namely 200 nm, 500 nm and 1000 nm, resulting in a matrix of 10 × 10, 4 × 4 and 3 × 3 irradiation sites, respectively. It is worth noting that when increasing the number of irradiation spots in an area with the same lateral extension, the dose per area unit increases drastically. The area dose, in fact, is evaluated as the single spot

dose multiplied by the number of irradiation sites divided by the area of the irradiation. Therefore, the 2 μm × 2 μm irradiated areas with 200 nm, 500 nm and 1000 nm spacing had an area dose equal to 87.5 nC/μm^2, 14 nC/μm^2 and 7.9 nC/μm^2, respectively. It is worth noting that prior to the irradiation of the area of interest, we carried out the electron irradiation of a sacrificial area in order to get rid of the carbon contaminant in the SEM chamber. The process was 40 min long using the following beam parameters for all used kinetic energies: beam current of 0.6 nA, dwell time of 6 s and step size of 100 nm. Raman and photoluminescence (PL) spectroscopies were carried out with a Renishaw InVia system, equipped with confocal microscope. In the case of PL measurements, a 473 nm excitation laser and a 2400 line/mm grating (spectral resolution 0.5 nm) were employed, while for Raman experiments a 532 nm excitation laser and an 1800 line/mm grating were used. The PL spectra were performed with the following parameters: excitation laser power 500 μW, acquisition time 10 s, spot size 800 nm using a 100× objective (NA = 0.85). The PL hyperspectral maps were acquired with an acquisition time of 1 s for each spot with a spot size of 500 nm × 500 nm pixel size. The Raman spectroscopic experiments were carried out increasing the excitation power to 1 mW and with an acquisition time of 1 s. The reported Raman spectra were averaged over 5 single acquisitions. The full width half maximum (FWHM) of the Raman spectrum was obtained by a Lorentzian fitting of the hBN peak. The Raman system resolution was 1 cm^{-1}.

3. Results

3.1. Electron Beam Parameters

Figure 1 clarifies the scheme of the electron irradiation experiments presented in this work. Flakes, with thickness of about 50 nm, were employed upon identification by optical contrast with respect to the SiO_2/Si substrate [50,51] (additional details are reported in the Supplementary Materials, Figure S1).

Firstly, we evaluated the effect of electron beam energy on the engineering of radiative recombination in hBN flakes. Three electron energy values were selected for the irradiation experiments: 10 keV, 15 keV and 20 keV. The variation of the beam energy modified the depth of the generation/recombination volume. Then, we evaluated the effect of patterned irradiation, by varying the spacing among the single irradiation spots. In particular, the irradiation pattern was performed on square areas with a lateral size of 2 μm × 2 μm, with a different spacing between single irradiation spots. The optical images of the hBN flakes, superimposed on the irradiation schemes with different spacing, are shown in Figure S2. In this perspective, the interaction of the different irradiation spots was evaluated.

Monte Carlo simulation was carried out in order to evaluate the interaction of the primary electron beam with the hBN flakes, with an average thickness of 50 nm, varying the beam energy. Figure 1b provides the depth profiles of the scattering events generating secondary electrons (SEs). As expected when increasing the beam energy, the peak of the depth distribution moved deeper into the sample. In fact, the depth profile peak was 650 nm, 1300 nm and 2100 nm for 10 keV, 15 keV and 20 keV, respectively. These values were obtained from the energy release maps reported in Figure S3 and indicate that the majority of the scattering events occurred in the silicon substrate. The increase in the beam energy also led to the enlargement of the generation/recombination volume. In particular, the radius of the generation/recombination volume was 400 nm, 1 μm and 1.7 μm, for 10 keV, 15 keV and 20 keV, respectively. In addition, we also considered the scattering events giving rise to backscattered electrons (Figure 1c) because they can participate in the defect formation dynamics in 2D materials [6,7]. Similarly to what occurs to the SE scattering events, the backscattered electron (BSE) depth distribution peaked deeper in the sample, increasing the electron beam energy. The BSE depth distribution peak occurs at 250 nm, 500 nm and 850 nm for the 10 keV, 15 keV and 20 keV irradiation, respectively. It is worth noting that, although the majority of the BSE-related scattering events occur in the substrate, a significant percentage of electrons were backscattered in the first 50 nm, i.e., in

the hBN flakes. The electron trajectory maps for the different electron beam energies are presented in Figure S3.

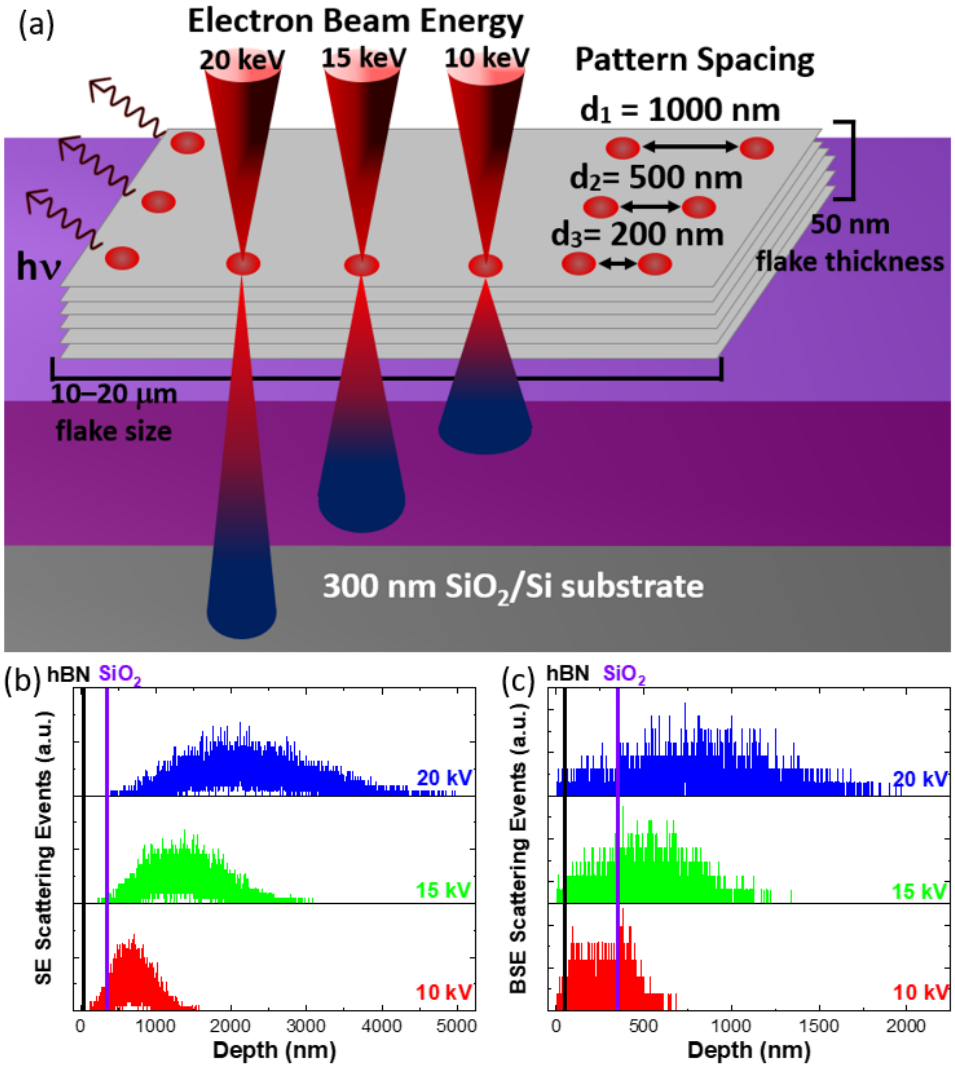


Figure 1. (**a**) Sketch of the different irradiation processes performed on the hBN flakes. Monte Carlo simulation of the depth penetration at different beam energies: (**b**) secondary electron-generating scattering events and (**c**) backscattering electron-generating scattering events. The black and purple vertical lines indicate the thickness of the hBN and of the SiO_2, respectively.

3.2. Effect of the Different Electron Beam Energies

The PL spectra obtained in areas irradiated with different beam energies are shown in Figure 2a in comparison with the reference spectrum of pristine hBN (black line). The PL spectrum of the pristine hBN presents no peculiar features in the whole analyzed range. The PL spectra of the electron-irradiated SiO_2/Si substrate are reported in Figure S4, in order to rule out any substrate-related light emission. The areas irradiated with 10 keV (red line) and 20 keV (blue line) electron beams present a broad emission in the orange–red range. In particular, the emission is composed of two main components at 610 nm and 660 nm, with a pronounced tail at the shorter wavelength side. The main difference between these two spectra is the intensity of the broad band. In fact, the 10 keV irradiation causes a PL intensity that is double the one obtained when irradiating hBN at 20 keV. The lower efficiency in emission engineering of the 20 keV irradiation process is mainly due to the deeper penetration depth of the 20 keV electron beam with respect to the 10 keV one, as demonstrated in Figure 1b,c. In fact, the energy release of the primary electron beam occurs

mainly at the SiO_2/Si interface in the case of the 20 keV beam while, in the 10 keV process, the electron energy is released, in larger part, at the hBN/SiO_2 interface (Figure S1).

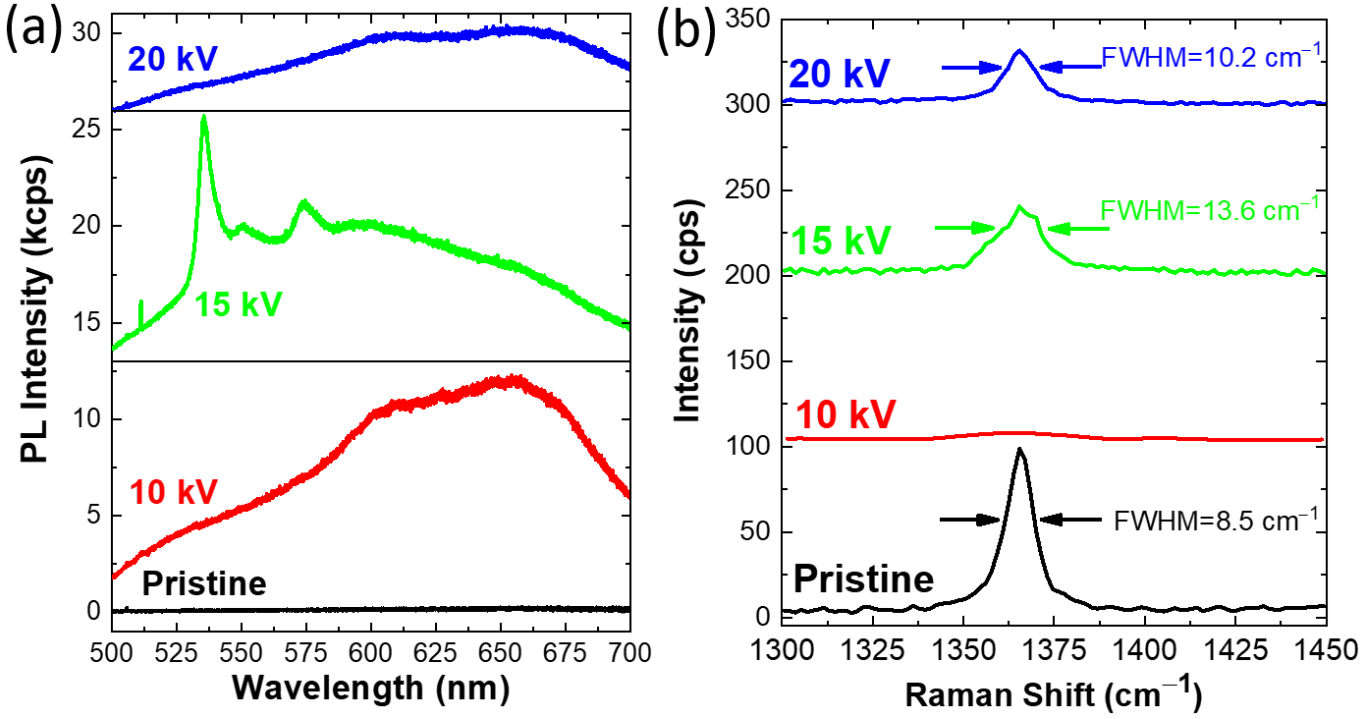


Figure 2. (**a**) PL spectra of the hBN irradiated with different electron beam energies: pristine hBN (black line), 10 keV (red line), 15 keV (green line), 20 keV (blue line) irradiation. (**b**) Raman spectra obtained in the irradiated areas. All spectra are vertically shifted for a better comparison.

Similarly to 10 keV and 20 keV, the 15 keV irradiated area (green line) shows a red–orange broad emission. In addition, the PL spectrum presents a sharp PL peak in the green range, namely at 535 nm, and two additional peaks at 550 nm and 575 nm. The latter peaks are attributed to photon replicas of the 535 nm zero phonon line (ZPL). Interestingly, the 15 keV irradiation is the only process to induce the appearance of the sharp 535 nm emission. The possible cause of this effect is the trade-off between the kinetic energy of electrons and their interaction with the substrate, i.e., energy release, scattering events and their depth distribution, in which the interface interaction may play a crucial role. However, it is necessary to consider the crystallographic attribution of this emission to gain a deeper insight into the effect of the 15 keV irradiation process. In order to quantify the crystalline disorder caused by the electron irradiation, Raman spectroscopy was carried out in the same areas where the PL spectra were acquired. The Raman peak that is conventionally investigated in hBN is at 1366 cm^{-1}. This Raman mode is attributed to the in-plane atom vibrations (E_{2g} mode) [52,53]. The benchmark for the crystalline quality of hBN is the FWHM of this peak. The Raman spectrum (black line), reported in Figure 2b, of the pristine hBN reports an FWHM of 8.5 cm^{-1}. The standard FWHM of the hBN, provided by the supplier, is ≈8.2 cm^{-1} as recently reported [54]. This agreement indicates that the exfoliation protocol, employed for the preparation of the flake, does not cause any worsening of the material crystallinity [55]. As expected, the electron irradiation dramatically affects the local crystallinity of hBN. In the case of the 10 keV process, the hBN Raman mode is completely quenched, suggesting a local amorphization of the lattice. In the case of the 15 keV and 20 keV processes, the hBN Raman mode suffers a decrease in intensity and a broadening of the FWHM. In particular, the FWHM increases up to 13.6 cm^{-1} and 10.2 cm^{-1} for the 15 keV and 20 keV processes, respectively, indicating a worsening of the crystallinity of hBN [55]. It is worth mentioning that no previous

works, to the best of our knowledge, has correlated the appearance of light emitting color centers by low-energy electron irradiation with the hBN crystallinity in terms of the FWHM of the hBN E_{2g} peak [44–46]. However, high-energy electron bombardment has been demonstrated to generate a moderate concentration of optically active defects without inducing any broadening of the Raman mode FWHM [48,49]. Two recent works have reported defect-activated Raman modes (analogous to graphene D peak) in hBN flake in the case of ion irradiation [56,57]. In the case of He ion irradiation, Liang et al. have reported the appearance of a broad bump at 1295 cm^{-1}, that becomes the dominant peak at an ion fluence of 1×10^{17} ions/cm^2, and Gu et al. have reported a broad band at 1609 cm^{-1} after irradiation of hBN with thallium ions with a fluence of 1×10^9 ions/cm^2. Both these Raman modes may actually be related to the presence of amorphous carbon, deposited during the irradiation process [58,59]. We discuss in the Supplementary Materials, Figure S5, similar findings in sacrificial areas of the sample, where the electron irradiation causes the deposition of amorphous carbon due to carbon residuals present in the SEM chamber.

The comparative PL and Raman analyses can give indications about the crystallographic attribution, giving rise to the aforementioned light emissions. The broad band composed of the 610 nm and the 660 nm peaks appears in areas having a high degree of crystalline disorder, as demonstrated by the broadening or the complete disappearance of the Raman peak. Therefore, the possible attributions to crystalline defects can be multiple, however, an intense double peak at around 610 nm with a shoulder at 660 nm has been localized at thickness step in mechanically exfoliated hBN flakes [55]. This emission has been recently attributed to substitutional boron atoms [60] or boron vacancy [61–63] in hBN grown with chemical vapor deposition. By comparing these results with theoretical calculations, the possible defects involved in these radiative recombinations may be the substitutional boron or interstitial boron atoms, despite the high formation energy [64].

The crystallographic origin of the 535 nm emission has been previously assigned to an array of dislocations in hBN [65]. Analogous electron-irradiation-induced generation of line defects has also been previously demonstrated in the case of MoS_2 [66]. However, such a radiative recombination has been detected in deformed few-atomic-layer hBN induced by substrate patterning [67] or close to morphological defects in mechanically exfoliated flakes [55].

Generally, the generation of the optical active centers can be ascribed to multiple mechanisms [68]. When irradiating with energies below the knock-off energy of hBN, we expect various mechanisms, that we can group in two main categories: the mechanisms that involve the substrate and the electron–hBN interaction. A possible substrate-involving mechanism is the Coulomb explosion arising from the charge accumulation in the SiO_2 layer, that is caused by a large number of scattering events occurring in this layer, as we reported in the Monte Carlo simulations [69]. Another possible mechanism related to the substrate is the backscattered electron (BSE) irradiation of hBN. BSEs are generated at the SiO_2/Si interface and cause an increase in the number of electron–hBN interaction events, as previously reported in case of graphene on SiO_2/Si substrate [7]. The last possible substrate-related mechanism is related to the generation of highly reactive oxygen species (ROS) due to the electron bombardment of the SiO_2. The electron-irradiation-generated ROS can induce point defects and even local oxidation of the hBN [70,71]. In the case of the direct effect of the electron irradiation of the hBN flake, the local Coulomb explosion has been previously demonstrated under 300 keV electron irradiation on hBN nanotubes [72]. In addition, a recent work [73] about the low-energy electron irradiation of MoS_2 monolayer has demonstrated that the formation of vacancies through ballistic energy transfer is possible at electron energies which are much lower than the knock-on threshold, when excitations are present in the electronic system. Instead, we rule out the local chemical etching of the hBN, considering that the irradiated area does not present any change in optical contrast, as shown in Figure S6 in the Supplementary Materials.

3.3. Effect of the Irradiation Spot Spacing

In order to evaluate the effect of the irradiation spot spacing, and thus the interaction between the single irradiation spots, different areas were irradiated increasing the spacing between the single irradiation spots (decreasing the area dose) for the 10 keV irradiation (Figure 3). The intensity PL map obtained at 660 nm in the case of an irradiation pattern with 200 nm spacing is reported in Figure 3a. The dashed yellow square highlights the primary irradiated 2 μm × 2 μm area. The map reveals that the primary impinging area presents a low PL intensity at 660 nm, while it increases in the region surrounding the irradiated area. It is worth noting that the annular surrounding area is composed of a first ring with high intensity extending ~1 μm around the irradiated area and a secondary ring with faint PL intensity, with a lateral size of 500 nm. A similar scenario occurs in the case of the pattern with 500 nm spacing. In fact, the high-intensity annular area is located around the edge of the primary impinging area, while the central area denoted by low PL intensity is smaller than the primary irradiated area. The secondary ring with low emission has a similar lateral extension. The spatial distribution of the irradiation-induced light emission is different in the case of the 1000 nm spaced pattern. The irradiated area presents the highest emission intensity, with decreasing PL intensity receding from it. However, the emission intensity remains high for the first 1 μm outside of the irradiated area and decreases drastically in a secondary ring with a 500 nm lateral extension. PL spectra of irradiated areas with different spacings were acquired (light red lines, Figure 3d) in order to carry out a more quantitative evaluation of the line shape modifications. The PL spectra acquired in the 200 nm and 500 nm spaced irradiated areas are broad bands peaking at 610 nm, showing an additional component at 660 nm and a broad tail in the short wavelength range. Conversely, the PL spectrum of the 1000 nm spaced area presents a higher intensity in the whole wavelength range with the 610 nm and 660 nm components with comparable intensities. For the sake of clarity, we report the PL spectra (dark red lines in Figure 3d) of the high-intensity annular areas for both the 200 nm and 500 nm spacings. In the case of the 200 nm spacing, the comparison of the irradiated area and its surrounding ring shows that the 610 nm and 660 nm emissions have an intensity increase of 400% and of 580%, respectively. On the contrary, the irradiated region with 500 nm spacing exhibits a lower increase in the emission intensity (330% and 420%, respectively). These data can be interpreted in view of the increasing area dose resulting from the different spacing: the shorter the spacing, the stronger the adjacent spot interactions. In fact, the electron irradiation with an area dose higher than 14 nC/μm^2 causes a cascade effect that induces the generation of non-radiative recombination paths that quench the light emission in the primary irradiated area. Similar results have been demonstrated, using molecular dynamics simulation, for high fluence ion irradiation, where the high fluence process creates a noticeable amount of complex vacancies, leading to amorphization and ultimately complete destruction of hBN [74]. The presence of the high-intensity rings is due to a lower effective area dose compared to the primary irradiated area, because the material is mainly affected by the irradiation sites on the edges of the irradiated area. The lateral extension of such rings is reliable with the radius of the generation/recombination volume obtained by Monte Carlo simulations (Figure S3).

Similar pattern spacing is used when irradiating with 15 keV, whose PL mapping is reported in Figure 4. The 535 nm PL maps of the 200 nm, 500 nm and 1000 nm spacings are presented in Figure 4a–c, respectively. The PL map of the 200 nm spaced irradiation reveals a similar intensity spatial distribution of the 500 nm spaced 10 keV irradiation, where the primary impinging area has a faint PL intensity at 535 nm, while the surrounding annular area has an intense PL emission with 1 μm extension. It is worth noting that in the case of the 15 keV irradiation the secondary annular area has a larger spatial extension (about 2 μm) with respect to the 10 keV irradiation. This effect also occurs in the 500 nm and 1000 nm irradiation patterns, where the surrounding annular areas have a lateral extension of 2 μm. However, both the 500 nm and 1000 nm spacings show an intense PL emission localized in the primary irradiated area. Comparing the PL intensities in the irradiated

areas, the 500 nm spacing is more efficient than the 1000 nm patterning in the generation of radiative centers emitting at 535 nm, reaching the maximum intensity value of 7 kcps. Figure 4d reports the PL spectra obtained in the irradiated areas with different spacings. All the PL spectra report that the sharp emission at 535 nm, with the related phonon replicas, appears in the case of all the different spacings. In the case of the 200 nm spacing, the main difference between the irradiated and the surrounding annular areas is the intensity of the emission, in fact, the line shape shows no peculiar differences. In the case of the 1000 nm PL spectrum, the 660 nm component appears more pronounced than in the other PL spectra. The FWHM maps of the hBN Raman mode for the different pattern spacings are reported in Figure S7 and representative Raman spectra are shown in Figure S8 in order to demonstrate the absence of amorphous carbon induced by electron beam deposition.

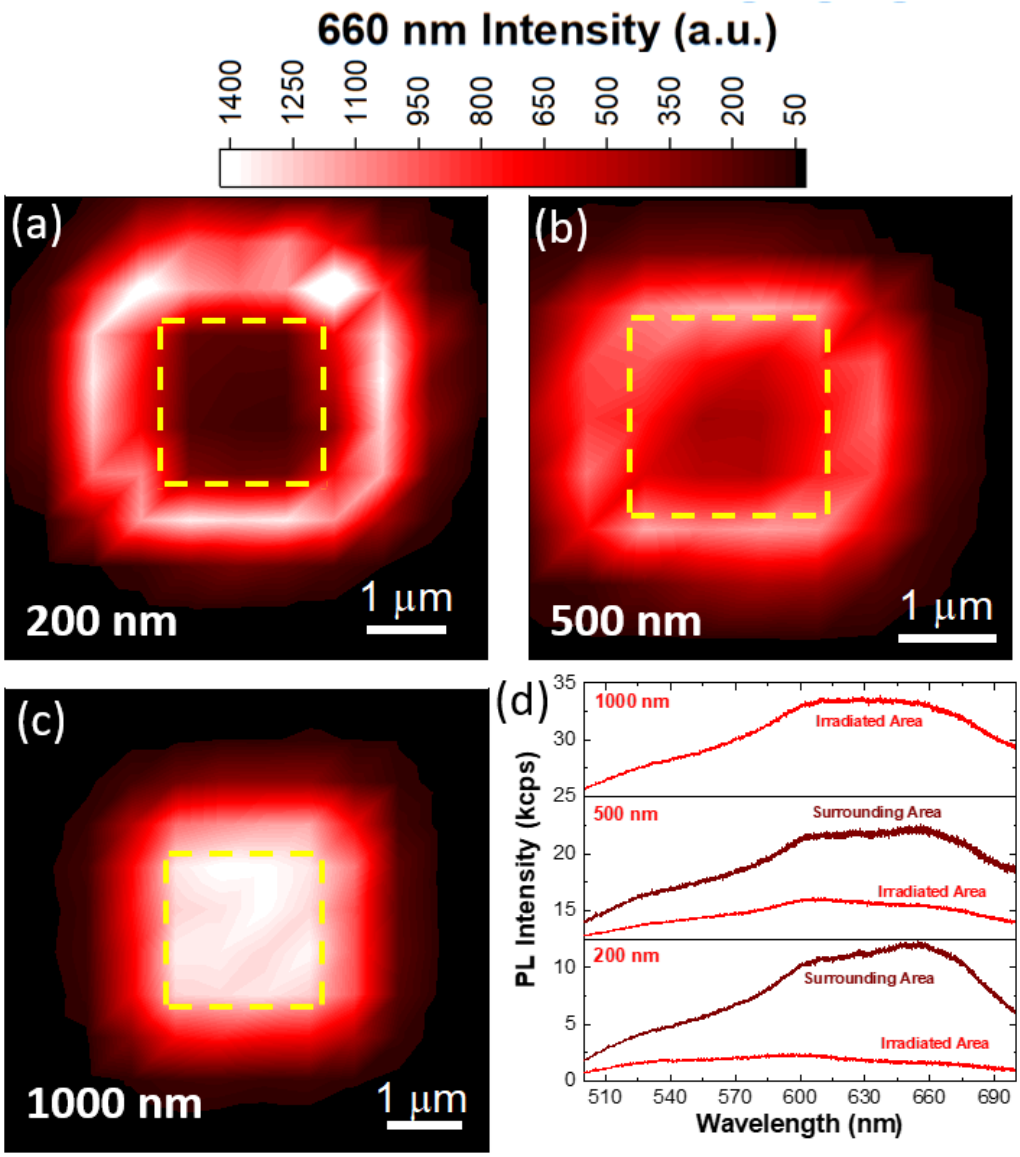


Figure 3. PL intensity map obtained at 660 nm for patterns with 200 nm (**a**), 500 nm (**b**) and 1000 nm (**c**) spacings. The upper color bar applies for all the maps. The dashed yellow square indicates the primary irradiated areas. (**d**) PL spectra of the 10 keV electron-irradiated hBN with different pattern spacings.

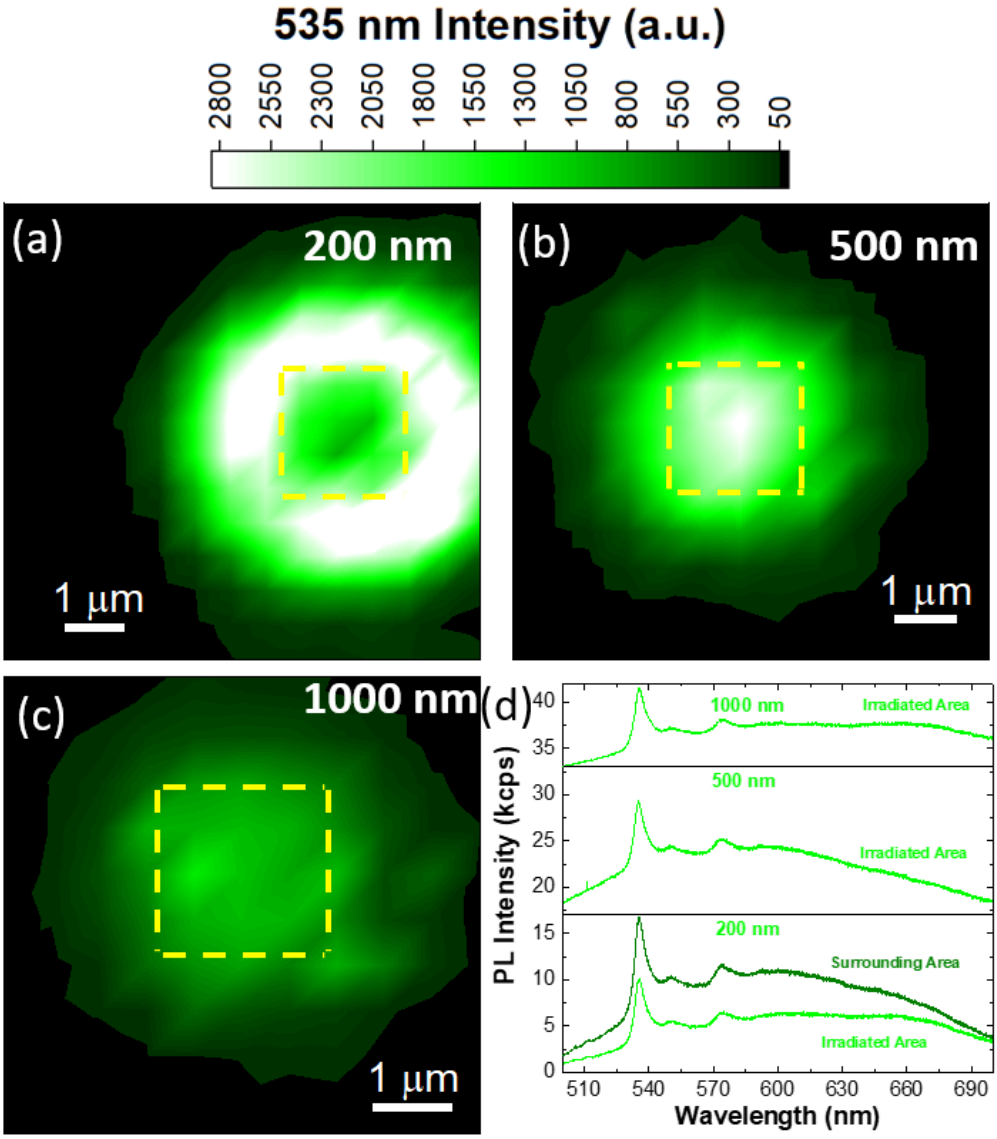


Figure 4. PL intensity map acquired at 535 nm for the 200 nm (**a**), 500 nm (**b**) and 1000 nm (**c**) spaced patterns. The upper color bar applies for all the maps. (**d**) PL spectra of the 15 keV electron-irradiated hBN with different pattern spacings.

3.4. Excitation Power Dependence of the 535 nm Emission

In order to gain more insights on the nature of the sharp emission at 535 nm, a power-dependent PL analysis was carried out (Figure 5). The PL spectra acquired varying the excitation power of the 473 nm laser are shown in Figure 5a. As expected, the phonon replicas at 550 nm and 575 nm appear more pronounced mainly at higher excitation power. Figure 5b summarizes the power-dependent intensity (black dots) and peak position (cyan dots) of the 535 nm band. The 535 peak intensity presents an exponential monotonic increase with the excitation power. It is worth noting that, even when increasing the excitation power over two orders of magnitude, we were not able to reach the saturation of the emission intensity. Moreover, by considering a double logarithmic scale graph (more details in the Supplementary Materials, Figure S9), indications on the nature of the radiative recombination process can be obtained from the slope of the intensity increase [75,76]. In this particular case, the slope shows a close linear behavior, suggesting that the emission is due to an excitonic recombination bound to an isoelectronic trap [75].

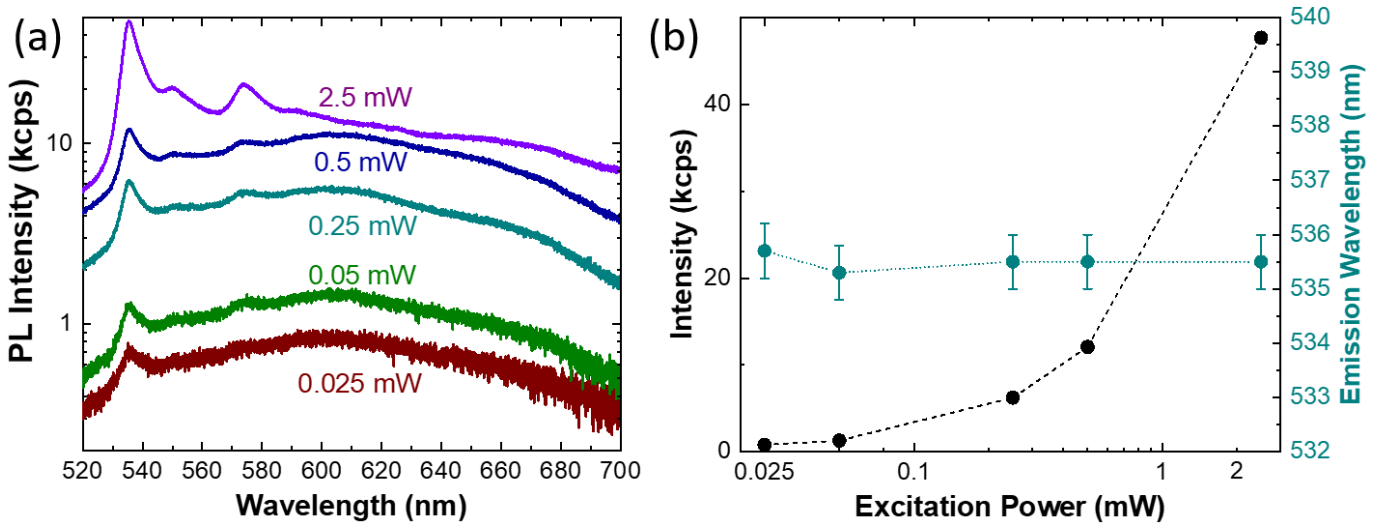


Figure 5. (**a**) PL spectra of the 15 keV electron-irradiated hBN with increasing 473 nm excitation power. (**b**) Power dependence of the 535 nm emission intensity (black symbols) and evaluation of the emission energy (cyan symbols), the lines are only a guide to the eye for the reader.

Finally, the power dependence of the peak position reveals no shift in the emission. This result gives interesting insights about the nature of the radiative recombination: the emission could arise from color centers generated in the irradiation process. Indeed, the absence of the emission shift rules out the possible attribution to donor–acceptor pair (DAP) radiative recombination [77]. In a DAP transition, the peak position is blue shifted due to the increasing of the Coulomb interaction with increased DAPs at high excitation intensity. Consequently, the power-dependent PL results suggest that one possible electronic transition is from a localized defect level to the valence band or conduction band [78].

4. Conclusions

In conclusion, we demonstrate that low-energy electron beam irradiation parameters are crucial for tailoring and tuning the light emission properties of hexagonal boron nitride flakes. The irradiation parameters can give rise to emissions at different wavelengths with different widths. Finding the best trade-off between flake thickness and electron beam energy (15 keV) allows engineering of a sharp emission at 535 nm, attributed to an excitonic recombination bound to an isoelectronic trap. Electron irradiation at a lower energy (10 keV) induces a high degree of crystalline disorder that causes the generation of broad emissions. The position-controlled irradiation permits the creation of irradiation patterns with different spacings with increasing area doses. The area dose increase demonstrates the presence of a threshold value, different for each electron beam energy, which, once exceeded, causes the generation of non-radiative recombination pathways in the primary irradiated area.

Supplementary Materials: The following supporting information can be downloaded at: https://www.mdpi.com/article/10.3390/nano13040739/s1, Figure S1: Atomic force microscopy analysis of the hBN flake. Figure S2: Optical images of the hBN flakes employed in the irradiation processes. Figure S3: Monte Carlo simulation of the primary electron beam interaction with the sample. Figure S4: Photoluminescence spectra of electron-irradiated bare SiO_2/Si substrate at different electron beam energies. Figure S5: Undesired electron-beam-induced carbon deposition procedure. Figure S6: Optical micrograph of the irradiated areas. Figure S7: Raman mapping of the 15 keV irradiated areas with increasing pattern spacing. Figure S8: Raman spectroscopy of the 15 keV irradiated areas with increasing pattern spacing. Figure S9: PL Power dependence fitting.

Author Contributions: Conceptualization, F.B. and F.F.; methodology, F.B., E.C., S.D.T., J.F. and F.F.; investigation, F.B., E.C. and F.F.; validation, E.C. and S.D.T.; writing—original draft preparation, F.B. and F.F.; writing—review and editing, F.B., E.C., S.D.T., J.F. and F.F. All authors have read and agreed to the published version of the manuscript.

Funding: F.F. and F.B. want to acknowledge the support of the project q-LIMA in the framework of the PRIN2020 initiative of the Italian Ministry of University and Research. J.F. acknowledges the support of the 20IND05 (QADeT) project, funded by the EMPIR program co-financed by the Participating States and from the European Union's Horizon 2020 research and innovation framework.

Data Availability Statement: The data presented in this study are available on request from the corresponding author.

Conflicts of Interest: The authors declare no conflict of interest.

References

1. Dash, A.K.; Mondal, M.; Verma, M.; Kumar, K.S.; Singh, A. Effect of electron-irradiation on layered quantum materials. *Bull. Mater. Sci.* **2021**, *44*, 227. [CrossRef]
2. Zhao, X.; Kotakoski, J.; Meyer, J.C.; Sutter, E.; Sutter, P.; Krasheninnikov, A.V.; Kaiser, U.; Zhou, W. Engineering and modifying two-dimensional materials by electron beams. *MRS Bull.* **2017**, *42*, 667–676. [CrossRef]
3. Krasheninnikov, A.V. Are two-dimensional materials radiation tolerant? *Nanoscale Horiz.* **2020**, *5*, 1447–1452. [CrossRef]
4. Yang, G.; Li, L.; Lee, W.B.; Ng, M.C. Structure of graphene and its disorders: A review. *Sci. Technol. Adv. Mater.* **2018**, *19*, 613–648. [CrossRef]
5. Jiang, J.; Xu, T.; Lu, J.; Sun, L.; Ni, Z. Defect Engineering in 2D Materials: Precise Manipulation and Improved Functionalities. *Research* **2022**, *2019*, 7507131. [CrossRef]
6. Melchioni, N.; Fabbri, F.; Tredicucci, A.; Bianco, F. Periodic Structural Defects in Graphene Sheets Engineered via Electron Irradiation. *Micromachines* **2022**, *13*, 1666. [CrossRef]
7. Basta, L.; Moscardini, A.; Veronesi, S.; Bianco, F. Substrate surface effects on electron-irradiated graphene. *Surfaces Interfaces* **2022**, *28*, 101694. [CrossRef]
8. Meyer, J.C.; Eder, F.; Kurasch, S.; Skakalova, V.; Kotakoski, J.; Park, H.J.; Roth, S.; Chuvilin, A.; Eyhusen, S.; Benner, G.; et al. Accurate Measurement of Electron Beam Induced Displacement Cross Sections for Single-Layer Graphene. *Phys. Rev. Lett.* **2012**, *108*, 196102. [CrossRef]
9. Tian, W.; Li, W.; Yu, W.; Liu, X. A Review on Lattice Defects in Graphene: Types, Generation, Effects and Regulation. *Micromachines* **2017**, *8*, 163. [CrossRef]
10. Tao, L.; Qiu, C.; Yu, F.; Yang, H.; Chen, M.; Wang, G.; Sun, L. Modification on Single-Layer Graphene Induced by Low-Energy Electron-Beam Irradiation. *J. Phys. Chem. C* **2013**, *117*, 10079–10085. [CrossRef]
11. Teweldebrhan, D.; Balandin, A.A. Modification of graphene properties due to electron-beam irradiation. *Appl. Phys. Lett.* **2009**, *94*, 13101. [CrossRef]
12. Selhorst, R.; Susner, M.A.; Muzzio, R.; Kao, I.-H.; Carpena-Núñez, J.; Islam, A.E.; Katoch, J.; Maruyama, B.; Rao, R. Electron-beam chemistry in graphene-Effect of environmental SEM parameters on patterning and defect engineering. *Vacuum* **2023**, *207*, 111686. [CrossRef]
13. Islam, A.E.; Susner, M.A.; Carpena-Núñez, J.; Back, T.C.; Rao, R.; Jiang, J.; Pachter, R.; Tenney, S.A.; Boeckl, J.J.; Maruyama, B. Defect engineering of graphene using electron-beam chemistry with radiolyzed water. *Carbon* **2020**, *166*, 446–455. [CrossRef]
14. Malekpour, H.; Ramnani, P.; Srinivasan, S.; Balasubramanian, G.; Nika, D.L.; Mulchandani, A.; Lake, R.K.; Balandin, A.A. Thermal conductivity of graphene with defects induced by electron beam irradiation. *Nanoscale* **2016**, *8*, 14608–14616. [CrossRef] [PubMed]
15. Lan, Y.-W.; Chang, W.-H.; Xiao, B.-T.; Liang, B.-W.; Chen, J.-H.; Jiang, P.; Li, L.-J.; Su, Y.-W.; Zhong, Y.-L.; Chen, C.-D. Polymer-Free Patterning of Graphene at Sub-10-nm Scale by Low-Energy Repetitive Electron Beam. *Small* **2014**, *10*, 4778–4784. [CrossRef]
16. Basta, L.; Bianco, F.; Moscardini, A.; Fabbri, F.; Bellucci, L.; Tozzini, V.; Heun, S.; Veronesi, S. Deterministic Covalent Organic Functionalization of Monolayer Graphene with 1, 3-Dipolar Cycloaddition Via High Resolution Surface Engineering. *arXiv* **2022**, arXiv:2202.06609. [CrossRef]
17. Zhang, A.; Wu, Y.; Ke, S.-H.; Feng, Y.P.; Zhang, C. Bandgap engineering of zigzag graphene nanoribbons by manipulating edge states via defective boundaries. *Nanotechnology* **2011**, *22*, 435702. [CrossRef]
18. Nourbakhsh, A.; Cantoro, M.; Vosch, T.; Pourtois, G.; Clemente, F.; van der Veen, M.H.; Hofkens, J.; Heyns, M.M.; De Gendt, S.; Sels, B.F. Bandgap opening in oxygen plasma-treated graphene. *Nanotechnology* **2010**, *21*, 435203. [CrossRef]
19. Yang, N.; Yang, D.; Chen, L.; Liu, D.; Cai, M.; Fan, X. Design and adjustment of the graphene work function via size, modification, defects, and doping: A first-principle theory study. *Nanoscale Res. Lett.* **2017**, *12*, 642. [CrossRef]
20. Liu, G.; Teweldebrhan, D.; Balandin, A.A. Tuning of Graphene Properties via Controlled Exposure to Electron Beams. *IEEE Trans. Nanotechnol.* **2011**, *10*, 865–870. [CrossRef]
21. Zhou, Y.; Jadwiszczak, J.; Keane, D.; Chen, Y.; Yu, D.; Zhang, H. Programmable graphene doping via electron beam irradiation. *Nanoscale* **2017**, *9*, 8657–8664. [CrossRef] [PubMed]

22. Lee, G.; Yang, G.; Cho, A.; Han, J.W.; Kim, J. Defect-engineered graphene chemical sensors with ultrahigh sensitivity. *Phys. Chem. Chem. Phys.* **2016**, *18*, 14198–14204. [CrossRef]
23. Kislenko, V.A.; Pavlov, S.V.; Kislenko, S.A. Influence of defects in graphene on electron transfer kinetics: The role of the surface electronic structure. *Electrochim. Acta* **2020**, *341*, 136011. [CrossRef]
24. Yuan, W.; Shi, G. Graphene-based gas sensors. *J. Mater. Chem. A* **2013**, *1*, 10078–10091. [CrossRef]
25. Cho, S.H.; Kwon, S.S.; Yi, J.; Park, W. Il Chemical and biological sensors based on defect-engineered graphene mesh field-effect transistors. *Nano Converg.* **2016**, *3*, 14. [CrossRef] [PubMed]
26. Fu, W.; Jiang, L.; van Geest, E.P.; Lima, L.M.C.; Schneider, G.F. Sensing at the Surface of Graphene Field-Effect Transistors. *Adv. Mater.* **2017**, *29*, 1603610. [CrossRef]
27. Yu, X.; Shen, Y.; Liu, T.; Wu, T.; Wang, Q.J. Photocurrent generation in lateral graphene p-n junction created by electron-beam irradiation. *Sci. Rep.* **2015**, *5*, 12014. [CrossRef]
28. Mohammad Haniff, M.A.S.; Muhammad Hafiz, S.; Wahid, K.A.A.; Endut, Z.; Wah Lee, H.; Bien, D.C.S.; Abdul Azid, I.; Abdullah, M.Z.; Ming Huang, N.; Abdul Rahman, S. Piezoresistive effects in controllable defective HFTCVD graphene-based flexible pressure sensor. *Sci. Rep.* **2015**, *5*, 14751. [CrossRef]
29. Ma, J.; Zhang, M.; Dong, L.; Sun, Y.; Su, Y.; Xue, Z.; Di, Z. Gas sensor based on defective graphene/pristine graphene hybrid towards high sensitivity detection of NO_2. *AIP Adv.* **2019**, *9*, 75207. [CrossRef]
30. Acevedo-Del-Castillo, A.; Águila-Toledo, E.; Maldonado-Magnere, S.; Aguilar-Bolados, H. A Brief Review on the High-Energy Electromagnetic Radiation-Shielding Materials Based on Polymer Nanocomposites. *Int. J. Mol. Sci.* **2021**, *22*, 9079. [CrossRef]
31. Alexandrou, K. Ionizing Radiation Effects on Graphene Based Field Effects Transistors. Ph.D. Thesis, Columbia University, New York, NY, USA, 2016.
32. Song, W.; Lee, S.I.; Kim, Y.; Jung, D.S.; Jung, M.W.; An, K.-S.; Park, C.-Y. Effect of MeV Electron Beam Irradiation on Graphene Grown by Thermal Chemical Vapor Deposition. *Jpn. J. Appl. Phys.* **2013**, *52*, 125104. [CrossRef]
33. Lin, Y.-C.; Dumcenco, D.O.; Huang, Y.-S.; Suenaga, K. Atomic mechanism of the semiconducting-to-metallic phase transition in single-layered MoS2. *Nat. Nanotechnol.* **2014**, *9*, 391–396. [CrossRef]
34. Elibol, K.; Susi, T.; Argentero, G.; Reza Ahmadpour Monazam, M.; Pennycook, T.J.; Meyer, J.C.; Kotakoski, J. Atomic Structure of Intrinsic and Electron-Irradiation-Induced Defects in MoTe2. *Chem. Mater.* **2018**, *30*, 1230–1238. [CrossRef]
35. Köster, J.; Ghorbani-Asl, M.; Komsa, H.-P.; Lehnert, T.; Kretschmer, S.; Krasheninnikov, A.V.; Kaiser, U. Defect Agglomeration and Electron-Beam-Induced Local-Phase Transformations in Single-Layer MoTe2. *J. Phys. Chem. C* **2021**, *125*, 13601–13609. [CrossRef]
36. Kretschmer, S.; Komsa, H.-P.; Bøggild, P.; Krasheninnikov, A.V. Structural Transformations in Two-Dimensional Transition-Metal Dichalcogenide MoS2 under an Electron Beam: Insights from First-Principles Calculations. *J. Phys. Chem. Lett.* **2017**, *8*, 3061–3067. [CrossRef]
37. Rotunno, E.; Fabbri, F.; Cinquanta, E.; Kaplan, D.; Longo, M.; Lazzarini, L.; Molle, A.; Swaminathan, V.; Salviati, G. Structural, optical and compositional stability of MoS_2 multi-layer flakes under high dose electron beam irradiation. *2D Mater.* **2016**, *3*, 025024. [CrossRef]
38. Moody, G.; Tran, K.; Lu, X.; Autry, T.; Fraser, J.M.; Mirin, R.P.; Yang, L.; Li, X.; Silverman, K.L. Microsecond Valley Lifetime of Defect-Bound Excitons in Monolayer WSe_2. *Phys. Rev. Lett.* **2018**, *121*, 57403. [CrossRef] [PubMed]
39. Wu, Z.; Zhao, W.; Jiang, J.; Zheng, T.; You, Y.; Lu, J.; Ni, Z. Defect Activated Photoluminescence in WSe2 Monolayer. *J. Phys. Chem. C* **2017**, *121*, 12294–12299. [CrossRef]
40. Dash, A.K.; Swaminathan, H.; Berger, E.; Mondal, M.; Lehenkari, T.; Prasad, P.R.; Watanabe, K.; Taniguchi, T.; Komsa, H.-P.; Singh, A. Controlled defect production in monolayer MoS2 via electron irradiation at ultralow accelerating voltages. *arXiv* **2022**, arXiv:2210.04662.
41. Parto, K.; Azzam, S.I.; Banerjee, K.; Moody, G. Defect and strain engineering of monolayer WSe2 enables site-controlled single-photon emission up to 150 K. *Nat. Commun.* **2021**, *12*, 3585. [CrossRef]
42. Wu, X.; Gu, Y.; Ge, R.; Serna, M.I.; Huang, Y.; Lee, J.C.; Akinwande, D. Electron irradiation-induced defects for reliability improvement in monolayer MoS2-based conductive-point memory devices. *NPJ 2D Mater. Appl.* **2022**, *6*, 31. [CrossRef]
43. Panasci, S.E.; Alessi, A.; Buscarino, G.; Cannas, M.; Gelardi, F.M.; Schilirò, E.; Giannazzo, F.; Agnello, S. Electron Irradiation Effects on Single-Layer MoS2 Obtained by Gold-Assisted Exfoliation. *Phys. Status Solidi* **2022**, *219*, 2200096. [CrossRef]
44. Gale, A.; Li, C.; Chen, Y.; Watanabe, K.; Taniguchi, T.; Aharonovich, I.; Toth, M. Site-Specific Fabrication of Blue Quantum Emitters in Hexagonal Boron Nitride. *ACS Photonics* **2022**, *9*, 2170–2177. [CrossRef]
45. Fournier, C.; Plaud, A.; Roux, S.; Pierret, A.; Rosticher, M.; Watanabe, K.; Taniguchi, T.; Buil, S.; Quélin, X.; Barjon, J.; et al. Position-controlled quantum emitters with reproducible emission wavelength in hexagonal boron nitride. *Nat. Commun.* **2021**, *12*, 3779. [CrossRef] [PubMed]
46. Tran, T.T.; Elbadawi, C.; Totonjian, D.; Lobo, C.J.; Grosso, G.; Moon, H.; Englund, D.R.; Ford, M.J.; Aharonovich, I.; Toth, M. Robust Multicolor Single Photon Emission from Point Defects in Hexagonal Boron Nitride. *ACS Nano* **2016**, *10*, 7331–7338. [CrossRef] [PubMed]
47. Choi, S.; Tran, T.T.; Elbadawi, C.; Lobo, C.; Wang, X.; Juodkazis, S.; Seniutinas, G.; Toth, M.; Aharonovich, I. Engineering and Localization of Quantum Emitters in Large Hexagonal Boron Nitride Layers. *ACS Appl. Mater. Interfaces* **2016**, *8*, 29642–29648. [CrossRef] [PubMed]

48. Ngoc My Duong, H.; Nguyen, M.A.P.; Kianinia, M.; Ohshima, T.; Abe, H.; Watanabe, K.; Taniguchi, T.; Edgar, J.H.; Aharonovich, I.; Toth, M. Effects of High-Energy Electron Irradiation on Quantum Emitters in Hexagonal Boron Nitride. *ACS Appl. Mater. Interfaces* **2018**, *10*, 24886–24891. [CrossRef]
49. Murzakhanov, F.F.; Yavkin, B.V.; Mamin, G.V.; Orlinskii, S.B.; Mumdzhi, I.E.; Gracheva, I.N.; Gabbasov, B.F.; Smirnov, A.N.; Davydov, V.Y.; Soltamov, V.A. Creation of Negatively Charged Boron Vacancies in Hexagonal Boron Nitride Crystal by Electron Irradiation and Mechanism of Inhomogeneous Broadening of Boron Vacancy-Related Spin Resonance Lines. *Nanomaterials* **2021**, *11*, 1373. [CrossRef]
50. Bing, D.; Wang, Y.; Bai, J.; Du, R.; Wu, G.; Liu, L. Optical contrast for identifying the thickness of two-dimensional materials. *Opt. Commun.* **2018**, *406*, 128–138. [CrossRef]
51. Gorbachev, R.V.; Riaz, I.; Nair, R.R.; Jalil, R.; Britnell, L.; Belle, B.D.; Hill, E.W.; Novoselov, K.S.; Watanabe, K.; Taniguchi, T.; et al. Hunting for Monolayer Boron Nitride: Optical and Raman Signatures. *Small* **2011**, *7*, 465–468. [CrossRef]
52. Geick, R.; Perry, C.H.; Rupprecht, G. Normal Modes in Hexagonal Boron Nitride. *Phys. Rev.* **1966**, *146*, 543–547. [CrossRef]
53. Kern, G.; Kresse, G.; Hafner, J. Ab initio calculation of the lattice dynamics and phase diagram of boron nitride. *Phys. Rev. B* **1999**, *59*, 8551–8559. [CrossRef]
54. Schué, L.; Stenger, I.; Fossard, F.; Loiseau, A.; Barjon, J. Characterization methods dedicated to nanometer-thick hBN layers. *2D Mater.* **2016**, *4*, 15028. [CrossRef]
55. Ciampalini, G.; Blaga, C.V.; Tappy, N.; Pezzini, S.; Watanabe, K.; Taniguchi, T.; Bianco, F.; Roddaro, S.; Fontcuberta, I.; Morral, A.; et al. Light emission properties of mechanical exfoliation induced extended defects in hexagonal boron nitride flakes. *2D Mater.* **2022**, *9*, 35018. [CrossRef]
56. Liang, H.; Chen, Y.; Yang, C.; Watanabe, K.; Taniguchi, T.; Eda, G.; Bettiol, A.A. High Sensitivity Spin Defects in hBN Created by High-Energy He Beam Irradiation. *Adv. Opt. Mater.* **2022**, *11*, 2201941. [CrossRef]
57. Gu, R.; Wang, L.; Zhu, H.; Han, S.; Bai, Y.; Zhang, X.; Li, B.; Qin, C.; Liu, J.; Guo, G.; et al. Engineering and Microscopic Mechanism of Quantum Emitters Induced by Heavy Ions in hBN. *ACS Photonics* **2021**, *8*, 2912–2922. [CrossRef]
58. Ferrari, A.C. Raman spectroscopy of graphene and graphite: Disorder, electron–phonon coupling, doping and nonadiabatic effects. *Solid State Commun.* **2007**, *143*, 47–57. [CrossRef]
59. Ferrari, A.C.; Robertson, J. Interpretation of Raman spectra of disordered and amorphous carbon. *Phys. Rev. B* **2000**, *61*, 14095–14107. [CrossRef]
60. Abidi, I.H.; Mendelson, N.; Tran, T.T.; Tyagi, A.; Zhuang, M.; Weng, L.-T.; Özyilmaz, B.; Aharonovich, I.; Toth, M.; Luo, Z. Selective Defect Formation in Hexagonal Boron Nitride. *Adv. Opt. Mater.* **2019**, *7*, 1900397. [CrossRef]
61. Feng, J.; Deschout, H.; Caneva, S.; Hofmann, S.; Lončarić, I.; Lazić, P.; Radenovic, A. Imaging of Optically Active Defects with Nanometer Resolution. *Nano Lett.* **2018**, *18*, 1739–1744. [CrossRef]
62. Curie, D.; Krogel, J.T.; Cavar, L.; Solanki, A.; Upadhyaya, P.; Li, T.; Pai, Y.-Y.; Chilcote, M.; Iyer, V.; Puretzky, A.; et al. Correlative Nanoscale Imaging of Strained hBN Spin Defects. *ACS Appl. Mater. Interfaces* **2022**, *14*, 41361–41368. [CrossRef] [PubMed]
63. Kozawa, D.; Rajan, A.G.; Li, S.X.; Ichihara, T.; Koman, V.B.; Zeng, Y.; Kuehne, M.; Iyemperumal, S.K.; Silmore, K.S.; Parviz, D. Observation and spectral assignment of a family of hexagonal boron nitride lattice defects. *arXiv* **2019**, arXiv:1909.11738.
64. Weston, L.; Wickramaratne, D.; Mackoit, M.; Alkauskas, A.; Van de Walle, C.G. Native point defects and impurities in hexagonal boron nitride. *Phys. Rev. B* **2018**, *97*, 214104. [CrossRef]
65. Jaffrennou, P.; Barjon, J.; Lauret, J.-S.; Attal-Trétout, B.; Ducastelle, F.; Loiseau, A. Origin of the excitonic recombinations in hexagonal boron nitride by spatially resolved cathodoluminescence spectroscopy. *J. Appl. Phys.* **2007**, *102*, 116102. [CrossRef]
66. Komsa, H.-P.; Kurasch, S.; Lehtinen, O.; Kaiser, U.; Krasheninnikov, A.V. From point to extended defects in two-dimensional MoS_2: Evolution of atomic structure under electron irradiation. *Phys. Rev. B* **2013**, *88*, 35301. [CrossRef]
67. Proscia, N.V.; Shotan, Z.; Jayakumar, H.; Reddy, P.; Cohen, C.; Dollar, M.; Alkauskas, A.; Doherty, M.; Meriles, C.A.; Menon, V.M. Near-deterministic activation of room-temperature quantum emitters in hexagonal boron nitride. *Optica* **2018**, *5*, 1128–1134. [CrossRef]
68. Kotakoski, J.; Jin, C.H.; Lehtinen, O.; Suenaga, K.; Krasheninnikov, A.V. Electron knock-on damage in hexagonal boron nitride monolayers. *Phys. Rev. B* **2010**, *82*, 113404. [CrossRef]
69. Walker II, R.C.; Shi, T.; Silva, E.C.; Jovanovic, I.; Robinson, J.A. Radiation effects on two-dimensional materials. *Phys. status solidi* **2016**, *213*, 3065–3077. [CrossRef]
70. Schindler, S.; Vollnhals, F.; Halbig, C.E.; Marbach, H.; Steinrück, H.-P.; Papp, C.; Eigler, S. Focused electron beam based direct-write fabrication of graphene and amorphous carbon from oxo-functionalized graphene on silicon dioxide. *Phys. Chem. Chem. Phys.* **2017**, *19*, 2683–2686. [CrossRef]
71. Collot, P.; Gautherin, G.; Agius, B.; Rigo, S.; Rochet, F. Low-pressure oxidation of silicon stimulated by low-energy electron bombardment. *Philos. Mag. B* **1985**, *52*, 1051–1069. [CrossRef]
72. Wei, X.; Tang, D.-M.; Chen, Q.; Bando, Y.; Golberg, D. Local Coulomb Explosion of Boron Nitride Nanotubes under Electron Beam Irradiation. *ACS Nano* **2013**, *7*, 3491–3497. [CrossRef]
73. Kretschmer, S.; Lehnert, T.; Kaiser, U.; Krasheninnikov, A.V. Formation of Defects in Two-Dimensional MoS2 in the Transmission Electron Microscope at Electron Energies below the Knock-on Threshold: The Role of Electronic Excitations. *Nano Lett.* **2020**, *20*, 2865–2870. [CrossRef] [PubMed]

74. Ghaderzadeh, S.; Kretschmer, S.; Ghorbani-Asl, M.; Hlawacek, G.; Krasheninnikov, A.V. Atomistic Simulations of Defect Production in Monolayer and Bulk Hexagonal Boron Nitride under Low- and High-Fluence Ion Irradiation. *Nanomaterials* **2021**, *11*, 1214. [CrossRef]
75. Weber, J.; Schmid, W.; Sauer, R. Localized exciton bound to an isoelectronic trap in silicon. *Phys. Rev. B* **1980**, *21*, 2401–2414. [CrossRef]
76. Scarangella, A.; Fabbri, F.; Reitano, R.; Rossi, F.; Priolo, F.; Miritello, M. Visible emission from bismuthdoped yttrium oxide thin films for lighting and display applications. *Sci. Rep.* **2017**, *7*, 17325. [CrossRef]
77. Zacks, E.; Halperin, A. Dependence of the Peak Energy of the Pair-Photoluminescence Band on Excitation Intensity. *Phys. Rev. B* **1972**, *6*, 3072–3075. [CrossRef]
78. Maharjan, N.; Joshi, P.; Rai, R.C.; Nakarmi, M.L. Atomic-like emissions in UV region from hexagonal boron nitride crystal powders. *J. Lumin.* **2021**, *234*, 117944. [CrossRef]

Disclaimer/Publisher's Note: The statements, opinions and data contained in all publications are solely those of the individual author(s) and contributor(s) and not of MDPI and/or the editor(s). MDPI and/or the editor(s) disclaim responsibility for any injury to people or property resulting from any ideas, methods, instructions or products referred to in the content.

Check for updates

ADVANCED QUANTUM TECHNOLOGIES
www.advquantumtech.com

Efficiency Optimization of Ge-V Quantum Emitters in Single-Crystal Diamond upon Ion Implantation and HPHT Annealing

*Elena Nieto Hernández, Elisa Redolfi, Claudia Stella, Greta Andrini, Emilio Corte, Selene Sachero, Sviatoslav Ditalia Tchernij, Fabio Picariello, Tobias Herzig, Yuri M. Borzdov, Igor N. Kupriyanov, Alexander Kubanek, Paolo Olivero, Jan Meijer, Paolo Traina, Yuri N. Palyanov, and Jacopo Forneris**

The authors report on the characterization at the single-defect level of germanium-vacancy (GeV) centers in diamond produced upon Ge^- ion implantation and different subsequent annealing processes, with a specific focus on the effect of high-pressure-high-temperature (HPHT) processing on their quantum-optical properties. Different post-implantation annealing conditions are explored for the optimal activation of GeV centers, namely, 900 °C 2 h, 1000 °C 10 h, 1500 °C 1 h under high vacuum, and 2000 °C 15 min at 6 GPa pressure. A systematic analysis of the relevant emission properties, including the emission intensity in saturation regime and the excited state radiative lifetime, is performed on the basis of a set of ion-implanted samples, with the scope of identifying the most suitable conditions for the creation of GeV centers with optimal quantum-optical emission properties. The main performance parameter adopted here to describe the excitation efficiency of GeV centers as single-photon emitters is the ratio between the saturation optical excitation power and the emission intensity at saturation. The results show an up to eightfold emission efficiency increase in HPHT-treated samples with respect to conventional annealing in vacuum conditions, suggesting a suitable thermodynamic pathway toward the repeatable fabrication of ultra-bright GeV centers for single-photon generation purposes.

1. Introduction

Color centers in diamond represent an emerging class of solid-state systems for single-photon emission,[1–8] with appealing applications in quantum-enhanced technologies, including quantum information processing and quantum sensing.[9–18] Among them, point-defects related to group-IV impurities have displayed promising properties in terms of high photon emission rate, relatively narrow spectral signatures, and spin-dependent emission properties.[19–26]

The identification of reliable pathways toward their reproducible fabrication is therefore crucial for a widespread adoption of these systems. The most convenient method to date is represented by the fabrication by ion implantation and subsequent high-temperature annealing, which enables in perspective the control on both the position and the number of individual emitters on a diamond chip.[19,27–29] It is therefore

E. Nieto Hernández, E. Redolfi, C. Stella, E. Corte, S. Ditalia Tchernij, P. Olivero, J. Forneris
Department of Physics
University of Torino
Torino 10125, Italy
E-mail: jacopo.forneris@unito.it

E. Nieto Hernández, E. Redolfi, G. Andrini, E. Corte, S. Ditalia Tchernij, P. Olivero, J. Forneris
Istituto Nazionale di Fisica Nucleare (INFN)
sezione di Torino
Torino 10125, Italy

The ORCID identification number(s) for the author(s) of this article can be found under https://doi.org/10.1002/qute.202300010

© 2023 The Authors. Advanced Quantum Technologies published by Wiley-VCH GmbH. This is an open access article under the terms of the Creative Commons Attribution License, which permits use, distribution and reproduction in any medium, provided the original work is properly cited.

DOI: 10.1002/qute.202300010

C. Stella, S. Ditalia Tchernij, F. Picariello, P. Olivero, P. Traina, J. Forneris
Istituto Nazionale di Ricerca Metrologica (INRiM)
Torino 10135, Italy

G. Andrini
Department of Electronics and Communications
Politecnico di Torino
Torino 10129, Italy

S. Sachero, A. Kubanek
Institute for Quantum Optics
Universität Ulm
D-89069 Ulm, Germany

T. Herzig, J. Meijer
Applied Quantum Systems, Felix-Bloch Institute for Solid-State Physics
Universität Leipzig
04103 Leipzig, Germany

Y. M. Borzdov, I. N. Kupriyanov, Y. N. Palyanov
V.S. Sobolev Institute of Geology and Mineralogy
Siberian Branch of the Russian Academy of Sciences
Academician Koptyug Ave., 3, Novosibirsk 630090, Russian Federation

crucial to define optimal post-implantation processing schemes, thus ensuring both the efficient formation of optically active color centers upon the implantation of individual ions[29–31] and guaranteeing optimal photon emission properties.[32,33]

One of the most significant limitations toward the reliable fabrication of group-IV-related emitters lies in the sub-optimal incorporation of atomically large impurities in the highly dense host diamond crystal upon irradiation at keV energies, which results in substantial lattice distortions[34,35] and residual radiation damage[36,37] affecting their emission properties, despite the adoption of annealing post-implantation processes up to 1200 °C temperature. A possible solution has been hinted for SnV and PbV centers by the adoption of high-pressure high-temperature (HPHT) post-implantation annealing. In these systems, treatments at 2100 °C temperature and 7.7 GPa pressure in keV-ion-implanted diamond which resulted in improved spectral emission properties and reduced contributions from competing impurity-related defect configurations.[3,38] Nevertheless, a systematic comparison of the effects on the single-photon emission properties of HPHT treatment with respect to conventional annealing processes has not been performed to date in the scientific literature. This work addresses this investigation on the group-IV-related germanium-divacancy complex (GeV center).[5,29,35] An emphasis is given toward the physical parameters needed to maximize the emission efficiency, in terms of optical excitation power and emission intensity, in order to optimize the throughput of generated photons with a minimal excitation energy.

2. Experimental and Results

2.1. Samples Preparation

The experiments were performed on three single-crystal type-IIa diamond samples supplied by ElementSix. Samples #1 and #2 were consisted of $2 \times 2 \times 0.5$ mm^3 "electronic grade" quality substrates, characterized by <5 ppb substitutional N and B concentrations. Sample #3 was consisted of a $3 \times 3 \times 0.3$ mm^3 "optical grade" substrate with nominal substitutional concentrations of $N_S < 1$ ppm and $B_S < 0.05$ ppm. Samples were implanted with 40 keV Ge^--ions at the low energy accelerator of the University of Leipzig. Several regions of $\approx 200 \times 200$ μm^2 area were implanted at fluences in the 10^{10}–10^{13} cm^{-2} range by means of a collimating mask. Generally, the fluence values were too high to enable a direct investigation of GeV centers at the single-emitter level within the implantation regions. Therefore, the analysis was carried in correspondence of the outer edges of the implanted regions, where individual color centers were formed due to the implantation of stray ions upon scattering with the collimating mask. No noticeable statistical differences were observed in the emission parameters of single GeV centers at the outer edges of regions implanted at different fluences. Sample #1 underwent two subsequent post-implantation annealing processes in vacuum (i.e., at pressures $<5 \times 10^{-6}$ mbar), namely, 900 °C (2 h duration), 1000 °C (10 h duration). Sample #2 was processed at 1500 °C for 1 h in vacuum. Sample #3 underwent an annealing treatment at 950 °C (after which no individual GeV centers could be isolated due to the intense background emission of native NV centers), followed by a 15 min annealing performed at 2000 °C under 6 GPa pressure for 15 min (referred to as "HPHT annealing" in the following).

2.2. Effects of HPHT Annealing

The HPHT treatment was performed at the IGM SB RAS (Novosibirsk) under a stabilizing pressure of about 6 GPa via a split-sphere multi-anvil apparatus (BARS).[39] Cesium chloride (CsCl) was used as pressure transmitting medium, providing quasi-hydrostatic conditions of annealing. The sample was annealed at ≈2000 °C for 15 min. As an increase of surface roughness was expected on the basis shown of previous studies on HPHT annealing of different classes of emitters,[40] a morphological assessment of the sample surface was performed by means of scanning electron microscope (SEM) imaging. The SEM map acquired from Sample #1 following 950 °C thermal annealing is shown in **Figure 1**a, to be compared with the morphology of Sample #3 surface upon HPHT annealing (Figure 1b). Sample #3 exhibits an inhomogenous increase in the surface roughness of the sample, denoted by both the growth of μm-sized seeds due to the HPHT conversion to diamond, to a much lesser extent, high-temperature-induced surface etching, indicating that the processing parameters for the HPHT annealing still require some optimization. Nevertheless, the confocal photoluminescence (PL) maps acquired from Sample #3 (Figure 1c) in the outer region of a Ge-implanted area are comparable with those obtained from Sample #1 (Figure 1d) and Sample #2. It can thus be concluded that increased surface roughness induced by the HPHT treatment did not hinder the formation of stable single-photon emitters.

The HPHT process outcome was monitored by comparing PL ensemble spectra acquired at liquid nitrogen temperature from the region implanted at 3×10^{12} cm^{-2} fluence before and after the treatment using a custom-built setup based on a Horiba JY iHR320 monochromator equipped with a Syncerity CCD detector. **Figure 2** shows the PL spectra acquired under 395 nm (Figure 2a) and 532 nm (Figure 2b) excitations, both before and after processing. Prior to the HPHT process, the spectra (black lines) are dominated by native NV centers emission with zero-phonon lines (ZPLs) at 575 and 637 nm,[41] whose intensity is significantly higher than that of the GeV centers (ZPL at 602 nm[5,13]). In addition, an emission band characterized by a ZPL at 467.7 nm (2.65 eV) and phonon replicas with 73 meV energy was observed in the spectrum excited with 395 nm, which is tentatively attributed to intrinsic vacancy-related defects.[42] Following the HPHT treatment, the PL spectra recorded from the same region (red line in Figure 2a,b) showed the complete disappearance of both the 467.7 nm feature and the NV-center-related emissions. This result is line with previous reports indicating the disaggregation of the NV and 467.7 nm centers at temperatures 1500–1700[43,44] and ≈1900 °C,[42] respectively. Consequently, the GeV center appears as the dominant PL feature after HPHT annealing. Furthermore, its relative intensity with respect to the first-order diamond Raman line appears significantly increased.

© 2023 The Authors. Advanced Quantum Technologies published by Wiley-VCH GmbH

25119044, 2023, 8, Downloaded from https://onlinelibrary.wiley.com/doi/10.1002/qute.202300010 by Universita Di Torino, Wiley Online Library on [13/05/2024]. See the Terms and Conditions (https://onlinelibrary.wiley.com/terms-and-conditions) on Wiley Online Library for rules of use; OA articles are governed by the applicable Creative Commons License

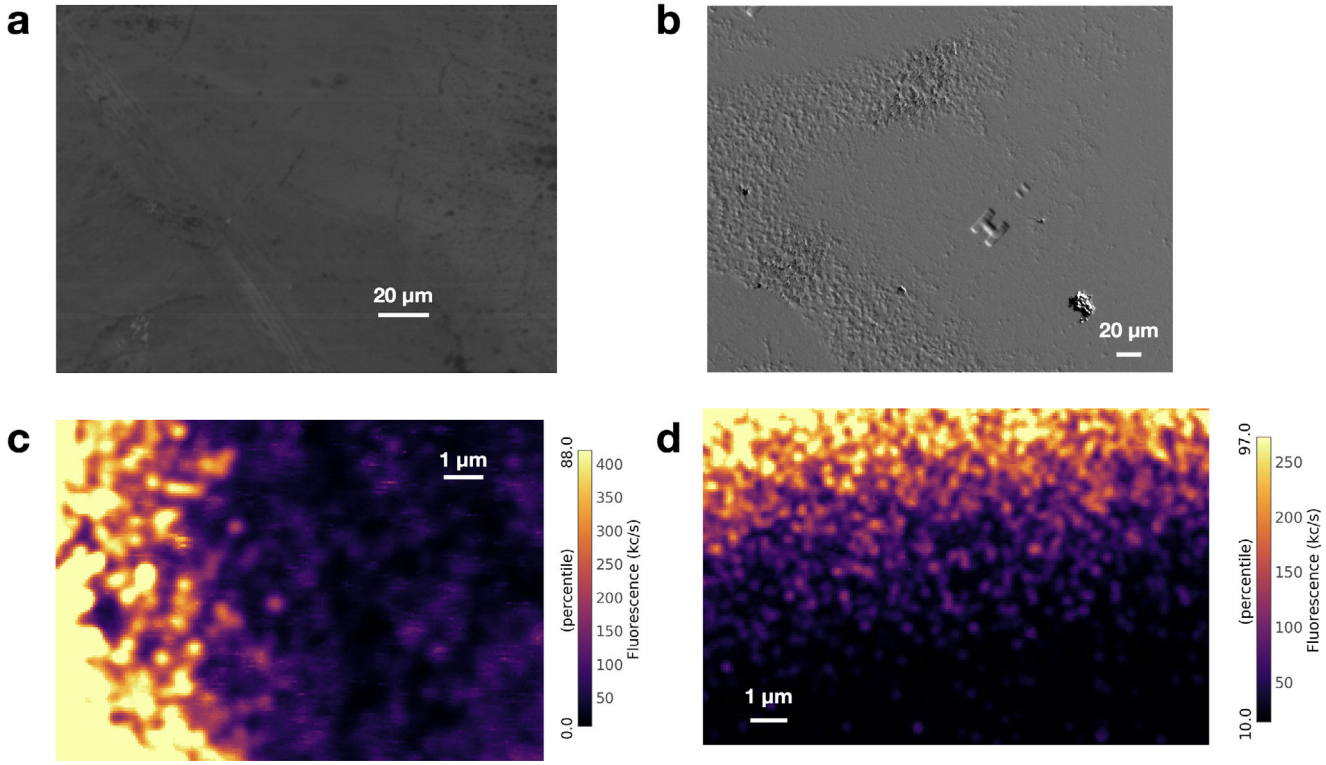


Figure 1. SEM image of the a) Sample #1 following 950 °C annealing in vacuum and b) Sample #3 after the HPHT treatment. The reference "H" marker at the center of the image was fabricated by focused-ion-beam milling prior to HPHT annealing. PL confocal microscopy map of the outer edge of a region implanted with 40 keV Ge^- ions on c) Sample #3 and d) Sample #1.

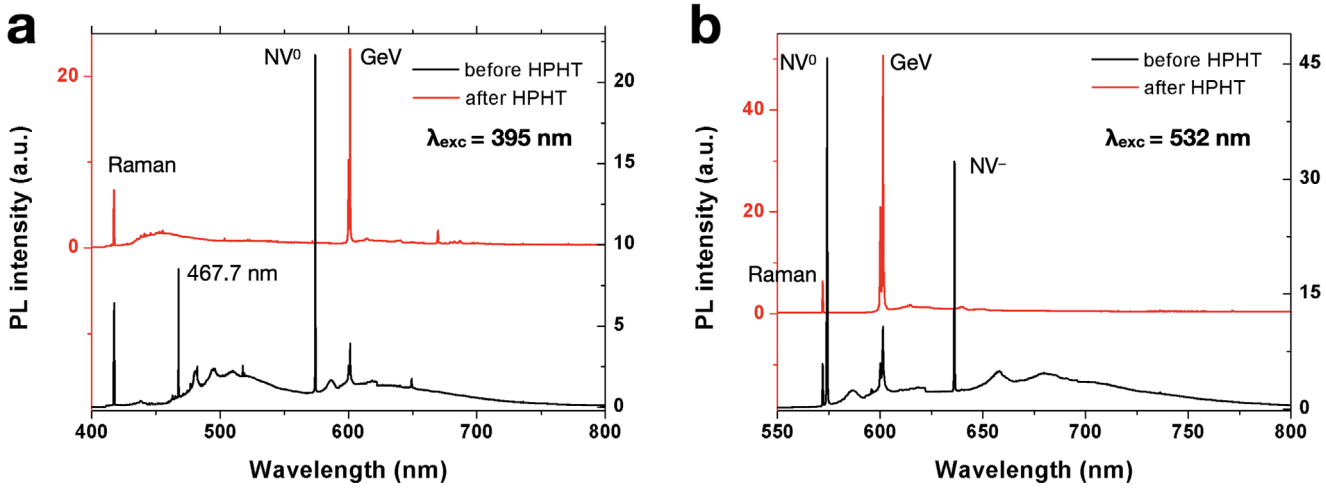


Figure 2. PL spectra acquired from Sample #3 under a) 395 and b) 532 nm CW laser excitation before (black line) and after (red line) HPHT annealing.

2.3. Single-Photon PL Emission Characterization

Each of the above-described treatments was followed by a systematic characterization at the single-photon emitter level in PL regime. The analysis was performed using a custom fiber-coupled single-photon-sensitive custom confocal microscope (100× air objective, 0.9 NA) under 520 nm CW laser excitation. A dichroic mirror and a set of optical filters ensured the detection of >550 nm wavelengths. The PL spectra were acquired with a single grating monochromator (1200 grooves mm^{-1}, 600 nm blaze, ≈4 nm spectral resolution) out-coupled via multimode fibers to a single photon avalanche diode (SPAD). The confocal microscope was equipped with a Hanbury-Brown and Twiss (HBT) interferometer, allowing the experimental characterization of single-photon emitters via the analysis of the second-order autocorrelation function.[1] The HBT interferometer was implemented by

© 2023 The Authors. Advanced Quantum Technologies published by Wiley-VCH GmbH

25119044, 2023, 8, Downloaded from https://onlinelibrary.wiley.com/doi/10.1002/qute.202300010 by Universita Di Torino, Wiley Online Library on [13/05/2024]. See the Terms and Conditions (https://onlinelibrary.wiley.com/terms-and-conditions) on Wiley Online Library for rules of use; OA articles are governed by the applicable Creative Commons License

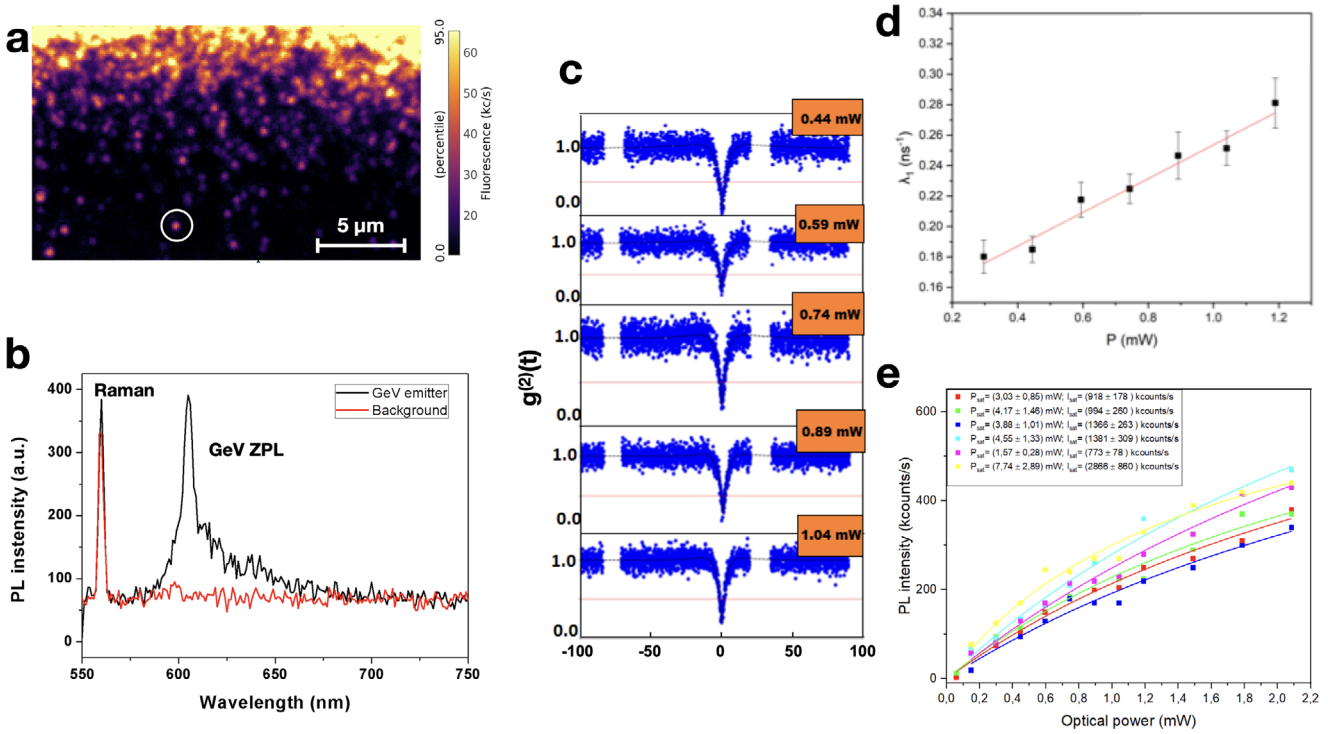


Figure 3. Exemplary steps in the systematic analysis of individual GeV centers formed by ion implantation and annealing. a) PL map of the outer edge of a region implanted with 40 keV Ge-ions and annealed at 900 °C for 2 h in vacuum. b) PL spectrum acquired under 520 nm CW laser excitation from the diffraction-limited spot (black line) circled in white in Figure 2a and from a pristine region of the sample (red line). c) Second-order autocorrelation chronograms acquired from the same spot under 0.44, 0.59, 0.74, 0.89, and 1.04 mW excitation powers. The dashed black lines indicate the fitting curves based on a three-level model. c) Linear regression of the λ_1 fitting parameter as a function of the optical excitation power. d) Intensity saturation curves of six individual GeV centers acquired from Sample #1.

a fiber-fused 50:50 beamsplitter connected to two independent SPADs.[45]

An assessment of the dependence of the emission properties of the GeV centers from the post-implantation treatment was then performed by means of a systematic study at the single-photon emitter level. The study was based on the following sampling: 15 GeV centers in Sample #1 following both the 900 and 1000 °C annealing in vacuum; 13 GeV centers in Sample #2 following the 1500 °C treatment in vacuum; 15 centers in Sample #3 following the HPHT process. The adopted experimental approach was the following for all the considered annealing conditions. First, PL mapping was performed to identify bright emission spots as potential single-photon emitters. **Figure 3**a shows an exemplary PL map acquired from the outer edge of a region of Sample #1 implanted at 3×10^{12} cm^{-2} fluence and subsequently annealed at 900 °C for 2 h in vacuum conditions. The color scale encodes the PL intensity value, in kcounts per second (kcps). The upper part of the map, corresponding to higher PL counts, is closer (i.e., few µm) to the edge of the implanted region and is thus denoted by a higher concentration of GeV centers. The spatial gradient toward lower PL intensity at increasing distance from the implanted region enables the identification of individual diffraction-limited spots, each of which potentially corresponds to an individual to single GeV emitters. Each emitting spot was characterized by PL spectroscopy to verify the occurrence of the GeV spectral fingerprint at 602 nm. Figure 3b shows as an example the typical emission spectrum (black line) observed from the spot highlighted by a white circle in Figure 3a at an excitation power of 0.6 mW, to be compared with the background spectrum acquired from a pristine region of the same sample (red line). The verification of the occurrence of individual GeV emitters was then validated by analyzing the background-subtracted HBT interferograms acquired under different excitation powers (Figure 3c).

The second-order autocorrelation chronograms were fitted according to the three-level system expression[46]

$$g^{(2)}(t) = 1 - A_1 \cdot \exp\left(-\lambda_1 |t|\right) + A_2 \cdot \exp\left(-\lambda_2 |t|\right) \quad (1)$$

where the A_1 parameter provides an estimate of the antibunching effect at $t = 0$ delay, and the λ_1 parameter (i.e., the reciprocal of the characteristic time constant) depends on the optical excitation power P through a linear coefficient α

$$\lambda_1 = \lambda_1(P) = \alpha \cdot P + \tau^{-1} \quad (2)$$

The study of the power-dependence of the A_2 and λ_2 parameters related to the system's shelving state was beyond the scope of this work, due to the overall weak bunching effect observed in all the considered emitters. The observation of a $g^{(2)}(t = 0)$ value well below (i.e., an A_1 parameter well above) 0.5 was adopted as the criterion to assess a single-photon emission from the considered diffraction-limited spot. The acquired second-order autocorrelation chronograms were also adopted to gain information on

© 2023 The Authors. Advanced Quantum Technologies published by Wiley-VCH GmbH

25119044, 2023, 8, Downloaded from https://onlinelibrary.wiley.com/doi/10.1002/qute.202300010 by Universita Di Torino, Wiley Online Library on [13/05/2024]. See the Terms and Conditions (https://onlinelibrary.wiley.com/terms-and-conditions) on Wiley Online Library for rules of use; OA articles are governed by the applicable Creative Commons License

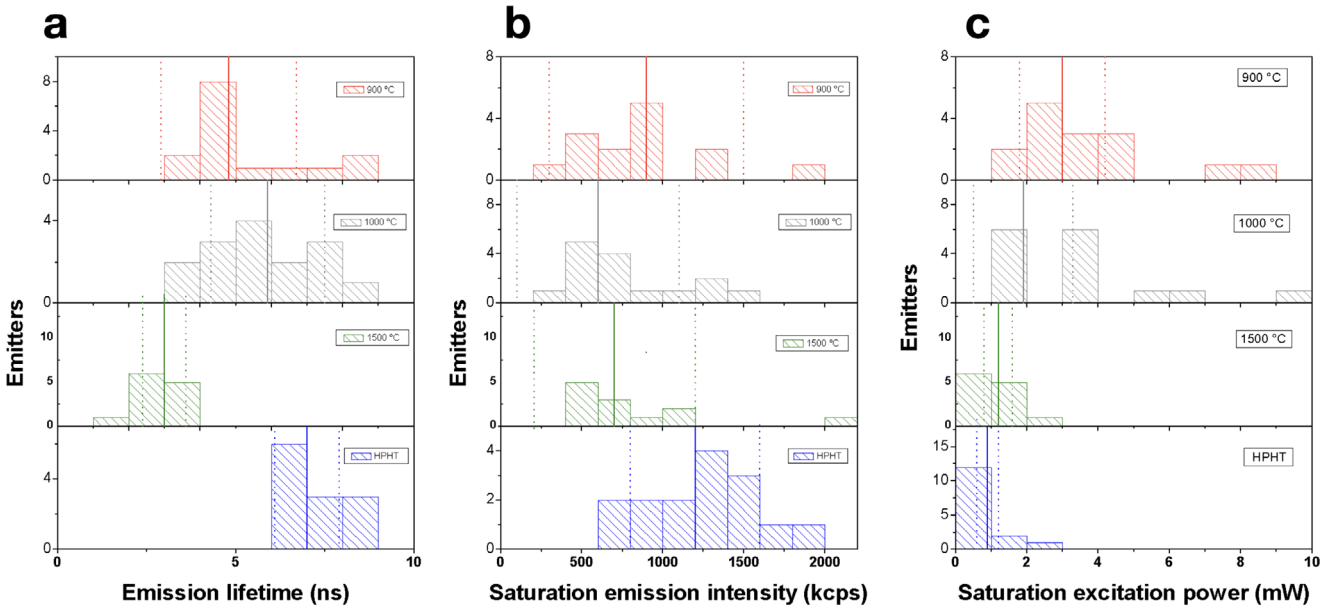


Figure 4. Histograms of the occurrence of a) emission lifetime, b) saturation emission intensity, and c) saturation excitation power, among a set of 57 single-photon emitters grouped by post-implantation annealing treatment. The color codes the different annealing temperatures (red: 900 °C, gray: 1000 °C, green: 1500 °C, blue: HPHT treatment). The vertical continuous lines indicate the median value of each distribution. The dashed lines indicate the standard deviation as evaluated by the Q3−Q1 interquartile assuming a normal distribution.

Table 1. Table of the median values of excited state lifetime, emission intensity at saturation, and optical excitation power at saturation extracted from the analysis of the histograms in Figure 4.

Post-implantation treatment	Crystal quality	Median excited state radiative lifetime [ns]	Emission intensity at saturation [kcps]	Optical excitation power at saturation [mW]
900 °C 2 h	Electronic grade	4.8 ± 1.9	900 ± 600	3.0 ± 1.2
1000 °C 10 h	Electronic grade	5.9 ± 1.6	600 ± 500	3.1 ± 1.4
1500 °C 1 h	Electronic grade	3.0 ± 0.6	650 ± 350	1.2 ± 0.5
HPHT (2000 °C, 6 GPa)	Optical grade	7.0 ± 0.9	1200 ± 400	0.9 ± 0.3

the lifetime τ of the excited state of each GeV center through a linear regression of the (λ vs P) curve (Figure 3d) according to the relation $\tau = \lambda_1(P = 0)^{-1}$. As an example, Figure 3d shows the linear regression corresponding to the dataset reported in Figure 3c. Finally, the intensity saturation emission of individual GeV centers was determined by measuring the PL count rate I as a function of the excitation optical power, upon subtraction of the background count rate acquired from an unimplanted region. Figure 3d shows exemplary families of intensity saturation curves acquired from a set of individual GeV centers on Sample #1 following 900 °C annealing. All curves acquired from individual emitters were fitted according to the saturation model[2,29]

$$I(P) = I_{sat} \cdot P / (P + P_{sat}) \quad (3)$$

where I_{sat} and P_{sat} are the emission intensity and optical power at saturation, respectively. The above-described characterization method was applied to investigate the statistical distribution of the key parameters for single-photon emission (**Figure 4**): excited state radiative lifetime (Figure 4a), emission intensity at saturation (Figure 4b), and saturation excitation optical power (Figure 4c). The figures show the histograms of each parameter for the four considered annealing processes. The median value of the distribution is superimposed to each histogram (continuous vertical line) together with the standard deviation (dashed lines), as derived from the Q3−Q1 interquartile difference, by assuming a normal distribution. These values are also reported in **Table 1**.

The statistical distribution of the emitters lifetime values (Figure 4a) did not highlight an apparent trend as a function of the considered annealing process. The median values for the 900 and 100 °C processes (i.e., 4.8 ± 1.9 and 5.9 ± 1.6 ns, respectively) are compatible with the results achieved both from the samples treated with the 1500 °C temperature (3.0 ± 0.6 ns) and HPHT (7.0 ± 0.9 ns) processes. Conversely, the latter two are not mutually compatible. The lifetime median values measured for the HPHT-treated crystal are compatible with those observed at the lowest annealing temperatures. This observation suggests that the adoption of an "optical grade" sample does not provide an environment-dependent modification (e.g., unintentional doping due to higher N contents of Sample #3) of the GeV emission properties with respect to "electronic grade" diamond. As a consequence, the HPHT treatment enables the utilization of cheaper material substrates for GeV-based technological applications. While such consideration is further supported (see below)

© 2023 The Authors. Advanced Quantum Technologies published by Wiley-VCH GmbH

25119044, 2023, 8, Downloaded from https://onlinelibrary.wiley.com/doi/10.1002/qute.202300010 by Universita Di Torino, Wiley Online Library on [13/05/2024]. See the Terms and Conditions (https://onlinelibrary.wiley.com/terms-and-conditions) on Wiley Online Library for rules of use; OA articles are governed by the applicable Creative Commons License

by the enhancement in the emission efficiency of the GeV defect upon HPHT annealing, the technological perspective of this method will depend on the assessment of spectral diffusion associated with the residual density of the optically inactive impurities and defects typically present in a lower grade crystal.

To the best of our knowledge, a systematic assessment of the GeV emission lifetime based on a statistical analysis of emitters has not been performed prior to this work. Indeed, the lifetime values reported in literature cover a 1.4–6.6 ns range on the basis of previous reports on a limited numbers of probed individual GeV centers.[24,29]

Concerning the emission intensity at saturation, the median I_{sat} values obtained for the four different annealing conditions (respectively: 900 ± 600, 600 ± 500, 650 ± 350, and 1200 ± 400 kcps) are fully compatible. This is however the net result of the fact that the 900 and 1000 °C processes lead to a wide variability in the I_{sat} parameter. It is worth noting that the >600 kcps values reported for each of these datasets represent an appealing experimental evidence of the very promising quantum-optical performance of this system, particularly if compared with the results of previous room-temperature characterization (i.e., in the 178 ± 4 to 790 ± 20 kcps range[24,29]). Incidentally, several individual emitters exceeding 1 Mcps emission rates were identified in previous works, which could be partially explained assuming different detection efficiencies for the adopted experimental setup. While the overall data variability did not enable to identify any significant trend as a function of the annealing temperature, it is worth mentioning that 60% of the emitters studied in the HPHT-treated sample exhibited >1 Mcps intensity at saturation, suggesting a substantial positive effect of the process on the opto-physical properties of the GeV center.

The statistical distribution of the observed optical excitation powers at saturation is summarized in Figure 4c. Similarly to lifetime and emission intensity parameters, the data do not provide strong evidence of significant differences in the P_{sat} parameter for the 900 °C (3.0 ± 1.2 mW) and 1000 °C (3.1 ± 1.4 mW) annealing processes. These results are also consistent with previous reports on individual emitters, with excitation powers at saturation in the 4.5–4.7 mW range for annealing at 1000–1200 °C temperatures.[24,29] Remarkably, the saturation power is considerably reduced when the annealing temperature increases to 1500 °C (1.2 ± 0.5 mW), and it is further decreased to 0.9 ± 0.3 mW upon HPHT treatment. This observation is in line with a recently proposed model for group-IV impurities in diamond[47] relating the charge state stability with the concentration of surrounding lattice divacancies. Divacancy are introduced in the diamond lattice as a byproduct of the ion implantation process performed to fabricate GeV centers. Although divacancies are still present in HPHT-treated diamonds, the high-pressure annealing is reported to efficiently promote the disaggregation of such defects even for short processes.[48] If the divacancy is identified as the optically inactive defect interfering with the charge stability of the GeV center, then its disaggregation upon HPHT annealing could be regarded as the origin of the improved emission efficiency of the latter.

The overall performance of GeV centers as single-photon emitters can be parametrized by considering the ratio between the saturation optical excitation power and the emission intensity at saturation, $E_{sat} = P_{sat}/I_{sat}$. This parameter, which is inversely proportional to the system quantum efficiency, can be regarded as an indicator of the effectiveness in the optical excitation and radiative response of the system. Lower values of E_{sat} indicate lower energy requested for single-photon emission, and thus a higher efficiency in the excitation–emission process. The achievement of low E_{sat} values is therefore a key requisite to enhance emission intensity with minimal optical power consumption, thus enabling ultra-bright emission from individual GeV centers. The same goal also offers to simultaneously address arrays of individual emitters (e.g., embedded in integrated photonic structures[49]) by using a single excitation source with modest optical output, thus minimizing heat dissipation and reducing the constraints on the device design. **Figure 5** shows box chart plots summarizing the distributions of the parameter evaluated for the populations of emitters under investigation. The decreasing trend of E_{sat} at increasing annealing temperatures is apparent, as the 1500 °C (1.5 ± 0.3 μJ kcps^{-1}) and the HPHT (0.5 ± 0.3 μJ kcps^{-1}) treatments lead to ×2.6 and ×7.8 increase with respect to the 900 °C annealing process (3.9 ± 1.6 μJ kcps^{-1}), respectively.

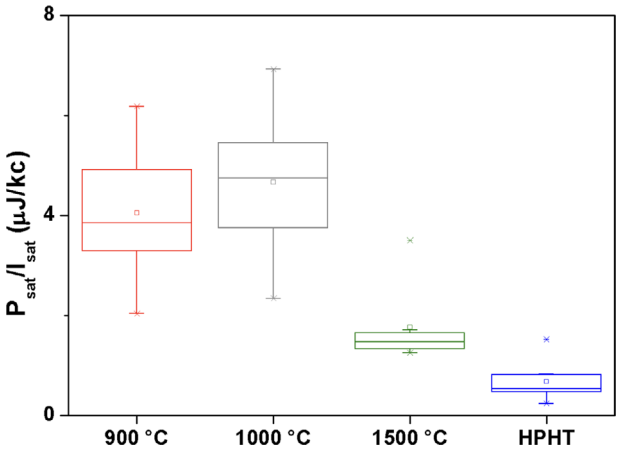


Figure 5. Box chart of the P_{sat}/I_{sat} ratio extracted for different post-implantation annealing processes.

3. Conclusions

We reported on a systematic investigation of the main emission parameters (namely, excited state radiative lifetime, saturation excitation power, and emission intensity at saturation) of GeV centers fabricated in diamond upon implantation following different annealing conditions. Our results show a significant trend toward lower optical excitation powers at increasing annealing temperatures. This result likely corresponds to an increase in the emission intensity, although the rather large variability in the data did not enable the identification of an unambiguous trend in such parameter. The overall effectiveness of the excitation and emission processes is described by the ratio between emission intensity and optical excitation power at saturation, which exhibits an eightfold improvement for the HPHT-treated sample with respect to conventional thermal annealing at 900–1000 °C in vacuum conditions. This remarkable increase in the single-photon source efficiency can be potentially extended to other classes of quantum emitters in diamond[3,4,45] and in other host material platforms.[50,51] It suggests an effective and highly controllable

© 2023 The Authors. Advanced Quantum Technologies published by Wiley-VCH GmbH

25119044, 2023, 8, Downloaded from https://onlinelibrary.wiley.com/doi/10.1002/qute.202300010 by Universita Di Torino, Wiley Online Library on [13/05/2024]. See the Terms and Conditions (https://onlinelibrary.wiley.com/terms-and-conditions) on Wiley Online Library for rules of use; OA articles are governed by the applicable Creative Commons License

processing route on the road toward the creation of ultra-bright GeV centers with optimal emission properties for single-photon generation purposes and quantum technology applications. The results obtained are significant both at the individual emitter level and for the parallel excitation of multiple sources in integrated devices for quantum information processing[45,52,53] and metrology.[54,55]

Acknowledgements

This work was supported by the following projects: "Intelligent fabrication of QUANTum devices in DIAmond by Laser and Ion Irradiation" (QuantDia) project funded by the Italian Ministry for Instruction, University and Research within the "FISR 2019" program; "Training on LASer fabrication and ION implantation of DEFects as quantum emitters" (LasIonDef) project funded by the European Research Council under the "Marie Skłodowska-Curie Innovative Training Networks" program; experiments ROUGE and PICS4ME, funded by the 5th National Commission of the Italian National Institute for Nuclear Physics (INFN); Project "Piemonte Quantum Enabling Technologies" (PiQuET), funded by the Piemonte Region within the "Infra-P" scheme (POR-FESR 2014–2020 program of the European Union); "Departments of Excellence" (L. 232/2016), funded by the Italian Ministry of Education, University and Research (MIUR); "Ex post funding of research – 2021" of the University of Torino funded by the "Compagnia di San Paolo." Y.M.B., I.N.K., and Y.N.P. acknowledge the IGM SB RAS assignment project no. 122041400159-3. The projects 20IND05 (QADeT) and 20FUN05 (SEQUME) and 20FUN02 (PoLight) leading to this publication have received funding from the EMPIR programme co-financed by the Participating States and from the European Union's Horizon 2020 research and innovation programme. The work of E.R. was supported by the European Union – Next Generation EU Programme. S.DT. gratefully acknowledge the support of the "Azione IV.6" program of "PON Ricerca e Innovazione 2014–2020" funding scheme of the Italian National Ministry of University and Research.

Conflict of Interest

The authors declare no conflict of interest.

Data Availability Statement

The data that support the findings of this study are available from the corresponding author upon reasonable request.

Keywords

annealing, brightness, high-pressure high-temperature (HPHT), ion implantation, single-photon source

Received: January 12, 2023
Revised: May 3, 2023
Published online: June 19, 2023

[1] R. Brouri, A. Beveratos, J. Poizat, P. Grangier, *Opt. Lett.* **2000**, *25*, 1294.
[2] C. Wang, C. Kurtsiefer, H. Weinfurter, B. Burchard, *J. Phys. B* **2006**, *39*, 37.
[3] T. Iwasaki, Y. Miyamoto, T. Taniguchi, P. Siyushev, M H. Metsch, F. Jelezko, M. Hatano, *Phys. Rev. Lett.* **2017**, *119*, 253601.
[4] S. Ditalia Tchernij, T. Lühmann, T. Herzig, J. Küpper, A. Damin, S. Santonocito, M. Signorile, P. Traina, E. Moreva, F. Celegato, S. Pezzagna, I. P. Degiovanni, P. Olivero, M. Jakšić, J. Meijer, P. M. Genovese, J. Forneris, *ACS Photonics* **2018**, *5*, 4864.
[5] Y. N. Palyanov, I. N. Kupriyanov, Y. M. Borzdov, N. V. Surovtsev, *Sci. Rep.* **2015**, *5*, 14789.
[6] R. Sandstrom, L. Ke, A. Martin, Z. Wang, M. Kianinia, B. Green, W. B Gao, I. Aharonovich, *Opt. Commun.* **2018**, *411*, 182.
[7] G. Prestopino, M. Marinelli, E. Milani, C. Verona, G. Verona-Rinati, P. Traina, E. Moreva, I. P. Degiovanni, M. Genovese, S. Ditalia Tchernij, F. Picollo, P. Olivero, J. Forneris, *Appl. Phys. Lett.* **2017**, 111105, *111*.
[8] T. Lühmann, S. Diziain, J. Meijer, S. Pezzagna, *ACS Photonics* **2022**, *9*, 1691.
[9] C. H. Su, A. D. Greentree, L. C. L. Hollenberg, *Phys. Rev. A* **2009**, *80*, 052308.
[10] D. Chen, Z. Mu, Yu Zhou, J E. Fröch, A. Rasmit, C. Diederichs, N. Zheludev, I. Aharonovich, W-Bo Gao, *Phys. Rev. Lett.* **2019**, *123*, 33602.
[11] A. Sipahigil, M. L. Goldman, E. Togan, Y. Chu, M. Markham, D. J. Twitchen, A. S. Zibrov, A. Kubanek, M. D. Lukin, *Phys. Rev. Lett.* **2012**, *108*, 143601.
[12] S. Rodt, S. Reitzenstein, *APL Photonics* **2021**, *6*, 010901.
[13] J. W. Fan, I. Cojocaru, J. Becker, I. V. Fedotov, M. H. A. Alkahtani, A. Alajlan, S. Blakley, M. Rezaee, A. Lyamkina, Y. N. Palyanov, Y. M. Borzdov, Y. P Yang, A. Zheltikov, P. Hemmer, A V. Akimov, *ACS Photonics* **2018**, *5*, 765.
[14] J. Li, H. Ebendorff-Heidepriem, B C. Gibson, A D. Greentree, M R. Hutchinson, P. Jia, R. Kostecki, G. Liu, A. Orth, M. Ploschner, E P. Schartner, S C. Warren-Smith, K. Zhang, G. Tsiminis, E M. Goldys, *APL Photonics* **2018**, *3*, 100902.
[15] J. Jeske, D. W. M. Lau, X. Vidal, L. P. Mcguinness, P. Reineck, B. C. Johnson, M. W. Doherty, J. C. Mccallum, S. Onoda, F. Jelezko, T. Ohshima, T. Volz, J. H. Cole, B. C. Gibson, A. D. Greentree, *Nat. Commun.* **2017**, *8*, 14000.
[16] J. Forneris, S. Ditalia Tchernij, P. Traina, E. Moreva, N. Skukan, M. Jakšić, V. Grilj, F. Bosia, E. Enrico, G. Amato, I. P. Degiovanni, B. Naydenov, F. Jelezko, M. Genovese, P. Olivero, *Phys. Rev. Appl.* **2018**, *10*, 014024.
[17] R. Sakurai, Y. Kainuma, T. An, H. Shigekawa, M. Hase, *APL Photonics* **2022**, *7*, 066105.
[18] J. L. Webb, L. Troise, N. W. Hansen, L. F. Frellsen, C. Osterkamp, F. Jelezko, S. Jankuhn, J. Meijer, K. Berg-Sørensen, J. F. Perrier, A. Huck, U. L. Andersen, *Phys. Rev. Appl.* **2022**, *17*, 064051.
[19] C. Bradac, W. Gao, J. Forneris, M. E. Trusheim, I. Aharonovich, *Nat. Commun.* **2019**, *10*, 5625.
[20] M. E. Trusheim, B. Pingault, N. H. Wan, M. Gündoğan, L. De Santis, R. Debroux, D. Gangloff, C. Purser, K. C. Chen, M. Walsh, J. J. Rose, J. N. Becker, B. Lienhard, E. Bersin, I. Paradeisanos, G. Wang, D. Lyzwa, A. R. P. Montblanch, G. Malladi, H. Bakhru, A. C. Ferrari, I. A. Walmsley, M. Atatüre, D. Englund, *Phys. Rev. Lett.* **2020**, *124*, 023602.
[21] M. H. Metsch, K. Senkalla, B. Tratzmiller, J. Scheuer, M. Kern, J. Achard, A. Tallaire, M. B. Plenio, P. Siyushev, F. Jelezko, *Phys. Rev. Lett.* **2019**, *122*, 190503.
[22] P. Siyushev, M. H. Metsch, A. Ijaz, J. M. Binder, M. K. Bhaskar, D. D. Sukachev, A. Sipahigil, R. E. Evans, C. T. Nguyen, M. D. Lukin, P. R. Hemmer, Y. N. Palyanov, I. N. Kupriyanov, Y M. Borzdov, L J. Rogers, F. Jelezko, *Phys. Rev. B* **2017**, *96*, 081201.
[23] D. D. Sukachev, A. Sipahigil, C. T. Nguyen, M. K. Bhaskar, R. E. Evans, F. Jelezko, M. D. Lukin, *Phys. Rev. Lett.* **2017**, *119*, 223602.
[24] M. K. Bhaskar, D. D. Sukachev, A. Sipahigil, R. E. Evans, M. J. Burek, C. T. Nguyen, L. J. Rogers, P. Siyushev, M. H. Metsch, H. Park, F. Jelezko, M. Lončar, M. D. Lukin, *Phys. Rev. Lett.* **2017**, *118*, 223603.
[25] J. N. Becker, J. Görlitz, C. Arend, M. Markham, C. Becher, *Nat. Commun.* **2016**, *7*, 13512.

© 2023 The Authors. Advanced Quantum Technologies published by Wiley-VCH GmbH

25119044, 2023, 8, Downloaded from https://onlinelibrary.wiley.com/doi/10.1002/qute.202300010 by Universita Di Torino, Wiley Online Library on [13/05/2024]. See the Terms and Conditions (https://onlinelibrary.wiley.com/terms-and-conditions) on Wiley Online Library for rules of use; OA articles are governed by the applicable Creative Commons License

[26] M. Ruf, N. H. Wan, H. Choi, D. Englund, R. Hanson, *J. Appl. Phys.* **2021**, *130*, 070901.
[27] D. N. Jamieson, W. I. L. Lawrie, S. G. Robson, A. M. Jakob, B. C. Johnson, J. C. Mccallum, *Mater. Sci. Semicond. Process.* **2017**, *62*, 23.
[28] S. Pezzagna, D. Rogalla, D. Wildanger, J. Meijer, A. Zaitsev, *New J. Phys.* **2011**, *13*, 035024.
[29] Yu Zhou, Z. Mu, G. Adamo, S. Bauerdick, A. Rudzinski, I. Aharonovich, W-Bo Gao, *New J. Phys.* **2018**, *20*, 125004.
[30] T. Lühmann, R. John, R. Wunderlich, J. Meijer, S. Pezzagna, *Nat. Commun.* **2019**, *10*, 4956.
[31] J. L. Pacheco, M. Singh, D. L. Perry, J. R. Wendt, G. Ten Eyck, R. P. Manginell, T. Pluym, D. R. Luhman, M. P. Lilly, M. S. Carroll, E. Bielejec, *Rev. Sci. Instrum.* **2017**, *88*, 123301.
[32] K. C. Wong, S. L. Ng, K. O. Ho, Y. Shen, J. Wu, K. T. Lai, M. Y. Leung, W. K. Leung, D. B. R. Dasari, A. Denisenko, J. Wrachtrup, S. Yang, *Phys. Rev. Appl.* **2022**, *18*, 024044.
[33] X. J. Wang, H. H. Fang, F. W. Sun, H. B. Sun, *Laser Photonics Rev.* **2022**, *16*, 2100029.
[34] U. Wahl, J. G. Correia, R. Villarreal, E. Bourgeois, M. Gulka, M. Nesládek, A. Vantomme, L. M. C. Pereira, *Phys. Rev. Lett.* **2020**, *125*, 45301.
[35] T. Iwasaki, F. Ishibashi, Y. Miyamoto, Y. Doi, S. Kobayashi, T. Miyazaki, K. Tahara, K D. Jahnke, L J. Rogers, B. Naydenov, F. Jelezko, S. Yamasaki, S. Nagamachi, T. Inubushi, N. Mizuochi, M. Hatano, *Sci. Rep.* **2015**, *5*, 12882.
[36] E. Corte, S. Sachero, S. Ditalia Tchernij, T. Lühmann, S. Pezzagna, P. Traina, I. P. Degiovanni, E. Moreva, P. Olivero, J. Meijer, M. Genovese, J. Forneris, *Adv. Photonics Res.* **2022**, *3*, 2100148.
[37] M. E. Trusheim, N. H. Wan, K. C. Chen, C. J. Ciccarino, J. Flick, R. Sundararaman, G. Malladi, E. Bersin, M. Walsh, B. Lienhard, H. Bakhru, P. Narang, D. Englund, *Phys. Rev. B* **2019**, *99*, 075430.
[38] P. Wang, T. Taniguchi, Y. Miyamoto, M. Hatano, T. Iwasaki, *ACS Photonics* **2021**, *8*, 2947.
[39] Y. N. Palyanov, I. N. Kupriyanov, Y. M. Borzdov, *Carbon* **2019**, *143*, 769.
[40] P. Wang, T. Taniguchi, Y. Miyamoto, M. Hatano, T. Iwasaki, *ACS Photonics* **2021**, *8*, 2947.
[41] K. M. C. Fu, C. Santori, P. E. Barclay, R. G. Beausoleil, *Appl. Phys. Lett.* **2010**, *96*, 121907.
[42] A. M. Zaitsev, N. M. Kazuchits, K. S. Moe, J. E. Butler, O. V. Korolik, M. S. Rusetsky, V. N. Kazuchits, *Diamond Relat. Mater.* **2021**, *113*, 108255.
[43] S. Pezzagna, D. Rogalla, D. Wildanger, J. Meijer, A. Zaitsev, *New J. Phys.* **2011**, *13*, 035024.
[44] Y. F. Meng, C. Yan, H. Mao, R. J. Hemley, *Proc. Natl. Acad. Sci. USA* **2008**, *105*, 17620.
[45] E. Corte, G. Andrini, E. Nieto Hernández, V. Pugliese, Â. Costa, G. Magchiels, J. Moens, S. M. Tunhuma, R. Villarreal, L. M. C. Pereira, A. Vantomme, J. G. Correia, E. Bernardi, P. Traina, I. P. Degiovanni, E. Moreva, M. Genovese, S. Ditalia Tchernij, P. Olivero, U. Wahl, J. Forneris, *ACS Photonics* **2022**, *13*, 101.
[46] S. C. Kitson, P. Jonsson, J. G. Rarity, P. R. Tapster, *Phys. Rev. A* **1998**, *58*, 620.
[47] J. Görlitz, D. Herrmann, P. Fuchs, T. Iwasaki, T. Taniguchi, D. Rogalla, D. Hardeman, P. O. Colard, M. Markham, M. Hatano, C. Becher, *npj Quantum Inf.* **2022**, *8*, 45.
[48] I. A. Dobrinets, V. G. Vins, A. M Zaitsev, *HPHT-Treated Diamonds, Springer Series in Materials Science*, Vol. *181*, Springer, Berlin, Heidelberg **2013**.
[49] N. H. Wan, T. J. Lu, K. C. Chen, M. P. Walsh, M. E. Trusheim, L. De Santis, E. A. Bersin, I. B. Harris, S. L. Mouradian, I. R. Christen, E. S. Bielejec, D. Englund, *Nature* **2020**, *583*, 226.
[50] N. H. Wan, T. J. Lu, K. C. Chen, M. P. Walsh, M. E. Trusheim, L. De Santis, E. A. Bersin, I. B. Harris, S L. Mouradian, I. R. Christen, E S. Bielejec, D. Englund, *Sci Adv.* **2020**, *6*, 226.
[51] A. M. Berhane, K. Y. Jeong, C. Bradac, M. Walsh, D. Englund, M. Toth, I. Aharonovich, *Phys. Rev. B* **2018**, *97*, 165202.
[52] D. Chen, N. Zheludev, W. B. Gao, *Adv. Quantum Technol.* **2020**, *3*, 1900069.
[53] D. Chen, J. E. Fröch, S. Ru, H. Cai, N. Wang, G. Adamo, J. Scott, F. Li, N. Zheludev, I. Aharonovich, W. Gao, *Nano Lett.* **2022**, *22*, 6306.
[54] D. Chen, N. Zheludev, W. B Gao, *Appl. Phys. B* **2022**, *128*, 1900069.
[55] D. Chen, J. E. Fröch, S. Ru, H. Cai, N. Wang, G. Adamo, J. Scott, F. Li, N. Zheludev, I. Aharonovich, W. Gao, *Metrologia* **2019**, *56*, 6306.

© 2023 The Authors. Advanced Quantum Technologies published by Wiley-VCH GmbH

25119044, 2023, 8, Downloaded from https://onlinelibrary.wiley.com/doi/10.1002/qute.202300010 by Universita Di Torino, Wiley Online Library on [13/05/2024]. See the Terms and Conditions (https://onlinelibrary.wiley.com/terms-and-conditions) on Wiley Online Library for rules of use; OA articles are governed by the applicable Creative Commons License